



Università degli Studi di Napoli *Federico II*

DOTTORATO DI RICERCA IN FISICA

Ciclo XXXIV

Coordinatore: prof. Salvatore Capozziello

The Archimedes experiment and the coupling between vacuum and gravity

Settore Scientifico Disciplinare FIS/01

Dottorando
Luciano Errico

Tutor
Prof. Enrico Calloni

Anni 2018/2022

Contents

Introduction	iii
1 The physics of the Archimedes experiment	1
1.1 Energy and gravity	1
1.2 Vacuum energy in QFT	3
1.3 The cosmological constant	4
1.4 The cosmological constant problem	5
1.5 The experimental path	8
1.5.1 The Casimir effect	8
1.6 A real multi-layered Casimir cavity: high- T_c superconductors	18
1.6.1 Vacuum energy modulation and superconductors	18
1.7 The energy modulation in real superconductors	19
1.8 Weighing a Casimir cavity	28
1.9 The Archimedes experiment	31
1.9.1 Expected sensitivity	33
2 Low seismic noise sites	36
2.1 Seismic noise in gravitational physics	36
2.2 Newtonian Noise	38
2.3 The Einstein Telescope Project	43
2.4 Sites Comparisons and latest results	48
3 Beam-balance prototype: measurements and results	52
3.1 The Balance working principle and its use as Tiltmeter in Virgo	52
3.1.1 Mechanical coupling of the arm tilt with the other degrees of freedom	53
3.1.2 Elasticity of the joints	53
3.1.3 Vertical positioning of the centre of mass	54

3.1.4	Optical sensing selection	56
3.1.5	Interferometer design	58
3.1.6	Actuators and controls	59
3.1.7	In air and remote tuning	60
3.1.8	The role of the prototype for ground tilt and NN studies in Virgo .	60
3.2	Tiltmeter results in Sos Enattos	62
3.3	The balance prototype and its use in low frequency	65
3.4	The balance in Sos Enattos and new recent results	68
3.4.1	Sample's suspension	68
3.4.2	In vacuum tuning and high power laser for thermal heating	69
3.4.3	Sensitivity	72
4	The Final Experiment	77
4.1	Seeting up the SAR-GRAV laboratory	77
4.2	Criostat and balance support	82
4.3	The balance	86
4.4	Towards a measurement for Tolman hypotesis	93
4.4.1	Sample's parameters choice	94
4.4.2	Preliminary heat deposition tests	96
5	Conclusions	101
A	Seismic glitchness at Sos Enattos site: impact on intermediate black hole binaries detection efficiency	103
B	High-bandwidth beam balance for vacuum-weight experiment and Newtonian noise subtraction	116
C	Picoradiant tiltmeter and direct ground tilt measurements at the Sos Enattos site	131
D	Progress in a Vacuum Weight Search Experiment	140
	Bibliography	iv

Introduction

The work of this thesis has been carried out by the candidate within the Archimedes collaboration, the national-wide net of physicists working on the Archimedes experiment.

Archimedes is a pure fundamental physics experiment devoted to uncertain the questioned interaction of quantum vacuum fluctuations with gravity, a profound topic in physics still unsolved 100 years after its first formulation. There are many ways to approach this topic. One way comes from cosmology and refers to this unsolved question as the cosmological constant problem. Another way, more close to the method with which the Archimedes experiment intends to investigate the question, is the following. Given our current knowledge of fundamental physics, there are 3 statement about gravity, energy and quantum mechanics which is useful to report here:

- General Relativity (GR) predicts that any form of energy interacts with gravity. In other words, given a massive body, its gravitational field – or, its tendency to be attracted by an external gravitational field – is not ruled only by the mass of its atoms, but it depends also by its internal energy and state of stress. For example, the heat stored inside the body or its rotational energy acts like an additional mass and contributes to the warping of the space-time. Since General Relativity is a classical theory, this statement refers only to classic energy terms.
- Quantum Field Theory (QFT) predicted new energy terms that have no counterpart in classical theories. These terms are linked to the fundamental states (or vacuum states) of quantum systems and are called zero-point energy terms (or vacuum energy terms). Even more, QFT states that the vacuum energy corresponding to the vacuum state of any physical quantum field is infinite. There are concrete proofs that vacuum energy is a physical entity, the most representative being the Casimir effect.

-
- General Relativity and Quantum Field Theory are not compatible. These theories are excellent tools to describe phenomena in two non-overlapping regimes (astronomical phenomena for GR, atomic and sub-atomic high energy phenomena for QFT), but they are based on different principles, they are developed with different mathematical tools and GR cannot be quantized because this theory is not renormalizable.

These 3 statements lead to the following questions: which role have vacuum energy stored inside massive bodies (or even massless fields) in terms of gravity? Does vacuum energy contribute to the gravitational field? Does vacuum energy affect the weight of massive bodies?

Since vacuum energy should be infinite, any simple attempt to take vacuum energy into account in General Relativity brings to paradoxical consequences. To this day, the physics community is still quite divided on what the misconceived assumptions are. This situation is remarkably resumed by the theoretical physicist Carlo Rovelli on saying that there is at the present time “a general theoretical confusion” regarding the motivations of the gravity apparent insensibility for the vacuum energy. From an experimental point of view it is remarkable that, in spite of this almost centenary question and in spite of a general expectation from the scientific community that it should be the case, an experiment to prove (or discard) that vacuum fluctuation gravitate didn't exist until Archimedes experiment has been started. Archimedes is an experiment that aims specifically to investigate and measure the coupling between vacuum energy and gravity by weighing a suitably realized Casimir cavity.

The Casimir effect is nowadays generally interpreted as a proof of the reality of the vacuum energy. If, in a Casimir cavity, is possible to modulate the reflectivity of the plates, then the vacuum energy stored inside it can be controlled; such cavities are naturally present in a class of high critical temperature superconductors, and their reflectivity (so their Casimir energy) can be modulated by varying its temperature around its critical temperature. Suspending two equal disks of these materials at the ends of a balance arm at rest in a gravitational field, such in a laboratory on the Earth, and modulating the Casimir energy only in one superconductor, the force acting on the balance arm should vary in time, and the balance arm should oscillate at the same frequency of the thermal modulation. This is essentially the way in which Archimedes will perform the measurement.

The Archimedes experiment is funded by Istituto Nazionale di Fisica Nucleare (INFN) since 2018.

During the work of this thesis the candidate has been engaged in several tasks. The first one is about testing the performances of a balance prototype in various sites in Italy, the best one being the Sos Enattos site in Sardinia, the Italian candidate site to host the future generation of European Gravitational Wave interferometer “Einstein Telescope”. Performances are meant in terms of torque sensitivity for the Archimedes experiment, but also in terms of ground-tilt sensitivity. As a matter of fact, when the balance prototype is not loaded with any sample it can be used as tiltmeter, i.e. as a sensor to monitor ground tilt oscillations. It’s worth to mention that the work performed in Sardinia also includes the development of the Sar-Grav laboratory, an INFN laboratory specifically dedicated to gravitational experiments, that needs low seismic noise.

The other main task has been the development of the final Archimedes’ balance. The candidate has designed the whole opto-mechanical apparatus, which now has been realized and it has been already assembled in Sar-Grav laboratory by the candidate himself. The very next step will be to run the first scientific measurements devoted to understand its ground-tilt and torque sensitivity, while the final vacuum weight measurements is planned in the next three years.

Chapter 1

The physics of the Archimedes experiment

The argument on which the Archimedes experiment intends to shed light straddles the two most complicated theories of fundamental physics. It is not intuitive to fully understand what the debated point of this topic is; for this reason, this chapter is devoted to explain in detail how energy and gravity are coupled, how vacuum energy arises from quantum mechanics and why vacuum energy cannot be coupled with gravity as well as classical energy.

1.1 Energy and gravity

In 1915-1916 Einstein completed his formulation of General Relativity [Einstein, 1915] and wrote his famous tensorial identity¹

$$R_{ab} - \frac{1}{2}g_{ab}R = 8\pi\frac{G}{c^4}T_{ab} \quad (1.1)$$

where

- g_{ab} is the metric tensor of the space-time;
- R_{ab} and R are the Ricci tensor and the scalar curvature, respectively, associated with the Levi-Civita covariant derivative defined on g_{ab} ;
- G and c are the gravitational constant and the speed of light, respectively;

¹The formula is written using the abstract index notation. A very clear and exhaustive discussion about this notation can be found in [Wald, 1984], paragraph 2.4 .

- T_{ab} is the energy-momentum tensor of the source deforming the space-time.

"Space-time tells matter how to move; matter tells space-time how to curve". This is Wheeler's succinct summary of Einstein's theory. The mutual dependence between space-time and matter is recognized in Einstein's equations which, in general, cannot be solved assuming g_{ab} or T_{ab} as a known term.

To give an idea of how these equations are to be used, let's assume that an initial condition $T_{ab}(t_0)$ for matter is known (i.e., we know the state of energy and stress for our matter at a given time t_0). If we want to solve Einstein's equations with no approximations, then we cannot make further assumptions. We cannot derive the dynamics of space-time for a given generic "evolving" matter (i.e. a matter whose motion and internal state of stress in time is given) $T_{ab}(t)$, because it is not guaranteed that for such a $T_{ab}(t)$ there will be a corresponding g_{ab} that satisfies Einstein's equations. This also means that it is not guaranteed that the chosen $T_{ab}(t)$ has a physical sense.

The only available option is the following: first, we have to solve Einstein's equation at the initial time t_0 to find an initial condition $g_{ab}(t_0)$ for the space-time which is compatible with $T_{ab}(t_0)$ (footnote: actually, not even the existence of this initial condition for spacetime is guaranteed, because not even $T_{ab}(t_0)$ can be assumed in a generic way. However, if $T_{ab}(t_0)$ represents a physical situation already encountered in nature, it is reasonable to assume it.). Then, Einstein's equations for any time t have to be solved for both g_{ab} and T_{ab} , simultaneously.

Mutual dependence between space-time and matter is not the only aspect of Einstein's equations that deserves comment. For our sake, it's also important to note that the term causing the warping of space-time is a whole energy-momentum tensor. It's not the tensor associated to a specific physical system. Any physical system that has an energy-momentum tensor associated to it is able to deform space-time. It is a huge change of paradigm with respect to Newtonian gravity, bringing with it two consequences:

- Gravity coming from massive bodies does not depend only from their mass, but also from all the forms of stress and energy stored inside those bodies [Kerr, 1963] [Tolman and Ehrenfest, 1930]. That's why Wheeler used the word "matter" in its sentence, instead of the word "mass".
- Gravity can be deformed also from massless fields [Misner et al., 1973].

1.2 Vacuum energy in QFT

The Lagrangian density of the electromagnetic field is [Peskin and Schroeder, 1995]

$$\mathcal{L}_{em} = -\frac{1}{4}F_{\mu\nu}F^{\mu\nu},$$

where $F_{\mu\nu} = \partial_\mu A_\nu - \partial_\nu A_\mu$ are the covariant electromagnetic field tensor components, A_μ being the covariant vector potential components, and $F^{\mu\nu} = g^{\mu\alpha}g^{\nu\beta}F_{\alpha\beta}$. Within the Coulomb gauge, so that A_μ can only be transverse, and passing in the Fourier space for the spatial coordinates, \mathcal{L}_{em} can be written as

$$\mathcal{L}_{em} = \int \frac{d\vec{k}}{(2\pi)^3} \frac{1}{8\pi} \sum_{s=1}^2 \left[\frac{1}{c^2} \dot{A}_{\mathbf{k},s}^* \dot{A}_{\mathbf{k},s} - |\vec{k}|^2 A_{\mathbf{k},s}^* A_{\mathbf{k},s} \right]$$

where the sum is over the two transverse components of the vector potential. Such a field $A_{\mathbf{k},s}$ will certainly have a non zero vacuum energy density, since its dynamics for each wave vector \mathbf{k} is the same one of an harmonic oscillator with square pulse $\omega_{\mathbf{k}}^2 = c^2|\vec{k}|^2$, as can be seen by the corresponding Euler-Lagrange equation

$$\frac{1}{c^2} \ddot{A}_{\mathbf{k},s} + |\vec{k}|^2 A_{\mathbf{k},s} = 0.$$

The quantization of the field is straightforward; passing to the hamiltonian density

$$\mathcal{H}_{em} = \int \frac{d\vec{k}}{(2\pi)^3} \frac{1}{2} \sum_{s=1}^2 \left[4\pi c^2 \Pi_{\mathbf{k},s}^* \Pi_{\mathbf{k},s} + \frac{\omega_{\mathbf{k}}^2}{4\pi c^2} A_{\mathbf{k},s}^* A_{\mathbf{k},s} \right]$$

where $\Pi_{\mathbf{k},s}$ is the conjugate momentum field of $A_{\mathbf{k},s}$, and considering the reality conditions for the fields in Fourier transform

$$\Pi_{\mathbf{k},s}^* = \Pi_{-\mathbf{k},s}, \quad A_{\mathbf{k},s}^* = A_{-\mathbf{k},s}$$

it's possible to promote $A_{\mathbf{k},s}$ and $\Pi_{\mathbf{k},s}$ to field operators with an appropriate commutation rule; let's write it in terms of ladder operators:

$$A_{\mathbf{k},s} = \sqrt{\frac{4\pi c^2 \hbar}{2\omega_{\mathbf{k}}}} (a_{-\mathbf{k},s} + a_{\mathbf{k},s}^\dagger), \quad \Pi_{\mathbf{k},s} = -i\sqrt{\frac{\hbar\omega_{\mathbf{k}}}{8\pi c^2}} (a_{-\mathbf{k},s} - a_{\mathbf{k},s}^\dagger) \quad (1.2)$$

$$[a_{\mathbf{k},s}, a_{\mathbf{k}',s'}^\dagger] = \delta(\mathbf{k} - \mathbf{k}') \delta_{ss'} \mathbb{I}. \quad (1.3)$$

They are interpreted as the annihilation and creation operators of a photon with a generalized momentum \mathbf{k} and in the polarization state s . Then, the hamiltonian density operator for the quantized electromagnetic field is

$$H_{em} = \int \frac{d\vec{k}}{(2\pi)^3} \sum_{s=1}^2 \hbar\omega_{\mathbf{k}} (a_{\mathbf{k},s}^\dagger a_{\mathbf{k},s} + \frac{1}{2}[a_{\mathbf{k},s}, a_{\mathbf{k},s}^\dagger]) \quad (1.4)$$

and its vacuum state is defined as

$$a_{\mathbf{k},s} |0\rangle = 0, \quad \forall \mathbf{k}, s. \quad (1.5)$$

The expectation value of H_{em} on the vacuum state gives finally the vacuum energy density desired. As anticipated, this energy density is divergent

$$\begin{aligned} \rho_{em}^{vac} = \langle 0 | H_{em} | 0 \rangle &= \int_0^\infty \frac{4\pi k^2 dk}{(2\pi)^3} \sum_{s=1}^2 \frac{1}{2} \hbar \sqrt{c^2 k^2} \\ &= \frac{1}{2\pi^2} \hbar c \frac{k^4}{4} \Big|_0^\infty \rightarrow \infty. \end{aligned} \quad (1.6)$$

Can this energy density enter in Einstein's equations? Such energy density is not compatible with the observed spacetime, as it will be described in the following.

1.3 The cosmological constant

The application to the whole universe of the General Relativity constituted the birth of modern Cosmology, together with the assumption of an homogeneous and isotropic universe, the so called *cosmological principle*. The results of this application are in fact two fundamental pillars in modern Cosmology: the Friedmann-Lemaître-Robertson-Walker (FLRW) line element [Misner et al., 1973]

$$ds^2 = -c^2 d\tau^2 + a^2(\tau) \left[\frac{dr^2}{1 - kr^2} + r^2 (d\theta^2 + \sin^2(\theta) d\phi^2) \right], \quad k = 0, \pm 1$$

as the only class of line elements consistent with the cosmological principle, and the Friedmann equations

$$\begin{cases} 3\left(\frac{\dot{a}}{a}\right)^2 = 8\pi G\rho - 3\frac{kc^2}{a^2} \\ 3\frac{\ddot{a}}{a} = -4\pi G\left(\rho + 3\frac{P}{c^2}\right) \end{cases}$$

to predict the evolution of the scale factor $a(\tau)$ depending on the topological factor k and the state equation on the whole matter, being ρ and P its mass density and its pressure, respectively.

The second Friedmann equation implies that for ordinary matter (i.e. $\rho > 0$, $P > 0$) $\ddot{a} \neq 0$; in other words, it's impossible to predict a static universe from (1.1). In 1917, under the assumption that the universe is static at cosmological scales, as shown by the observations at that time, Einstein modified his own equations adding a term proportional to g_{ab}

$$R_{ab} - \frac{1}{2}g_{ab}R + \Lambda g_{ab} = 8\pi \frac{G}{c^4}T_{ab}. \quad (1.7)$$

This modification is such that (1.7) will still imply the local conservation of energy and momentum as well as (1.1); on the other hand, with the new Friedmann equations obtained

$$\begin{cases} 3\left(\frac{\dot{a}}{a}\right)^2 = 8\pi G\rho - 3\frac{kc^2}{a^2} + \Lambda c^2 \\ 3\frac{\ddot{a}}{a} = -4\pi G\left(\rho + 3\frac{P}{c^2}\right) + \Lambda c^2 \end{cases}$$

it's possible to describe a static universe. The multiplicative factor Λ is the so called cosmological constant.

As already said, the first historical account involving Λ was about the actual static of the universe. It's well known that in the 1920s further astronomical observations were made and the evidence of an expanding universe was found [Hubble, 1929], making the cosmological constant unnecessary for the original purpose. But the use of this constant is still far to be obsolete; in fact, the discovery of an *accelerating* expansion of the universe [Riess et al., 1998] in the 1990 can still be interpreted today as an indication of a cosmological factor present in Einstein's equations.

1.4 The cosmological constant problem

The cosmological constant problem has emerged, instead, within another context, although always during the first years after the publication of General Relativity. One of the best description of this problem can be found in [Weinberg, 1989].

Since those years, as it will be described in the following, the cosmological constant problem remained a deep fundamental problem in physics and still nowadays is subject of long debate [Cree et al., 2018; Kohri and Matsui, 2017; Lombriser, 2019; Padmanabhan, 2016; Padmanabhan and Padmanabhan, 2014; Solà Peracaula, 2013].

Even before the discovery of the accelerating expansion of the universe, the case of

a non zero cosmological factor could not be discarded from the possible models, and the reason is related to the concept of vacuum energy density developed in Quantum Mechanics. It is well known that in all the formulations of the quantum theory (from the first single particle theories with no spin due to Schrödinger and Heisenberg, up to the most recent quantum field theories with more internal degrees of freedom), even for the simplest systems, the energy associated to the fundamental state is often not zero.

In the context of the quantum field theories, the fundamental state of a field is generally interpreted as the configuration of the field in which there are no particles ²; for this reason this state is usually called the vacuum state of the quantum field under consideration, and the energy density related to it is then named vacuum energy density.

Things are even more different from the classical physics perspective, because for all the quantum fields used nowadays in particle physics the vacuum energy density is a diverging quantity. As explained in many textbooks [Peskin and Schroeder, 1995] this infinite energy shift cannot be detected experimentally in particle Physics, since experiments measure only energy *differences* from the ground state to an excited state, and the absolute vacuum energy density cancels out in the calculations of these differences.

However, there is a way that the absolute vacuum energy could potentially be observed, and that is through the coupling of the vacuum energy to gravity, and this is where the cosmological constant problem emerges. In the Einstein's equations the source of gravitational field is present through its energy-momentum tensor; this tensor should take into account also the contribution of the vacuum state to the energy density. In this way, *anything that contributes to the energy density of the vacuum in Einstein's equations acts just like a cosmological constant*. In fact, Lorentz invariance tells us that for the vacuum state, the energy-momentum tensor must take the form ³

$$T_{\mu\nu}^{vac} = -\rho^{vac} g_{\mu\nu}$$

A check of (1.7) shows that this has the same effect as adding a term $8\pi G\rho_{vac}/c^4$ to the effective cosmological constant

$$\Lambda_{\text{eff}} = \Lambda + 8\pi \frac{G}{c^4} \rho^{vac}.$$

In the literature this result is also equivalently expressed saying that the Einstein cos-

²Precisely, it's the state in which there are no *real* particles, while it's allowed to have *virtual* particles.

³This formula is not a tensorial identity, but an equality between coordinate components of two tensors; the greek indices are used just to point it out. Actually, also the corresponding tensorial identity holds; however, in this case the use of greek indices was favoured to avoid confusion, since also the label *vac* - standing for vacuum - is present in the equality.

mological constant contributes a term $\Lambda c^4/8\pi G$ to the total effective vacuum energy

$$\rho_{\text{eff}} = \rho^{\text{vac}} + \frac{\Lambda c^4}{8\pi G} = \frac{\Lambda_{\text{eff}} c^4}{8\pi G}. \quad (1.8)$$

Measurements of the cosmological expansion exclude a large effective vacuum energy density. The current limit is

$$|\rho_{\text{eff}}| \lesssim 10^{-29} \text{ g/cm}^3 \approx 10^{-47} \text{ GeV}^4. \quad (1.9)$$

The trouble with this is that the energy density ρ^{vac} of empty space is likely to be enormously larger than 10^{-47} GeV^4 . The empty space is actually the configuration in which all the physical quantum fields are in their respective vacuum states: among all, let's estimate the vacuum energy density for the quantum electromagnetic field. The choice is not random; as will be better shown later, the Archimedes experiment will specifically investigate about the weight of the electromagnetic vacuum state.

The divergence of equation 1.6 is cured imposing a wave number cutoff Ω summing the zero-point energies of all normal modes. Assuming that General Relativity is valid up to the Planck scale $l_P = \sqrt{\hbar G/c^3}$, then it's reasonable to take $\Omega \simeq 2\pi/l_P$, which would give

$$\rho_{em}^{\text{vac}} \approx \frac{\hbar c}{16\pi^2} \left(2\pi \sqrt{\frac{c^3}{\hbar G}} \right)^4 = \frac{\pi^2 c^7}{\hbar G^2} \approx 10^{71} \text{ GeV}^4.$$

This result, together with (1.9), implies that the terms ρ^{vac} and $\Lambda c^4/8\pi G$ in (1.8) must cancel to more than 118 decimal places.

Another way to point out the problem is calculating the radius of the Einstein static universe taking into account ρ_{em}^{vac} but with a cut-off related to the classical electron radius $\lambda_e = e^2/m_e c^2 \simeq 10^{-15} \text{ m}$, as historically performed by Pauli [Kragh and Overduin, 2014]. During his attempt to describe a static universe, Einstein found a static solution for a universe filled with dust of zero pressure and energy density $\rho = \Lambda c^2/8\pi G$, $\Lambda > 0$. Its geometry was that of a sphere S_3 , with a proper circumference $2\pi r$, where

$$r = \frac{c^2}{\sqrt{8\pi G \rho}}. \quad (1.10)$$

Using the vacuum energy density ρ_{em}^{vac} with a cut-off $\Omega \simeq 2\pi/\lambda_e$ in place of ρ in (1.10), the estimated radius of the universe would be

$$\rho = \frac{1}{16\pi^2} \hbar c \left(\frac{2\pi}{\lambda_e} \right)^4 = \frac{\pi^2 \hbar c}{\lambda_e^4} \implies r = \frac{c^2}{\sqrt{8\pi G}} \cdot \frac{\lambda_e^2}{\pi \sqrt{\hbar c}} \approx 31 \text{ Km}.$$

As Pauli commented, the radius of the Einstein universe would then "*not even reach to the moon*", because the cosmological constant would be too big; a reason more to discard this cosmological model, even before the evidence of a non static universe.

These two ways of approaching the cosmological constant problem show vividly how unnatural it is to get a reasonably small effective cosmological constant, which is basically the core of the problem.

There is also another aspect of the problem that deserves to be remarked. The efforts to get a small Λ_{eff} are made not only to fit the observational data (1.9), but also for deep theoretical reasons. In fact, the appearance of an effective cosmological constant makes it impossible to find any solutions of the Einstein field equations in which $g_{\mu\nu}$ is the constant Minkowski term $\eta_{\mu\nu}$. That is, the original symmetry of general covariance, which is always broken by the appearance of any given metric $g_{\mu\nu}$, cannot, without fine-tuning, be broken in such a way as to preserve the subgroup of space-time translations. This situation, again, is unusual.

1.5 The experimental path

This long irreconcilability between Quantum Mechanics and General Relativity has had many theoretical investigations that, until now, have never reached a result considered satisfactory. The situation is made even more complex by the fact that there is no experimental result that has at least proved if the vacuum fluctuations follow in a naive way the laws of gravitation (and therefore there is something unknown that cancels the effect) or do not follow the laws of gravitation in a way analogous to the classical case. Archimedes proposes exactly to settle this question and to put the first experimental bases for the future theoretical speculation. The experimental method of verification of the interaction of vacuum fluctuations with gravity is the measurement of the weight variation of a Casimir cavity whose vacuum energy is modulated in time.

1.5.1 The Casimir effect

The Casimir effect, discovered around 70 years ago by Casimir (1948), is unanimously considered as one of the most direct manifestations of the existence of vacuum oscillations. Starting from 1970s it has been closely studied and experimentally checked, and nowadays the comprehension of this effect is such that it is applied in many researches in Fundamental Physics. An extensive literature has been produced during the years about this argument [Bordag et al., 2009].

In its simplest and original form, the Casimir effect is the attraction between two electrically neutral, infinitely large, parallel conducting planes placed in a vacuum. This is an entirely quantum effect, because in classical electrodynamics the force acting between two neutral planes is equal to zero. So, it is only the vacuum of the quantized electromagnetic field, i.e. the ground state of quantum electrodynamics, which causes the planes to attract each other⁴. Let's derive the results for this configuration, dealing carefully with all the theoretical details present in the calculus.

A configuration of two parallel planes of very large area S spaced a distance a apart is shown in Figure 1.1. Mathematically, the area S of each plane is supposed to be

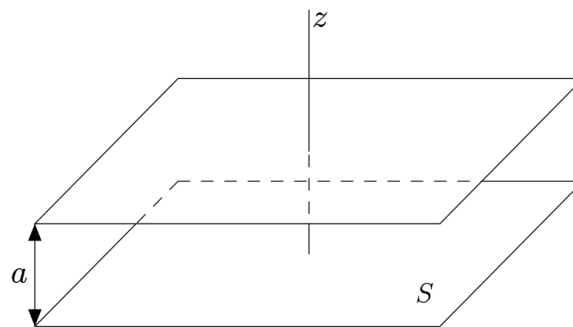


Figure 1.1: Two parallel ideal-metal planes of area S spaced a distance a apart.

infinitely large. However, the results obtained are applicable for the condition $a \ll \sqrt{S}$. From classical electrodynamics, the electric field and the magnetic induction, of both polarizations, satisfy the following boundary conditions on the surface of an ideal metal:

$$E_t(t, \mathbf{r})|_S = B_n(t, \mathbf{r})|_S = 0, \quad (1.11)$$

where \mathbf{r} is the radius vector of any point, \mathbf{n} is the unit vector normal to the surface, and the index "t" denotes the tangential component, which is parallel to the planes. The conditions (1.11) imply that an electromagnetic field can exist only outside an ideal conductor.

Let's formulate the problem in terms of the vector potential in Coulomb gauge, used in the previous section. Moreover, let's assume that both the electric field and magnetic induction vary sinusoidally in time, which is always true for any static configuration of

⁴Actually, a similar situation can be modelled using also other quantum fields, like scalar or spinorial fields. The effect can be significantly different from the electromagnetic case - a *repulsive* force instead of an attractive one - but the cause is always related to the vacuum fluctuations of the field took into account. However, only for the electromagnetic case are available experimental confirmations.

boundary surfaces, so that it's possible to separate the time variable. The first boundary condition can be equivalently rewritten as

$$A_{\mathbf{k},t}(\mathbf{r})|_S = 0, \quad (1.12)$$

where

$$A_{\mathbf{k},\mu}(t, \mathbf{r}) = \frac{1}{\sqrt{\omega_{\mathbf{k}}}} e^{-i\omega_{\mathbf{k}}t} A_{\mathbf{k},\mu}(\mathbf{r}).$$

The second boundary condition follows from (1.12) considering that $\mathbf{B} = \nabla \times \mathbf{A}$. With the separation of the time variable the Maxwell equations for the free electromagnetic field, written in terms of A_μ

$$\square A_\mu = 0$$

became

$$-\nabla^2 A_{\mathbf{k},\mu}(\mathbf{r}) = \omega_{\mathbf{k}}^2 A_{\mathbf{k},\mu}(\mathbf{r}).$$

This, together with the Dirichlet type boundary condition (1.12), defines an elliptic boundary problem. Let's fix the same reference frame shown in Figure 1.1, with z -axis perpendicular to the parallel planes, whose coordinates now are $z = 0$ and $z = a$. The set of solutions for our elliptic problem takes the form

$$\mathbf{A}_{\mathbf{k}}(\mathbf{r}) = \mathbf{A}_{\mathbf{k}_\perp, n}(\mathbf{r}) = \begin{pmatrix} Ab_x \cos(k_x x) \sin(k_y y) \sin(k_{z,n} z) \\ Ab_y \sin(k_x x) \cos(k_y y) \sin(k_{z,n} z) \\ Ab_z \sin(k_x x) \sin(k_y y) \cos(k_{z,n} z) \end{pmatrix}. \quad (1.13)$$

Here, $\mathbf{k}_\perp = (k_x, k_y)$ is the projection of the wave vector onto the metal planes, $k_\perp = |\mathbf{k}_\perp| = (k_x^2 + k_y^2)^{1/2}$ and $k_{z,n} = n\pi/a$, $n = 0, 1, 2, \dots$, while A is a dimensional multiplicative constant to keep the correct physical dimensions.

As required by (1.12), the first two components of the vector potential vanish on the planes. It's easy to see that the normalization condition

$$\int_V d\mathbf{r} \mathbf{A}_{\mathbf{k}}^*(\mathbf{r}) \mathbf{A}_{\mathbf{k}'}(\mathbf{r}) = 4\pi A^2 \delta_{\mathbf{k}, \mathbf{k}'} = 4\pi A^2 \delta(k_x - k'_x) \delta(k_y - k'_y) \delta_{n, n'}$$

with $\int_V d\mathbf{r} \equiv \int_{-\infty}^{\infty} dx \int_{-\infty}^{\infty} dy \int_0^a dz$, and the Coulomb gauge-fixing condition $\text{div} \mathbf{A}_{\mathbf{k}_\perp, n} =$

0, leads to the following values of the coefficients b_x and b_z :

$$b_x = b_y = \frac{4\sqrt{2\pi}}{\sqrt{a}} \frac{k_{z,n}}{\sqrt{(k_x + k_y)^2 + 2k_{z,n}^2}},$$

$$b_z = -\frac{4\sqrt{2\pi}}{\sqrt{a}} \frac{k_x + k_y}{\sqrt{(k_x + k_y)^2 + 2k_{z,n}^2}}.$$

The boundary conditions (1.12) allow the definition of two orthonormal polarization vectors $\epsilon_{\mathbf{k}}^{(s)}$:

$$\epsilon_{\mathbf{k}}^{(s)} \cdot \epsilon_{\mathbf{k}}^{(s')} = \delta_{s,s'}, \quad s, s' = 1, 2$$

perpendicular to the wave vector \mathbf{k} . They can be written in the form

$$\epsilon_{\mathbf{k}}^{(1)} = \frac{1}{k_{\perp}} \begin{pmatrix} k_y \\ -k_x \\ 0 \end{pmatrix}, \quad \epsilon_{\mathbf{k}}^{(2)} = \frac{1}{kk_{\perp}} \begin{pmatrix} k_x k_{z,n} \\ k_y k_{z,n} \\ -k_{\perp}^2 \end{pmatrix}. \quad (1.14)$$

Here, it is worthwhile to introduce some nomenclature. The plane formed by the wave vector $\mathbf{k} = (k_x, k_y, k_{z,n})$ and the normal to the boundary plane \mathbf{n} is called the plane of incidence. The vector $\epsilon_{\mathbf{k}}^{(1)}$ is perpendicular to \mathbf{k} and to the plane of incidence, whereas $\epsilon_{\mathbf{k}}^{(2)}$ is perpendicular to \mathbf{k} but parallel to the plane of incidence. The electromagnetic wave with \mathbf{E} parallel to $\epsilon_{\mathbf{k}}^{(1)}$ is called the transverse electric (TE) mode. For the TE mode, the magnetic induction \mathbf{B} is in the plane of incidence. The electromagnetic wave with \mathbf{E} parallel to $\epsilon_{\mathbf{k}}^{(2)}$ is called the transverse magnetic (TM) mode. For the TM mode, \mathbf{B} is perpendicular to the plane of incidence.

The space dependent part of the vector potential $\mathbf{A}_{\mathbf{k}}(\mathbf{r})$ can be expanded in terms of different polarizations:

$$\mathbf{A}_{\mathbf{k}}(\mathbf{r}) = \sum_{s=1}^2 \tilde{A}_{\mathbf{k},s}(\mathbf{r}) \epsilon_{\mathbf{k}}^{(s)},$$

where the expansion coefficients are given by the scalar products⁵

$$\tilde{A}_{\mathbf{k},s}(\mathbf{r}) = \mathbf{A}_{\mathbf{k}}(\mathbf{r}) \cdot \epsilon_{\mathbf{k}}^{(s)}.$$

⁵Here has been recovered a notation similar to the one in the previous section, with two indices to specify the wave vector and the transverse component. But in that case the potential was Fourier transformed from the space domain. Moreover, a tilde over the component $A_{\mathbf{k},s}$ has been added to highlight that it is written in the particular orthonormal reference frame where $\{\epsilon_{\mathbf{k}}^{(s)}, \mathbf{k}\}$ are basis vectors.

From (1.13) and (1.14), we can find these coefficients,

$$\begin{aligned}\tilde{A}_{k_{\perp},n,1}(\mathbf{r}) &= A \frac{b_x}{k_{\perp}} \left(\frac{\partial}{\partial x} - \frac{\partial}{\partial y} \right) \cos(k_x x) \cos(k_y y) \sin(k_{z,n} z), \\ \tilde{A}_{k_{\perp},n,2}(\mathbf{r}) &= -A \frac{1}{k k_{\perp}} \left(b_x \frac{\partial^2}{\partial x \partial z} + b_x \frac{\partial^2}{\partial y \partial z} + b_z k_{\perp}^2 \right) \sin(k_x x) \sin(k_y y) \cos(k_{z,n} z).\end{aligned}$$

For all $n \geq 1$ there are two different polarizations of the electromagnetic field confined between the parallel planes, but at $n = 0$, i.e. when \mathbf{k} is tangent to the planes, only one polarization survives, because the TE mode is forbidden by (1.11).

Now it's possible to estimate the vacuum energy of the quantized electromagnetic field in this configuration. The canonical quantization of this field has been shown in the previous section; using the ladder operators defined in (1.3), the polarization vectors (1.14) and the time dependence assumed, the field operator $\mathbf{A}(\mathbf{r}, t)$ can be written as

$$\mathbf{A}(\mathbf{r}, t) = \int_{-\infty}^{\infty} \frac{dk_x}{2\pi} \int_{-\infty}^{\infty} \frac{dk_y}{2\pi} \sum_{n=0}^{\infty} \sum_{s=1}^2 \frac{1}{\sqrt{\omega_{\mathbf{k}}}} \epsilon_{\mathbf{k}}^{(s)} \left[e^{-i\omega_{\mathbf{k}} t} \tilde{A}_{\mathbf{k},s}(\mathbf{r}) a_{\mathbf{k},s} + e^{i\omega_{\mathbf{k}} t} \tilde{A}_{\mathbf{k},s}^*(\mathbf{r}) a_{\mathbf{k},s}^{\dagger} \right]$$

where now the constant A in $\tilde{A}_{\mathbf{k},s}(\mathbf{r})$ can assume only discrete values and depends on \hbar and $\omega_{\mathbf{k}}$ ⁶.

Substituting this expression as a classical variable, it's possible to derive the hamiltonian density operator or, equivalently, the 00-component of the energy-momentum tensor operator, reminding that

$$T_{\mu\nu} = \frac{1}{4\pi} \left(F_{\mu\beta} F_{\nu}^{\beta} + \frac{1}{4} g_{\mu\nu} F_{\beta\gamma} F^{\beta\gamma} \right).$$

After that, the vacuum energy will be given by the expectation value of this operator over the vacuum state defined in (1.5), integrated over the space between the planes. The result can be presented in the form

$$E_0(a) = \frac{\hbar}{2} \int_0^{\infty} \frac{k_{\perp} dk_{\perp}}{2\pi} \left(\omega_{k_{\perp},0} + 2 \sum_{n=1}^{\infty} \omega_{k_{\perp},n} \right) S, \quad (1.15)$$

⁶Its exact expression depends on the measurement units used.

where the oscillator frequencies are given by

$$\omega_{\mathbf{k}} = \omega_{k_{\perp},n} = c\sqrt{k_{\perp}^2 + \left(\frac{\pi n}{a}\right)^2}. \quad (1.16)$$

The respective vacuum energy of the quantized electromagnetic field in the free Minkowski space-time, in the volume between the planes but with no boundary conditions is given by⁷

$$\begin{aligned} E_{0M}(a) &= \hbar a \int_{-\infty}^{\infty} \frac{dk_x}{2\pi} \int_{-\infty}^{\infty} \frac{dk_y}{2\pi} \int_{-\infty}^{\infty} \frac{dk_z}{2\pi} \omega_{\mathbf{k}} S \\ &= \frac{\hbar a}{\pi} \int_0^{\infty} \frac{k_{\perp} dk_{\perp}}{2\pi} \int_0^{\infty} dk_z \omega_{\mathbf{k}} S \end{aligned} \quad (1.17)$$

where

$$\omega_{\mathbf{k}} = c|\mathbf{k}| = c\sqrt{k_{\perp}^2 + k_z^2}. \quad (1.18)$$

The expressions (1.15) and (1.17) are both infinite, even assuming a finite area S of the planes. They diverge at large values of n and \mathbf{k} , and thus this is one of the manifestations of the problem of ultraviolet divergences in quantum field theory. Within this theory, these infinite quantities are usually treated with a *regularization procedure* to make them finite and to use them in a meaningful way.

There are many different regularization procedures that have been proposed in the literature. Some of them can be more simple than others, or more advantageous from a mathematical point of view, depending on the purpose. However, no physical meaning there should be behind these procedures: they are used only as a tool to make logically possible the calculus of the measurable quantities. So, after all the operations with the regularized finite quantities have been performed, it is necessary to prove that the result obtained does not depend on the specific regularization procedure.

Let's use the most simple one, which introduces an exponential cutoff function of the forms $\exp(-\delta c\sqrt{k_{\perp}^2 + k_{z,n}^2})$ and $\exp(-\delta c\sqrt{k_{\perp}^2 + k_z^2})$ after the summation and integration signs in (1.15) and (1.17), respectively, where $\delta > 0$ is a parameter. The resulting regularized vacuum energies are

$$E_0(a) = \hbar \int_0^{\infty} \frac{k_{\perp} dk_{\perp}}{2\pi} \left[\frac{\omega_{k_{\perp},0}}{2} \exp(-i\delta c k_{\perp}) + \sum_{n=1}^{\infty} \omega_{k_{\perp},n} \exp\left(-i\delta c\sqrt{k_{\perp}^2 + \left(\frac{\pi n}{a}\right)^2}\right) \right] S$$

⁷In the previous section the same vacuum energy density used here has been calculated, but using spherical coordinates, not cylindrical like in this case.

and

$$E_{0M}(a) = \frac{\hbar a}{\pi} \int_0^\infty \frac{k_\perp dk_\perp}{2\pi} \int_0^\infty dk_z \omega_{\mathbf{k}} \exp\left(-i\delta c \sqrt{k_\perp^2 + k_z^2}\right) S.$$

Now these quantities are ready to be used in other calculations; another standard procedure in quantum field theory consists in subtracting from the vacuum energy of the quantized electromagnetic field in the presence of ideal-metal planes the vacuum energy of the same field in free Minkowski space-time. It's interesting to notice that it was Casimir who first suggested this procedure. The motivation under this choice is that in all fields of physics, with the exception of Einstein's gravitational theory, energy is defined only up to an additive constant. Thus it is generally assumed that all physical energies should be measured starting from the top of the infinite vacuum energy in the free Minkowski space-time.

Let's calculate this difference, namely the Casimir energy, per unit area:

$$\begin{aligned} E(a) &\equiv \frac{E_0(a)}{S} - \frac{E_{0M}(a)}{S} \\ &= \hbar \int_0^\infty \frac{k_\perp dk_\perp}{2\pi} \left[\frac{\omega_{k_\perp,0}}{2} f(\delta, 0) + \sum_{n=1}^\infty \omega_{k_\perp,n} f(\delta, n) - \int_0^\infty dk_z \omega_{\mathbf{k}} f(\delta, k_z) \right] \end{aligned}$$

where $f(\delta, n)$ and $f(\delta, k_z)$ are the exponential cutoff functions.

The last two terms on the right-hand side of this equation can be simplified with the help of the *Abel-Plana formula*⁸:

$$\sum_{n=1}^\infty F(n) - \int_0^\infty F(t) dt = -\frac{1}{2}F(0) + i \int_0^\infty \frac{dt}{e^{2\pi t} - 1} [F(it) - F(-it)], \quad (1.19)$$

where $F(z)$ is an analytic function in the right half-plane. In our case, this function corresponds to

$$F(n) = \hbar \omega_{k_\perp,n} f(\delta, n).$$

It is evident that in the limiting case $\delta \rightarrow 0$, the integral on the right-hand side of (1.19) does not depend on the specific form of $f(\delta, n)$. This follows from the exponentially fast convergence of this integral, which permits taking the limit $\delta \rightarrow 0$ under the integral. Thus, one can simply omit the cutoff function in all calculations, as we do below. At the same time, the independence of the results obtained of the form of the cutoff function is automatically guaranteed.

⁸Other authors [Itzykson and Zuber, 1980] prefer to compute this difference using the Euler-MacLaurin formula, obtaining the same results presented here, as a proof of the fact that the physical quantities derived must not depend on which mathematical strategy has been adopted.

Moreover, the term $-F(0)/2$ in (1.19) is equal to $-\hbar\omega_{k_\perp,0}/2$, and it goes to simplify the opposite term in the Casimir energy. Then

$$E(a) = i \frac{\pi \hbar c}{2a} \int_0^\infty \frac{k_\perp dk_\perp}{2\pi} \int_0^\infty \frac{dt}{e^{2\pi t} - 1} [G_A(it) - G_A(-it)],$$

where $t = ak_z/\pi$ and the function $G_A(t)$ is defined by

$$G_A(t) \equiv (A^2 + t^2)^{1/2}, \quad A \equiv \frac{k_\perp a}{\pi}.$$

There is a new difference to estimate. It's useful to consider the more general function $G_A^{(\alpha)}(z)$, which is defined by

$$G_A^{(\alpha)}(z) = e^{\alpha \ln(A^2 + z^2)}.$$

This has branch points $z_{1,2} = \pm iA$. By going around the branch points, one can prove the equality

$$G_A^{(\alpha)}(it) - G_A^{(\alpha)}(-it) = 2ie^{\alpha \ln(t^2 - A^2)} \sin(\pi\alpha)\theta(t - A),$$

where $\theta(x)$ is the step function. For $\alpha = 1/2$, one obtains

$$G_A(it) - G_A(-it) = 2i(t^2 - A^2)^{1/2}\theta(t - A).$$

The application of this formula leads to the Casimir energy between the planes,

$$E(a) = -\frac{\pi^2 \hbar c}{a^3} \int_0^\infty y dy \int_y^\infty \frac{\sqrt{t^2 - y^2}}{e^{2\pi t} - 1} dt, \quad (1.20)$$

where the dimensionless variable $y = k_\perp a/\pi$ has been introduced instead of k_\perp . It is notable that $E(a)$ is finite. To evaluate (1.20), it's sufficient to change the order of the integration:

$$\begin{aligned} E(a) &= -\frac{\pi^2 \hbar c}{a^3} \int_0^\infty \frac{dt}{e^{2\pi t} - 1} \int_0^t y \sqrt{t^2 - y^2} dy \\ &= -\frac{\pi^2 \hbar c}{3a^3} \frac{1}{(2\pi)^4} \int_0^\infty \frac{v^3 dv}{e^v - 1}, \end{aligned}$$

when one more new variable, $v = 2\pi t$, has been introduced. After integration of this last expression, we finally obtain

$$E(a) = -\frac{\pi^2 \hbar c}{720 a^3}. \quad (1.21)$$

This is the Casimir energy between two ideal-metal planes. It's a meaningful quan-

tity, arising from the difference between two energy levels corresponding to two different vacuum states. It's interesting to remark that this subtraction procedure is usually interpreted as a *renormalization* of some physical constant in the bare effective action. In the simple case considered, the subtraction of the vacuum energy can be formally interpreted as a renormalization of the cosmological constant [Bordag et al., 2009], which connects the Casimir effect directly to the cosmological constant problem.

In order to stress about the fact that this quantity is independent from the regularization procedure, let's briefly derive it again from the (1.15), but adopting a completely different strategy. Firstly, we could notice that the first term in (1.15) gives a contribution to the vacuum energy that is independent from the separation distance. Such constant term can be interpreted as the proper energy of the ideal-metal planes, and they do not influence measurable quantities such as the Casimir force or pressure that are defined as derivatives of the energy with respect to the separation. Because of this, we could disregard it. After that, we could regularize the sum of the frequencies not introducing a cutoff function, but rather changing the power of the frequencies, leading to

$$E_0^{(s)}(a) = \hbar c \sum_{n=1}^{\infty} \int_0^{\infty} \frac{k_{\perp} dk_{\perp}}{2\pi} \left(k_{\perp}^2 + \frac{\pi^2 n^2}{a^2} \right)^{(1-2s)/2} S.$$

This procedure is called *zeta function regularization* because, making the change of variable $k_{\perp} = \pi n y/a$, the vacuum energy can be expressed in terms of the Riemann zeta function:

$$\begin{aligned} E_0^{(s)}(a) &= \hbar c \frac{1}{2\pi} \left(\frac{\pi}{a} \right)^{3-2s} \sum_{n=1}^{\infty} \frac{1}{n^{2s-3}} \int_0^{\infty} y dy (y^2 + 1)^{(1-2s)/2} S \\ &= \hbar c \frac{1}{2\pi} \left(\frac{\pi}{a} \right)^{3-2s} \zeta_R(2s-3) \int_0^{\infty} y dy (y^2 + 1)^{(1-2s)/2} S. \end{aligned}$$

The Riemann zeta function is well defined when its argument is greater than one, i.e. for $\Re(s) > 1$. We, however, need the value of $\zeta_R(z)$ at $z = -3$ in the limit of removing the regularization, $s \rightarrow 0$. This can be achieved using the well defined analytic continuation of the Riemann zeta function to the entire complex plane; its value for $\Re(z) < 0$ can be obtained from the reflection relation

$$\Gamma\left(\frac{z}{2}\right) \zeta_R(z) = \pi^{(2z-1)/2} \Gamma\left(\frac{1-z}{2}\right) \zeta_R(1-z),$$

where $\Gamma(z)$ is the well known gamma function. This results in $\zeta_R(-3) = 1/120$. The

integral in $E_0^{(s)}(a)$ can also be calculated at $\Re(s) > 3/2$:

$$\int_0^\infty y dy (y^2 + 1)^{(1-2s)/2} = -\frac{1}{3-2s}.$$

Substituting the regularized values for both the sum and the integral, and replacing $E_0^{(s)}(a)/S$ with $E(a)$ in the limiting case $s \rightarrow 0$, we obtain just the Casimir energy per unit area (1.21).

It should be noted that with the use of analytic continuation of zeta function at $z = -3$, not only did the vacuum energy remain finite, but this procedure also made this energy equal to the physical value obtained in cutoff regularization after the subtraction of the vacuum energy in free Minkowski space-time. Thus, the application of this method to two parallel planes is sometimes referred to as renormalization by zeta function regularization.

So, the Casimir effect in this very simple configuration is basically the attraction between the two planes due to the pressure

$$P(a) = -\frac{\partial E(a)}{\partial a} = -\frac{\pi^2 \hbar c}{240 a^4}. \quad (1.22)$$

Although the derivation within the frame of ideal-metal planes is very useful to point directly out to the Casimir effect, it's also true that this is a very basic model of a real configuration. To make it more realistic, these other additional contributions are usually considered:

- The real material boundaries of the planes and the dielectric properties of the medium between them, since in the experiments it is never a pure empty space. So, a model for the specific materials used needs to be provided too.
- The thermal corrections, being the apparatus in thermal equilibrium with an environment at finite temperature T . The results shown above correspond to the case of zero temperature, since all excitations of the real particles were neglected.
- The so called *radiative corrections*, arising from the interaction of the electromagnetic field with the electron-positron field. The vacuum energy, as we have considered it so far, can be represented in terms of Feynman graphs in the lowest order with respect to this interaction. This is referred as *one-loop* contribution. The radiative corrections are two- and higher-loop contributions.

These theoretical efforts, together with the development of experimental techniques, allowed to verify the Casimir effect with an increasing agreement during the years. The

Casimir force was measured for the first time in 1954 by Sparnay with 100% error bar, measured for the first time in the original configuration of metallic flat planes by [Bressi et al., 2002] and today is verified with accuracy of less than 1% in agreement with theoretical expectations [Klimchitskaya et al., 2009].

Any way, given a volume of space, the Casimir effect suggests an experimental procedure to decrease the vacuum energy of the electromagnetic field inside this volume. Within the context of the cosmological constant problem, this can be an useful tool to verify the coupling between the quantized electromagnetic field and gravity.

1.6 A real multi-layered Casimir cavity: high- T_c superconductors

1.6.1 Vacuum energy modulation and superconductors

For a single Casimir cavity with $S \approx 1 \text{ dm}^2$ and $a \approx 1 \mu\text{m}$, the Casimir energy would be far too small to allow any experimental verification of its weight. To actually perform any measurement, the body has to consist in a multi-layer of many cavities to enhance the effect. Furthermore, a key point in modulation is that *the energy supplied to the system should be at most of the same order of magnitude of the Casimir energy modulation*, otherwise it will be extremely difficult to recover the Casimir contribution. Some recent techniques, as an example, even if deep in modulating the Casimir energy [Klimchitskaya et al., 2009], cannot be applied in our case because the efficiency is very low: only a few parts on a billion of the energy supplied to the system are converted in Casimir energy variation.

Our proposed way is to use superconductors. In the past years many activities have been developed within Archimedes' group to evaluate and measure the variation of Casimir energy at the cavity plate superconducting transition. The field was quite new and so the analysis started considering superconductors of type I and then it has been extended to high- T_c stratified superconductors.

It has been demonstrated that the Casimir energy is indeed changed when the plates exhibit a transition and a suitable cavity has been dimensioned to prove experimentally the effect. In particular Archimedes' group demonstrated that when the plate is part of the cavity and its temperature is lower than superconducting transition T_c , i.e. the plate is superconducting, the energy to be supplied to it to destroy the superconductivity and recover normal conductivity *is higher than in case of plate stand alone*. This additional energy is needed to overcome the Casimir energy, which is more negative in the

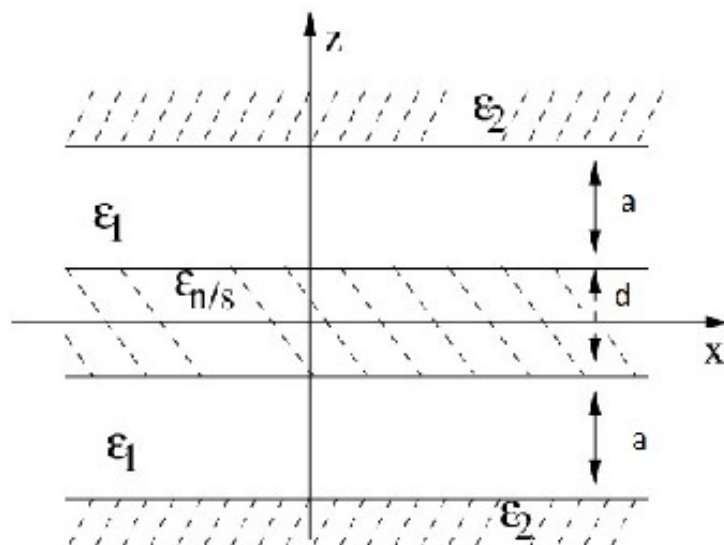


Figure 1.2: Five-layer cavity: a thin superconducting film of thickness d is placed between two thick metallic slabs, which constitute the plates of the cavity. The gaps of width a that separate the film from the plates are filled with insulating material.

superconducting state [Bimonte et al., 2005a,b]. The energy is measured by the external magnetic field needed to recover the normal state and indeed it has been measured that a higher magnetic field is needed for the plate being part of a cavity, compatible with the expectations [Allocca et al., 2012; Bimonte et al., 2008a].

Based on this analysis, the actual experimental sample will be a stratified superconductor, namely GaBCO.

1.7 The energy modulation in real superconductors

To fix the ideas consider a double cavity, consisting of two identical plane parallel mirrors, made of a non-superconducting and non-magnetic metal, between which a plane superconducting film of thickness D (order of few nanometers) is placed, separated by a non-conducting material gap of equal width L (order few nanometers) from the two mirrors, as in Figure 1.2. If the superconductor is of type I, for any temperature T lower than the transition temperature T_c the transition Gibbs free energy ΔF can be written as the sum of the condensation energy $\mathcal{E}(T)$ and the variation of Casimir energy $\Delta E_{\text{cas}}(T)$

:

$$\Delta F = \mathcal{E}(T) + \Delta E_{\text{cas}}(T).$$

In writing these equations, we have exploited the fact that all quantities referring to the film, like the penetration depth, condensation energy, etc., are not affected by virtual photons in the surrounding cavity. This is a very good approximation, since the leading effect of radiative corrections is a small renormalization of the electron mass as discussed in [Bimonte et al., 2005a,b]. The variation of Casimir energy at the transition can be calculated starting from the theory of Casimir energy in stratified media, derived in [Bordag, 2006]. We consider first the $T = 0$ case. The Casimir energy is given by the sum over the cavity modes; the wave numbers k are discretized in the z direction (orthogonal to the plates) and continuous in the parallel directions (the xy plane). The variation of Casimir energy $\Delta E_{\text{cas}}^0(a, d)$ at the transition can then be written as

$$\Delta E_{\text{Cas}}^0(a, d) = S \frac{\hbar}{2} \int \frac{dk_1 dk_2}{(2\pi)^2} \left\{ \sum_p (\omega_{\mathbf{k}_\perp, p}^{(n, TM)} + \omega_{\mathbf{k}_\perp, p}^{(n, TE)}) - \sum_p (\omega_{\mathbf{k}_\perp, p}^{(s, TM)} + \omega_{\mathbf{k}_\perp, p}^{(s, TE)}) \right\}, \quad (1.23)$$

where $S \gg a^2$ is the area of the cavity, $\mathbf{k}_\perp = (k_1, k_2)$ denotes the two-dimensional wave vector in the xy plane, while $\omega_{\mathbf{k}_\perp, p}^{(n/s, TM)}$ ($\omega_{\mathbf{k}_\perp, p}^{(n/s, TE)}$) denote the proper frequencies of the TM (TE) modes, in the n/s states of the film, respectively.

By exploiting the Cauchy integral formula, and by subtracting the contribution corresponding to infinite separation a (for details, we refer the reader to [Bordag, 2006, Chapter 4]), one can rewrite the renormalized sums in (1.23) as integrals over complex frequencies $i\zeta$:

$$\left(\sum_p \omega_{\mathbf{k}_\perp, p}^{(n, TM)} - \sum_p \omega_{\mathbf{k}_\perp, p}^{(s, TM)} \right)_{\text{ren}} = \frac{1}{2\pi} \int_{-\infty}^{\infty} d\zeta \left(\log \frac{\Delta_n^{(1)}(i\zeta)}{\tilde{\Delta}_{n\infty}^{(1)}(i\zeta)} - \log \frac{\Delta_s^{(1)}(i\zeta)}{\tilde{\Delta}_{s\infty}^{(1)}(i\zeta)} \right), \quad (1.24)$$

where $\Delta_{n/s}^{(1)}(i\zeta)$ is the expression in [Bordag, 2006, Eq. 4.7] (evaluated for $\epsilon_0 = \epsilon_{n/s}$) and $\tilde{\Delta}_{n/s\infty}^{(1)}(i\zeta)$ denotes the asymptotic value of $\Delta_{n/s}^{(1)}(i\zeta)$ in the limit $a \rightarrow \infty$ (corresponding to the limit $d \rightarrow \infty$ with the notation of [Bordag, 2006]). A similar expression can be written for the TE modes, which involves the quantity $\Delta_{n/s}^{(2)}(i\zeta)$ defined in [Bordag, 2006, Eq. 4.9].

Upon inserting (1.24), and the analogous expression for TE modes, into (1.23) one gets the following expression for the (renormalized) variation $\Delta E^{(C)}(a, d)$ of the Casimir en-

ergy:

$$\Delta E_{\text{cas}} = S \frac{\hbar}{2} \int \frac{d\mathbf{k}_{\perp}}{(2\pi)^2} \int_{-\infty}^{\infty} \frac{d\zeta}{2\pi} \left(\log \frac{Q_n^{TE}}{Q_s^{TE}} + \log \frac{Q_n^{TM}}{Q_s^{TM}} \right), \quad (1.25)$$

where we set

$$Q_I^{(TM/TE)}(\zeta) \equiv \frac{\Delta_I^{(1/2)}(i\zeta)}{\tilde{\Delta}_I^{(1/2)}(i\zeta)}, \quad I = n, s.$$

The $d\mathbf{k}_{\perp}$ integration can be re-expressed through the dp integration by means of the standard formula $k_{\perp}^2 = (p^2 - 1)\zeta^2/c^2$. The above expression for $\Delta E_{\text{cas}}(a, d)$ turns therefore into

$$\Delta E_{\text{cas}} = \frac{\hbar S}{4\pi^2 c^2} \int_1^{\infty} p dp \int_0^{\infty} d\zeta \zeta^2 \left(\log \frac{Q_n^{TE}}{Q_s^{TE}} + \log \frac{Q_n^{TM}}{Q_s^{TM}} \right), \quad (1.26)$$

where the coefficients $Q_I^{(TM/TE)}$ read as

$$\begin{aligned} Q_I^{TE/TM}(\zeta, p) &= \\ &= \frac{(1 - \Delta_{1I}^{TE/TM} \Delta_{12}^{TE/TM} e^{-2\zeta K_1 \frac{L}{c}})^2 - (\Delta_{1I}^{TE/TM} - \Delta_{12}^{TE/TM} e^{-2\zeta K_1 \frac{L}{c}})^2 e^{-2\zeta K_I \frac{D}{c}}}{1 - (\Delta_{1I}^{TE/TM})^2 e^{-2\zeta K_I \frac{D}{c}}}, \end{aligned}$$

with

$$\Delta_{jl}^{TE} = \frac{K_j - K_l}{K_j + K_l}, \quad \Delta_{jl}^{TM} = \frac{K_j \epsilon_l(i\zeta) - K_l \epsilon_j(i\zeta)}{K_j \epsilon_l(i\zeta) + K_l \epsilon_j(i\zeta)}, \quad (1.27)$$

$$K_j = \sqrt{\epsilon_j(i\zeta) - 1 + p^2}, \quad I = n, s; \quad j, l = 1, 2, n, s. \quad (1.28)$$

The generalization of these formulas to the case of finite temperature T can be done with the well-known technique of Matsubara frequencies. This consists in replacing in (1.25) the integration $\int d\zeta/2\pi$ by the summation $kT/\hbar \sum_l$ over the Matsubara frequencies $\zeta_l = 2\pi l/\beta$, where $\beta = \hbar/(kT)$. This leads to the following expression for the variation $\Delta E_{\text{cas}}(T)$ of Casimir free energy:

$$\Delta E_{\text{cas}}(T) = S \frac{kT}{2} \sum_{l=-\infty}^{\infty} \int \frac{d\mathbf{k}_{\perp}}{(2\pi)^2} \left(\log \frac{Q_n^{TE}}{Q_s^{TE}} + \log \frac{Q_n^{TM}}{Q_s^{TM}} \right). \quad (1.29)$$

Equations (1.26 - 1.29) involve the dielectric functions $\epsilon(i\zeta)$ of the various layers evaluated at imaginary frequencies $i\zeta$. For the outermost metal plates, the Drude model for the dielectric function can be used:

$$\epsilon_D(\omega_p) = 1 - \frac{\Omega^2}{\omega(\omega + i\gamma)}, \quad (1.30)$$

where Ω_p is the plasma frequency and $\gamma = 1/\tau$, with τ the relaxation time. We denote by Ω_{p2} and τ_{p2} the values of these quantities for the outer plates. As is well known, the Drude model provides a very good approximation in the low-frequency range $\omega \approx 2kT_c/\hbar \simeq 10^{11} \div 10^{12}$ rad/sec which is involved in the computation of $\Delta E_{cas}(T)$.

The continuation of (1.30) to the imaginary axis is of course straightforward and gives

$$\epsilon_D(i\zeta) = 1 + \frac{\Omega^2}{\zeta(\zeta + \gamma)}. \quad (1.31)$$

For the insulating layers, a constant dielectric function can be taken, as a good approximation [Bimonte et al., 2005b; Bordag, 2006], equal to the static value:

$$\epsilon_1(\omega) = \epsilon_1(0). \quad (1.32)$$

As far as the film is concerned, in case of type-I superconductors, the Drude expression (1.30) can be used in the normal state, with appropriate values for the plasma frequency Ω_n and the relaxation time τ_n .

In the superconducting state, the technical details are more involved, but the theory is still based on firm ground. The real part of the conductivity $\sigma(\omega)$ has a semi-explicit form, derived by the BCS theory, that we report in [Bimonte et al., 2005b], and shows the lowering of absorption component for frequencies $\hbar\omega$ less than the condensation energy gap $\Delta(T)$, and tends to the Drude expression for higher frequencies.

From the real part of the conductivity $\sigma'(\omega)$ one can obtain the imaginary part of the dielectric function $\epsilon''(\omega)$ with the standard relation

$$\epsilon''(\omega) = \frac{4\pi}{\omega} \sigma'(\omega). \quad (1.33)$$

Last, from the dispersion relation, the dielectric function at imaginary frequency can be found in the form

$$\epsilon_s(i\zeta) - 1 = \frac{2}{\pi} \int_0^\infty d\omega \frac{\omega \epsilon_s''(\omega)}{\zeta^2 + \omega^2}. \quad (1.34)$$

With this recipe it is possible to calculate the variation of free energy at the transition. In general, for a stand-alone superconductor, not being part of a Casimir cavity, the free energy variation at the transition is equal to the source magnetic energy necessary to destroy the superconductivity:

$$\frac{V}{2\mu_0} \left(\frac{B_{c\parallel}(T)}{\rho} \right)^2 = \mathcal{E}_{\text{cond}}(T), \quad (1.35)$$

where V is the volume of the superconducting film. The term ρ takes into account that for a thin film, of thickness $d \ll \lambda, \xi$ (with λ the penetration depth and ξ the correlation length), placed in a parallel magnetic field, expulsion of the magnetic field is incomplete, and consequently the critical field increases from B_c (the bulk value) to $B_{c\parallel}$. Following the Ginzburg-Landau theory, the transition is a second-order transition (no latent heat) and as B approaches $B_{c\parallel}$ the order parameter (energy gap, "number of superconducting electrons", or Ginzburg-Landau ψ function) approaches zero continuously while the penetration depth λ increases from $\lambda(T)$, the value at zero field, to infinity Tinkham [1975]. The coefficient ρ has the approximate expression

$$\rho \approx \sqrt{24} \frac{\lambda}{d} \left(1 + \frac{9d^2}{\pi^6 \xi^2} \right), \quad (1.36)$$

where the second term inside the brackets accounts for surface nucleation.

If the film is part of a cavity, the variation of energy at the transition is the sum of the condensation energy and the Casimir energy, so that the previous equation becomes

$$\frac{V}{2\mu_0} \left(\frac{B_{c\parallel}^{\text{cav}}(T)}{\rho} \right)^2 = \mathcal{E}_{\text{cond}}(T) + \Delta E_{\text{cas}}(T). \quad (1.37)$$

This equation shows that it is possible to measure the contribution of Casimir energy to the total free energy variation: it consists in measuring the critical magnetic field for a stand-alone film and compare it with a film that is part of a Casimir cavity. The relative shift is

$$\frac{\delta B_{c\parallel}}{B_{c\parallel}} \approx \frac{\Delta E_{\text{cas}}}{2 \mathcal{E}_{\text{cond}}(T)}. \quad (1.38)$$

For suitable choice of the parameters, like superconductor and metal and dielectric materials, thicknesses, temperatures, it is possible to show experimentally that the Casimir effect enhances the critical field. The measurement has been indeed performed and shown to be fully compatible with the expectations [Allocca et al., 2012; Bimonte et al., 2008a].

The use of type-I superconductors for measuring the vacuum energy at the transition is thus meaningful and relies upon firm ground. Nevertheless, since the type-I superconductors are good conductors also in normal state, the modulation of Casimir energy, with respect to total Casimir energy, $\eta = \frac{\Delta E_{\text{cas}}}{E_{\text{cas}}}$, is quite small, of order $\eta \approx 10^{-8}$ for a few nanometers thicknesses and temperatures of order 1 K [Bimonte et al., 2005b]. With this tiny modulation it is possible to measure the effect on the critical field and on the

variation of transition energy, because also the condensation energy, in type-I superconductors, is small. But it is not sufficient to prove the weight of the vacuum, because it is in absolute too small. It is therefore necessary to consider high- T_c superconductors.

Some of their properties are of particular interest: generally high- T_c superconductors, particularly cuprates, are by construction multilayered cavities, being composed by Cu-O planes, that perform the superconducting transition, separated by non-conducting planes. More important, in normal state, also the Cu-O planes are poor conductors, so that the variation of Casimir energy is high at the transition.

In these systems the evaluation of Casimir energy is not yet completely exploited. A first important step has been the recent analysis on the Casimir energy of a cavity composed by two flat plasma sheets at zero temperature ???. The theoretical foundation is the same as for dielectric materials and conductors described above and it is based on the summation over zero-point energies of electric modes. The approximations of plasma sheet, with no internal dissipation, and zero temperature give to the result the status of a work that can be used as providing the order of magnitude of the effect. The calculation of the renormalized energy E_{cas} brings thus to the usual formula for two planes separated by a distance a :

$$E_{\text{cas}} = -\frac{\hbar}{2c} \int \frac{d\mathbf{k}_{\perp}}{(2\pi)^2} \int_{k_0}^{\infty} dk \frac{k}{\pi \omega(\mathbf{k}_{\perp}, ik)} \log t(ik), \quad (1.39)$$

where the lower integration boundary $k_0 = \mathbf{k}_{\perp}$ and the transmission coefficients t , for plasma sheets, for the TE and TM modes are given by ?

$$(t(ik))^{-1} = 1 - \left(\frac{\Omega}{k + \Omega} \right)^2 e^{-2ka}, \quad (TE), \quad (1.40)$$

and

$$(t(ik))^{-1} = 1 - \left(\frac{\Omega k}{\mathbf{k}_{\perp}^2 - k^2 - \Omega k} \right)^2 e^{-2ka}, \quad (TM). \quad (1.41)$$

The parameter Ω is proportional to the density of the carrier in the plasma sheet ???:

$$\Omega \equiv \frac{nq^2}{2mc^2\epsilon_0}, \quad (1.42)$$

where n is the surface density of delocalized particles, q their electric charge, m their mass. For small separation a the above integrals lead to the expression for energy

$$E_c(a) = -5 \times 10^{-3} \hbar \frac{cA}{a^{5/2}} \sqrt{\Omega}. \quad (1.43)$$

An estimate of the parameter Ω has been proposed recently by ? with the aim of evaluating the Casimir effects in High- T_c cuprates. The particles' density is estimated as $n = 10^{14} \text{ cm}^{-2}$, the charge $q = 2e$, the mass $m = 2\alpha m_e$ with $\alpha = 5$. Inserting these values in Eq. (1.43), the reduction factor of Casimir energy with respect to the ideal case, at typical separation $a \approx 1 \text{ nm}$ turns out to be $\eta(a) = 4 \times 10^{-4} \times \sqrt{\frac{a}{1nm}}$. Considering that in normal state the layer is very poorly conductive, this factor is (almost) equal to the variation of Casimir energy in the transition. Thus, the use of High- T_c superconductors leads to the gain of about 4 orders of magnitude in the modulation of Casimir energy.

The other key point is the ratio between the variation in Casimir energy at the transition and the total energy variation. In his paper ?, Kempf, checking his hypothesis with a calculation of the critical temperature T_c , has conjectured that in cuprates the whole energy variation at the transition could be due to Casimir energy. A check of this hypothesis can be done by comparing the estimated variation of Casimir energy with the total variation of the energy of the superconductor at the transition. As reported in Appendix B of ref Calloni et al. [2014], in type-II superconductors the energy variation is determined by the thermodynamical critical field $B_c(T)$. In cuprates the critical field is of order of 1 Tesla (for a detailed description and calculation see Calloni et al. [2014]). The energy density variation ΔU is about

$$\Delta U \approx \frac{B_c^2}{2\mu_0} \approx 4 \times 10^5 \text{ J/m}^3. \quad (1.44)$$

The variation of Casimir energy density ΔU_{cas} is, following the Kempf estimate,

$$\Delta U_{\text{cas}} \approx \eta(a) \frac{N\pi^2 \hbar c}{720 a^3} \approx 2 \times 10^5 \text{ J/m}^3, \quad (1.45)$$

where $N \approx 10^9$ is the number of cavities per unit height. The two energies are indeed, roughly, of the same order of magnitude.

Notice that, as stated in Ref. ?, the separation among the plates being of order of 1 nm, the "Casimir" energy is dominated by plasmons (i.e. by the Van der Waals) energy with respect to vacuum energy. Thus, our assumption of Kempf's hypothesis is needs to be refined with an accurate analysis on coupled cavities to better uncertain each mode contribution. Indeed in parallel with this assumption work has been done during the years of Archimedes in commission II, on the evaluation of Casimir contribution in superconductor considering the actual case of coupled cavities. This is the second and more solid path to formulate a complete calculation on the evaluation of vacuum energy contribution in stratified media. The approach has been to consider layered

systems composed by layers of superconductor separated by dielectric. In this approach the superconductor is of type one, to maintain the simulation well under control for the point of view of compounds, the layers are of the order of few nanometers and the separations are of the same order of magnitude and the coupling of the layers is taking into account by imposing boundary conditions on the layers.

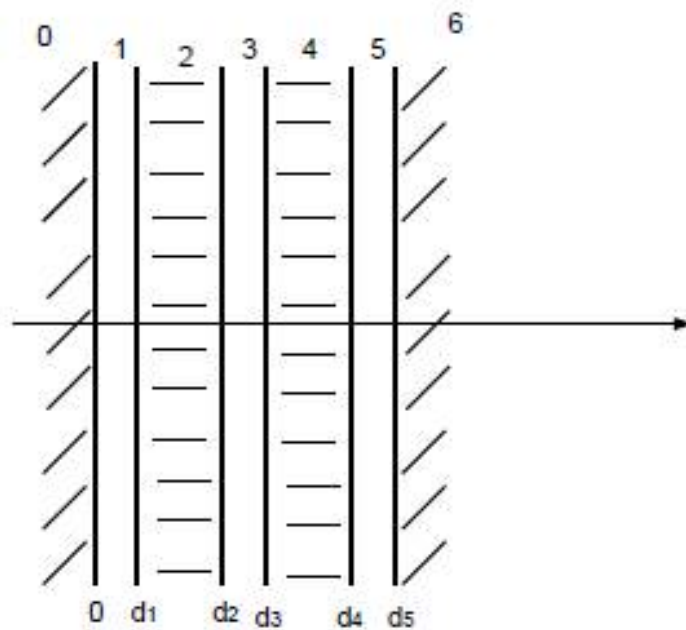


Figure 1.3: A three layer cavity. In the 0,2,4, and 6 zone there is Nb; in the 1,3,5 vacuum. d_i is the thickness of the i -th slab

In case of coupled cavities the calculations are again cumbersome and are the subject of a paper submitted to PRD Rosa et al. [2017].

The main important result, that is in strong support of previous assumptions, is that coupled superconducting cavities exhibits a much higher Casimir variation at the transition with respect to a single cavity in which only one plate becomes superconductor, about three orders of magnitude, due essentially to the Matsubara TM zero mode and higher transition temperature of about 10 K. This result have been checked against

a thorough numerical analysis, using Nb as superconductor, that confirmed the huge contribution from the Matsubara TM zero mode. While the dynamical structure of the modes requires a proper analytic continuation to real frequencies, the Matsubara zero mode is strictly related to the mode at zero real frequency, thus an important role is played by the static TM. This physically arises because, while a static electric field in a superconductor (and in a metal as well) is rapidly screened on short length-scales, the magnetic field parallel to the vacuum-Nb interface can penetrate over a substantial distance, set by the London penetration depth. This length is shortest in clean Nb, but still of the order of tens of nm, and increases in the presence of impurities. It is not surprising therefore, that the zero-frequency TM mode links the various adjacent cavities, providing a substantial inter-cavity contribution to the Casimir energy.

This enhancement, whenever to be recovered also for high T_c layered structures, fills the gap from the modulation depth of a type I superconductor low temperature not coupled cavity, $\eta_l \approx 10^{-8}$ to the Kempf assumed modulation depth of $\eta_K \approx 10^{-4}$ in high T_c superconductors.

The actual modulation of the effect will be performed by temperature modulation in vanishing field. No latent heat is present.

The quantity that will generate the variation of gravitational force on the sample is (the variation of) the internal energy UV , where V is the volume of the sample of the superconductor. The variation of internal energy density U is evaluated in ?. It is given by the equation

$$\Delta U = \int_T^{T_c} C_n dT + \frac{B_0^2}{2\mu_0} [1 - (T/T_c)^2]^2 + 2 \left(\frac{T}{T_c} \right)^2 [1 - (T/T_c)^2]. \quad (1.46)$$

This is the sum of three terms: the internal energy variation of normal state, the contribution of the Gibbs energy and the contribution of entropy. The third term, for temperatures near T_c , gives the biggest contribution. This equation shows that the variation of internal energy is proportional to, and roughly of the same order of magnitude of the energy of the thermodynamical critical field and, under the Kempf estimate, it is expected to be of the same order of magnitude of Casimir energy variation. Thus, as stated before, we assume the Kempf hypothesis and estimate the energy variation as totally due to Casimir effect. It is very important to stress that, as will be shown in Secs. III, even if the contribution of Casimir energy were of order of just a few over a thousand of the total energy at the transition, we might ascertain whether it gravitates.

1.8 Weighing a Casimir cavity

As already explained in the Introduction, the effort of the Archimedes experiment to solve the cosmological constant problem will consist in a direct measurement. Specifically, it will test if the force necessary to hold an extended object, avoiding that it will fall freely into the gravitational field of the Earth, is dependent or not by the vacuum energy of the electromagnetic field stored inside the volume of the object.

In order to do this, it's necessary to know first the order of magnitude of the force produced by vacuum fluctuation. In fact, this estimation has been the theoretical activity within the Archimedes experiment in the past years [Bimonte et al., 2006, 2007, 2008b; Calloni et al., 2014, 2002]. Here, the main points, some fineness and the results of this activity have been reported, referring to further publications for the details.

The suitable configuration for Archimedes' purposes is that of the Casimir cavity in Figure 1.1 in a weak gravitational field, like the one perceived, for instance, by a laboratory at rest on the surface of the Earth. In this reference frame the cavity is motionless; moreover, the Casimir cavity is assumed as a *rigid* body. Usually in Mechanics, the definition of rigid body makes use of concepts like distance and size; since here General Relativity is involved, this way to think about a rigid body can be tricky. Then, to avoid confusion, we will say that the Casimir cavity is rigid as if the two parallel planes are held together on the edge by a dielectric frame with an infinite stiffness, so that any force acting on a point of the cavity is somehow transmitted to the whole body, dragging or pushing it. It's important to clarify this aspect, and the reasons will be evident in the following.

A laboratory at rest on the Earth's surface is a non-inertial (or *accelerated*) observer in General Relativity. As shown in [Misner et al., 1973, pp. 327-332], the line element near this observer, using the Fermi normal coordinates and neglecting rotations, is

$$ds^2 = -(1 + 2A_j x^j)(dx^0)^2 + \delta_{jk} dx^j dx^k + O_{\alpha\beta}(|x^j|^2) dx^\alpha dx^\beta. \quad (1.47)$$

Here $c^2 \vec{A}$ (with components $(0, 0, |\vec{g}|)$), the observer's acceleration with respect to the local freely falling frame, shows up in the correction term $-2A_j x^j$ to g_{00} , which is proportional to the distance along the acceleration direction. Note that first-order corrections to the line element are unaffected by space-time curvature. Only at second order, which is beyond our aims, does curvature begin to show up.

For this observer, the force to keep a rigid Casimir cavity steady, against its free fall (i.e., the equivalent of the weight in General Relativity), can be calculated in different

ways. Surely, when a force is applied to a stressed body, it is in general expected that also the spatial components of the energy-momentum tensor contribute to the mass. This was firstly shown by [Einstein, 1907] and it is reported, for example, in [Misner et al., 1973, Eqs. 5.53-5.54], where one considers a stressed body in a locally inertial frame that is accelerated with $a^k = dv^k/dt$. The mass density is described by the tensor $m^{ik} = T^{\hat{0}\hat{0}}\delta^{ik} + T^{\hat{i}\hat{k}}$, where the hat over the indices denotes the energy-momentum tensor in the rest reference frame of the medium and the force is defined as $F^j = \sum_k m^{jk} \frac{dv^k}{dt}$. In analogy, since the Casimir cavity is a stressed body, one could expect that the measurement of its weight would end in measuring the stressed-body mass and not only simply the mass associated to the $T^{\hat{0}\hat{0}}$ term. In this case, considering that the energy-momentum tensor in the rest reference frame of a Casimir cavity is given by [Brown and Maclay, 1969]⁹

$$\langle T^{\mu\nu} \rangle = \frac{\pi^2 \hbar c}{180a^4} \left(\frac{1}{4} \eta^{\mu\nu} - \hat{h}^\mu \hat{h}^\nu \right),$$

where $\hat{h}^\mu = (0, 0, 0, 1)$ is the unit spacelike 4-vector orthogonal to the plates' surface, one could expect that the cavity, of volume $V = aS$, placed with plates parallel to the Earth's surface, would have a mass $m^{33} = V(T^{\hat{0}\hat{0}} + T^{\hat{3}\hat{3}}) = 4aST^{\hat{0}\hat{0}} = 4E_{Cas}/c^2$, where $E_{Cas} = -S \frac{\pi^2 \hbar c}{720a^3}$ is the energy of the system, the Casimir energy. This would result in the force

$$\vec{F} = 4 \frac{E_{Cas}}{c^2} \vec{g}.$$

Although this result is compliant with General Relativity, it is nevertheless somewhat surprising, because usually one is accustomed to attributing, to a body of rest energy E , the weight $\vec{F} = \frac{E}{c^2} \vec{g}$. The surprise is indeed correct, because in fact the previous result does not correspond to the actual force measured in a weight experiment where the cavity is rigid and hanged at a single fixed point (or placed on a plate of a balance). To correctly evaluate the force measured in these cases, since the cavity is rigid and the forces are transmitted to the suspension point, *the force densities acting on the various points must be red-shifted*: [Fulling et al., 2007] and in particular [Bimonte et al., 2007] clarified that, if the total force acting on an extended body is defined as the sum of red-shifted force densities, the mass is independent of the spatial energy-momentum tensor. Let's consider the forces on each plate, expanded to first order in $\epsilon \equiv 2ga/c^2$, derived in [Bimonte et al., 2006]. In that work the regularized and renormalized energy-

⁹The calculation of this tensor for such a system cannot be done straightforward, due to its quantum nature and its ultraviolet divergences. The angular brackets around $T^{\mu\nu}$ in the following formula are used to indicate the regularized and renormalized energy-momentum tensor.

momentum tensor $\langle T^{\mu\nu} \rangle$ has been obtained from the Hadarmard Green function of a Casimir apparatus in a weak gravitational field. The forces on the plates are the components of the resulting energy-momentum tensor and, for the z -direction, have been evaluated as (hereafter Q_2 refers to the upper plate and Q_1 to the lower plate)

$$\vec{f}_{Q_2} \approx -\frac{\pi^2}{240} \frac{S\hbar c}{a^4} \left[1 - \frac{g}{c^2} \left(\frac{2}{3}a \right) \right] \hat{z}$$

and

$$\vec{f}_{Q_1} \approx \frac{\pi^2}{240} \frac{S\hbar c}{a^4} \left[1 + \frac{g}{c^2} \left(\frac{2}{3}a \right) \right] \hat{z}.$$

The mere addition of such forces (as it might be obtained by independently measuring the forces acting on the two plates of a non-rigid system) would lead to the quantity \vec{f}_{ind} equal to

$$\vec{f}_{ind} = \vec{f}_{Q_1} + \vec{f}_{Q_2} \approx 4 \frac{\pi^2}{720} \frac{S\hbar c}{a^3} \frac{g}{c^2} \hat{z} = 4 \frac{E_{Cas}}{c^2} \vec{g}$$

that is exactly the same force derived previously by analogy. Interestingly, \vec{f}_{ind} is the sum of two contribution:

$$\vec{f}_{ind} \approx \left(\frac{|E_{Cas}|}{c^2} g + F_{Cas} \delta\phi \right) \hat{z}$$

the vacuum weight part $\frac{E_{Cas}}{c^2} g$ and the Casimir pressure difference, multiplied by the surface, $SP_{Cas} \delta\phi$, on passing from one plate to the other ($\delta\phi = ga/c^2$ has been explicitly written as the variation of the gravitational potential on passing from lower to upper plate). This difference in pressure is physical, and it implies the red-shifting of vacuum density in the gravitational field.

In the measurement we are interested in, however, the plates are weighed by acting on one and the same point, i.e. the suspension point of the rigid Casimir apparatus. In this case, as shown in [Bimonte et al., 2007], the gravitational red-shift must be taken into account when summing the force to obtain the total force acting on the body. By red-shifting the force up to the common point Q_2 , the total force is given by

$$\begin{aligned} \vec{F} = \vec{f}_{Q_2} + r_{Q_2}(Q_1) \vec{f}_{Q_1} &\approx \frac{\pi^2 S\hbar c}{240a^4} \left\{ - \left[1 - \frac{g}{c^2} \left(\frac{2}{3}a \right) \right] + \left[1 - \frac{g}{c^2} a \right] \left[1 + \frac{g}{c^2} \left(\frac{2}{3}a \right) \right] \right\} \hat{z} \\ &\approx \frac{\pi^2 S\hbar c}{240a^4} \frac{1}{3} \frac{ga}{c^2} \hat{z} = \frac{E_{Cas}}{c^2} \vec{g}. \end{aligned}$$

This is the force that must be tested against observation in the Archimedes experiment, and it is in full agreement with the expectation of the equivalence principle. It is directed

upwards and it is equal to the weight of the modes of the vacuum that are removed from the cavity. Therefore it can be interpreted as an Archimedes buoyancy force in vacuum.

In our force measurement the consideration about the red-shift is remarkably important: if, contrary to the expectations, the vacuum pressure term would not suffer the red-shift in a gravitational field, the measured weight would depend on the cavity orientation and, for planes perpendicular to \hat{z} , would be 4 times the expected value. Thus Archimedes is also a null experiment for the first verification of red-shifting of vacuum pressure in gravitational field.

Actually, the object that will be weighed in Archimedes is a superconducting material whose microscopic structure consists in a multi-layer cavity. As will be better explained later, Archimedes will measure only the differential force \vec{F}_s due to the *variation* of the Casimir energy within this cavity¹⁰

$$\vec{F}_s = \frac{\Delta E_{Cas}}{c^2} \vec{g}.$$

It will be shown that the variation of Casimir energy density is approximately

$$\Delta U_{Cas} \approx 2 \times 10^5 J/m^3.$$

Thus, if the weighed object is a disk-shaped superconducting material of radius $r \approx 5 \cdot 10^{-2}m$ and thickness $h \approx 5 \cdot 10^{-3}m$, the order of magnitude of $|\vec{F}_s|$ will be

$$|\vec{F}_s| \equiv F_s = \frac{\Delta U_{Cas} \pi r^2 h}{c^2} g \approx 5 \cdot 10^{-16} N. \quad (1.48)$$

1.9 The Archimedes experiment

This is the best measurement strategy and Archimedes' apparatus is designed to work this way. It consists in a *cryogenic balance*, whose scheme is shown in the Figure 1.4. A 3-D rendering of the fundamental parts is shown in the Figure 1.5

The balance is composed by a reference arm and a measurement arm, with length of 1.40 m and weight of approximately 1.2 kg. These dimensions allow a simple insertion of the superconducting samples and temperature actuators inside the cryostat, as well as an easy reaching of low resonance frequency. Temperature modulation of the samples is the way in which the Casimir energy will be periodically changed.

Use of reference arm is foreseen to assure a common mode rejection factor for the seismic

¹⁰In the following chapters it will also called the "signal force", as the index "s" suggests.

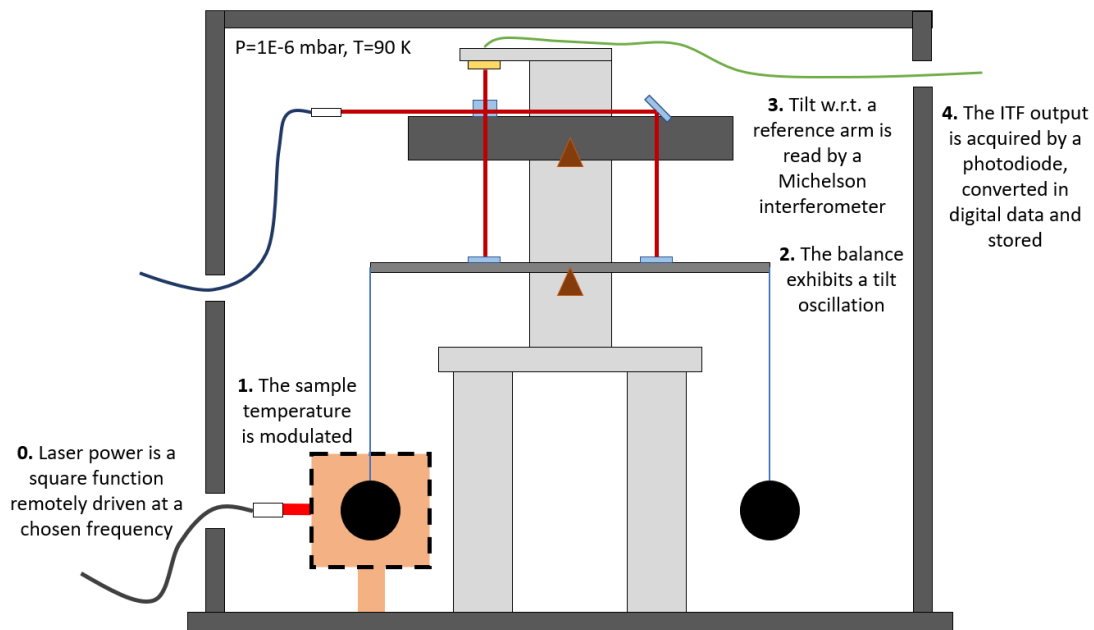


Figure 1.4: Scheme of the balance. Two arms, in gray, each suspended to the same support so to have common seismic noise. The lower arm suspends the samples, that are placed 1 meter lower the arm to allow efficient thermal screening of the arm from thermal actuators (in brown). The torque signal is read with a Michelson interferometer as a difference signal in the two optical path sensing the distance among the arms in the two ends, as sketched in the figure. The two arms are controlled by electrostatic actuators (not shown).

transverse noise. The measurement arm suspends at each end a sample, hanged with two wires. Each arm rotates around a joint whose bending point is set within less than ten microns from the center of mass axis, to reduce transverse seismic motion to arm's tilt. So, a periodic signal force acting on one end of the measurement arm will make it oscillate with the same frequency, i.e. will produce a periodic tilt difference between the two arms.

The tilt difference is sensed with a Mach-Zender interferometer illuminated with few mW power. Each arm is controlled in feed-back to maintain the interferometer in the working point for long time by electrostatic actuators. The whole experimental system is maintained at the cryogenic temperature of about 100 K, corresponding to the superconducting transition temperature of the samples, because this is the temperature around which the Casimir energy modulation can take place. Not less important, the experiment must be exploited in a quiet seismic site.

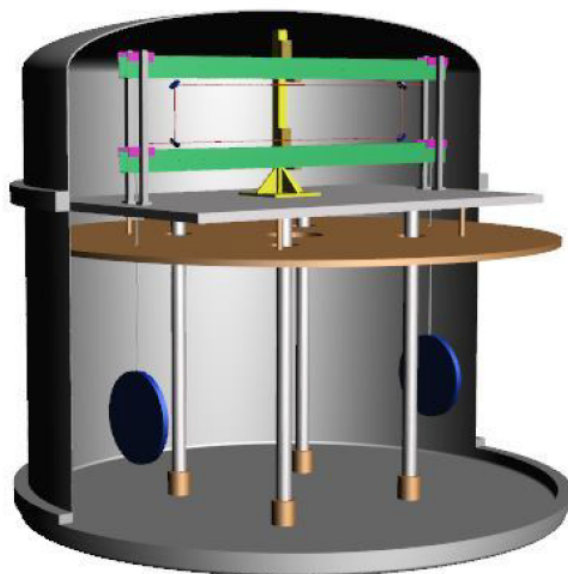


Figure 1.5: 3-D rendering of the fundamental parts of the Archimedes apparatus.

There are many crucial points in the development of this apparatus. The most important of all concerns the variation ΔE_{Cas} : it is necessary to know this value at best, specifically for our superconducting material, in order to have a reliable estimate of the signal force \vec{F}_s . This estimate has already been presented in the previous chapter; in the next section, the motivations behind the choice of superconductors and the theoretical activity within Archimedes' group about the modelling of real stratified superconductors, including ΔE_{Cas} , will be discussed in detail.

Another crucial point is about seismic isolation. Local earthquakes can be a source of limiting noise for this measurement, and particular attention about the choice of the site is required. In the following it will be explained how this search had been conducted.

1.9.1 Expected sensitivity

Given the constraints and the major sources of noise shown in the previous paragraphs, it is now possible to remind the critical parameters of the balance and obtain a sensitivity curve that assure us the feasibility of the experiment. One of the most critical parameters is the loss angle of the joints that will affect the thermal noise. Several studies have already been conducted on material and the presently foreseen loss angle is estimated of about $\phi = 10^{-6}$. This value is surely reachable with silica joints and is presently under test with metallic joints, in particular with aluminium joints, which are

known to acquire a higher quality factor at low temperatures. The arm length will be 1.4 m: this value guarantees sufficient space to allocate thermal actuators. The expected torque of $3.5 \cdot 10^{-13} \text{ Nm}/\sqrt{\text{Hz}}$ will correspond to an angular spectral density of about $10^{-11} \text{ mrad}/\sqrt{\text{Hz}}$. To read this signal it is not sufficient an optical lever system and thus we will use an interferometric read-out. The interferometer will not be critical from the sensitivity point of view, because few mW of input power are already sufficient to full fill the requirements for this sensitivity. On the contrary, it will be critical because it will be operate in a cryogenic environment with very few possibilities of remote control. In particular this interferometer could suffer from misalignments induced by the typical material contractions passing from room temperature to about 90 K. For this reason a suitable interferometer has been designed and tested in the present thesis that has demonstrated excellent results.

Given the above parameters as well as all the other discussed in the previous paragraphs, we can draw a sensitivity curve that is reported in Figure 1.6. The major contri-

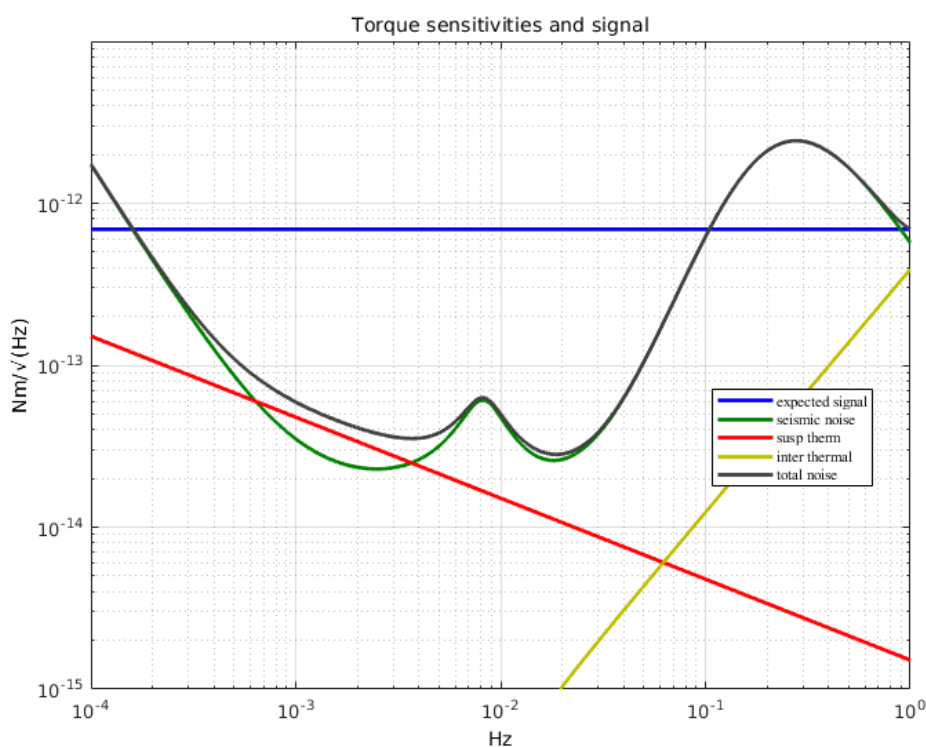


Figure 1.6: Expected sensitivity.

bution are suspension thermal noise and seismic noise. This figure shows again the need

to perform the experiment in a quiet seismic environment. If the SAR-GRAV laboratory will be ready in the next year the Archimedes experiment will start to be assembled on the final site.

Chapter 2

Low seismic noise sites

2.1 Seismic noise in gravitational physics

In the last decades fundamental physics related to gravity has made extremely remarkable progress. The most relevant part is certainly given by interferometers for gravitational waves detection [Abbott et al., 2016a,b, 2017a,b, 2021; Acernese et al., 2015; Harry, 2010], joined by important advances in the detection of small forces with torsion pendulums both for direct measurements of gravitation (such as the LAG experiment - [Bassan et al., 2019a]) and for the application to detectors of gravitational waves in space ([Bassan et al., 2016]).

Since the initial GW-projects, which by now dates back to around the 1980s, it was understood that one of the most important noises that would determine the measurement of small forces and, in particular, the success of gravitational wave detection, was seismic noise: ground vibrations of both natural and anthropogenic origin. These vibrations are typically always present, with day-night variability of anthropogenic origin, and are far greater than the displacements induced by gravitational waves on the test masses of GW-interferometers.

For example, at the Virgo site, as shown in figure 2.1, in the low range of the frequency region of interest for gravitational waves, around 10 Hz, the seismic noise in spectral power is of the order of $3 \cdot 10^{-11} m^2/s^4/Hz$ (with large variability), corresponding to the displacement of about $10^{-9} m/\sqrt{Hz}$.

As illustrated in the figure 2.2, that shows the expected sensitivity of Advanced Virgo, the minimal detectable amplitude of gravitational waves is of the order of $\tilde{h} = 10^{-21} 1/\sqrt{Hz}$. Considering that the Virgo interferometer arms have length $L = 3km$, gravitational waves of this amplitude generate displacements of the masses $\Delta\tilde{L} = \tilde{h} \cdot \tilde{L} \approx$

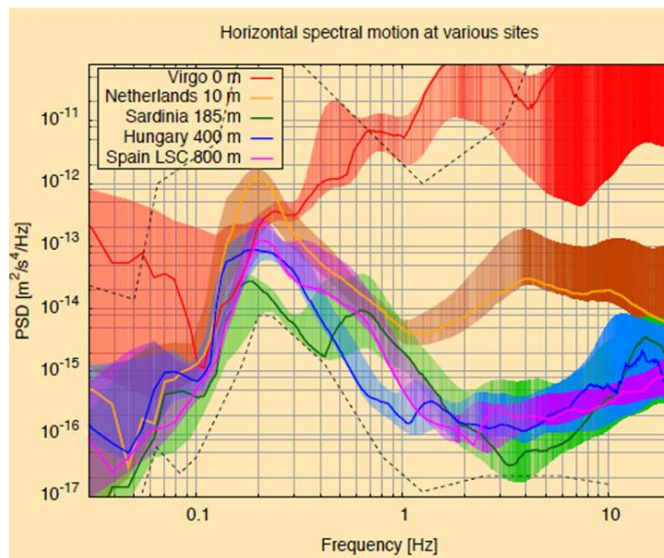


Figure 2.1: Peterson seismic noise curves. The lowest red curve is called NLNM (New Low Noise Model) and represents the envelop of the lowest seismic noise measured in the various sites in the world.

$3 \cdot 10^{-18} \text{m}/\sqrt{\text{Hz}}$. This means that the seismic noise must be attenuated by 10 orders of magnitude to allow for an effective measurement.

Seismic noise attenuation required a great deal of technological effort [Abbott et al., 2002; Acernese et al., 2010; Hua et al., 2004; Losurdo, 2002], which resulted in the realization of the Seismic Noise Superattenuator currently employed in Virgo. It is a multipendular chain from which each test mass is suspended, where each pendulum element is in effect a 6-D oscillator, as illustrated in the figure 2.3, with resonant frequencies all confined well below the 1 Hz, so as to achieve the desired attenuation at 10 Hz. In Virgo's configuration, each test mass (i.e., each interferometer mirror) is suspended separately to its chain, as we see in the figure 2.4, where each tower contains a Superattenuator and its suspended element. This configuration avoids couplings between test-masses motions and causes each pendulum element to be connected to the previous one by a single wire, which in turn avoids couplings between the various degrees of freedom.

The detectors LIGO (U.S.) and Advanced Virgo have enabled the detection of gravitational waves and currently constitute the worldwide network of detectors that has paved the way for Gravitational and Multimessenger Astronomy. These great successes of gravitational wave physics have prompted the scientific community to design next-generation detectors that allow to explore regions of the universe even more distant than the current ones and to reach a sensitivity such as to investigate phenomena, such as the

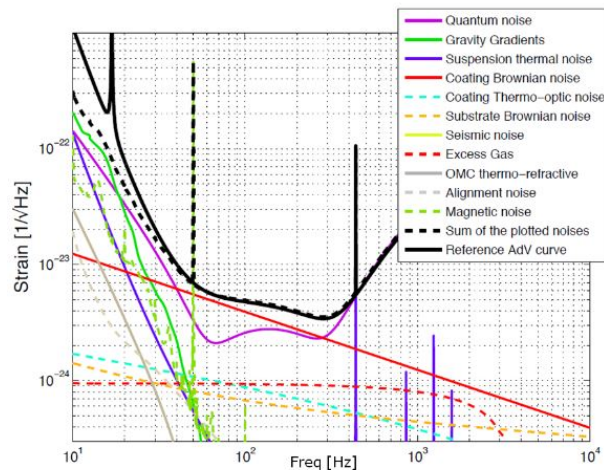


Figure 2.2: Expected sensitivity for Advanced Virgo detector, with fundamental noise contributions.

equations of state of pulsars or resonances of the normal modes of black holes, which are still precluded to observation. Currently the European scientific community is focused in the project "Einstein Telescope" (ET) while the American community is focused in the detector "Cosmic Explorer" (CE), as will be explained in the next paragraph.

2.2 Newtonian Noise

The direct effect of seismic noise, i.e. that of causing the test masses to vibrate, can be reduced by appropriate seismic isolation, so that the imprinted motions in the test masses recode by many orders of magnitude. There is, however, a second way in which seismic noise can enter and degrade the sensitivity of a detector, and this is the so-called Newtonian Noise (NN) [Beker et al., 2011]. This is given by the variation of the gravitational field that is generated by the ground mass, which moves during the seismic disturbance. Although the ground actually moves only a few fractions of a micrometer, the mass in play, the one up to a few hundred metres away from the detector, is large enough to exert a variable force on the test masses. Since this force is gravitational, it is in principle indistinguishable from the force of the gravitational wave, and so an effective way of minimising it is to build the detector at sites with low seismic noise and underground detectors are clearly preferred.

In underground detectors the main sources of Newtonian Noise can be caused both from surface as well as by the body waves, both compressional or primary (P) and

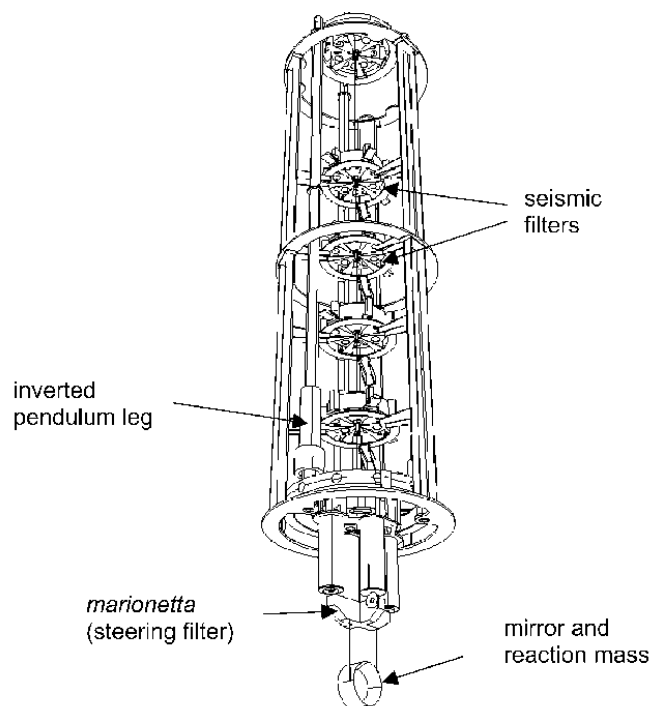


Figure 2.3: A scheme of Virgo Superattenuator.

shears or secondary (S) ones [Harms, 2019]. At the present, the noise projections are still under studies, to take into account the scattering from the cavern, the scattering from the inhomogeneities of the soils. For what concerne the surface wave, it is presently expected that if the seismic noise measured at the surface is lower that approximately 50 time the NLNM and the detector is located underground at a depth bigger than few hundreds meter, the Newtonian noise on the underground detector is negligible [Harms, 2019]. In the Sos Enattos site, as shown in [Naticchioni et al., 2014], the seismic noise at the surface is well below this limit and, at the state of present knowledge, can be neglected in evaluating the Newtonian Noise contribution. Under this condition, the main contribution to Newtonian noise is expected to come from the body waves [Harms, 2019]. In the rest of the paper we will follow this assumption: we will estimate the Newtonian noise in the detector by measuring the underground seismic noise at 84 m depth and project it on the ET sensitivity assuming that it is entirely composed by body waves. This estimation is conservative because we do not consider any attenuation of the surface waves component of the measured seismic noise at 84 m depth in estimating the Newtonian noise at 250 m depth.

The body waves are described with the help of the seismic displacement vector $\vec{\xi}$,



Figure 2.4: A picture of central part of Advanced Virgo. Each of the tall vacuum-chambers is hosting a Superattenuator.

which is a useful method because it can be measured directly:

$$\vec{\xi}^{P,S} = \vec{e}^{P,S} \xi_0^{P,S}(\vec{k}^{P,S}, \omega) \exp(i(\vec{k}^{P,S} \cdot \vec{r} - \omega t)) \quad (2.1)$$

The indexes P and S distinguish respectively the compressional (P) and shear (S) waves, \vec{k} is the wavenumber, \vec{e}_k is the polarization unit vector, and ω is the frequency. Compressional waves are longitudinal: $\vec{e}^P = \frac{\vec{k}^P}{k^P}$ while shear waves are transversal: $\vec{e}^S \cdot \vec{k}^S = 0$. Following the Newton law the acceleration $\delta\vec{a}$ of a mass placed at the point \vec{r}_0 is given by:

$$\delta\vec{a}(r_0, t) = -G \int dV \rho(\vec{r}) \left(\vec{\xi}(\vec{r}, t) \cdot \vec{\nabla}_0 \right) \frac{\vec{r} - \vec{r}_0}{|\vec{r} - \vec{r}_0|^3} \quad (2.2)$$

In the first approximation the underground cavities of the detector can be assumed to be spherical, with radius much shorter than the seismic wavelengths and the mass in the center [Harms, 2019]. Further, assuming that the density variations in space and time can be neglected and $\rho(\vec{r}, t) = \rho_0$ assumed constant, the above integral can be solved to give:

$$\delta\vec{a}(\omega) = \frac{4\pi}{3} G \rho_0 \left(2\vec{\xi}^P(\omega) - \vec{\xi}^S(\omega) \right) \quad (2.3)$$

The projection of the noise on the ET sensitivity is performed in the approximation

that the noise on the four test masses of the interferometer is incoherent and supposing that the polarization of the waves $p = 1/3$. The mixing parameter p is defined using the power spectral density of the measured seismic noise $S(\xi, \omega)$ and by the relations: $S(\xi^P, \omega) = pS(\xi, \omega)$ and $S(\xi^S, \omega) = (1 - p)S(\xi, \omega)$. The choice of $p = 1/3$ is motivated by the fact that P-wave contributions to displacement have usually been observed to be relatively minor compared to S-wave content. Under this hypothesis the amplitude spectral density of the noise \tilde{h}_{NN} is given by:

$$\tilde{h}_{NN} = \frac{2\sqrt{(2)\frac{4\pi}{3}}G\rho_0}{L(2\pi f)^2}\tilde{x} \quad (2.4)$$

where \tilde{x} is the amplitude spectral density of the measured seismic noise. It is very important to note that this equation assumes the arm length of 10 km and the sensitivity equal to the interferometer with 90 degrees arm angle. This equivalence is valid as long as the noises in the three LF interferometers are not coherent, as it is assumed for ET sensitivity curve.

The expected contribution, dated back on 2009, of Newtonian Noise for the ET sensitivity is illustrated in the bottom graph of figure 2.6: it is expected that the low frequency part of ET sensitivity will be dominated by Newtonian Noise, that will finally determine the sensitivity of the detector. In those evaluation it was assumed that the NN correspond to a quite quiet site, with also an optimistic reduction of factor 3 thanks to active noise reduction techniques.

This noise is in any case extremely site dependent. If the detector will be installed in a quiet site ET will be able to reach the desired sensitivity, otherwise it will be extremely difficult to reach it. Long studies have been devoted in the past to reduce actively the Newtonian Noise by measuring the ground motion with seismic sensors, deduce from the measurements the gravitational noise induced in the test masses and hence subtract it from the interferometer signal [Badaracco and Harms, 2019]. These techniques are still under investigation and, even if not yet tested on a real detector, promise some reduction of the noise, about a factor 3, that has been taken into account in first noise evaluations. Presently is yet to be demonstrated such reduction, so a more conservative approach of evaluation without reduction is applied. In this conditions it is very important to find a quiet site, that fulfill the specificagtions for ET realization. Part of the work of the thesis has been the analysis of the seismic noise at Sos Enattos site, candidated to host the ET observatory.

The site is located in Sardinia island (Italy), near the city of Nuoro, in the mairy of Lula.

The site has a mine, not anymore in operation but still maintained in order to prevent environmental perturbations, and in the mine it had been possible to install several sensors to analyze the noise.

Usually, the evaluation of Newtonian noise is done by assuming stationary noise, obtaining the spectral power density and comparing it with the expected sensitivity. This is certainly useful, but it is not everything. In particular, considering that seismic noise, especially in its anthropogenic component, is not stationary, it implies that the expected reduction from seismic and projection measurement techniques on the gravitational signal may not always be effective. Therefore, together with the evaluation of the spectral power density, it is important to evaluate the time-dependent behaviour of the glitches. Since, in frequency, Newtonian noise is decisive at a few Hz, in order to understand possible consequences on detectability, it is important to understand which gravitational wave sources whose detectability would possibly be most impaired by having glitches in the region around a few Hz.

As illustrated in the article in Appendix A, such sources are precisely the coalescences of intermediate-mass black holes, among the most interesting new sources for the detector. The analysis, which is the subject of the article, has therefore focused on these sources and, considering that the signal duration in the detector is on average one minute, on the seismic glitches of that duration. For each one-minute time-slot, the amplitude of the Newtonian noise was checked and compared with the expected amplitude. A site that has a low rate of one-minute glitches in which the noise is above the desired sensitivity is a suitable site for ET. Conversely, a site with a high number of glitches is destined not to be able to observe the coalescence of intermediate-mass black holes.

As is shown in Appendix A, Sos Enattos is a site that allows for a very good duty cycle, above 90%. What is more important, these measurements were taken with the sensor placed in the mine, therefore not shielded from the anthropogenic noise generated by the activities still carried out there. In the last part of this chapter we will illustrate the most recent measurements made with the sensor located in a bore-hole at a depth of 250 m.

Finally, it should be noted that the Sos Enattos site is not the only candidate site for hosting ET. A competing site is Terziet, in Limburg (Netherlands). In the published article, for reasons of expediency for the whole collaboration, comparative results with

respect to the Dutch site were not published, but were presented internally at the collaboration conferences. These results will also be reported in the last part of this chapter.

2.3 The Einstein Telescope Project

The present generation of detectors for gravitational waves, namely Virgo and LIGO, have paved the way for the birth of gravitational astronomy and will be the detectors that will observe future sources for at least the next two decades. These detectors will be joined by the Japanese interferometer Kagra, with hopefully comparable sensitivity, in this decade. Although these detectors have been the keystone in the observation of gravitational waves and therefore can be looked upon as a great success by the scientific community, they are the culmination technical progresses and in this sense are showing the pace in the difficulty of further leaps in level. It is indeed likely that in the next decade these observatories will succeed in further improving their sensitivity, but it is also true that they are faced with structural conditions, typical of a first generation, that must be overcome with completely new instruments.

The most important and heavy conditions come now from the infrastructure. As we have seen, the passage of a Gravitational Wave of amplitude h , arriving in a direction perpendicular to the interferometer plane, generates in the test masses the displacement $\Delta L = h \cdot L$, where L is the length of the interferometer arms, so the sensitivity increases as the arm length increases. At the time of the construction of Virgo and LIGO, compatibly with the costs that the community and governments could accept, distances in the order of a few kilometres were chosen, namely 3 km for Virgo and 4 km for LIGO. Today, having demonstrated the enormous scientific potential of these observatories, the scientific community and governments are ready to accept larger funding, and so a leap forward in sensitivity can be made by building interferometers with arms of tens of kilometres.

To date, the world's two most important ground-based gravitational wave observatory projects are the European Einstein Telescope (ET) and the US Cosmic Explorer (CE). The Einstein Telescope, whose initial design dates back to 2009, has 10 km arms and a triple-triangle design, which will be explained later. Cosmic Explorer, on the other hand, has a classic L-shaped Michelson interferometer design, and proposes arms of 20 km or even 40 km. Following a similar scheme to LIGO, Cosmic Explorer proposes the construction of two interferometers, one of which could have arms of 40 km. Einstein

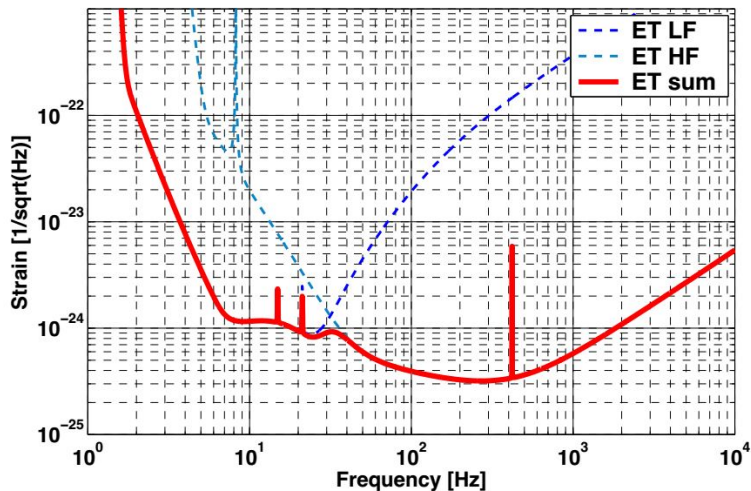


Figure 2.5: Expected sensitivity of the Einstein Telescope. Note the ‘xylophone’ configuration. The sensitivity of the low-frequency cryogenic interferometer is shown in the dashed dark blue curve and the one of the high-frequency room temperature one in a dashed blue-green tone. The sum of both is given by the solid bright red curve

Telescope, in view of these recent US proposals, is reconsidering the design of the detector, in particular the length of the arms, and the L-shaped design, with 20 km arms, so as to be at least comparable with the US design, is gradually becoming the preferred solution.

A key point that distinguishes the ET design from Cosmic Explorer is the underground construction. In fact, while the ET detector will be installed about 250 m underground, Cosmic Explorer is designed to be above ground. The main reason for building the detector underground is to minimise seismic noise, as it will be hereafter. The expected sensitivity of the detector is shown in figure 2.5. Three curves are highlighted in the figure because the ET configuration is called xylophone: each interferometer is split into two parallel interferometers, one of which is optimised for the low frequencies while the other is optimised for the high frequencies. The reason for this choice is that the techniques required for the different frequency bands point to different strategies in either case.

For example, the power of the light circulating in the cavities: in order to optimise the high frequency it is necessary to maximise the power, so as to minimise the shot-noise, which determines the sensitivity at frequencies above a hundred Hz. At low frequencies, on the other hand, the laser fluctuations that determine sensitivity are the power fluctuations: since the displacement (Fourier transform) of the masses, with the same force, depends as $\Delta\tilde{L} = -\tilde{F}/m \cdot \omega^2$, and the radiation pressure \tilde{F}_p , in the low squeezing limit, is

proportional to the root of the power, low powers are favoured at low frequencies. Similar arguments, e.g. on mirror temperature or cavity losses, imply non-compatible choices in the choice of high or low frequencies, so that in ET a splitting of interferometers has been decided.

The sensitivities of the high-frequency and low-frequency detectors are shown in figure 2.6. Particularly is the part concerning low frequency. The sensitivity is extended downwards to frequencies of 2 Hz, compared to the current limit of 10 Hz. This is a peculiarity of ET, not only compared to current detectors but also to Cosmic Explorer, as shown in figure 2.7. From a scientific and in particular astrophysical point of view, this choice deprives the search and observation of large-mass sources, intermediate-mass black holes, and the accuracy with which the parameters of coalescences of smaller masses can be measured because, as explained later, the time in which the source is visible to the detector increases considerably. The most important structural condition to reach such low frequency sensitivity is to lower the effect of seismic noise. As we will see in the next paragraph, such condition is determined not only by the direct displacement on the test masses due to ground motion, but also more subtly by the gravitational coupling of ground mass motion with the interferometer's test masses, the so called Newtonian Noise. Minimization of this noise can be reached only by placing the instruments underground, and in particularly quiet sites, where seismic noise much lower with respect to present Virgo and LIGO sites.

Finally, to conclude the ET overview, we observe that the ET detector is actually composed of three pairs of interferometers, as shown in figure 2.8. In each interferometer the angle between the two arms is 60 degrees (not 90 as in the classical L-shaped configuration) and each pair has the beam-splitter at each vertex of an equilateral triangle of side $L = 10$ km. In this way, the ET detector actually consists of 6 interferometers (three optimised for low frequency and three for high frequency). The peculiarity of this configuration is that if we imagine it as the only detector in the world, it would be able to resolve both the amplitude and the polarisation of the gravitational wave. With some difficulty, it would also be able to reconstruct the direction of the source. Since when ET was conceived, GWs had not yet been discovered and it was not clear that there would be the possibility of investing in more detectors, this possibility was considered a very good feature. As said before, nowadays, in the light of the discoveries made and in the new world scenario, this triangular configuration is reconsidered and in the present state of the thesis it remains as one of the two possible reference configurations.

As already stated, the location of ET will be near the Sos Enattos mine and will cover

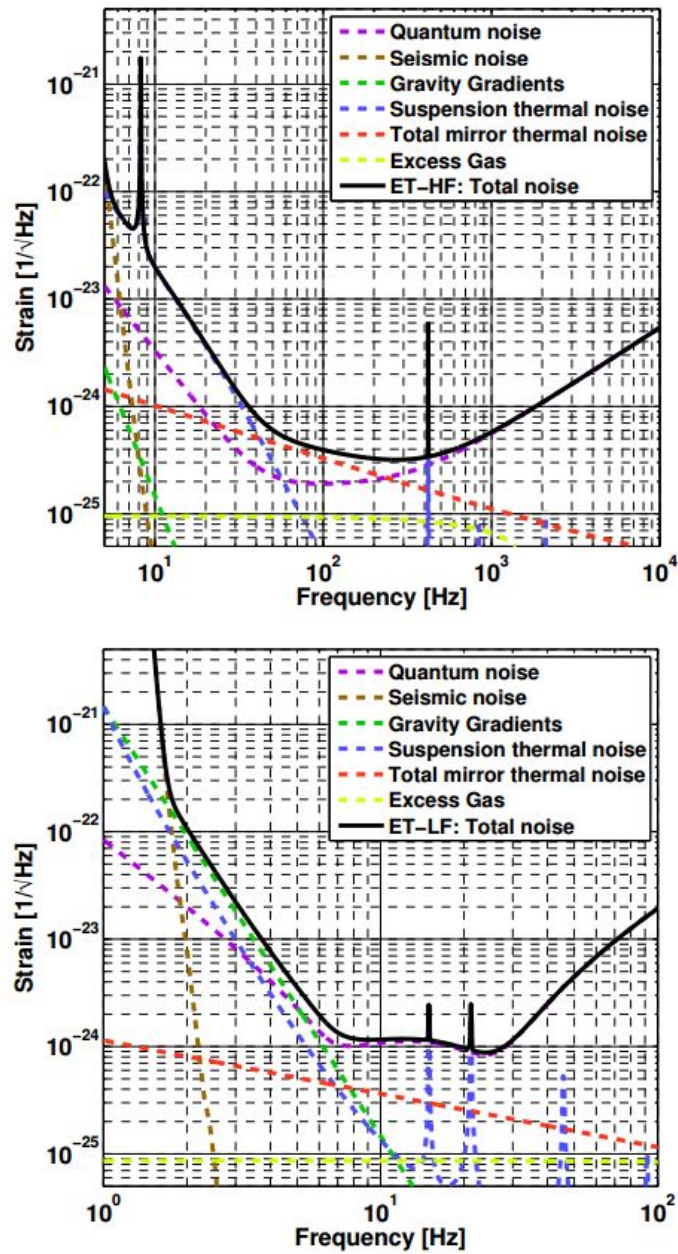


Figure 2.6: The two sensitivity curves and noise budgets for the ET xilophone interferometers

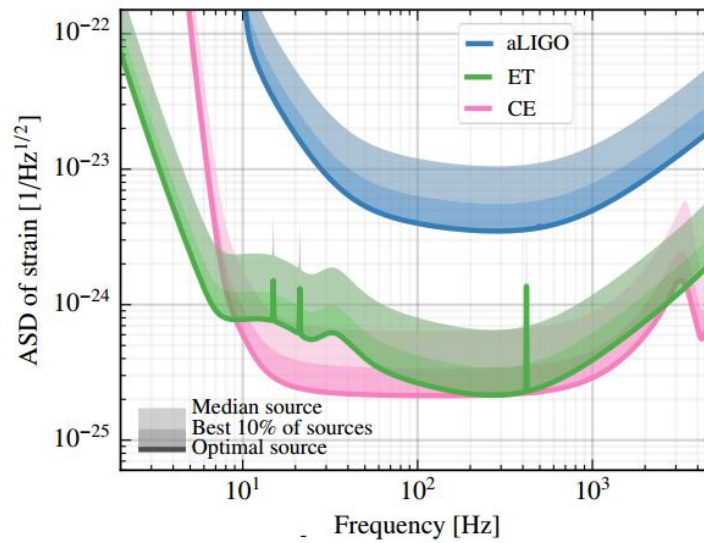


Figure 2.7: Expected sensitivity of the Einstein Telescope in comparison with CE and LIGO (similar to Virgo). Notice the different expected sensitivity at low frequency. While CE stops at around 5 Hz, ET points towards 2 Hz.

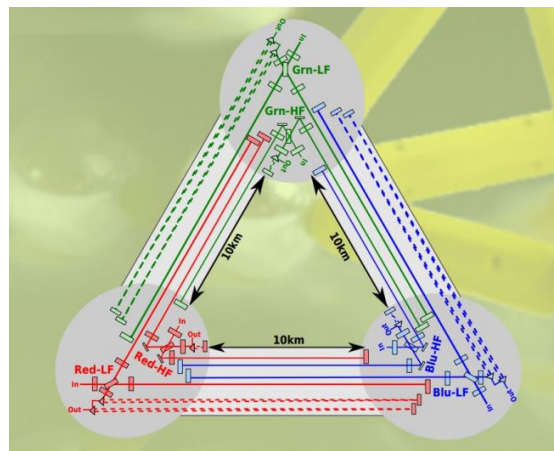


Figure 2.8: ET layout. Each xilophone, composed by two interferometer, is indicated with a colour and it is composed by two interferometers: an interferometer optimized for the high frequencies, siglated HF, and the other optimized for the low frequencie, LF. All the interferometers have 10 km armlengths. Dashed are also indicated the auxiliary squeezing cavities, so called filter cavities, whose lenght is here taken as 10 km, while their actual lenght is still under investigation

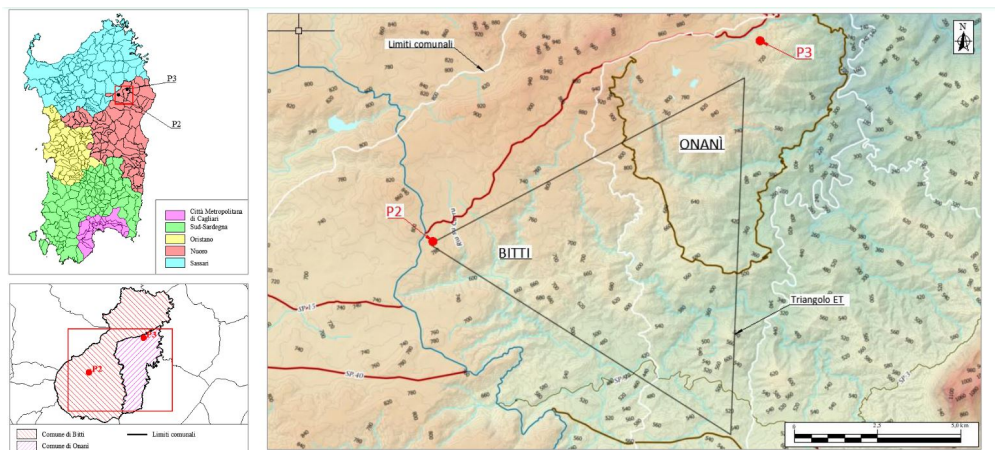


Figure 2.9: ET planned position in Sardinia. Also shown are the bore-holes points P2 and P3 used to measure seismic noise in all the three vertices

vairous mairies. The position is illustrated in the figure2.9, where there are shown also two points P2 and P3 that are the locations of two bore-holes that have been excavated in order to measure the seismic noise not only in the vertex of Sos Enattos but also near the other vertexes.

2.4 Sites Comparisons and latest results

The data at the Sos Enattos site were then compared with the data acquired simultaneously at the Terziet site. In the latter case the sensor is placed at a depth of 250 metres in a bore-hole. Therefore, while for Sos Enattos the measurement is conservative, because the sensor cannot be completely isolated from anthropogenic noise sources, in the case of Terziet it is at the best, because in the reality of ET implementation it can only be the same or worse. The most important results are shown in the figure below. As can be seen, the Terziet situation is very problematic, because the ratio indicated with NTR (Noise to Target Ratio) is always greater than unity and most of the time around a factor 3. In fact, the reduction of noise by a factor 3 would bring the possibility of observing a coalescence of intermediate mass binaries with non-degraded noise to the value of 0.64. This means that unfortunately, even such an optimistic reduction would leave the duty cycle around this unacceptable 64% value. Only a reduction of a factor of 5, which is currently not possible, would bring the duty cycle down to around 92%.

The same analysis has been carried out more recently, thanks to two bore-holes installed at the two other vertices of ET as planned in the triangular configuration. The

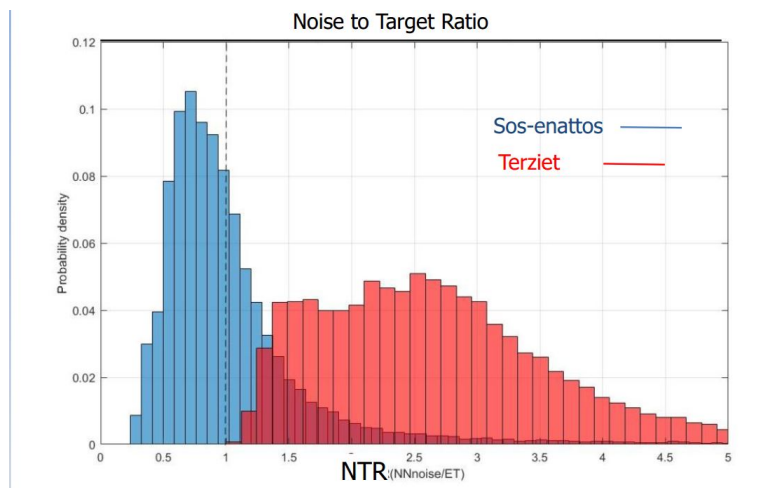


Figure 2.10: Comparison of Noise to Target Ratio (NTR) probability densities for Sos Enattos - conservative in the mine, and Terziet - optimistic in the bore-hole. Even in this optimistic condition Terziet site would require a NN reduction more effective than a factor three

position of the bore-holes is shown in figure 2.9. Very interesting are in this case the seismic noise measurements. In figure 2.11 the spectral power density of seismic noise measured at the noisiest point (P2) is shown, compared with the Terziet seismic noise measurement and with the two Peterson limits representing the global maximum and minimum envelope observed with sensors in all relevant parts of the globe [Peterson, 1993]. In the region of interest for ET, where the NN limits are expected, i.e. above 2 Hz up to about 7 Hz, the noise of the Sardinian vertex is better than Terziet by a factor ranging from 3 to 7 depending on the frequency. Around 5 Hz the noise reaches the minimum Peterson curve. Similar results are obtained for point P3.

The glitchness analysis is reported in figure 2.12, where the curves of the various sites are shown, referring for all sites to the period October 1, 2021 to November 20, 2021. In purple the curve for Terziet (bore-hole), in yellow the curve for Sos Enattos (mine), in orange the curve for the second Sardinian site, P2 (bore-hole) and finally in blue the curve for the third Sardinian site P3 (bore-hole). From the graph we can see that, as expected, the noise in the bore-hole, far from anthropic sources, is better than the noise at the Sos Enattos vertex, obtained with the mine measurement. For both site P2 and P3 the curve is spiked well below unity, with negligible probability of being greater than unity. The realisation of ET at this site would thus have the important simplification of not having to resort to active Newtonian noise reduction, a technique that has not yet been demonstrated and is certainly quite complex to implement.

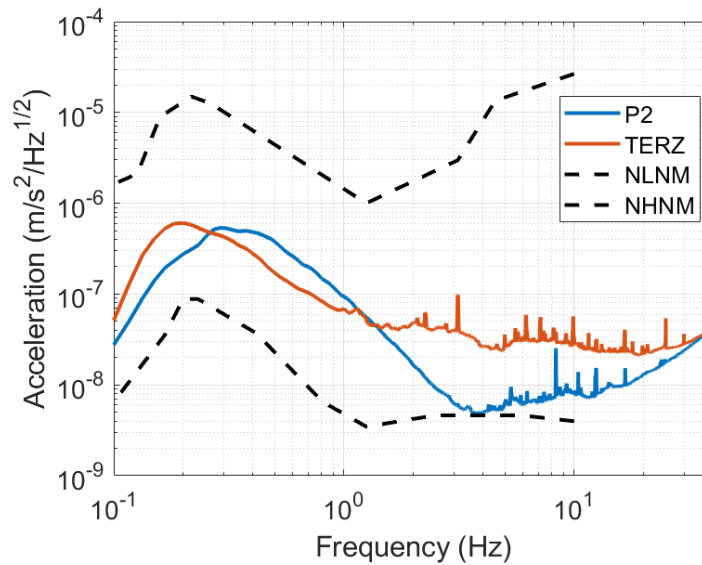


Figure 2.11: Amplitude Spectral Density of ground acceleration measured in P2 and compared with Terziet

These measurements are also useful to understand how human activity can deteriorate the seismic noise of a site. In fact, one of the most careful activities planned for ET installations is the study of installations that do not introduce excessive noise during observatory data collection. Studies are focusing, for example, on vacuum pumps, electrical installations, residual mechanical movements, e.g. air recirculation, temperature maintenance, cryogenic apparatus, etc. Such a study has in fact already begun with the Archimedes experiment, which is being carried out at the Sos Enattos site on the surface. Despite the fact that the site is not at its best, the seismic noise during the absence of immediate anthropogenic activity, e.g. at night, is very quiet and the Archimedes data sockets are designed so as not to disturb this condition.

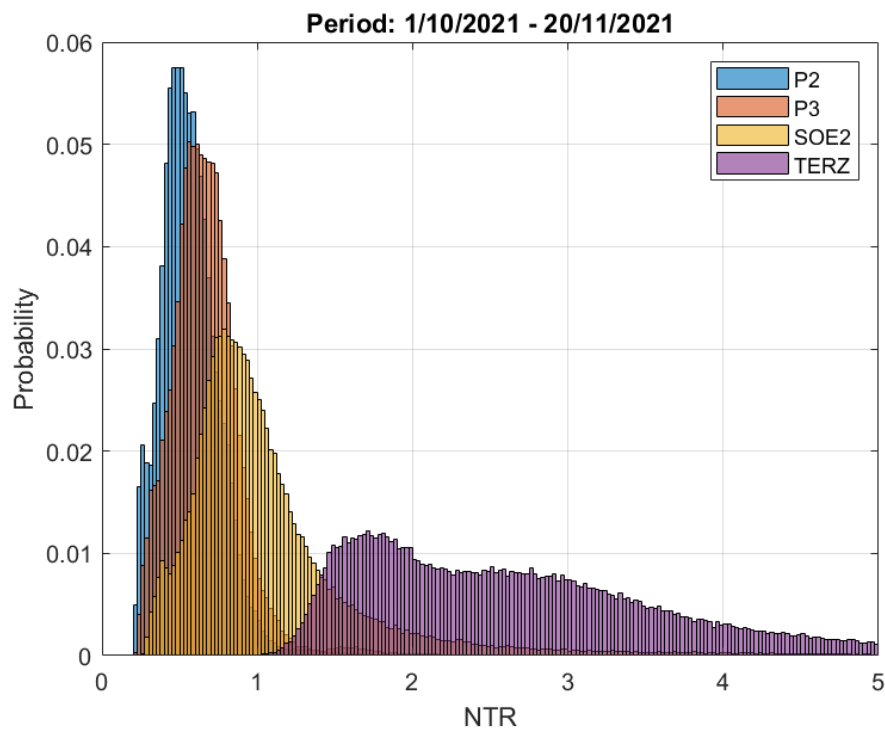


Figure 2.12: Probability density of NTR for the vertexes of ET in Sardinia and in the bore-hole in Terziet. As expected the bore-hole in Sardinia show a noise well below the sensitivity limit, while Terziet would not warrant a good duty cycle even with a reduction a factor three of the noise

Chapter 3

Beam-balance prototype: measurements and results

3.1 The Balance working principle and its use as Tiltmeter in Virgo

The Archimedes project is highly original, as there are currently no balances as sensitive as the experiment requires, and therefore intensive prototyping was required to design the final scale.

There are many important and delicate points in the design of the balance. We list them briefly here, leaving a detailed description to the rest of this chapter, where we report the published papers:

- Mechanical coupling of the arm tilt with the other degrees of freedom
- Elasticity of the joints
- Vertical positioning of the centre of mass
- Optical sensing selection
- Interferometer design
- Actuators and controls
- In air and remote tuning

3.1.1 Mechanical coupling of the arm tilt with the other degrees of freedom

In the mechanical design of the balance, one of the delicate points is the method of suspension of the moving arm. A first possibility is a single-wire suspension, as for torsion pendulums. This solution was not chosen because of the complication of also having to check the rotational degrees of freedom around the vertical and longitudinal pendulum axes, and it was decided to leave only the tilting degree of freedom of the arm soft.

For the suspension of the arm, one possibility is represented by knives, i.e. an extremely sharp blade on which the arm rests. This solution has been discarded due to thermal noise problems: it is not easy to control the friction that the blade exerts on the arm when it rotates, and therefore it is very complex to evaluate and control the oscillator loss angle, with consequent unreliability of thermal noise projections.

It was therefore decided to suspend the arm with two elastic elements, one on each side. The last possible variant in this solution is to use wires or joints for the elastic elements. The choice fell on couplings, illustrated in the following subsection, because it is possible to make a single-piece machining for the joint and the attachments on the arm and the suspension column as in the figure 3.1.

This avoids friction between the spring element and the attachment points, which could increase thermal noise. Note that this choice is not the only one possible, depending on how the wire and the wire attachment are designed. For example, in Virgo the mirrors are suspended from silica wires. In this case, however, the wire forms a whole with the attachment body because it is soldered by silicate bonding to a fin, which in turn is soldered by silicate bonding to a lateral protuberance of the mirror, called the ear. The upper part of the wire is in turn soldered to the upper fin and then, again by silicate bonding, to the suspension element immediately above the mirror, called the marionette.

3.1.2 Elasticity of the joints

Another important point in the design of the balance are the joints, the elastic element which suspends the arm and provides the pull force. Since the balance has to be very light, in particular the moment of inertia I of the arm has to be as small as possible ($I = 1.3 \cdot 10^{-2} \text{kg} \cdot \text{m}^2$ with brass counterweights and before sample installation, $I = 2 \cdot 10^{-2} \text{kg} \cdot \text{m}^2$ with suspended sample and one brass counterweight) in order to give

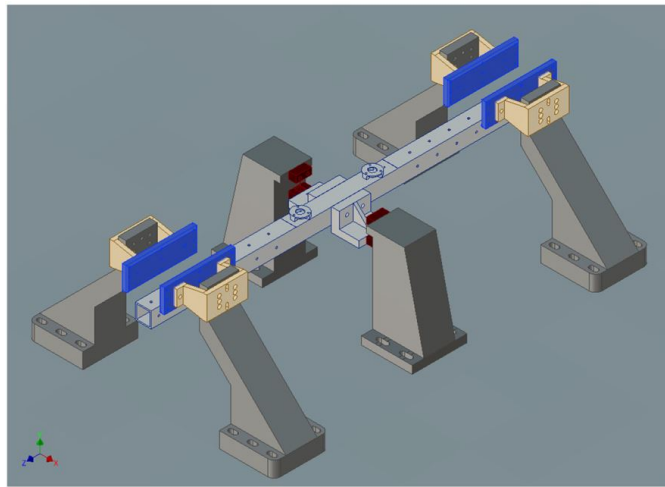


Figure 3.1: Balance arm suspension design. Note the dark-orange components, the joints. The arm is suspended by the joints and can rotate around the horizontal axis thanks to their elastic behavior. The blue plates are the electrostatic actuators

appreciable displacements in the presence of small forces, it follows that the stiffness of the joints has to be very small, in order to keep the resonance frequency of the balance around tens of mHz.

The design of the joints is shown in the figure 3.2: the small stiffness is achieved by drawing a bundle, thin enough to provide the desired stiffness and at the same time robust enough to be handled and installed. The dimensions in the case of the Virgo prototype were: thickness of 0.1 mm, height of 6 mm, and width of 0.5 mm and allowed a resonant frequency of 25 mHz, with the non-zero gravitational stiffness given by the distance of about $15\mu\text{m}$ between the centre of mass and the point of rotation of the arm. Subsequently, couplings with a width of up to 0.1 mm were constructed and used in the balance currently in use.

3.1.3 Vertical positioning of the centre of mass

Beam balances and tiltmeter signals should not be induced by translation ground motion, but only by weight variations or ground rotations, respectively. It is known that, if the tiltmeter center of mass does not lie on its rotation axis, a ground acceleration along the arm direction \ddot{z} generates a torque on the arm $\tau = m\delta\ddot{z}$, where m is the arm mass and δ is the distance from the center of mass to the rotation axis. This means that, in order to minimize the coupling between \ddot{z} and the arm tilt, the distance δ needs to be

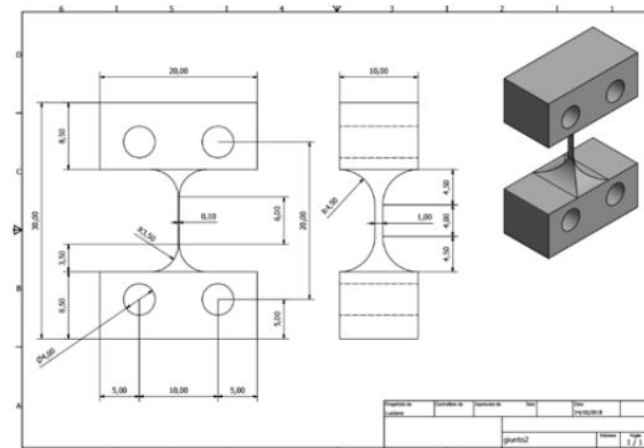


Figure 3.2: Schematic working principle of an optical Lever: a tilt of the mirror is read as a displacement of the reflected beam on the position sensing device

tuned as close as possible to zero. Several tests have been performed to ascertain the difficulties in setting this distance within the limits of about $10 \mu m$, as required by the Archimedes experiment. The tuning of the center of mass position is done by regulating a set of screws placed on the arm. With the finest screw rotation, the center of mass can be moved by about $1 \mu m$. Tuning operations are performed in air, and tiny mechanical displacements can occur while going into vacuum.

Adjusting the centre of mass in air was used both during the O3 run and to date. As described in the following article, there are several possibilities to verify that, once in vacuum, the centre of mass remained in an acceptable position, in particular the direct measurement of the coupling between the longitudinal ground motion, measured with accelerometers placed close to the balance, and the tilt of the balance itself. Further confirmation comes from the sensitivity to distant earthquake signals. In this case, the first waves to arrive are the Primary waves, which are translation (compression) waves and therefore are expected to induce considerable signals in the accelerometers but negligible in the balance. Then come the Secondary waves, which are superficial, and bring with them the tilt so that one expects both the accelerometers and the balance to see a signal. This is what was actually observed during the Virgo data taking.

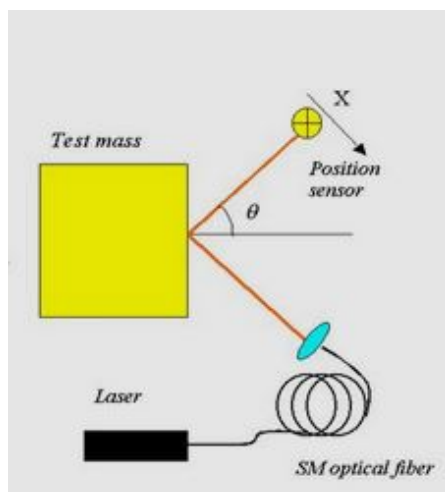


Figure 3.3: Schematic working principle of an optical Lever: a tilt of the mirror is read as a displacement of the reflected beam on the position sensing device

3.1.4 Optical sensing selection

The main choice of optical design is the use of either optical levers or an interferometer to measure the tilt of the arm. An optical lever consists of a laser beam that is reflected by a mirror attached to the system whose angle is to be measured and where the position of the reflected beam is read with a position-sensitive photodiode, such as a Position Sensing Device (PSD) or a Quadrant Photodiode (QP), as in the figure 3.3.

Optical levers would be preferable for ease of use but, at least in the single pass configuration, they do not achieve sensitivities $\tilde{\theta}_n$ better than $\tilde{\theta}_n \approx 10^{-8} \text{ rad}/\sqrt{Hz}$ in low frequency regime (tens of mHz) and about $\tilde{\theta}_n \approx 10^{-8} \text{ rad}/\sqrt{Hz}$ in high frequency regime (tens of Hz) Bassan et al. [2019b].

These limits are unfortunately not sufficient for the sensitivity θ_{An}^{\sim} required in Archimedes at low frequency, which is of the order of $\theta_{An}^{\sim} \approx 3 \cdot 10^{-10} \text{ rad}/\sqrt{Hz}$ and are not compatible even with use as a tiltmeter for high-frequency Virgo Harms and Venkateswara [2016] where it is required at least $\theta_{Vn}^{\sim} \approx 10^{-11} \text{ rad}/\sqrt{Hz}$.

One possibility for increasing the sensitivity of the optical levers is to implement a multi-pass, i.e. to make the beam reflect n times on the mirror so as to increase the final reflection angle and thus the displacement on the photodiode by n times. With an accurate opto-mechanical design n can even reach a value of $n = 30$ and thus, at least in principle, achieve the desired sensitivity. The fundamental problem, however, is

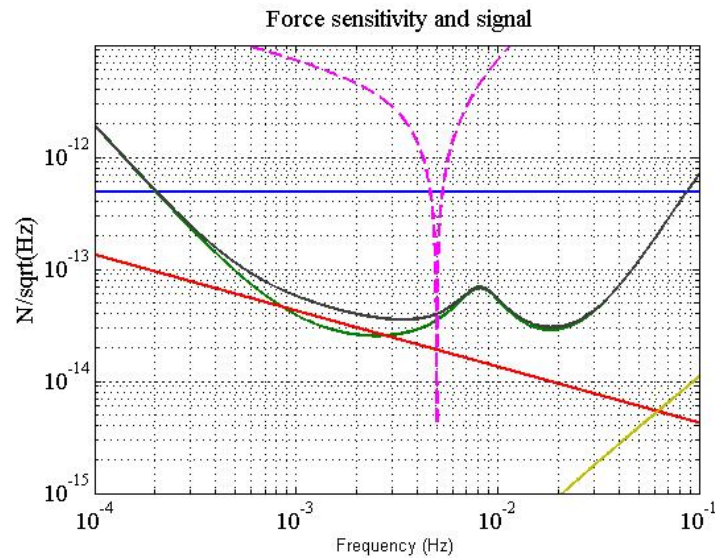


Figure 3.4: Archimedes sensitivity curve in case of interferometric and optical lever sensor. Note that if an optical lever is used the bandwidth is reduced at small bandwidth, around the resonance frequency of the balance, supposed at 5 mHz. The temperature modulation would be chosen inside this bandwidth.

that the optical lever itself, due to the mechanical mounting of the laser or the optical fibre from which the beam comes out, is also subject to mechanical or thermal tilt. This causes the input beam to undergo angular deviations indistinguishable from the rotation of the mirror and typically not less than the desired values. The optical design and the opto-mechanical realisation are therefore extremely delicate, and it has been decided to resort directly to an interferometric scheme.

A further possibility which could enable the use of optical levers is to modulate the vacuum weight signal, i.e. perform thermal modulation, exactly at the resonance frequency of the balance. If the measuring equipment is limited by sensing (as in the case of using optical levers) then the mechanical transfer function can be used to bring the signal out of the noise. (This is not true for e.g. force noise, like actuator noise: here measuring at resonance frequency would give no gain). This can be seen in figure 3.4. The signal, in blue, is higher than the noise of the optical lever, dashed, only around the resonance frequency. Although this possibility would have allowed for a simpler optical scheme, being able to work only at a certain frequency was deemed too restrictive for the thermal modulation system and the interferometric solution was preferred.

Even the design and implementation of an interferometer system is not without its

difficulties. In fact, while on the one hand an interferometer guarantees immediately better sensitivity than optical levers, it is typically weak with respect to misalignments and furthermore, for tilt shifts that generate optical path differences greater than half a fringe, it has a non-linear signal with respect to the shift. The first condition contains the risk that, for tilts even of the order of mrad, the interferometer will no longer have a signal, and the second that the interferometer must work in a closed loop, because in a soft system such as a highly sensitive balance, displacements even in stationary conditions are expected to be well above half a fringe.

Both of these difficulties required an appropriate optical and mechanical design, in order to meet the conditions without overcomplicating either the optical scheme or its implementation, which will be described in the following paragraphs.

3.1.5 Interferometer design

The interferometer has been designed with the following requirements: (1) minimize coupling with undesired degrees of freedom; (2) maintain good contrast even for relatively high tilts; and (3) allow realignment by moving optical elements not lying on the reference nor on the measurement arm. This last requirements is of great importance because the arm of the balance must be free of moving. Electrical connections or others contacts needed to move remotely actuators on the arm would destroy the softness, re-couple the seismic noise and finally destroy the sensitivity. In the final balance also the reference arm will be suspended, so also for the reference arm it is forbidden to have remptely moving parts. The optics must be designed so to have an interferometer capable to be re-aligned just by moving only the input optics, which stands outside the interferometer itself and let both the arms free from reinjection of noise.

The first condition has been obtained with the beams impinging on the mirrors perpendicularly. To keep a simple optical scheme, a Michelson interferometer with physically unequal arm lengths has been chosen, for a path length difference of 10 cm. In the first version of the prototype, used in the tilt measurement in Virgo during the run O3, the path difference was not compensated.

After the run O3 the balance was upgraded and an optical delay line has been installed in the shorter arm, as shown in figure 3.5. The The second condition has been fulfilled by designing the interferometer in such a way that the angular and translation separations of the two interfering beams are of the second order with respect to the arm tilts. This has been obtained by adding in both the beam paths a lens with focal length f equal to the

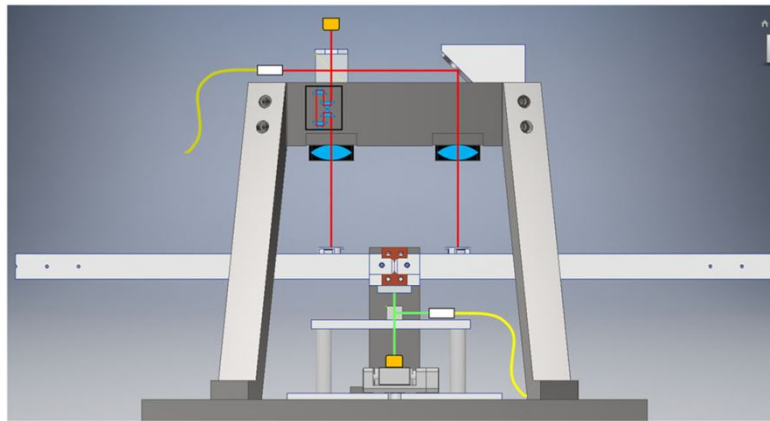


Figure 3.5: Balance optical scheme. The red line identifies the path of the laser light in the interferometer. The light is injected with the fiber (in yellow at the top left) and split by the beam splitter. In the shorter interferometer arm, there is a delay line, consisting of prisms, which equalizes the pathlength. The two lenses, shown in blue, have focal lengths equal to their distance from the balance arm, so that the interferometer contrast is sensitive only to the second order to the tilts of the arm itself. Below the arm is the optical lever, which serves as an initial alignment reference

distance between the lens itself and the mirror, so that the beam is focused on the arm mirror (see figure 3.5). This scheme allows also the fulfillment of the third specification. Indeed, if the arm tilt α is higher than a few mrad, the interferometer can be realigned by translating the input beam vertically by the quantity $\delta y = Lf\alpha$. In this condition, the beams impinge again orthogonally on the arm mirrors; then, they are reflected on the incoming path and recombine correctly at the beam splitter, as sketched in figure 3.5. Notice that in any case the optical lever has not been completely abandoned. The readout is completed by an auxiliary optical lever, powered by a superluminescent diode (SLED) and read by a quadrant photodiode. The lever is designed to have the beam impinging perpendicularly on a mirror placed on the lower face of the balance arm, and it is used as an initial reference position for the arm tilt.

3.1.6 Actuators and controls

In accordance with the choice of using interferometric readings, it was decided to work in closed loop. Electrostatic actuators were chosen as the feedback system. In contrast to magnetic actuators, such as coil-magnets, this avoids having magnetic elements on the arm, which could couple with the external campomagnetic and generate unwanted forces. The design of the actuators is relatively simple and consists of plates placed in

front of the arm, on the side. The plates are placed a little higher than the arm, as in the figure 3.1, and cover only a part of the side surface of the arm, so that by applying a potential to the actuator (the arm is electrically grounded) there is a pull force directed upwards.

The lateral design has been preferred to a typical frontal design, i.e. with the plates above or below the arm, in order to leave a free surface of the arm where to insert any counterweights and to allow easy manoeuvring.

Finally, the control electronics is digital: in the case of the Virgo run, the acquisition and control electronics provided by the experiment were used (see next article), while in the Archimedes run, National Instruments electronics were used.

3.1.7 In air and remote tuning

A final important point concerns the lateral balancing and vertical positioning of the mass centre. As mentioned above, the vertical positioning is performed in air, then the vacuum chamber is closed with the dome lid and evacuated. In this process it has been observed that the vertical position of the centre of mass does not undergo appreciable variations and therefore, at least in the prototype phase, it has been considered acceptable.

Balancing is more complex. Especially in the current version of the prototype, where the joints are very soft, balancing is performed in air but is strongly disturbed by the operation of closing the chamber. In the final Archimedes balance this problem is solved by remote adjustments, which can be performed with the chamber closed. The prototype balance initially had no such adjustments and, once the chamber was closed and evacuated, the correct horizontal position of the arm was recovered by means of electrostatic actuators. The problem with this solution is the noise reintroduced by the low-frequency actuators. For operation in Virgo as a tiltmeter, whose required measurement bandwidth is around tens of Hz, this was not a problem and in this configuration the data taking was achieved. For operation in Archimedes, even in the prototype phase, when the scale was installed in the low-noise site of Sos Enattos, it was remotely adjusted to allow the use of low-voltage actuators that do not produce low-frequency noise.

3.1.8 The role of the prototype for ground tilt and NN studies in Virgo

As we have seen in the reference [Harms and Venkateswara, 2016] tiltmeters can be very important tools for active reduction of Newtonian noise. At high frequencies, around

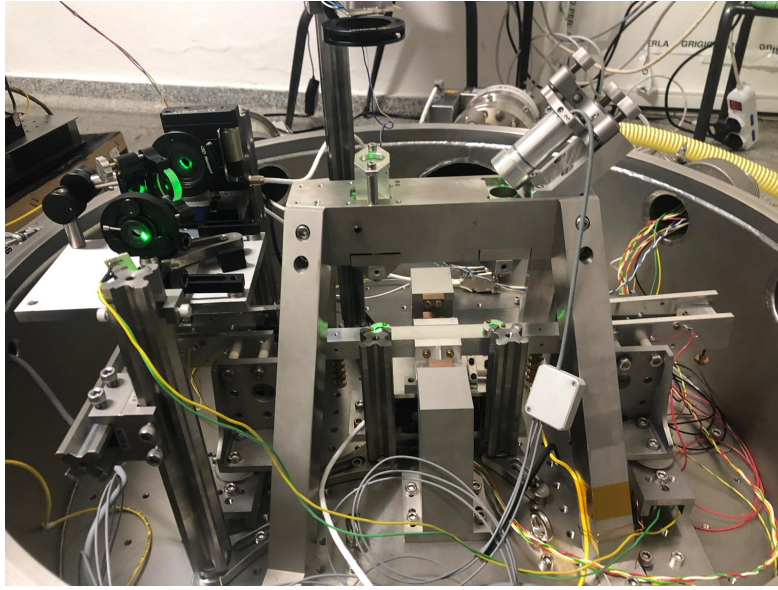


Figure 3.6: A picture of the balance installed at the North End building in Virgo. Notice the arm with no-suspended samples.



Figure 3.7: The balance installed at the North End building in Virgo.

tens of Hz, which are of interest for Newtonian noise, the balance, on which specially suspended samples are not mounted, can be used as a tiltmeter: in fact the suspended arm, having the resonance frequency much lower than 10 Hz, can be considered inertial. If the supporting plane of the balance undergoes an inclination, the interferometer measures a relative tilt of the arm with respect to the ground, correctly attributing it to the movement of the ground.

The sensitivity of the interferometer is such that the measurement is effective and can be used in gravitational-wave detectors.

The prototype balance, not equipped with suspended samples (see figure 3.6), was then installed on the Virgo site, in the North-End building, at a distance of about 5 m from the Superattenuator and performed a 3-month data-taking during the Virgo O3 run (summer 2019, see figure 3.7).

In the same building and at the same time a series of strategically placed accelerometers was installed by the Virgo collaboration to be used again to study active Newtonian noise reduction. The tiltmeter and the accelerometers worked in parallel for a common reconstruction of the ground tilt. The paper reported in Appendix B presents the results obtained with the tiltmeter, both with respect to coherence with the accelerometers and with respect to coherence with the dark fringe (the main signal of the Virgo interferometer). The Virgo collaboration also performed new joint analyses of the tiltmeter and accelerometer constellation signals with respect to ground tilt reconstruction [Singha et al., 2021], which verified in further detail the results presented here.

Among the most important results of this paper is the demonstration that the prototype has achieved good sensitivity at high frequencies, that the Virgo site is still a good site from a ground tilt point of view, and that there are nevertheless interesting coherences with the dark fringe, not attributable to Newtonian noise but probably to couplings of the seismic noise with the Virgo strain signal through scattered light effects.

3.2 Tiltmeter results in Sos Enattos

From a chronological point of view, the balance, after data taking in Virgo, was transferred to Sos Enattos. The main reason for this was to be able to push and study the sensitivity limits of the balance, given the extremely quiet site, which, as we shall see, is one of the quietest in the world. This possibility is all the greater when one thinks of the activities at Archimedes, but it also plays an important role when one thinks of the use of tiltometry in Virgo and also of the verification of the potential of Sos Enattos

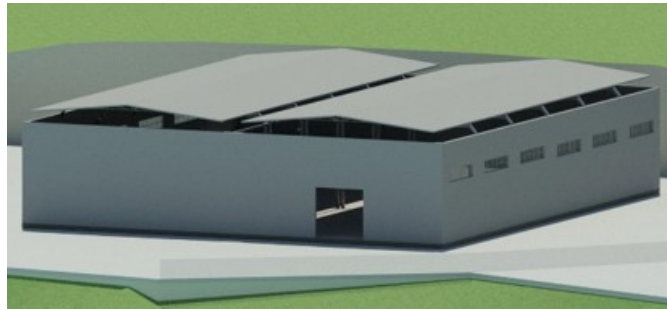


Figure 3.8: Schematic view of the Edificio Graniti

to host the Einstein Telescope.

At the time of the start of this thesis, and also at the time of the transfer of the balance (November 2019) to Sos Enattos, there was no laboratory. Previously, a Programme Agreement (Accordo di Programma) had been signed between the Regione Sardegna, the University of Sassari, the Istituto Nazionale di Fisica Nucleare and IGEA (the company managing the mine on behalf of the Region of Sardinia) for the creation of a laboratory, named SAR-GRAV, to host at the site of Sos Enattos experiments on gravitation and in support to the Gravitational Waves observatories.

Following the agreement it was decided to proceed with the creation of the laboratory in the so-called “Edificio Graniti”, a large shed of about 2000 m^2 , on surface.

The Edificio Graniti, as long as the mine was in operation, had been used for the cutting and processing of granite extracted partly in the vicinity of the mine and partly from outside. At the time of Archimedes’ arrival, these activities were no longer being carried out, but some minor carpentry work remained and, above all, the building still contained the old machinery and was extremely dusty, too poor to house an optical experiment. A technical drawing of the building is shown in the figure 3.8 and a photograph is shown in the figure 3.9 when part of the building had been cleared of machinery.

Due to this working condition, the Archimedes collaboration proposed to use two small rooms, located towards the back of the building, and closed in relation to the central part where to host the prototype. In the first room a small laboratory was installed and in the second a control room.

The main important point of the room was their standing on the concrete, so that the quietness of the site was preserved (no noise amplification due to fake floors).

In figure 3.10 it is shown the very first installation of the lab, with an optical bench and the balance on the side. In figure 3.11 the first installations on the control room are



Figure 3.9: Picture of the internal of the Edificio Graniti, once part of the machines have been removed



Figure 3.10: Picture of the first installations on the optics laboratory hosting the prototype balance.

showed.

Once the balance had been transferred, work was devoted both to improve the laboratory equipment and to operate a number of improvements on the balance, described in details in the following article included in the thesis. They were mainly dedicated to improving low-frequency sensitivity: the length asymmetry of the arms was reduced with the introduction of the delay-line obtained with the series of prisms in the shortest arm, a pick-off photodiode was installed at the interferometer input to normalize the error signal and thus reduce the laser amplitude noise, and further improvements were taken to adjust the center of mass.

The first important result of this activity, which is the topic of the article in Appendix C, is the measurement of the ground tilt of Sos Enattos. Here, we have to recall that the



Figure 3.11: First installations on the Control Room

balance was installed in the Edificio Graniti, where carpentry works were still performed. Thus the measurement of the sensitivity were performed during nights or week-end. The results are reported in figure 3.12 . As it is seen, in the frequency band of Virgo, from 10 to about 20 Hz, and the frequency band of interest for Einstein Telescope, above 2 Hz, the measured ground tilt $\tilde{\theta}_s$ lies in the region of few picoradians/ \sqrt{Hz} . This level of noise is about two orders of magnitude better than in Virgo site and it is one of the best never measured in the world.

Actually, also the sensitivity reached by the balance, in this use as tiltmeter, is at our knowledge the best in the world. In any case, it is better than sensitivities shown by similar tiltmeters used in gravitational wave detection, planned to be used for newtonian noise reduction.

3.3 The balance prototype and its use in low frequency

Although the results of the prototype balance as a tiltmeter are extremely encouraging and already make the tiltmeter a very useful instrument in view of the reduction of Newtonian noise in gravitational wave detectors, the main use of the prototype balance is towards Archimedes, and therefore mainly towards low frequencies and towards the use with hanged samples.

At low frequencies, the complexity is somewhat greater when achieving optimal sensitivities, for several reasons. The first is the seismic noise, which increases at low frequencies, then there are the optical noises, such as the laser frequency and amplitude noise, and the electronic control and especially actuation noise, which also increases with low fre-

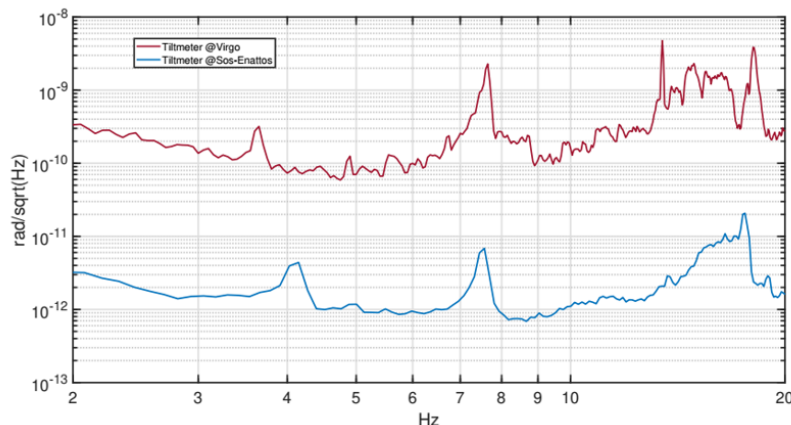


Figure 3.12: Ground tilt measurement in Sos Enattos (blue curve) and in Virgo (red curve). All measurements and commissioning are explained in the following article. Here we underline that this extreme sensitivity has been demonstrated thanks to the extreme seismic sensitivity of the Sos Enattos site. The result is the best sensitivity in the world, to our knowledge, and especially the further demonstration of the suitability of the site of Sos Enattos to host the ET interferometer.

quencies.

The first analysis of this noise is given in the following article, which is dedicated to the balance and especially the control loop. In the article in Appendix D the important part is precisely the definition of the loop, which proves to be sufficient to close in feed-back the movement of the arm. The signal used in this case is an optical lever signal, given the impossibility of using the interferometer because all tests were conducted in the Naples laboratory, which is too noisy to allow an effective closed loop on an interferometric signal. The other fundamental consideration arising from this article is that operating in high seismic noise environments makes it extremely difficult to achieve the required sensitivities, especially at low frequencies, and has forced the Archimedes experiment, including the most important prototypes, to work directly on the Sos Enattos site. In fact, in the case of the system in Naples, the balance was installed on top of a commercial seismic isolation system (Minus-K technology) see figures 3.13 which guaranteed an overall resonant frequency of about 0.5 Hz. This attenuation is certainly excellent for high frequencies, and allowed a first good measurement of the behaviour around Hz.



Figure 3.13: The balance installed over the Minus-K platform in the Naples laboratory

3.4 The balance in Sos Enattos and new recent results

As we have seen in the previous articles, both the work on low frequencies, carried out especially in Naples, and the work on high frequencies, carried out both in Virgo and Sos Enattos, have made it possible to obtain a satisfactory closure of the loop and, in the high frequencies, have led to an extremely sensitive tiltmeter. However, considerable final work was needed on the prototype to allow it to be a true balance and to achieve, even in this capacity, remarkable sensitivity. The first part of the work consisted of designing the system for attaching the sample to the arm. The sample has a mass $m = 250$ gr, in accordance with the mass of the superconducting sample which will be suspended in the final balance. The fundamental point of this coupling is that since the mass of the sample is significant it must be suspended in such a way that the suspension point has the same vertical position as the center of rotation of the arm. Failure to do so would imply a significant displacement of the center of mass with respect to the pivot point, with significant coupling with the seismic translational noise. In addition, the sample must be suspended by means of sufficiently soft wires, so as to decouple, at first order, the tilt of the arm from the vertical displacement of the sample. The suspension of the sample is shown in figure 3.14:

3.4.1 Sample's suspension

The suspension wires are made of tungsten and have a diameter of 0.08 mm. Each of them is clamped to a thin, perforated copper tube with a hole diameter of 0.1 mm, which in turn is soldered to a screw. This screw is screwed onto the arm, in order to adjust the height of the sample. To prevent the wires from twisting when the screws are tightened, the other end of each wire is not attached directly to the sample (this would in fact make adjustment impossible) but is also attached to a screw on which a counter-screw is placed that is screwed onto the body of the sample.

In the figure 3.14, the upper adjusting screws, screwed into the arm, are indicated with the term “screws for the tuning of the sample quote”, while the counter-screws, which are part of the sample, are indicated with the term “counter-screws for quote regulation”. In figure 3.15 it is shown a zoom of the sample suspended to the arm. The regulating screws, blacks, are visible on the top, on the upper part of the arm, while the counter-screws, in aluminum, are visible on the body of the sample.

The procedure for mounting the sample on the arm is the following: the arm is fixed on the optical table with the helps of stopping mechanics, the sample is mounted on the

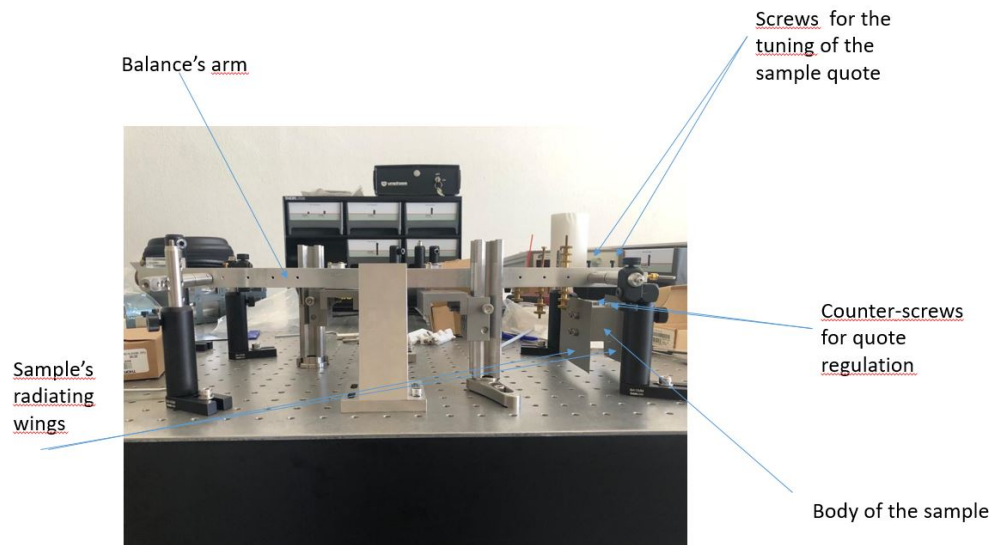


Figure 3.14: The balances's arm on the optica table for sample suspension and regulation. The arm is blocked with auxiliary mechanical stops and the sample is mounted.

arm and the first quote regulation is done thanks to a visual inspection of the position of the first free point of the wires with respect to the center of the arm. Hence the arm is let free to oscillate around its joints and, by iteration, the quote is regulated until the resonance frequency of oscillation reached the tens of mHz.

At this point the operation is considered finished and each other tuning of the resonance frequency (i.e. the tuning of the vertical position of center of mass with respect to rotation point) is obtained by adjusting the counterweights once the arm is mounted on the balance.

The sample has the mass of 250 gr and it is made of aluminum. It is equipped with two wings, to radiate heat and maintain the sample always in thermal equilibrium in case of accidental light impinging on the sample. Also the wings are indicated in figure sampleDescription.

Once the first tuning on the optical bench is done the arm is mounted on the balance, inside the vacuum chamber. In figure 3.16 it is shown the final position of the arm and the sample inside the chamber.

3.4.2 In vacuum tuning and high power laser for thermal heating

In the figure 3.16, next to the sample, other elements of the system are shown. The first is the pair "Screw on the arm for in vacuum arm balancing" and "Feedthrough for

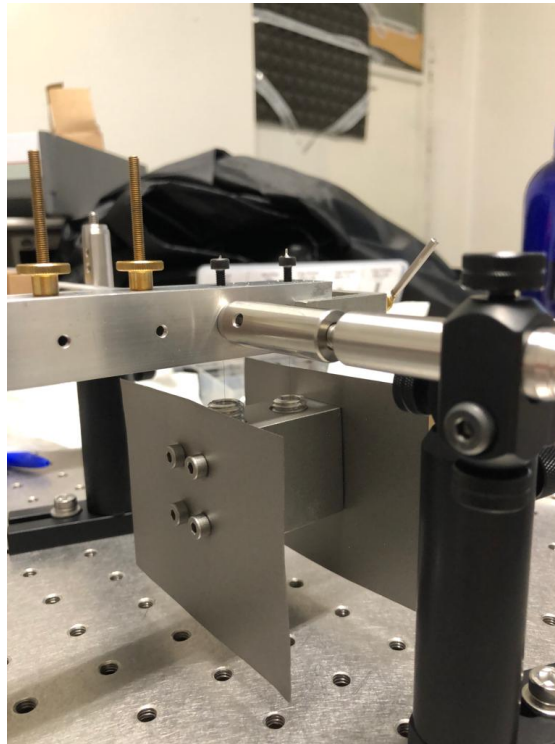


Figure 3.15: A zoomed picture of the sample suspended to the arm. The regulating screws are visible on the top, on the upper part of the arm, and the counter-screws are visible on the body of the sample.

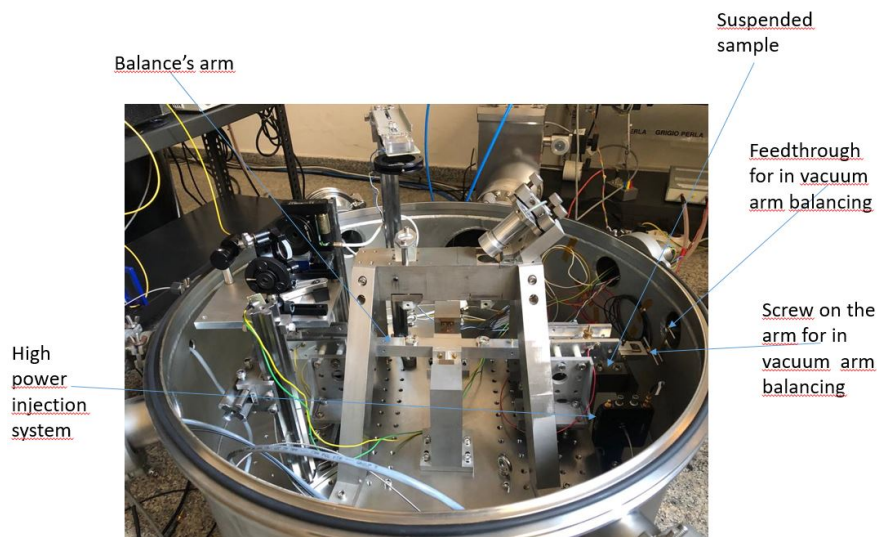


Figure 3.16: The balances's arm inside the vacuum chamber

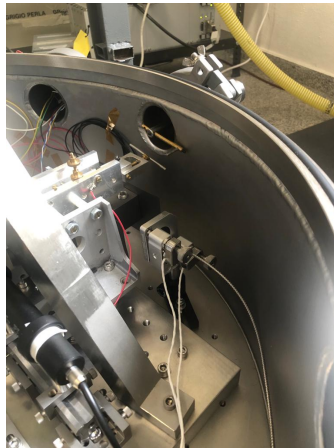


Figure 3.17: Zoom of the vacuum chamber part where the sample, the arm regulation screw and the high power laser fiber are located

in vacuum arm balancing”. This pair allows re-balancing of the arm once the system is placed in a vacuum. In fact, since the balance is extremely soft, even if it is balanced before evacuating the chamber, once in vacuum it is out of balance again. Typically the voltage value to be applied to the actuators to bring the arm back to horizontal is of the order of 500 V and this would be compatible with the dynamic range of voltage amplifiers, which reach 2000 V. As we have said, however, the actuation noise is proportional to the applied voltage and so to make the actuators work around lower voltages, in the order of tens of volts, rebalancing is also carried out in vacuum. The screw-feedthrough pair was made completely “in home” for initial testing. Once the positive response was obtained, commercial feedthroughs were purchased, to be used in the final balance as well.

In the balancing procedure the arm is first stopped with a remotely adjustable stop (not shown in the picture for simplicity), then the screw position is adjusted with the feed-through and finally the stop is released. The procedure is hierarchical until a position of the arm is reached that allows a satisfactory interferometric signal. Recall here that the interferometer is designed to maintain a good contrast even for relatively large tilt signals: this means that it has a certain ease in balancing the arm and above all that the force required to close the loop is very small, because it is equivalent to remain within the first useful fringe. As we have already said, good external tuning allows external voltages to be as small as tens of V.

The second element indicated in figures 3.16 and 3.17 is the high power fiber, pow-



Figure 3.18: The Os-Tech diode laser utilized for thermal studies in balance prototype

ered with a high power laser diode, with maximum output power of about 50 W. The laser diode is produced by Os-Tech, the model is dso11-la50v03, can be modulated in amplitude, the wavelength is 808 nm and it exit in fiber, as shown in figure 3.18. The fiber is mounted on a Physic Instrument tip-tilt mounting, remotely driven.

This laser beam is foreseen to be used for calibration purposes and also to test effects of temperature modulation on the sensitivity of the balance. Preliminary tests done with several powers, modulated at tens of mHz, did not shown indications of sensitive variation in sensitivity. feed back stability or other effects

3.4.3 Sensitivity

As described in previous paragraphs and papers, le balance equipped with the improvements made after the run in Virgo and equipped with its suspended sample has been tuned to work also in low frequency. The best activity to be performed is to reach a good balancing, so to have the need of small voltage from actuator, tune horizontally the vacuum chamber plane to avoid stresses on the balance components and carefully turn off not necessary equipments to avoid environmental noise.

The control loop transfer function has been measured and it is reported in figure 3.19: the unity gain is at 350 mHz, the balance resonance frequency is at 35 mHz. The electronic filter has a real pole at 1 mHz, two real zeros before the resonance to compensate the π resonance phase rotation and two poles above 1 Hz to avoid noise reinjection. Further, two more resonant zeros, compensate with low Q resonant poles, are inserted at 1.8 and 2.2 Hz to compensate for resonance picks in the open loop transfer function to fundamental oscillation of the suspended sample and of its coupling in rotational degree of freedom.

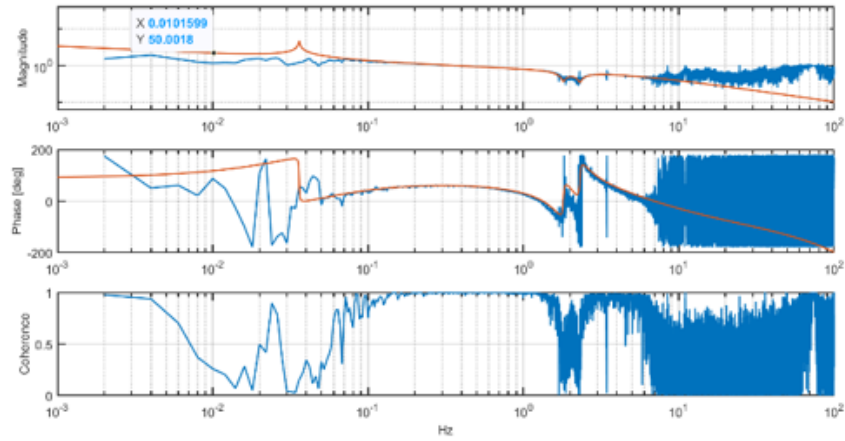


Figure 3.19: Open Loop transfer function: measurement (blue curve) and fit (red curve)

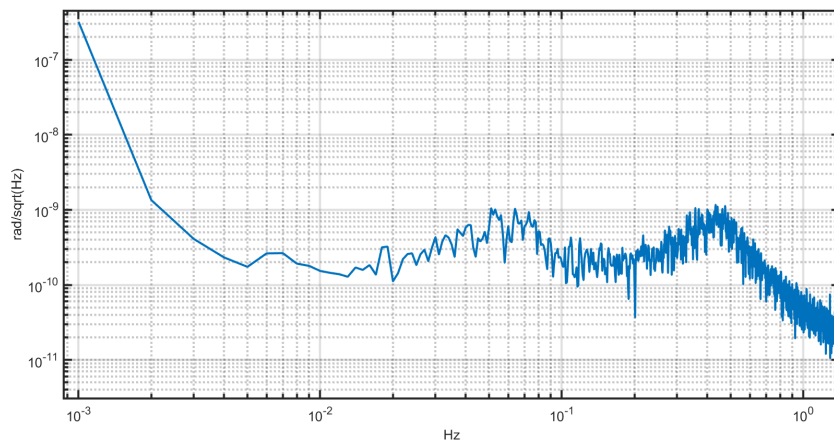


Figure 3.20: Closed Loop error signal of tilt

The closed loop measurement of tilt $\tilde{\theta}_s$, which is a mean over one hour data taking during night, is reported in figure 3.20. They are transposed in torque sensitivity \tilde{M} taking into account of the loop with the use of:

$$\tilde{M} = \tilde{\theta}_s \frac{1 + G \cdot H}{G} \quad (3.1)$$

where $G \cdot H$ is the open loop transfer function measured above while G is the plant function of the free balance when excited by a torque \tilde{M} :

$$G = \frac{1}{I(-\omega^2 + \omega_0^2 + i\omega\omega_0/Q)} \quad (3.2)$$

where Q is the balance oscillation quality factor and I is the moment of inertia of the arm. In this measurement and also in the previous measurement not all can be measured completely. In fact the momentum of inertia I is calculated by taking into account all the masses and their position on the arm. In this process an error in the accuracy of 10% is possible. The measurement of the closed loop transfer function GH is performed by using a colored injection noise, due to the different response at very low frequency (where the signal is suppressed by loop), at frequency around the resonance frequency (where can be a residual amplification) and at high frequency, where the signal is suppressed by the plant.

From equation 3.1 the equivalent in torque sensitivity is recovered and it is reported in figure 3.21. In the figure it is reported also the best sensitivity reached during the data taking in Virgo (even if at that time there were no suspended samples). The two curves show the increasing in sensitivity in moving is Sos Enattos and also implementing the different upgrades discussed above.

The most remarkable improvement, of about 1 order of magnitude, is around 10 mHz, because in this region of frequency we will very probably perform the final Archimedes measurement of vacuum weight.

Quite remarkable this sensitivity is, at our knowledge, the best reached in the world for a balance. A part from this consideration, what is important is that the sensitivity is approaching the desired final one \tilde{M}_d , which, being about $\tilde{M}_d = 7 \cdot 10^{-13} \text{ Nm}/\sqrt{\text{Hz}}$ is now distant less than one order of magnitude. It is important to point out that the results of the prototype are still open to further improvements, for several reasons, driven by the fact that the low frequency commissioning is yet to be concluded. The first is that the system can be made softer by a better tuning of the resonance. At the present the resonance has been left at 33 mHz for keeping the rest of the operation easier. Tuning the

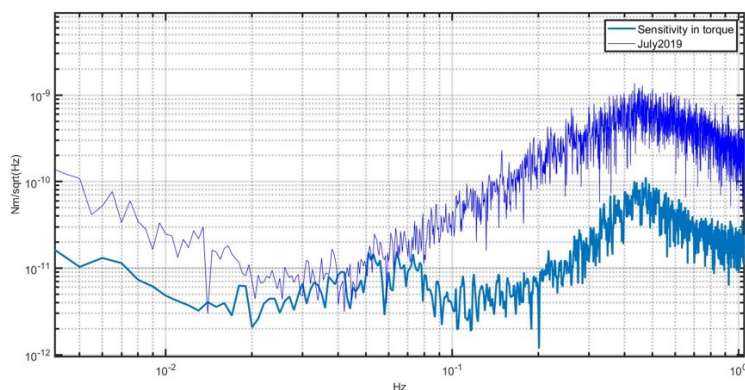


Figure 3.21: Torque sensitivity in Sos Enattos (light blue curve) and in Virgo site (dark blue curve)

resonance would also reduce the horizontal seismic coupling, which is still present as can be seen by observing the ocean peak in the hundreds mHz region. The second is that the optical sensing can yet be improved: if the low frequency noise is laser frequency noise, this could be reduced by better tuning of pathlength difference. On this subject we point out that the final balance, thanks to all the heritage of the prototype, will be equipped with a very stable laser (Coherent - Mephisto) to run above frequency and amplitude instabilities.

Contrary to torque sensitivity, the present prototype is not the best tiltmeter at low frequency. Indeed if the equivalent free tilt noise $\tilde{\theta}_n$ is recovered by the use of the closed loop equation 3.3 the result is a noise shown in figure 3.22.

$$\tilde{\theta}_n = \tilde{\theta}_s \cdot (1 + G \cdot H) \quad (3.3)$$

The low frequency tilt noise is estimated to be slightly better than $\tilde{\theta}_n \approx 10^{-8}$ rad/ \sqrt{Hz} around 10 mHz, which is slightly worse than similar measurement in LIGO tiltmeter [Venkateswara et al., 2014]. The difficulty in reaching a very good sensitivity also in tilt is given by the fact that the balance arm is very light, in order to have a low moment of inertia and have a very soft system capable of measuring small forces. This condition makes the joint and actuator design more difficult and limited until now the possibility to improve also the sensitivity in tilt.

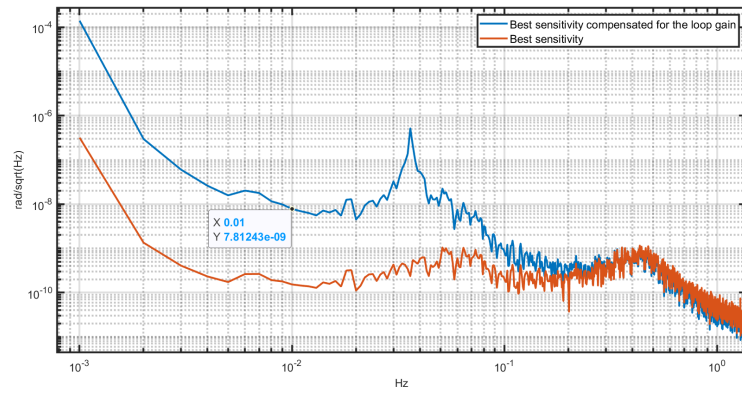


Figure 3.22: Tilt sensitivity in Sos Enattos at low frequency

Chapter 4

The Final Experiment

4.1 Seeting up the SAR-GRAV laboratory

For a long time, since the first approaches of Adalberto Giazotto with the then President of the Region of Sardinia, Renato Soru, the Italian Gravitational Waves scientific community had proposed Sardinia as the ideal region to host the new generation of Gravitational Waves observatories.

However, despite the scientific quality of the proponents and also a certain political willingness, the steps followed one another in a very uncertain, slow and laborious way. A first small breakthrough came when Fulvio Ricci's direct search for a mining site willing to host at least the instruments for seismic measurements met with the positive response of the Director of the Sos Enattos mine, Luca Loddo.

This allowed the first installations inside the mine, which led, around 2010, to the seismic measurements that were included in the first submission of the Einstein Telescope project to the European community.

However, the site of Sos Enattos remained relegated only to hosting small instruments for seismic measurements until, thanks to the support of the University of Sassari, it became realistic to propose the construction of a real laboratory, around 2017.

This need was also perceived by the National Institute of Nuclear Physics. In fact, the international ET community had in the meantime identified another candidate to host the observatory: the site of Terziet, in the Netherlands, which was also supported by the simultaneous creation of an ad hoc laboratory intended to host a prototype interferometer to test ET technologies. Although the site of Sos Enattos appeared to be better from the seismic point of view, a partial and incomplete characterisation of the site would not have been sufficient to convince the scientific community of the superior

suitability of the site to host the observatory. It was therefore necessary to create at Sos Enattos a laboratory that would act as a scientific coadjutant for the new activities of Gravitation Physics, act as a pole for the complete characterisation of the site and, once demonstrated its great potential, allow to support Sardinia as the ideal region to host the new ET observatory. This push for a new laboratory would have been possible if there had been at least one experiment in Gravitation Physics of significant importance to the National Institute of Nuclear Physics, so as to justify its commitment and investment. This experiment was Archimedes.

In the years 2014-2016 Archimedes had started its journey in the feasibility demonstration phase at the INFN V group and in the years around 2016-2017 the Archimedes collaboration was selecting possible sites, necessarily at low seismic noise, where to install the final apparatus. Therefore, the condition that Archimedes would act as a driving force for the realization of a low seismic noise laboratory was considered by the Archimedes collaboration, the Italian ET community and INFN as an ideal condition for the birth of the new laboratory, which was funded by the Sardinia Region with a Program Agreement together with the University of Sassari, INFN and INGV: thus, in 2018, the SAR-GRAV laboratory was born. Of course, at the time of the laboratory's creation, the mine was far from being a physics laboratory. The large shed, already described in the previous chapter, the Edificio Graniti, was identified as the place to start the activities. As mentioned in the previous chapter, unfortunately the Edificio Graniti was very dusty and still occupied by the large machines for cutting and transporting granite, so the collaboration chose to start from two rooms adjoining the building, which served as offices, to create the first small laboratory and the first control room.

It was also decided to install in this first laboratory the prototype of Archimedes and to design the new laboratory in the area of the shed, where the final experiment would be carried out. In the meantime, the group of the University of Rome La Sapienza, Department of Civil and Environmental Engineering, realized the project for the construction of the underground laboratory, destined to host the future activities of Archimedes and of Gravitation Physics, which require a site with low seismic noise.

In figure 4.1an aerial picture of the mine is reported and in the figure 4.2 a scheme of the project for the underground laboratory. Finally, in picture 4.3 a picture of installation of a seismometer in the mine.

Part of my thesis work also consisted of understanding the needs of both the laboratory where the prototype is installed and the design of the surface laboratory for the



Figure 4.1: A panoramic view of the Sos Enattos minierary site

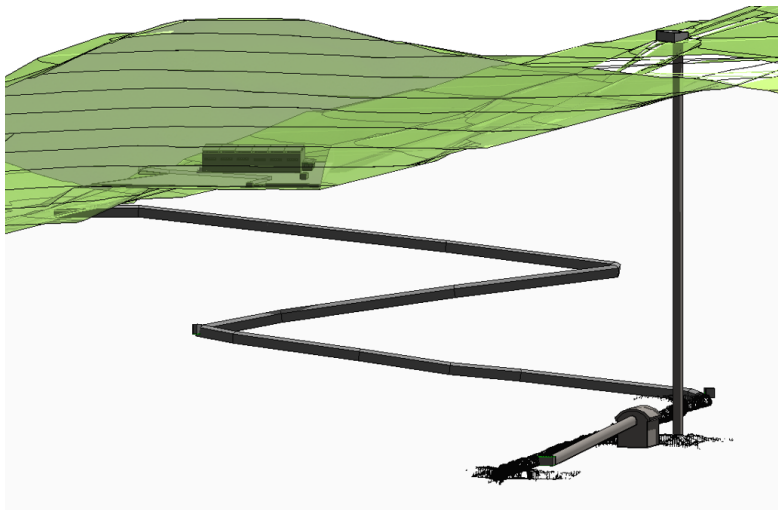


Figure 4.2: The project for the underground laboratory. The Experimental hall is at about -150 m underground, and it is reached with a the tunnel called "Rampa Tupeddu". The project plans also the realization of a shaft for air conditioning and emergency exit



Figure 4.3: Installation of a seismometer in the mine

final apparatus.¹ The description of the prototype and the small laboratory where it was installed was made in the previous chapter. We now focus on the surface laboratory where, as we shall see, the final balance was installed. The initial area of the shed is visible in the figure 4.4. As we can see, just after having cleared half of the shed, much work remained to have a sufficiently flat and relatively clean floor.

After a first recovery of the floor, it was decided to install two experimental chambers: a real chamber for the installation of the experiment, with a surface of 50 m^2 , a height of 5 m, with an opening roof, so that the parts of the large cryostat containing the balance could be easily assembled and disassembled, and a storage chamber for the bulkier parts of the experiment, waiting to be finally installed. Having an opening roof made it simple the installation of a crane, that can be maintained externally with respect to the experimental hall, simplifying the hall construction.

The figure 4.5 shows an overview of the experimental and storage rooms after their completion. The dimensions of the main room have been chosen in order to allow an easy arrangement of the apparatus elements, in particular the cryostat, the optical table and other support equipment for the final apparatus. It should be noted that the vacuum pumps, both in the case of the prototype and in the case of the final balance, are located outside the room, in suitably obtained and acoustically isolated rooms, so as to minimise the environmental noise induced on the measurement apparatus.



Figure 4.4: Schematic view of the Edificio Graniti just after that the half part of the surface has been set free from cutting machines



Figure 4.5: Picture of the two halls with the stockage room hosting the upper part of the criostat stored

4.2 Criostat and balance support

All the final equipment will be installed in the Planck Room. The first installation is the internal shield of the cryostat, which is the vacuum chamber in which the balance is located. A diagram of the cryostat is shown in figure 4.6. It consists of three shields. The outer cylinder is 2.40 m high and 2 m in diameter. The inner shield is 2 m high and has a diameter of 1.60 m. Each cylinder is connected to the next by a conduit at the top and the last one ends with a mushroom-shaped structure, on which the vacuum feedthroughs for the optical and electrical lines and the pumping system are attached.

Inside the vacuum chamber (the inner part of the cryostat) is the support for the balance. This is an imposing aluminium structure, whose task is not only to serve as a support for the balance but also to serve as a coupling point for all the electrical and optical cables and to allow effective heat exchange, so as to keep the balance in thermal equilibrium during cryogenic operation. The assembly procedure of the system was carried out in three stages. In the first step the cryostat was installed in the experimental room, as shown in the figure. Then in the second phase, the upper part of the cryostat, including the side cylinder and the upper base, was separated from the base and stored in the storage room (suitably protected from dust), as can be seen in figure refinsiemeInterno. Finally, in the third step, the base of the cryostat was fitted with the scale holder. Figure 4.8 shows the balance support installed on the base of the cryostat. The protection of the cryostat base can be seen, allowing the balance to be safely installed and commissioned.

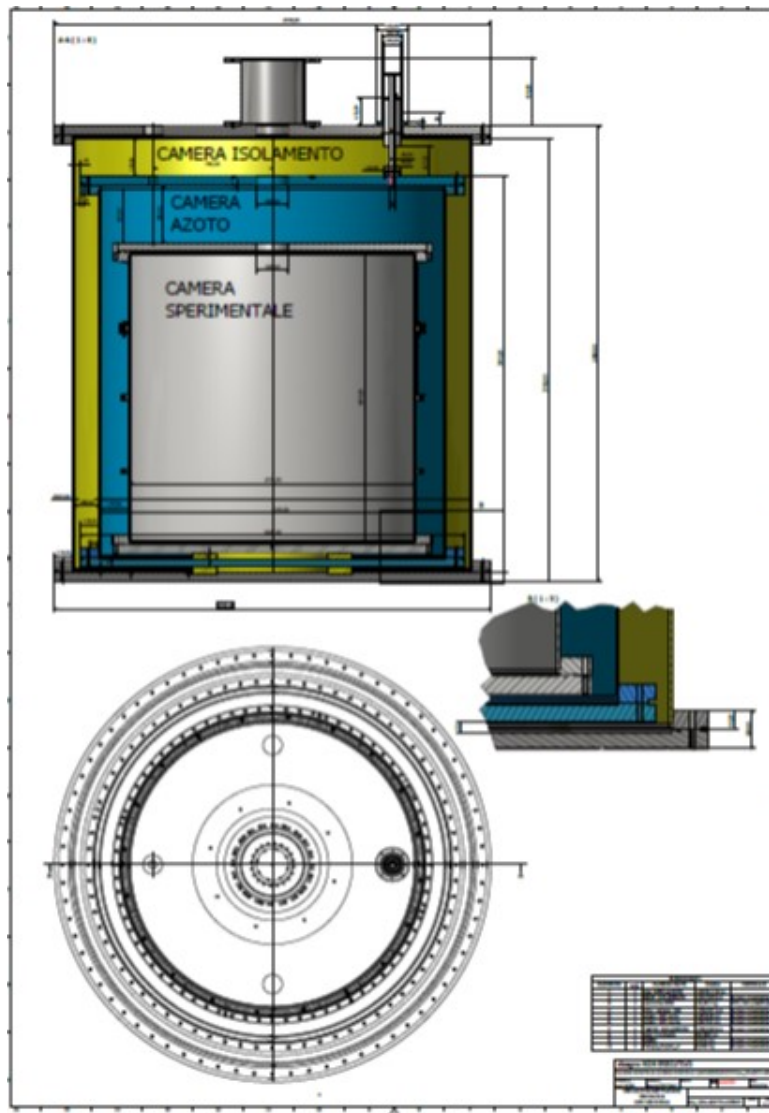


Figure 4.6: Scheme of the cryostat. Note that each shield lies on a proper base, separated by the previous one in order to have the possibility to realize and test each cylinder in a separate way.



Figure 4.7: Installation of the cryostat in the Planck Hall



Figure 4.8: The balance support installed over the balance base

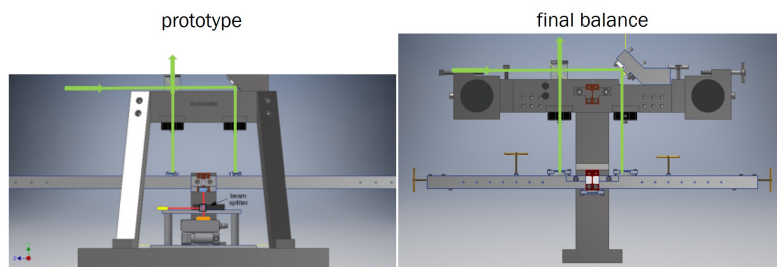


Figure 4.9: Comparison between prototype and new balance. The optical scheme is preserved but all critical optics are suspended. Further the reference arm is evidenced, particularly its geometry that results in a high momentum of inertia

4.3 The balance

The new balance shares many constructional choices with the prototype but, thanks to the accumulated experience, also has several improvements. The first important point is the optical scheme, which, similarly to the prototype, is a Michelson interferometer whose arms are made equal by a delay line inserted in the arm which, by construction, would be shorter. However, there is also a conceptually important difference between the new balance and the prototype: all the optical parts that define the arms of the interferometer are suspended. In particular, the optical parts that were previously fixed to the ground now form a second suspended arm positioned above the measuring arm. In this way the tilt measurement, which was previously referenced to the ground, becomes referenced to the new suspended arm, which thus becomes the reference arm, as in figure 4.9.

In order to have the reference arm isolated from the seismic motion, the resonance frequency is chosen a decade lower than the measurement frequency. This arm, not having the function of a balance, i.e. to measure small applied forces, but on the contrary being a stable reference with respect to the measurement arm (and more stable than the ground), is designed with a large moment of inertia in a similar way to the tiltmeters Ross et al. [2020]; Venkateswara et al. [2014]. A list of the characteristics of the new balance compared to the prototype is given in the table 1.

In terms of optics, there are several significant changes between the prototype and the final apparatus. First of all, the laser that will be used is a Coherent-Mephisto laser, with fibre output. This laser is a non-planar ring oscillator (NPRO), which is extremely stable in both amplitude and frequency. These characteristics mean that the sensitivity of the balance is not expected to be limited by amplitude or frequency noise. In addition, the laser is also controllable in both amplitude and frequency. In this way, if even the

	Prototype	Final Balance
ITF optical parameters		
ITF laser wavelength	532 nm	1064 nm
ITF input laser power	50 mW	500 mW
Laser frequency tunability	No	Yes
Laser amplitude tunability	No	Yes
Faraday isolator	In-fiber	In-fiber
Injection active axes	X, Y (remote) θ_x, θ_y (manual)	X, Y (remote) θ_x, θ_y (remote)
ITF optics roughness	Polished ($\lambda/10$)	Superpolished ($\lambda/100$)
Absorptive ND Filters	No (<i>postem</i>)	Yes (<i>ab initio</i>)
Measurement-arm parameters		
Arm-length	0.5 m	1.4 m
Section	20 x 20 mm (hollow)	20 x 20 mm (hollow)
Mass (with no samples)	0.2 Kg (+ 0.4 Kg)	0.6 Kg
Material	Aluminium 6061	Aluminium 6061
Momentum of inertia	0.013 Kg·m ² (2 brass ctrweights) 0.02 Kg·m ² (sample & ctrweigh)	0.13 Kg·m ² (no samples) 0.38 Kg·m ² (with samples)
Joints dimensions	0.1 x 0.25 x 6 mm	0.1 x 0.25 x 6 mm
Joints material	Cu-Be alloy	Cu-Be alloy (investigating sapphire and fused silica)
Reference-arm parameters		
Suspended	No	Yes
Arm-length	-	0.42 m
Section	-	50 x 50 mm (solid)
Mass	-	12 Kg
Material	-	Steel AISI 304 (+ ctrweights Tungsten W 99%)
Momentum of inertia	-	0.3 Kg·m ² (phase 1)
Joints dimensions	-	0.1 x 3 x 6 mm
Joints material	-	Cu-Be alloy (investigating sapphire and fused silica)

Figure 4.10: List of critical parameters in prototype and new balance

process of injection of the beam in the interferometer will induce additional noise this can be actively reduced. The laser wavelength is increased from 532 nm to 1064 nm. This makes it possible to utilise the extensive knowledge and experience gained in the Virgo detector, which uses the same wavelength. In particular, the coating of the mirrors and the scattered light dampers will be similar to the auxiliary mirrors used in Virgo and the dampers already tested in this experiment.

In the final balance also, the positions of the dampers are already included in the optical design, which makes the whole system more efficient in absorbing scattered light. Finally, both devices use optical levers for rough positioning of the balance arm. Finally, a further improvement in optics will be the degrees of freedom that can be controlled remotely. In the case of the prototype the degrees of freedom with which the position of the input beam can be changed are vertical and horizontal translations. As written in chapter 3, this already makes possible the realignment of the interferometer even in the presence of large arm tilts. In the final balance, as shown in table 1, the input beam can also be remotely controlled with rotational degrees of freedom. This additional controllability adds to the robustness of the entire apparatus and is considered all the more important considering that the balance will be at cryogenic temperature.

From a mechanical point of view, as we have mentioned, the most important difference between the prototype and the final apparatus is the suspension of the reference arm. However, there are also important differences with regard to the measuring arm. First of all, the new measuring arm is now 1.4 m long, compared to the current 0.5 m. This is to improve the sensitivity to small forces, applied to the end of the arm. In the prototype, we observe that, in spite of the shorter length, the mass of the arm has been chosen to be equal to the final measurement arm mass. This was done in order to study the dynamics of the arm using the same joints, with the same applied tension. However, the momentum of inertia of the final balance is higher, and it is therefore expected to be easier to achieve a low resonance frequency with the same joints. The material chosen for the joints is Cu-Be in prototype. In the final balance same material is used, but there is room left to study the possibility to use silica or sapphire joints.

In the new balance, both the horizontal balancing and the vertical positioning of the centre of mass can be performed remotely, for both arms. The diagram of the reference arm (in this case 0.50 m long) with all adjustments is shown in the figure 4.11. The electrostatic actuators, at the ends of the arm, and the vertical positioning system of the

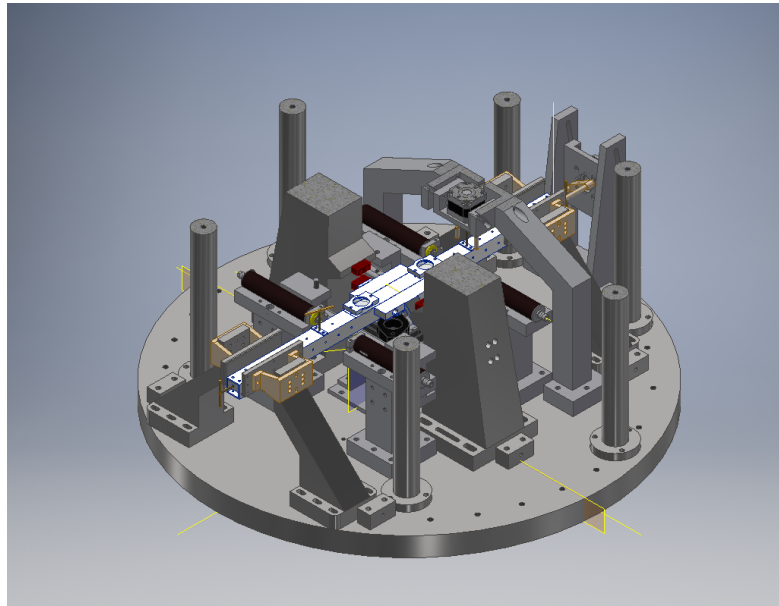


Figure 4.11: Design of the lower part of the balance, showing in particular the measurement arm and the control parts

centre of mass, made with a pair of screws, symmetrically arranged with respect to the centre of the arm, each of which can be rotated, and therefore screwed into the arm, with a remote rotator, are also visible in the figure (for simplicity of visual reading only one rotator is shown in the figure).

The balance consists of two floors. In the lower floor there is the measuring arm and all related adjustments and controls. This realization is shown in the figure 4.12. From the lower floor there are two large columns supporting the joints where the two arms are suspended. We note that the two arms are suspended from the same column, so that any seismic noise is shared, favouring subtraction. The two floors are composed of the bases and all the auxiliary parts of optics, control systems and regulators, similar in the two arms and shown schematically, for the measuring arm in the figure 4.11.

The reference arm, mounted on the balance, is shown in the figure 4.13. As shown in table 1, the arm is significantly heavier than the measuring arm, because it has to serve as a stable reference. The relatively high mass and moment of inertia allow a less critical joint design and an easier achievement of a low resonance frequency than a lighter arm (like the measuring arm). To make the arm sufficiently heavy, two tungsten counterweights were also fitted. As shown in the figure, the reference arm is also equipped with remote centre-of-mass adjustment systems, both horizontally and vertically. In the

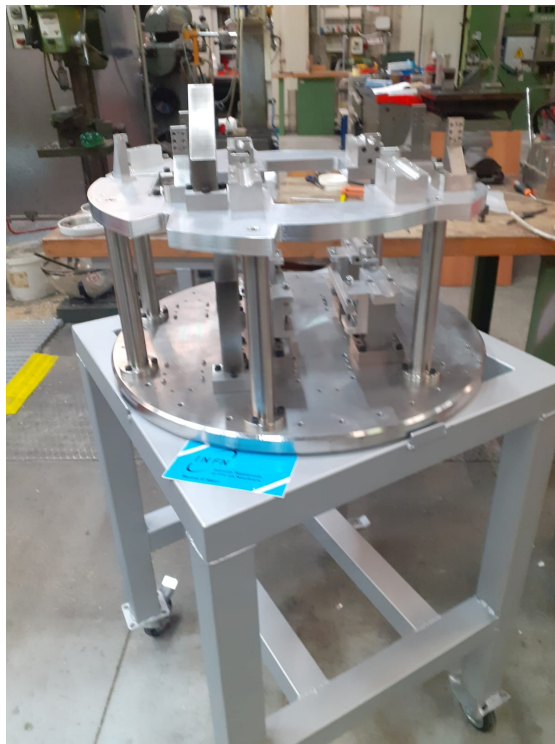


Figure 4.12: The assembly phase of the balance when the two basis are clearly visible



Figure 4.13: The reference arm installed on the balance

figure, the tungsten counterweight, in grey, and the horizontal adjustment screws are visible in the foreground. Visible on the arm are the beam-splitter and the deflection mirror and, before the beam-splitter, the two vertical adjustment screws (the reference arm has a total of four vertical adjustment screws). Further down are the joints from which the arm is suspended (brown). Notice how in this figure the arm is blocked by the two clamps (black).

Finally, a photograph of the complete balance, as installed at Sos Enattos, is shown in the figure 4.14. We observe the two bases that support the control elements for each arm, the two columns on which the joints are mounted, which protrude from the upper base. Finally, on the right-hand side of the figure, we observe the step-by-step rotator used to turn the balancing screw for the centre of mass of the lower arm, with a scheme similar to that used for the balancing of the prototype in which, however, the adjustment is manual via a vacuum feed-through.

At present, the mechanical part of the balance and the related optics have been installed in Sos Enattos, in the support installed on the base of the cryostat, as described in the previous paragraph. It now remains to complete the electrical wiring and the

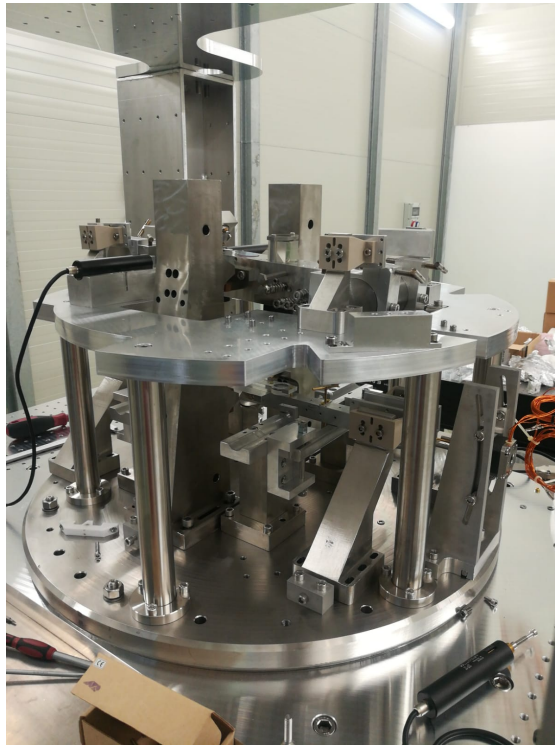


Figure 4.14: The balance installed at Sos Enattos

injection optics. This important work is expected to be completed within the year. The most important part of the balance, i.e. all the mechanics with the associated optics, is now correctly installed. It should be noted that all the mechanical parts have been checked not only in their assembly but also in their operation (vices, rotators, joints) and the optical part has been checked in its fundamental functions, such as alignment and beam path-length. These solid foundations are the basis for the continuation of the activities.

4.4 Towards a measurement for Tolman hypothesis

The Archimedes experiment is designed to measure the interaction of vacuum fluctuations with gravity. However, as we have seen, it has brought with it some interesting measurements already at this stage, such as the first measurement of seismic ground tilts at the level of $\tilde{\theta}_s = 10^{-12}$ rad/ \sqrt{Hz} and the first demonstration of a balance that reaches the torque sensitivity $\tilde{\tau}$ of some Nm/ \sqrt{Hz} . These interesting results, and above all the remarkable sensitivity reached in the measurement of torque, can open the way to a further measurement, complementary to the measurement of the weight of vacuum, but very interesting: the measurement of the weight of heat.

Heat is a classical form of energy, so it is not questionable that it follows the law of gravitation in all respects in the same way as any other form of energy. However, at the level of laboratory measurements, there is no experimental verification and, more importantly, no experimental evidence that thermodynamic quantities follow gravity. This circumstance is all the more relevant when one considers the intriguing relationship of thermodynamics with gravity, proposed by various and different theories that started with the early works of Beckenstein, Hawking and others on black hole entropy [Bardeen et al., 1973; Bekenstein, 1972, 1973] and, even earlier, by the works of Tolman who first formulated the heat weight hypothesis in 1930 [Tolman, 1930; Tolman and Ehrenfest, 1930]. With respect to the latter hypothesis, it is remarkable that to date, after more than 90 years, no experimental verification exists. Equally important is the consideration that the relation between gravity and thermodynamics is one of the most intriguing and complex subjects of contemporary physics, which has led to remarkable theoretical reinterpretations of gravity as being intimately linked to the thermodynamics of space-time [Carroll and Remmen, 2016; Padmanabhan, 2002a,b, 2015]. Although much of the work linking gravity to thermodynamics, and in particular entropy, derives from the early work on black hole entropy and temperature, in recent years the entropy of classical

systems in the gravitational field with horizon has also started to be investigated, such as a photon gas in a Schwarzschild field or in an accelerated Rindler reference system [Kolekar and Padmanabhan, 2010]. In a situation involving both matter sources and gravity, it is not quite clear what precisely is the inter-relationship between the usual thermodynamic entropy of matter and the entropy of the horizon.

All the works on gravity in interrelation with thermodynamics are theoretical works. It has not yet been possible to verify experimentally any of the results of these theories, nor to lay the experimental foundations for a possible future investigation. Bearing in mind this lack of any experimental verification the present thesis has proposed to investigate the possibility of carrying out a first measurement of a relation of a thermodynamic quantity with gravity. The proposed measure is classical and must be considered as a first step towards future experimental proofs of the many theories proposed and never verified. The measure proposed is the weight of heat. This measurement, as we have seen, would represent the first experimental verification of Tolman's hypothesis and, considering that the final state of the system being weighed changes its temperature and entropy, the measurement would be the first experimental verification of the weight of entropy (multiplied by temperature) ever carried out.

At the time of writing this thesis, it was not yet possible to carry out such a measurement up to the end, but preliminary tests have been performed which are very useful both for the measurements that will be carried out with the prototype and to take experience in temperature modulation for the final balance case. The tests have been done using the *OS – Tech* high power laser described in section 3 and injecting about 1 Watt of power on the suspended sample. In order to obtain an efficient modulation, both theoretical studies and sample sizing have been carried out, to finalize the measurement of the heat weight in the next months. In the following we describe the sample sizing and the measuring system.

4.4.1 Sample's parameters choice

The measurement of the heat weight can be made on the suspended sample. The first tests will be made on the suspended sample in the prototype balance. The chosen shape of the sample is a parallelepiped to which two plates are added for heat dissipation. The dimensions and parameters of the sample must be chosen in such a way that in the time of a modulation the heat is first deposited on the sample (illuminating the sample with a power laser) and then, once the source is switched off, in the second half of the modulation it re-emits the heat by radiation in order to be able to start the cycle again.

In this cycle of heating and re-emission, the main source of spurious signal is the radiation pressure. If the beam were to impact vertically on the arm, the vertical force exerted on the arm by radiation pressure would be about 8 orders of magnitude greater than the weight force. The method by which the effect of radiation pressure can be reduced is by making the direction of the beam as horizontal as possible, and by observing that the weight of the sample is the integral of the power input, and therefore lags behind the power input. For example, in an ideal sinusoidal modulation the weight of heat would lag behind the radiation pressure by $\pi/2$.

With regard to the sample parameters, the following procedure is followed. The laser power $P(t)$ which is sent to the sample can be written as:

$$P(t) = \frac{P_{max}}{2} (1 + \cos\omega_0 t) = \frac{P_{max}}{2} + A \cos(\omega_0 t) \quad (4.1)$$

where P_{max} is the maximum power incident on the arm and for sake of simplicity the modulation amplitude $A = \frac{P_{max}}{2}$ has been defined. Taking into account only the heat absorption of the sample and the radiation, the main parameters that determine the temperature of the sample are the specific heat C_v , the mass m of the sample, the emissivity σ of the plates, the surface S of the plates. In this evaluation other effects on temperature, mainly heat conduction, are neglected. Indeed the wires coupling with the sample can be made with thermal insulator.

Under this conditions the heat equation can be written as:

$$mC_v \dot{T} = \alpha \frac{P_{max}}{2} + A \alpha \cos(\omega_0 t) - S \epsilon \sigma (T^4 - T_0^4) \quad (4.2)$$

where α is the absorption coefficient of the metal at 808nm and ϵ is the emissivity coefficient, C_v is the specific heat of the sample, m is the mass of the sample, T_0 is the environmental temperature. In order to solve the equation a first order approximation can be made, considering the temperature $T = T_M + \delta T$, where T_M is the mean temperature during the modulation process.

In this way, neglecting the terms of higher order with respect to $\frac{\delta T}{T_M}$, one recover a first order linear equation

$$mC_v \dot{T} = \alpha A \cos(\omega_0 t) - 4 \epsilon S \sigma T_M^3 \delta T \quad (4.3)$$

with T_M given by the condition:

$$\alpha \frac{P_{max}}{2} = S \epsilon \sigma (T_M^4 - T_0^4) \quad (4.4)$$

The first parameter that can be fixed is the power P_{max} of the laser. By using the high power laser *OS – Tech* the power can be fixed at 22 Watt, which is the maximum value that it has been obtained at the output of the fiber inside the vacuum chamber, measured with power meter.

The mean temperature T_M equation furnishes a condition to set the surface S at $S = 26.5 \cdot 10^{-3} \text{ m}^2$. The absorption coefficient at 808 nm is estimated in $\alpha = 0.5$ and the black body coefficient is estimated in $\epsilon = 0.5$. Notice that this coefficient has been measured after having coated the sample with a proper silver paint to increase both absorption and radiation efficiency. With this coefficient and parameters the mean temperature will be few tens of degrees (Kelvin) above the environmental temperature, allowing to make the first tests on heating the sample via laser radiation.

The linear equation 4.3 results in the usual Fourier transformed solution:

$$\delta\tilde{T}(\omega_0) = \frac{\alpha A}{4S\epsilon\sigma T_M^3 + \omega_0 m C_v} \quad (4.5)$$

The material chosen for the sample is aluminum, the $C_v = 896 \text{ J/kg}$. The mass of the sample is 0.225 kg so that the amplitude of the expected temperature modulation and phase delay, corresponding to the integration effect, is not too much affected by radiative effect once reached the steady state. Indeed, by inserting the values described before the amplitude of temperature modulation is almost defined by the absorption coefficient, so that the heat modulation is almost equal to photon energy deposition and the phase is almost $\pi/2$, as expected by integration.

4.4.2 Preliminary heat deposition tests

As stated above we have performed preliminary tests on the prototype. The sample has been irradiated with modulation amplitude $P_{max} = 1 \text{ W}$ and frequency $f_0 = \frac{\omega_0}{2\pi} = 20 \text{ mHz}$. The high power fiber is mounted on a tip-tilt remotely driven, in order to minimize the effect of radiation pressure. The tip-tilt is a commercial PI angular step motor with minimum tilt step of $0.5 \mu\text{rad}$ and a range of 16 degrees. In order to maintain the interferometer locked even with a radiation pressure vertical component not negligible, a stronger control loop have been implemented. With respect to the filter described in Chapter 3, we added a zero-pole couple at frequency 1 mHz for the pole and 15 mHz for the zero. The amplitude F_p of the vertical force due to radiation pressure, considering an initial misalignment θ (due to manual regulation of the angle of the beam) of few angular degrees, equal to $\theta = 0.1 \text{ rad}$, is initially $F_p \approx \frac{P_{max}\theta}{2c} = 1.7 \cdot 10^{-10} \text{ N}$ and requires a quite strong control to not lose the locking; the filter transfer function is reported in

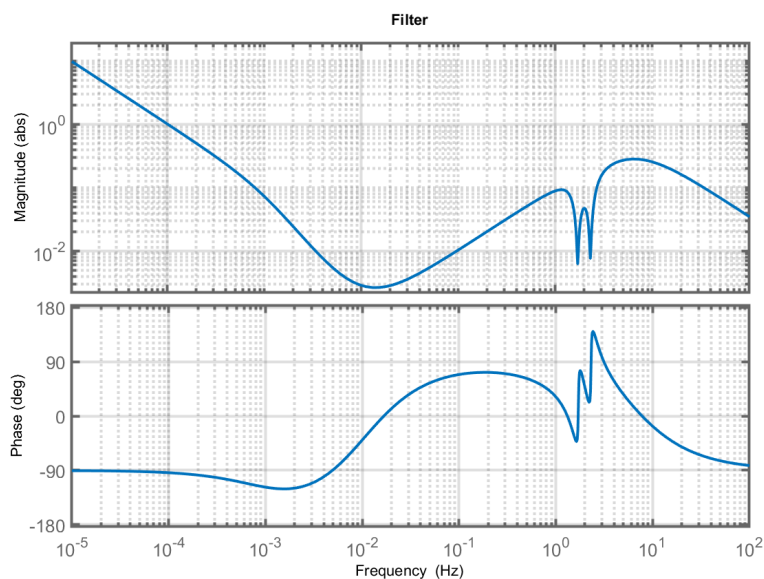


Figure 4.15: Control filter for power injections: a pole-zero couple is added in low frequency to enhance the low frequency gain

figure 4.15 and the open-loop transfer function is reported in figure 4.16.

The tip-tilt is varied to explore the various regions of angular power beam injection, to minimize the coupling of radiation pressure with balance tilt. The run performed until now is reported in figure 4.17. The time duration of the data taking is about 2 hours and we see that the error signal is lowered towards 10^{-3} V. In this measurement the conversion factor from Volt to radiant is $2 \cdot 10^{-6}$ rad/V; the value of this factor is due to some setting of the interferometric read-out, such as the contrast mainly. The gain of the feedback in this frequency is $G=40$ (as shown in figure 4.16); remembering that the momentum of inertia is around $2 \cdot 10^{-3} \text{kg} \cdot \text{m}^2$ and the arm of the force is 0.23 m, this oscillation corresponds to a force of about $F_p = 10^{-11} \text{N}$. In terms of torque τ this force corresponds to about $\tau_p = 2.5 \cdot 10^{-12} \text{Nm}$, In this preliminary tests we did not succeeded in nulling the radiation pressure effects on tilt, the above value of torque corresponds to an equivalent residual angular misalignment of $\theta = 3 \cdot 10^{-3}$ rad.

. This is probably due to the fact that the application point of the radiation pressure is also varying when the angular direction of the beam is varied and the total effect is the sum of the vertical component of the radiation pressure and the coupling of the other degrees of freedom and parameters with the tilt. Further work is planned in order

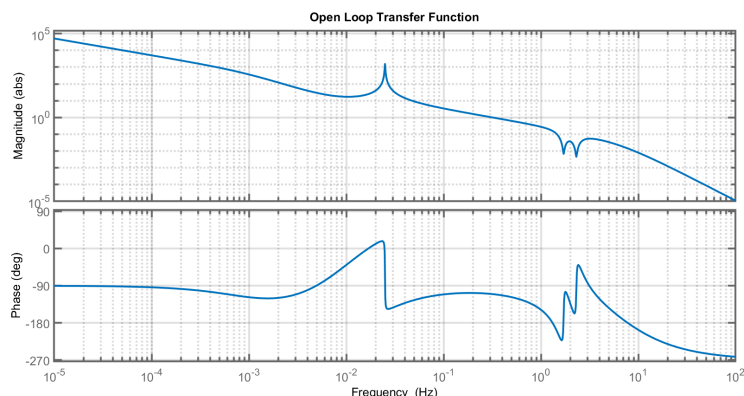


Figure 4.16: Open loop transfer function: the unity gain is kept at about 3 mHz

to adjust the beam initial incident position to null, by varying the incident angle, the radiation pressure effect.

Together with the lowering of the amplitude of radiation pressure long studies are needed on the phase of the signal with respect to modulation phase. Actually, the heat weight measurement is based on the 90 degrees phase delay: the fact that the weight signal is 90 degrees rotated with respect to power modulation let us to perform a kind of “polarization” measurement, or better a time delay measurement. The phase delay $\delta\Psi$ of the balance arm tilt with respect to beam power modulation due to the presence of the weight component is given by

$$\delta\Psi = \text{tg}^{-1}(\tau_w/\tau_p) = \frac{\frac{Pg}{c^2\omega_0}}{\frac{P\theta}{c}} = \frac{g\theta^{-1}}{c\omega_0} \quad (4.6)$$

Assuming $\theta = 10^{-3}$ rad and modulation frequency of 20 mHz, $\delta\Psi = 2.5 \cdot 10^{-4}$ rad. At the modulation frequency of 20 mHz this phase delay correspond to the time delay $\delta T = \frac{\delta\Psi T}{2\pi} = 2 \cdot 10^{-3}$ s, which in principle can be easily measured.

The actual measurement cannot be a single phase delay, because it will measure the transfer function phase due to the mechanics and control loop. The actual measurement is a difference of two time delays in different alignment conditions. The first measurement is taken with θ relatively high, so that the phase delay due to weight effect is negligible. The resulting phase delay is taken as the reference. Then a second measurement is taken with θ (much) smaller with respect to the first measurement and the phase delay is again measured. The difference among this two phase delays corresponds to equation 4.6 and gives the contribution of heat weight.

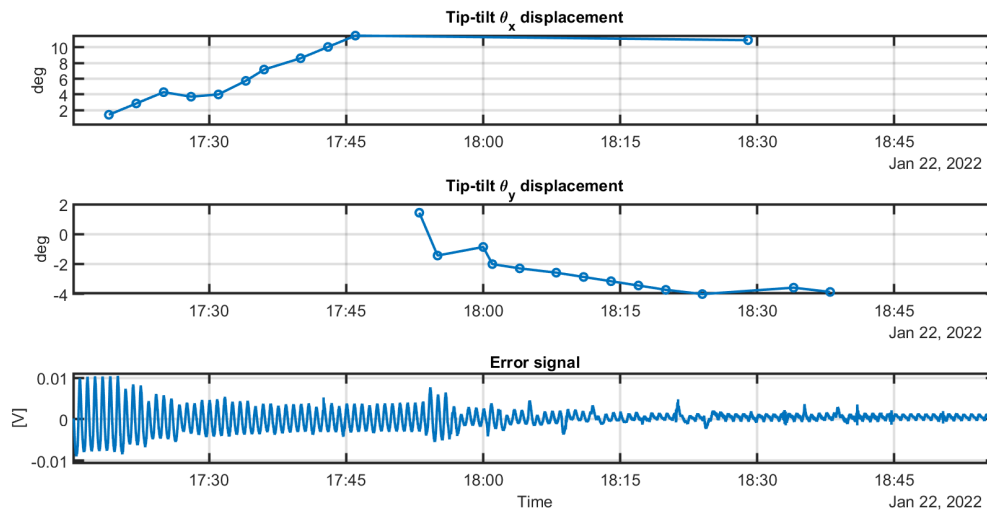


Figure 4.17: Tilt in function of time in the run. The lowest graph is the time-series of the balance oscillation

Two time-series, obtained with different positions of beam-tilt, are illustrated in figure 4.18 and 4.19. A very first estimation of phase delays uncertainties has been performed using the correlation function in MATLAB, resulting in about $\delta\Psi \approx 1.2 \cdot 10^{-2}$ rad. This value is still 50 times larger with respect to the target measure of $\delta\Psi \approx 2.5 \cdot 10^{-4}$ but we must consider that this is just a very first test. In this sense it is encouraging because as described above many parameters must yet be set and a long measurement with fixed parameters have to be performed.

Together with better positioning of the beam on the sample, during next runs it is also planned to increase the laser power to about 20 Watt of maximum power, to increase sensitivity. We notice also that with the prototype all this studies will be particularly devoted mostly to acquire experience with power modulation. With the final balance, in which the same modulation will be done with a system symmetric on the two sides of the sample, with the sample distant from the arm and with a upgraded sample parameters a measurement of the weight is expected to be possible.

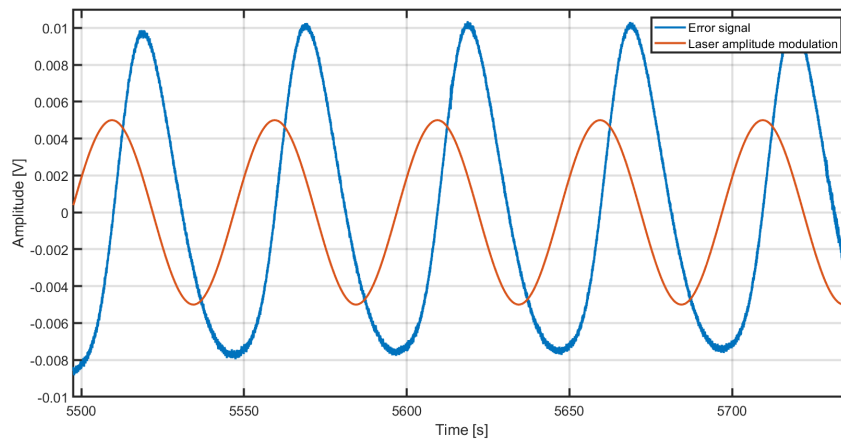


Figure 4.18: Time-series balance oscillations (in blue) with modulation frequency of 20 mHz and initial angular beam-misalignment. It has also been reported in arbitrary units, in orange, the time-series power beam oscillations, to give an idea on the total amount of phase delay, which is the sum also of the delays due to mechanics and control loop.

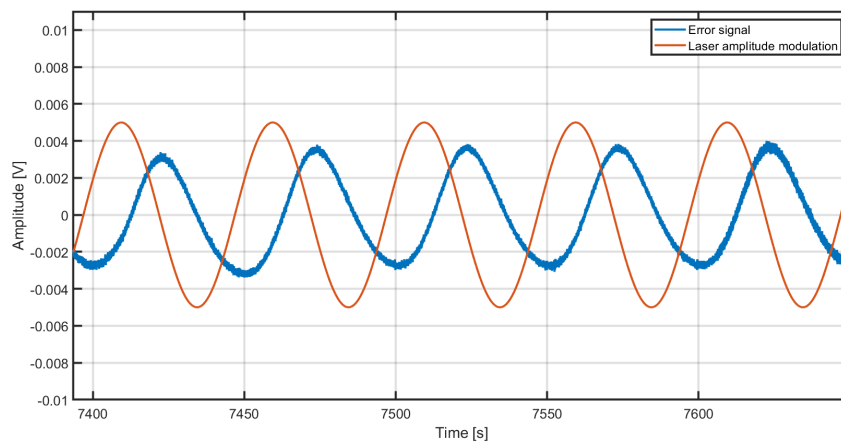


Figure 4.19: Time-series balance oscillations (in blue) with modulation frequency of 20 mHz and reduced angular beam-misalignment. In orange the same time-series power beam oscillations reported in the previous picture. The phase delay useful to determine the weight of the heat is the one between the blue curve in this picture and the blue curve in the previous picture.

Chapter 5

Conclusions

The work in this thesis focused on an experiment, Archimedes, for measuring the debated interaction of quantum vacuum fluctuations with the gravitational field. The experiment is now being installed and commissioned for the first time, and during the thesis many steps were taken to achieve this partial but important result.

The first step was to check the feasibility of the experiment, analysing the most critical points and then designing and testing appropriate construction solutions. First of all the mechanics, designing the dimensions of the joints, the measuring arm and the reference arm, and all the auxiliary components, such as the rotators and translators for balancing and remote positioning of the centre of mass, up to the clamps to allow safety operations from remote. Then there is the optical part: in this case an extremely sensitive optical sensing system was designed, based on a Michelson interferometer, but also very robust with respect to misalignments and frequency and amplitude fluctuations, with appropriate and original devices to keep both construction and operation simple.

In addition, the control part, with the somewhat obligatory but ultimately successful choice of using, with appropriate laboratory tuning, a commercial system for the implementation of the acquisition and feed-back system. Finally, the choice of site. Such a sensitive system needs to work in an extremely quiet environment from the seismic point of view and this led to the choice of the Sos Enattos site, and in particular SAR-GRAV as the laboratory where the experiment was to be carried out.

All these solutions were first implemented in a prototype, designed and built during the thesis, which proved in the field, i.e. on the Sos Enattos site, to be the best tiltmeter in the world (to our knowledge) for measuring high-frequency tilts and the best low-frequency balance.

The experience gained on the prototype was also transferred to the final experiment. The thesis work consisted of the design of all the opto-mechanical parts of the final scale, the verification of all the construction parts and finally the installation and assembly of the balance at the final site of Sos Enattos. A not insignificant part of the installation also consisted of the realisation of the laboratory itself, especially with regard to the choice of the size of the experimental rooms, the definition of the minimum equipment and the design of the laboratory.

Last but not least, part of the thesis work also consisted in assessing the possibility of carrying out fundamental physics measurements, in particular with the final balance, which are also of viatrical importance to the final measurement. In this, the measurement of the weight of the heat was identified, which would constitute the first laboratory measurement of Tolman's hypothesis and the first verification of gravitation with respect to thermodynamic variables. As reported in Chapter 4, the very first measurements of this kind showed that the balance prototype is able to measure phase delays one order of magnitude (around 50 times) greater than the delays expected to be produced by the weight of the heat. Such results are extremely encouraging, since the experiment can be easily refined and repeated. Thus, the measure of the weight of the heat is expected to be feasible with the final balance, but probably also with the prorotype.

The final balance is currently being installed and is scheduled for completion and first vacuum test by the end of the year. If the progress of activities continues with the verve it has shown so far, we expect to be able to measure the interaction of quantum vacuum fluctuations with gravity over the next few years.

Appendix A

Seismic glitchness at Sos Enattos
site: impact on intermediate black
hole binaries detection efficiency



Seismic glitchness at Sos Enattos site: impact on intermediate black hole binaries detection efficiency

A. Allocca^{1,2}, A. Berbellini³, L. Boschi^{3,4,5}, E. Calloni^{1,2,a} , G. L. Cardello^{6,7}, A. Cardini⁸, M. Carpinelli^{6,7,9}, A. Contu^{8,10}, L. D'Onofrio^{1,2}, D. D'Urso^{6,7}, D. Dell'Aquila^{6,7}, R. De Rosa^{1,2}, L. Di Fiore², M. Di Giovanni^{11,12,13}, S. Di Pace^{14,15}, L. Errico^{1,2}, I. Fiori⁹, C. Giunchi¹¹, A. Grado¹⁶, J. Harms¹², E. Majorana^{14,15}, V. Mangano^{14,15}, M. Marsella^{14,15}, C. Migoni⁸, L. Naticchioni^{14,15}, M. Olivieri³, G. Oggiano^{6,7}, F. Paoletti¹⁷, M. Punturo¹⁸, P. Puppò¹⁵, P. Rapagnani^{14,15}, F. Ricci^{14,15}, D. Rozza^{6,7}, G. Saccorotti¹¹, V. Sequino^{1,2}, V. Sipala^{6,7}, I. Tosta E Melo^{6,7}, L. Trozzo²

¹ Università Federico II Napoli, 80126 Napoli, Italy

² INFN - sezione di Napoli, 80126 Napoli, Italy

³ INGV - sezione di Bologna, 40128 Bologna, Italy

⁴ Università degli studi di Padova, 35131 Padova, Italy

⁵ Sorbonne Université, 75005 Paris, France

⁶ Università degli Studi di Sassari, 07100 Sassari, Italy

⁷ INFN - Laboratori Nazionali del Sud, 95125 Catania, Italy

⁸ INFN - sezione di Cagliari, 09042 Monserrato, CA, Italy

⁹ European Gravitational Observatory, 56012 Cascina (PI), Italy

¹⁰ INAF - Osservatorio Astronomico di Cagliari, 09042 Cagliari, Italy

¹¹ INGV - sezione di Pisa, 56123 Pisa, Italy

¹² Gran Sasso Science Institute, 67100 L'Aquila, Italy

¹³ INFN - Laboratori Nazionali del Gran Sasso, 67100 Assergi, AQ, Italy

¹⁴ Università di Roma La Sapienza, 00185 Roma, Italy

¹⁵ INFN - sezione di Roma 1, 00185 Roma, Italy

¹⁶ INAF - Osservatorio Astronomico di Capodimonte, 80131 Napoli, Italy

¹⁷ INFN - sezione di Pisa, 56127 Pisa, Italy

¹⁸ INFN - sezione di Perugia 1, 06123 Perugia, Italy

Received: 5 March 2021 / Accepted: 16 April 2021

© The Author(s) 2021

Abstract Third-generation gravitational wave observatories will extend the lower frequency limit of the observation band toward 2 Hz, where new sources of gravitational waves, in particular intermediate-mass black holes (IMBH), will be detected. In this frequency region, seismic noise will play an important role, mainly through the so-called Newtonian noise, i.e., the gravity-mediated coupling between ground motion and test mass displacements. The signal lifetime of such sources in the detector is of the order of tens of seconds. In order to determine whether a candidate site to host the Einstein Telescope observatory is particularly suitable to observe such sources, it is necessary to estimate the probability distributions that, in the characteristic time scale of the signal, the sensitivity of the detector is not perturbed by Newtonian noise. In this paper, a first analysis is presented, focused on the Sos Enattos site (Sardinia, Italy), a candidate to host the Einstein Telescope. Starting from a long data

^a e-mail: enrico.calloni@na.infn.it (corresponding author)

set of seismic noise, this distribution is evaluated considering both the presently designed triangular ET configuration and also the classical "L" configuration.

1 Introduction

The recent discovery of gravitational waves [1–3] has prompted the scientific community toward the realization of the so-called third-generation gravitational wave detectors. Among the most important technical improvements, there are the extension of the observation bandwidth at low frequency and the gain of about a factor ten in sensitivity in the bandwidth covered by present detectors [4,5].

In particular, the Einstein Telescope (ET) [5] will be an underground, cryogenic detector, composed by three pairs of Michelson interferometers arranged in an equilateral triangle configuration, as shown in Fig. 1; each pair composes a xylophone, being constituted by an interferometer optimized for low frequencies and an interferometer optimized for high frequencies.

The low-frequency limit of the bandwidth will be extended from the present 10 Hz down to 2 Hz. The study of several interesting sources of gravitational waves is expected to benefit from the extension of the bandwidth: rotating pulsars, coalescing binaries, and, of course, possible yet unknown sources [6]. Among possible new sources, a remarkable interest is given by Intermediate Mass Black Hole Binaries: coalescing binary systems with total mass ranging from about few hundreds solar masses up to several thousands and more [7].

Evidence of the existence of such sources was obtained from the observation of the GW190521 event: the mass of the initial black holes was 85 and 64 solar masses, and the final mass of the merger (142 solar masses) classifies it as an intermediate-mass black hole [8,9].

The duration of these signals within the new observational window depends on several parameters. Indeed, depending on mass asymmetry, spin and distance, the duration of such signals in the detection bandwidth can vary from several tens of seconds to a few minutes.

Considering that a number of non-stationary noise can affect the detector [10,11], it is important to investigate the behavior of such noises in the same time scale of the signal. Among the noises that are expected to mostly affect the detector in that bandwidth, the seismic noise has a key role. Indeed it can couple with the interferometer both through indirect ways, like for example by modulating the diffused light [12], or also in a direct way, through the variation of gravitational field due to displacements of ground masses nearby the interferometer test masses.

The latter is known as Newtonian noise [13], and the ET requirements are so stringent that the interferometer will be positioned underground, at a depth of about 250 m, where the seismic noise is strongly reduced compared to the surface. Even in this condition, the Newtonian noise (NN) remains one of the most critical noise sources, affecting in particular the bandwidth where the new detectors should extend. [13].

In the evaluation of the sites that could host such a third-generation detector, a first estimation of the residual noise has been obtained by evaluating the power spectral density of the seismic noise, during a long data-taking, to assess its median value. Presently two sites remain the candidate to host ET: the Dutch site Terziet, near Maastricht, at the border of Belgium, the Netherlands and Germany [14] and the Italian Sos Enattos (Lula - NU, in Sardinia) [5,15,16].

In view of the detection of transients of the order of one minute, it is nevertheless important also to assess the distribution of the seismic noise over this time scale to evaluate, for example,

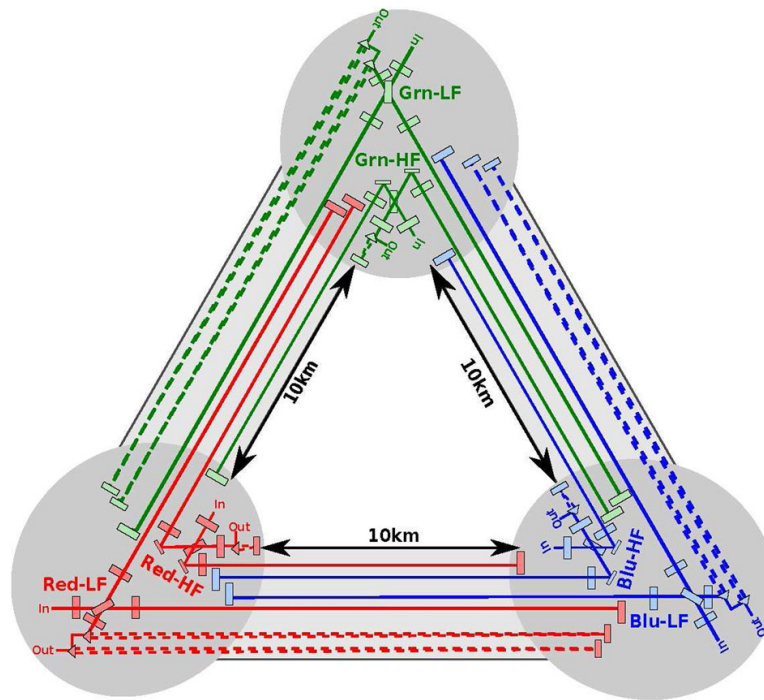


Fig. 1 Schematic Layout of the ET detector: each color represents a xylophone detector, composed an LF (Low-Frequency) and an HF (High-Frequency) interferometer. The continuous lines represent the interferometers' cavities, while the dashed lines represent the auxiliary filter cavities

the probability to have the contribution of NN below a certain threshold during the transient gravitational wave (GW) signal.

In the present paper, after recalling the fundamental layout of the ET detector we motivate the choice of the time scale of our seismic noise analysis by considering the search of intermediate-mass black holes binaries. Hence, we describe and show the seismic noise in the Sos Enattos site, we estimate the NN induced in the ET detector and the probability distribution to not perturb the detection during the signal transient.

2 ET optical layout

The optical layout of the ET detector is reported in Fig. 1. It is composed by a total of six Michelson interferometers each lying on two sides of an equilateral triangle. The total observation bandwidth will extend from 2 Hz to several kHz, obtained by using a xylophone configuration, i.e., two kinds of interferometers: the LF (Low Frequency), optimized to the low frequency part of the spectrum, and the HF (High Frequency) optimized for the intermediate and high part of the spectrum. The arms of each interferometer form an angle of 60 degrees, and each arm is actually a 10 km long Fabry-Perot cavity whose input mirror is placed close to the interferometer beam splitter. Multi-interferometer triangular configuration has been designed to improve, with a single detector, the sensitivity to the two GW polarizations. So the different outputs of each interferometer are used to reconstruct the direction and polarization of the gravitational wave [5]₀₆

A Newtonian noise glitch lasting several seconds is expected to enter in the three low-frequency interferometers of the ET detector, degrading the sensitivity of the whole detector.¹ This can be more clearly appreciated by observing the optical layout of the ET detector, in particular by paying attention to the LF interferometers. Each corner station hosts the two input test masses of one interferometer and one end test mass belonging to each of the two other interferometers. So, each interferometer will have at least a cavity-test mass nearby a cavity mass of both the other interferometers. The distances among these masses, in the present design, will be of the order of one km, so it is expected that all the three interferometers will suffer the Newtonian glitch. A deep NN correlation study has yet to be carried out. The present analysis follows the prescription in [17] where the noise projection on the whole ET sensitivity is obtained by considering the effect of NN on a single Detector, without accounting for the 60 angle, and considering the body waves polarization $p = 1/3$. (see the section Newtonian “Noise estimation by Seismic Noise”)

3 Choice of time window

The gravitational wave from a coalescing a binary system is the well tested “*chirp*” [1, 18], composed by three phases: inspiral, merger and ring down. During the inspiral phase, the amplitude and frequency of the wave smoothly rise until the beginning of the merger phase, a fast transient where the amplitude reaches its maximum and then decrease; once merged, in the ring down phase, the system relaxes losing energy by oscillating in its quasi-normal modes, at higher frequencies and much lower amplitude.

Until now, the well-observed gravitational signals correspond to the latest cycles of the inspiral phase and to the merger, and we will focus on these signals to choose the time duration of the “*glitch*” in our seismic analysis. For the purpose of the present paper, we focus on the inspiral phase, because it produces a clear gravitational signal made of several cycles that allow the analysis to clearly distinguish it from other spurious burst. The upper frequency reached by the gravitational wave during the inspiral phase can be approximated as two times (to take into account quadrupolar radiation) the frequency f_{ISCO} of the last stable orbit [18, 19]:

$$f_{ISCO} \approx 2.2 \text{ kHz} \left(\frac{M_{\odot}}{m} \right) \quad (1)$$

where M_{\odot} is the solar mass, $m = m_1 + m_2$ is the total mass of the binary system and m_1 and m_2 the masses of the two components. If we concentrate on the gravitational wave bandwidth of 2–10 Hz, the maximum frequency f_{\max} of the inspiral phase corresponds to binary systems of total mass of about $440 M_{\odot}$, in the detector frame.

The time to coalescence, τ for a binary systems is given by:

$$\tau \approx 2.18 \text{ s} \left(\frac{1.21 M_{\odot}}{M_c} \right)^{5/3} \left(\frac{100 \text{ Hz}}{f} \right)^{8/3} \quad (2)$$

being M_c the chirp mass:

$$M_c = \frac{(m_1 m_2)^{3/5}}{(m_1 + m_2)^{1/5}}$$

¹ Actually it enters in all the six interferometer; we are interested to the three low-frequency interferometers because their better low-frequency sensitivity could be affected by NN. On the contrary, the high-frequency interferometers, having a worst sensitivity at low frequency, are not affected by NN.

For a total mass $m = 440 M_{\odot}$ with equal single masses $m_1 = m_2$, the chirp mass is $M_c \approx 200 M_{\odot}$. If we consider the signal entering in the observation bandwidth at the frequency $f = 2$ Hz, it will remain within the observation band, until its merging, for a time $\tau = 16$ s. Less symmetric systems, with correspondingly smaller chirp mass, will stay longer in the detection bandwidth. As an example, a system with the same total mass but with a mass ratio of $m_1/m_2 \approx 20$, as given by an intermediate black hole with $m_1 = 420 M_{\odot}$ and a stellar black hole with $m_2 = 20 M_{\odot}$, will end the inspiral phase at 10 Hz, after having lived about 90 s in the bandwidth. In the same way, more massive systems will end the inspiral phase at lower frequencies and will remain in the bandwidth from tens of seconds to several minutes depending on the mass ratio.

Guided by these considerations, we choose a time duration of 1 minute to define a seismic time window, where a burst of seismic noise would be potentially invasive for the search of coalescing Intermediate Mass Black Hole binary systems.

4 Newtonian noise estimation by seismic noise

In underground detectors, the main sources of Newtonian noise are both surface and body waves. At present, the noise projections are still under study, to take into account the scattering from the cavern and from the inhomogeneity of the soils [13]. For what concerns the surface wave, it is presently expected that their contribution to NN is negligible if the detector is located underground at a depth of few hundreds meter [20], as in the case of the ET interferometer.

Under this condition, the main contribution to NN is expected to come from body waves [17, 20]. In the rest of the paper, we will follow this assumption: we will estimate the Newtonian noise on the detector by the seismic noise measurements at 84 m depth and project it on the ET sensitivity assuming that it is entirely composed by body waves.

Body waves are described with the help of the seismic displacement vector ξ [13], which is a useful method because it can be measured directly:

$$\xi^{P,S}(\mathbf{r}, t) = \mathbf{e}^{P,S} \xi_0^{P,S}(\mathbf{k}^{P,S}, \omega) \exp(i(\mathbf{k}^{P,S} \cdot \mathbf{r} - \omega t)) \tag{3}$$

The indexes P and S distinguish the compressional (P) and shear (S) waves, respectively, \mathbf{k} is the wave vector, \mathbf{e}_k is the polarization unit vector, and ω is the angular frequency. Compressional waves are longitudinal: $\mathbf{e}^P = \mathbf{k}^P/k^P$ while shear waves are transversal: $\mathbf{e}^S \cdot \mathbf{k}^S = 0$.

Following the Newton law, the acceleration $\delta \mathbf{a}$ of a mass placed at the point \mathbf{r}_0 is given by:

$$\delta \mathbf{a}(\mathbf{r}_0, t) = -G \int dV \rho(\mathbf{r}) (\xi(\mathbf{r}, t) \cdot \nabla_0) \frac{\mathbf{r} - \mathbf{r}_0}{|\mathbf{r} - \mathbf{r}_0|^3} \tag{4}$$

In the first approximation, the underground cavities of the detector can be assumed to be spherical, with radius much shorter than the seismic wavelengths and the mass in the center [13]. Furthermore, assuming that the density variations in space and time can be neglected, setting $\rho(\mathbf{r}, t) = \rho_0$ constant, the above integral can be solved, giving in the frequency domain:

$$\delta \mathbf{a}(\omega) = \frac{4\pi}{3} G \rho_0 \left(2\xi^P(\omega) - \xi^S(\omega) \right) \tag{5}$$

The projection of the noise on the ET sensitivity is performed in the approximation that the NN contribution on the four test masses of the interferometer is not coherent [21]. The Power Spectral Density (PSD) of the measured seismic noise $S(\xi, \omega)$ can be expressed as the superposition of P and S contribution by defining a mixing parameter p as the fraction of compressional contribution: $S(\xi^P, \omega) = pS(\xi, \omega)$ and $S(\xi^S, \omega) = (1 - p)S(\xi, \omega)$. Following the discussion in [17], we assume that all three body-wave polarizations carry the same average displacement power and set $p = 1/3$.

Under these hypothesis, the amplitude spectral density (ASD) of the Newtonian noise contribution to the detector output $h(t)_{NN}$ is given by:

$$\tilde{h}_{NN}(f) = \frac{4\pi}{3} G \rho_0 \frac{2\sqrt{2}}{L} \frac{1}{(2\pi f)^2} \tilde{x}(f) \quad (6)$$

where f is the frequency, \tilde{x} is the ASD of the measured seismic noise and L the arm-length of each interferometer.

5 Amplitude spectral density

The measurement campaign used for this work follows a previous long data taking performed for more than one year in the Sos Enattos mine. The results of those measurements are reported in a previous paper and refer mostly to data collected by two seismometers placed at different depths. Both instruments are Nanometrics Trillium 240; the first (SOE1) is placed at the depth of 84 m and the second (SOE2) at 111 m. Detailed description on seismometer installations, site geological characterization and median on seismic measurements can be found in [22].

The long-term analysis of the seismic data has proven that the Sos Enattos site is very quiet in terms of seismic noise at depth. This leads to the need of reconfiguring the digitizer gain since the standard configuration was hitting its self-noise level in the frequency band 1-20 Hz. The present study uses data from the update configuration for the period August 1 - August 26, 2020.

The results mediated on the period are summarized in Fig. 2. The black curve is the design total noise of ET, that is expected to be limited by NN in the region from 2 to about 7 Hz [21]. The target Newtonian noise contribution in ET project is given by the dashed line. The red line is the median amplitude spectral density (ASD) of the Newtonian noise in Sos Enattos with the seismic noise being measured with SOE1 and projected on the sensitivity following Eq. 6 and assuming $\rho_0 = 2.7 \cdot 10^3 \text{ kg/m}^3$.

It can be appreciated that the median is compatible with the ET Newtonian noise project in almost the whole range of frequency. In the lowest range of frequencies, between 2 and 3 Hz, an active reduction of about a factor of two would be sufficient to bring the whole curve below the project curve.

These results are extremely encouraging, in particular because they are conservative: although not in operation, there are accesses to the mine for maintenance and environment protection and the ET detector will be located at higher depth with respect to SOE1.

In Fig. 3, the ASD median on the whole period is reported, together with the ASD median on the holiday period (August 8th–August 23rd) when the mine was closed and the median ASD during the nights of the whole period. It can be observed that during holidays there is a small reduction of the noise while during nights the noise level is remarkably lower than ET design in almost the whole bandwidth.

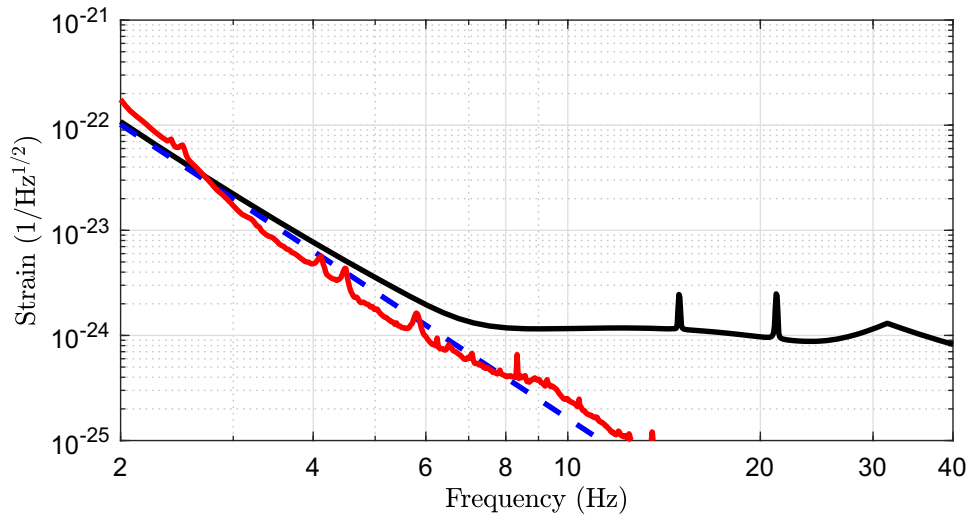


Fig. 2 ASD of ET target sensitivity (black) compared with target NN contribution (dashed blue) and projected NN noise based on the median ASD of the seismic noise measurement (red)

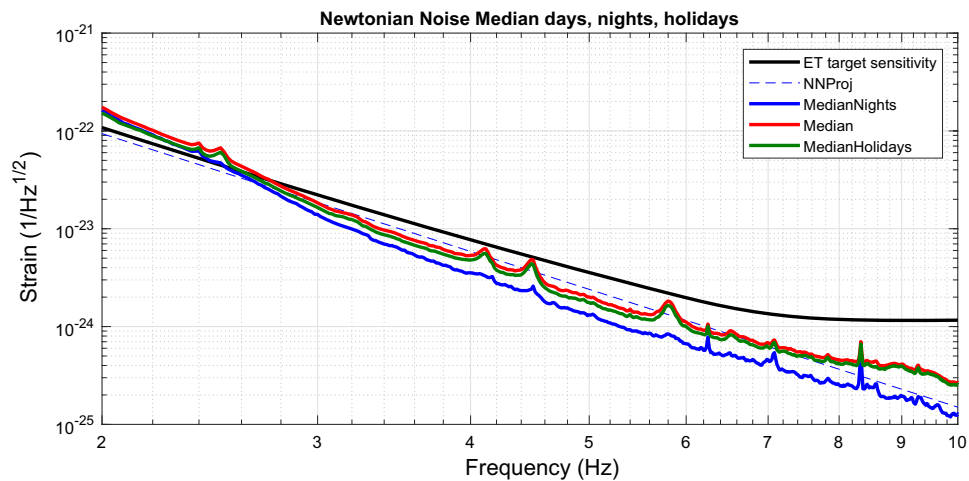


Fig. 3 ET target sensitivity and NN contribution zoomed in the bandwidth 2–10 Hz

6 Noise distribution

The median of amplitude spectral density of NN is extremely encouraging. Nonetheless, the seismic noise is typically not stationary and its variability can be due both to long night-day variations and fast transients of anthropic or natural origin. We thus performed a first analysis on the distribution of the noise, to evaluate the probability to have the sensitivity of the detector degraded by Newtonian noise during the arrival of an IMBHs coalescence gravitational wave. Based on the considerations of the above sections, we focus our analysis in 1-minute windows and calculate the noise-to-target ratio (NTR) of the Newtonian noise with respect to the ET sensitivity defined as:

$$NTR = \sqrt{\frac{1}{\Delta f} \int_{f_1}^{f_2} df \frac{\tilde{N} * \tilde{N}}{S_h}} \tag{7}$$

S_h is the PSD of the ET target sensitivity and $\tilde{N} * \tilde{N}$ is the PSD of the Newtonian noise. As usual, the normalization to the bandwidth assures that if the NN is equal to the ET target sensitivity the value $NTR = 1$ is obtained. Considering that in 2–10 Hz bandwidth, NN is

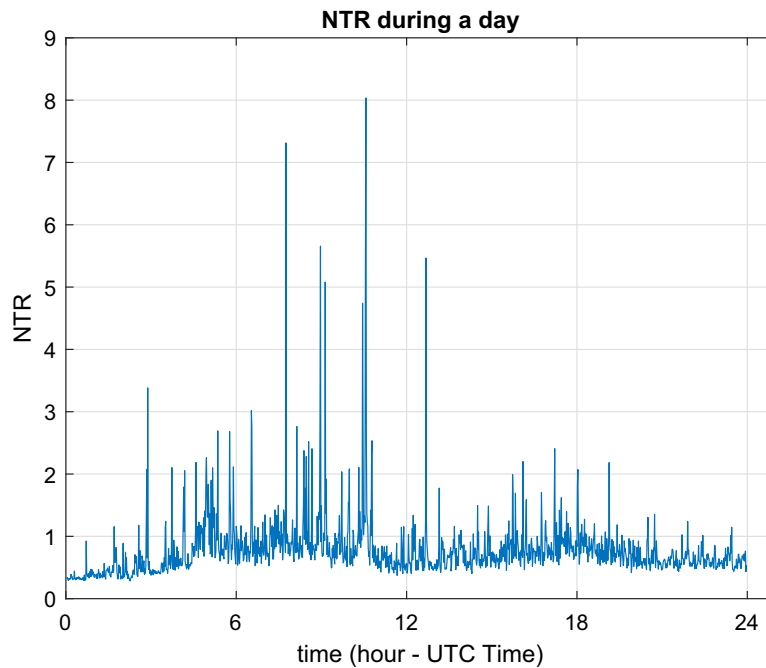


Fig. 4 Time evolution of the 2–10 Hz 1-minute NTR during a day. The time is UTC, the local time being UTC+2 hours

expected to limit (2–7 Hz) or contributing (7–10 Hz) to ET noise, unity can be taken as the critical value to assess if an excess of Newtonian noise, in the minute considered, is degrading the target sensitivity.

The time variability of seismic noise can be appreciated, for example in Fig. 4, where it is reported the NTR value, in 1-minute windows, in the bandwidth 2–10 Hz, evaluated in each minute for a whole day. The floor follows a night-day variation, and fast transients are more frequent during the morning.

In Fig. 5, it is reported the same NTR value, evaluated in each minute for a whole day, in the different days. The time axis is UTC, so the local time is 2 hours more than what reported in the time axis. It can be appreciated that the noise events appear early in the morning, around 4 to 5 o'clock local time and last until late early afternoon. During nights, the noise events reduce drastically. Also it can be appreciated that during the second part of the month, corresponding to holidays, the events are less with respect to the first days. This behavior is consistent with a prevalent anthropic local excitation of the site, that will be further investigated.

The results with respect to degradation of ET sensitivity are reported in Fig. 6 for the whole period. The distribution is picked at a value lower than unity. The corresponding probability of having a NTR lower than unity is $P(\text{NTR} < 1) = 0.60$ in agreement with the value of the median shown in Fig. 2. The probability of having $\text{NTR} < 1.5$, thus admitting a small degree of degradation, is about 0.8. If the noise reduction of a factor 2 in the 2–3 Hz band is taken into account (see [20]), the NTR probability of being better than unity increases to about 97%.

These values are extremely encouraging, in particular, if we take into account that human activities still occur into the mine. This can result in an overestimation of the intrinsic noise of the site.

To further remark this point, in Fig. 7 we report the NTR distribution during the nights and in Fig. 8 the NTR distribution during the two summer holidays weeks.

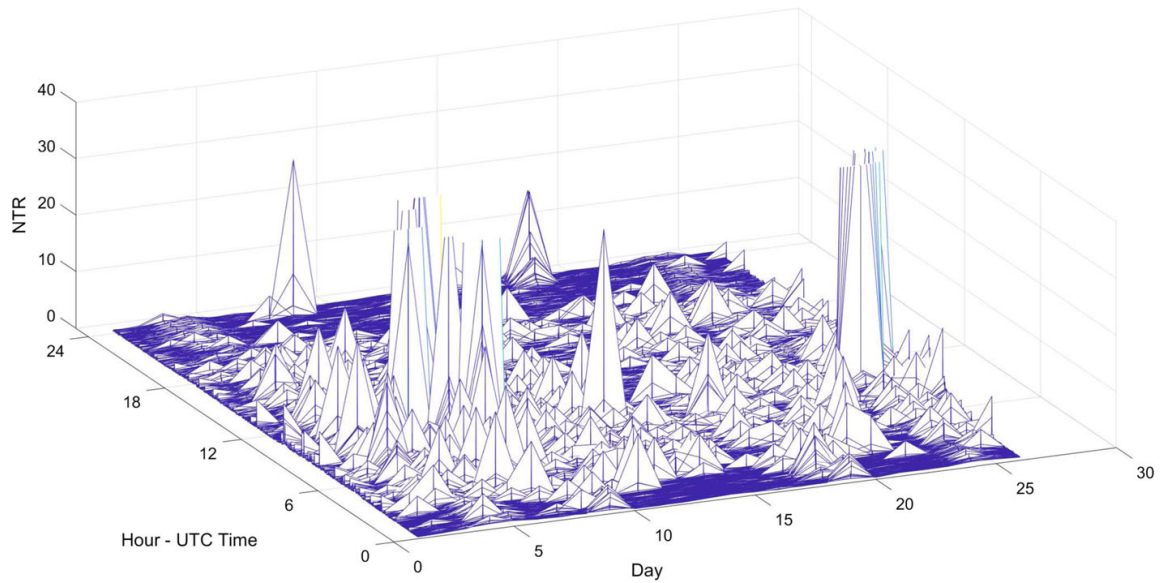


Fig. 5 Time evolution of the 2–10 Hz 1-minute NTR during the various days

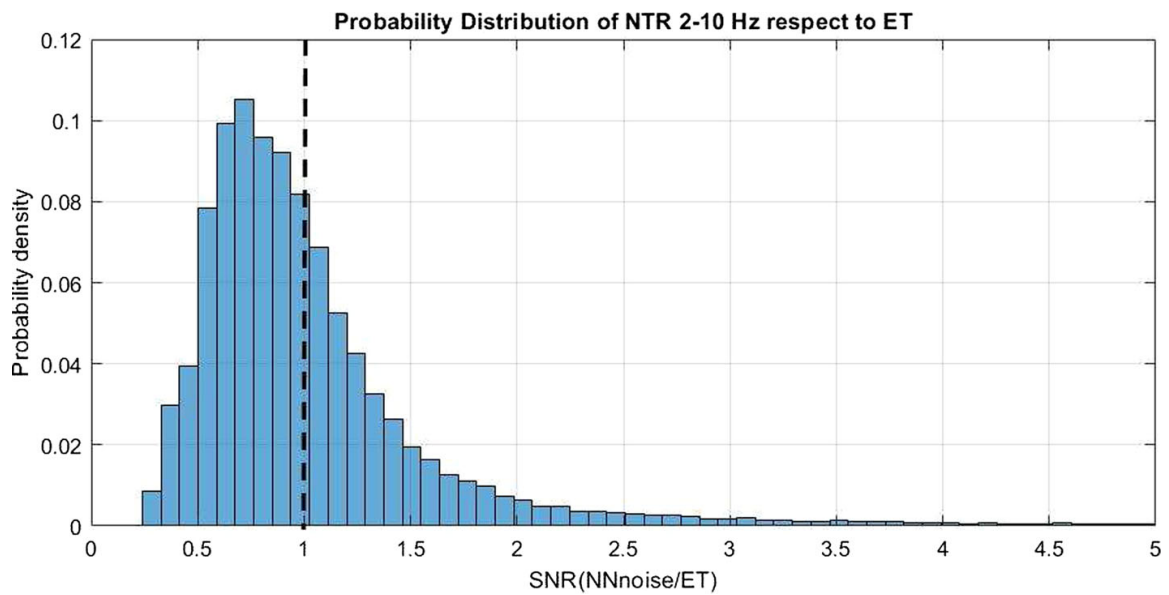


Fig. 6 NTR probability distribution over the whole period

During night, the probability to be better than unity is 86% without any reduction and increases to 95% if a slight degradation to NTR up to 1.5 is considered. Finally, when the 16 days of holidays are considered, from August 8th to August 23rd, the probability to be better than unity becomes 76%. Let us remark that also in this condition the present results are conservative. Indeed the mine, even in absence of environmental works, is still operated with maintenance bilge pumps, guardian’s movements and free to be accessed up to the entrance by sheep and tourists.

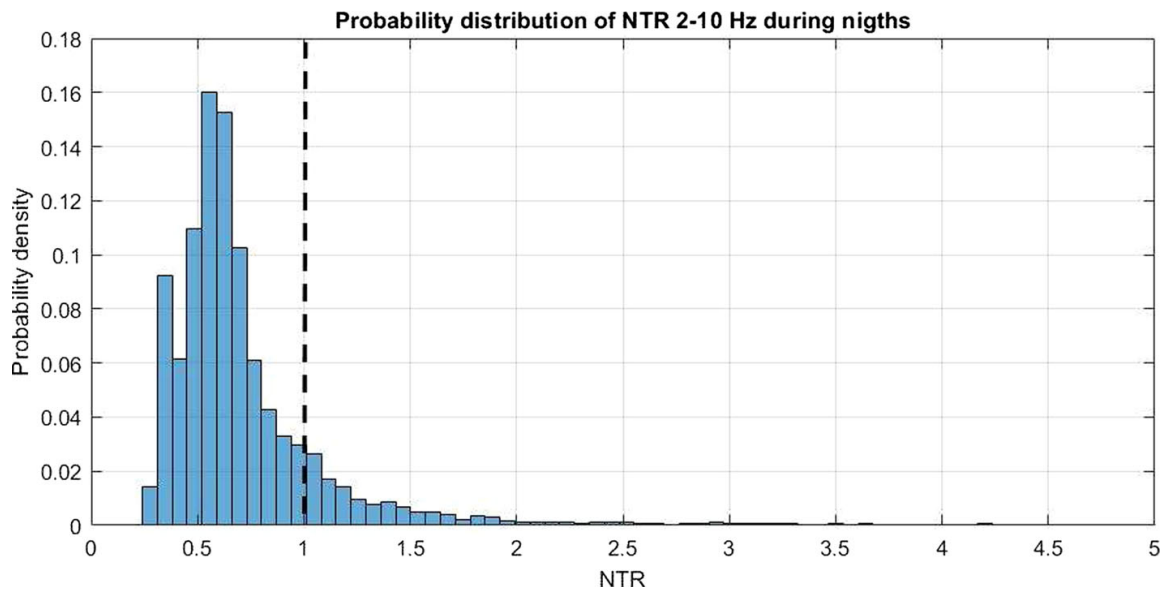


Fig. 7 NTR probability distribution during the nights

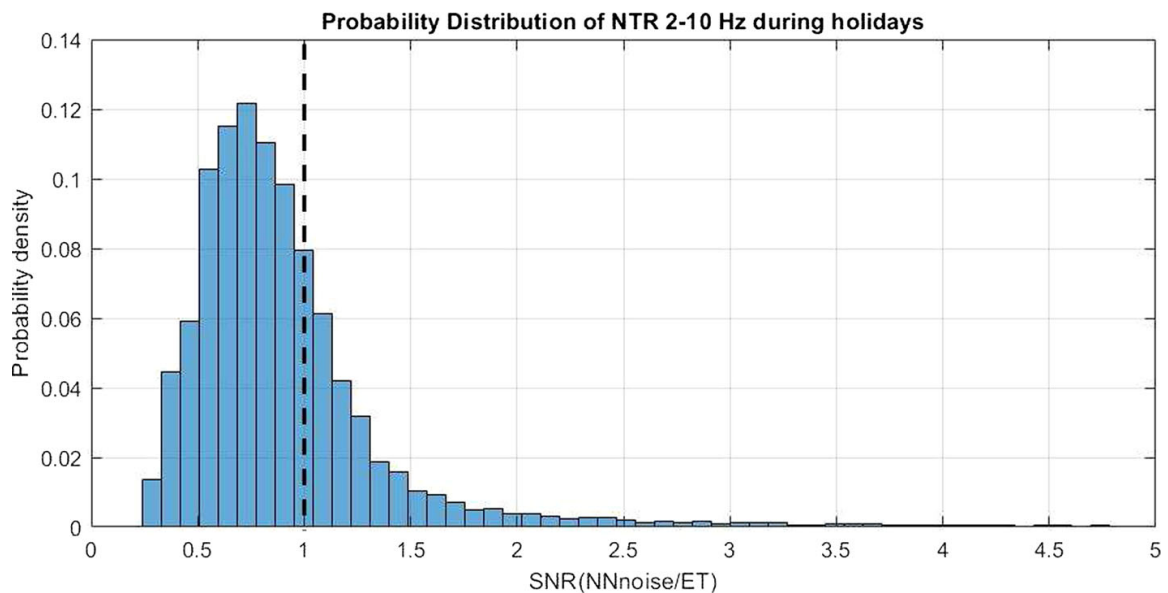


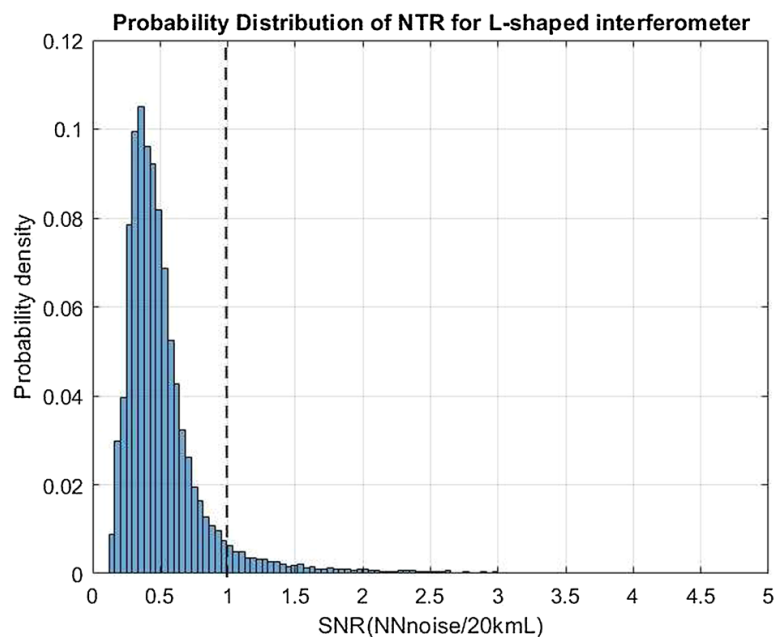
Fig. 8 NTR probability distribution during the holidays weeks

7 Interferometer L shaped

The classical L-shape interferometer is still an option for ET or for other third-generation detectors. If operated in a network, this would warrant a very efficient detection of the direction and the polarization of the GW sources, with a simpler realization.

In the following, we analyze the NTR assuming a single xylophone interferometer, composed of 20 km long arms, with target sensitivity equal to the one planned for ET. The results, referred to the whole data set, are reported in Fig. 9. The probability that the Newtonian noise degrades the sensitivity is about 5%, compatible with the typical duty cycle of gravitational wave detectors. When this configuration is considered, very likely the NN reduction would not be necessary.

Fig. 9 NTR probability distribution during the period for Sos Enattos (blue) for a 20 km L-shaped detector



8 Discussion

From this preliminary analysis, it results that the ET detector, if hosted by the Sos Enattos site, will be for the great majority of time in the position of detecting the new sources like IMBH with no degradation of sensitivity even not considering any reduction of the Newtonian noise. These results, whenever showing an optimal site for hosting the detector, can be considered as preliminary for three main reasons. The first is that the noise projection of Eq. 6 is an approximation that does not consider in detail the coherence among the masses of each interferometer and among the signals of the three LF interferometers. Second, the mine is still maintained, various activities are performed in the immediate neighborhood, and the seismometers are not yet placed at their ultimate depth of 250 m. In these sense, the presented results can be considered as upper limits in the noise, as it can be particularly appreciated by looking at the behavior during nights and holidays. Part of the next activity will be the better isolation of the seismometers and, if needed, an evaluation of the seismic noise of the site with boreholes at 250 m depth. Third, a study aimed to locate the different sources of seismic noise is undergoing, with the aim also to help in the design of low self-noise generating ET infrastructures. Finally, the case of single 20 km arm L-shaped xylophone interferometer has been considered. The Newtonian noise is not degrading the sensitivity for more that about 5% of time, which implies that no Newtonian noise reduction would be needed in this case.

Acknowledgements This work has been supported by: INFN with Protocollo di Intesa tra Ministero dell'Università e della Ricerca, la Regione Autonoma della Sardegna, l'Istituto Nazionale di Fisica Nucleare e l'Università degli Studi di Sassari; University of Sassari with Accordo di Programma tra la Regione Autonoma della Sardegna, l'Università degli Studi di Sassari, l'Istituto Nazionale di Fisica Nucleare, l'Istituto Nazionale di Geofisica e Vulcanologia, l'Università degli Studi di Cagliari e l'IGEA S.p.a (progetto SAR-GRAV, funds FSC 2014-2020 Patto per lo sviluppo della Regione Sardegna); COST Action CA17137; Sapienza University of Rome "Fondi di Ateneo 2017; Università degli Studi di Sassari with "Fondo di Ateneo per la ricerca 2019"; Istituto Nazionale di Fisica Nucleare and by the Italian Ministero dell'Università e della Ricerca with PRIN 2017 Research Program Framework, n. 2017SYRTCN. The authors thanks L. Loddo and IGEA miners for their support during operation in Sos Enattos.

Funding Open access funding provided by Università degli Studi di Napoli Federico II within the CRUI-CARE Agreement.

Data Availability Statement This manuscript has associated data in a data repository. [Authors' comment The datasets generated and analysed during the current study are available from the corresponding author on reasonable request.]

Open Access This article is licensed under a Creative Commons Attribution 4.0 International License, which permits use, sharing, adaptation, distribution and reproduction in any medium or format, as long as you give appropriate credit to the original author(s) and the source, provide a link to the Creative Commons licence, and indicate if changes were made. The images or other third party material in this article are included in the article's Creative Commons licence, unless indicated otherwise in a credit line to the material. If material is not included in the article's Creative Commons licence and your intended use is not permitted by statutory regulation or exceeds the permitted use, you will need to obtain permission directly from the copyright holder. To view a copy of this licence, visit <http://creativecommons.org/licenses/by/4.0/>.

References

1. B.P. Abbot et al., Observation of Gravitational Waves from a Binary Black Hole Merger. *Phys. Rev. Lett.* **116**, 061102 (2016)
2. B.P. Abbot et al., GW170817: Observation of Gravitational Waves from a Binary Neutron Star Inspiral. *Phys. Rev. Lett.* **119**, 161101 (2017)
3. B. P. Abbot et al. (2019) GWTC-1: A Gravitational-Wave Transient Catalog of Compact Binary Mergers Observed by LIGO and Virgo during the First and Second Observing Runs, *Phys Rev X*, 9: 031040
4. D. Reitze et al. (2019) Cosmic Explorer: The US CoNTRibution to Gravitational-Wave Astronomy beyond LIGO, *Bull. Am. Astron. Soc.*, 51: 51
5. M. Punturo et al., The Einstein Telescope: A third-generation gravitational wave observatory. *Class. Quantum Grav.* **27**, 194002 (2010)
6. B. Sathyaprakash et al., Scientific Objectives of Einstein Telescope, *Class. Quant. Grav.*, **29**, (2012) 124013 and *Class. Quant. Grav.*, **30**, (2013) 079501 (erratum)
7. M. Mezcuca, Observational evidence for intermediate-mass black holes. *Int. J. Mod. Phys. D* **26**, 1730021 (2017)
8. B.P. Abbot et al., GW190521: A Binary Black Hole Merger with a Total Mass of 150M. *Phys. Rev. Lett.* **125**, 101102 (2020)
9. B. P. Abbot et al., (2020) Properties and Astrophysical Implications of the 150 M Binary Black Hole Merger GW190521, *Astrophys J Lett*, 900(1): L13
10. B.P. Abbot et al., Characterization of transient noise in Advanced LIGO relevant to gravitational wave signal GW150914. *Class. Quantum Grav.* **33**, 134001 (2016)
11. I. Fiori et al., The hunt for environmental noise in virgo during the third observing run. *Galaxies* **8**, 82 (2020)
12. T. Accadia et al., Noise from scattered light in Virgo's second science run data. *Class. Quantum Grav.* **27**, 194011 (2010)
13. J. Harms, Terrestrial gravity fluctuations. *Living Reviews in Relativity* **22**, 6 (2019)
14. S. Koley et al, First results of seismic studies of the Belgian-Dutch-German site for Einstein Telescope, NIKHEF public report, <https://www.nikhef.nl/wp-content/uploads/2019/10/Terziet-Drilling-Campaign-Final-NoC.pdf>
15. L. Naticchioni et al., (2014) Microseismic studies of an underground site for a new interferometric gravitational wave detector, *Class. Quantum Grav.*, 31:105016
16. L. Naticchioni et al., Characterization of the Sos Enattos site for the Einstein Telescope. *J. Phys. Conf. Ser.* **1468**, 012242 (2020)
17. F. Amann et al. (2020) Site-selection criteria for the Einstein Telescope, *Rev. Sci. Instrum.* 91: 9
18. B. P. Abbot et al., Tests of general relativity with GW150914 *Phys. Rev. Lett.*, **116**, (2016) 221101, and *Phys. Rev. Lett.*, **121**, (2018) 129902 (erratum)
19. M. Maggiore (2008) *Gravitational Waves vol. 1 Theory and Experiments*, Oxford University Press, Oxford
20. F. Badaracco, J. Harms, Optimization of seismometer arrays for the cancellation of Newtonian noise from seismic body waves. *Class. Quantum Grav.* **36**, 145006 (2019)
21. S. Hild et al., Sensitivity studies for third-generation gravitational wave observatories. *Class. Quantum Grav.* **28**, 094013 (2011)
22. M. Di Giovanni et al., A seismological study of the Sos Enattos area, the Sardinia candidate site for the Einstein Telescope. *Seismol. Res. Lett.* **92**, 352–364 (2021)

Appendix B

High-bandwidth beam balance for vacuum-weight experiment and Newtonian noise subtraction



High-bandwidth beam balance for vacuum-weight experiment and Newtonian noise subtraction

Enrico Calloni^{1,a} , Archimedes Collaboration², Virgo Collaboration³

¹ Università degli Studi di Napoli Federico II, Naples, Italy

² SAR-GRAV Laboratory, Sos Enattos, Lula, Nuoro, Italy

³ European Gravitational Observatory, Cascina, Pisa, Italy

Received: 19 November 2020 / Accepted: 9 February 2021

© The Author(s) 2021

Abstract We report the experimental results of a prototype balance for the Archimedes experiment, devoted to measure the interaction between quantum vacuum energy and gravity. The prototype is a *beam balance* working at room temperature which shares with the final balance several mechanical and optical components. The balance sensitivity has been tested at the site of the Virgo gravitational wave detector in order to benefit from its quiet environment and control facilities. This allowed also the test of the coherence of the balance data with the Virgo interferometer signal and with the environmental data. In the low-frequency regime, the balance has shown a sensitivity of about $8 \times 10^{-12} \text{Nm}/\sqrt{\text{Hz}}$, which is among the best in the world, and it is very promising toward the final Archimedes measurement. In the high-frequency region, above a few Hz, relying on the behavior of the balance as a rotational sensor, the ground tilt has been measured in view of the next work devoted to Newtonian noise subtraction (NNS) in Virgo. The measured ground tilt reaches a minimum of about $8 \times 10^{-11} \text{rad}/\sqrt{\text{Hz}}$ in the few Hz region and ranges from 10^{-10} to $10^{-9} \text{rad}/\sqrt{\text{Hz}}$ in the 10–20 Hz region, where a very interesting coherence, at some frequencies, with the Virgo interferometer signal is shown.

1 Introduction

In recent years, the measurement of small forces with macroscopic detectors has experienced an enormous development, driven by the interferometers for gravitational wave detection [1–7] and by the improvement of instruments like torsion pendulums and beam-balance rotational sensors [8–11]. Remarkably, torsion balances and rotational sensors, typically working in the mHz region, have shown a considerable overlap of interests both with space-based interferometers and with the ground-based gravitational wave detectors. In this latter case, the control loops, which keep the interferometers on their working point, can benefit, in the sub-Hz region, from a ground tilt signal provided by the rotational sensors [11, 12]. Furthermore, the sensitivity in the low-frequency range (around 10 Hz) of the ground-based detectors is expected to be limited by the so-called Newtonian noise in the next scientific runs [13, 14]. Rotational sensors will provide ground-motion signals useful to reconstruct the

^a e-mail: enrico.calloni@na.infn.it (corresponding author)

variation of the gravitational field and hence contribute to the subtraction of Newtonian noise from the gravitational wave signal [15].

Within the framework of macroscopic detectors of small forces, Archimedes collaboration recently proposed a beam balance to measure the force exerted by the gravitational field on a rigid Casimir cavity. The force to be measured is called the *Archimedes force of vacuum*, as it corresponds to the weight of the vacuum fluctuation modes that are expelled by the Casimir cavity [16, 17]. The measurement consists in detecting the weight variation of a layered type II superconductive sample around its transition [17]. The core of the apparatus will be a cryogenic balance whose design torque sensitivity is about $\tilde{\tau} = 6 \times 10^{-13} \text{Nm}/\sqrt{\text{Hz}}$ in the frequency range of tens of mHz or lower [18].

As described in this paper, the apparatus is a rotational sensor. Its characteristic features are low moment of inertia, low restoring force and low resonant frequency in order to maximize the sensitivity to the applied force [18]. To study the feasibility of such an extremely sensitive balance, a prototype working at room temperature has been built. To warrant high sensitivity, the balance readout is an interferometric system. Moreover, the final apparatus will work in a cryogenic environment that implies a long recovery time for each intervention on the balance. For this reason, the readout of the prototype balance has already been designed to be particularly robust and to have a high dynamic range, in order to pledge its capability in recovering the correct interferometer signal even in case of high deviations from the working point. The balance has been initially assembled and tested in the Naples laboratory; then, it has been installed at the Virgo site, which is seismically more quiet, specifically in the North-end building. In this setup, the balance has been tested for the torque sensitivity in the low-frequency regime, while at high frequencies it has been operated as a tiltmeter (rotational sensor). The results of these tests suggest that the balance is presently limited at low frequencies by actuator and sensing noises, while at high frequencies the balance is enough sensitive to measure the ground tilts and can be used for Newtonian noise subtraction. Interestingly, the balance signal is coherent, at some frequencies, with the output of the Virgo interferometer. Although this coherence is not due to Newtonian noise coupling of the ground tilt, it would help in identifying particular noise sources like, for example, diffused light from vibrating elements excited by ground motion.

The paper is organized as follows: In Sect. 2, the mechanical and optical schemes of the prototype balance are described. In Sect. 3, its low-frequency behavior is shown, and a discussion on the reached sensitivity and its possible increase is presented. In Sect. 4, the high-frequency behavior is illustrated, in particular, the use of the balance as a tiltmeter. Finally, the next steps toward further improvements for the balance performance is outlined in Sect. 5.

2 The balance prototype

The working prototype of Archimedes is a short-arm version of the final balance, with no samples suspended from its ends. Its core consists of a 50-cm-long arm, attached at its center through two thin wirelike suspensions (Fig. 1), in a configuration similar to LIGO rotation sensor [11]. Unlike this latter, however, the balance requires a high torque-to-tilt transfer function, which implies that momentum of inertia as well as suspension restoring force has to be as low as possible. To fulfill these specifications, the suspended arm is hollow and made of aluminum, leading to a momentum 0.013kg m^2 in the case of the prototype. In the final design of the balance, instead, the momentum is 0.72kg m^2 , since the arm length is 1.4 m and superconducting samples are suspended from its ends. The restoring force is kept low

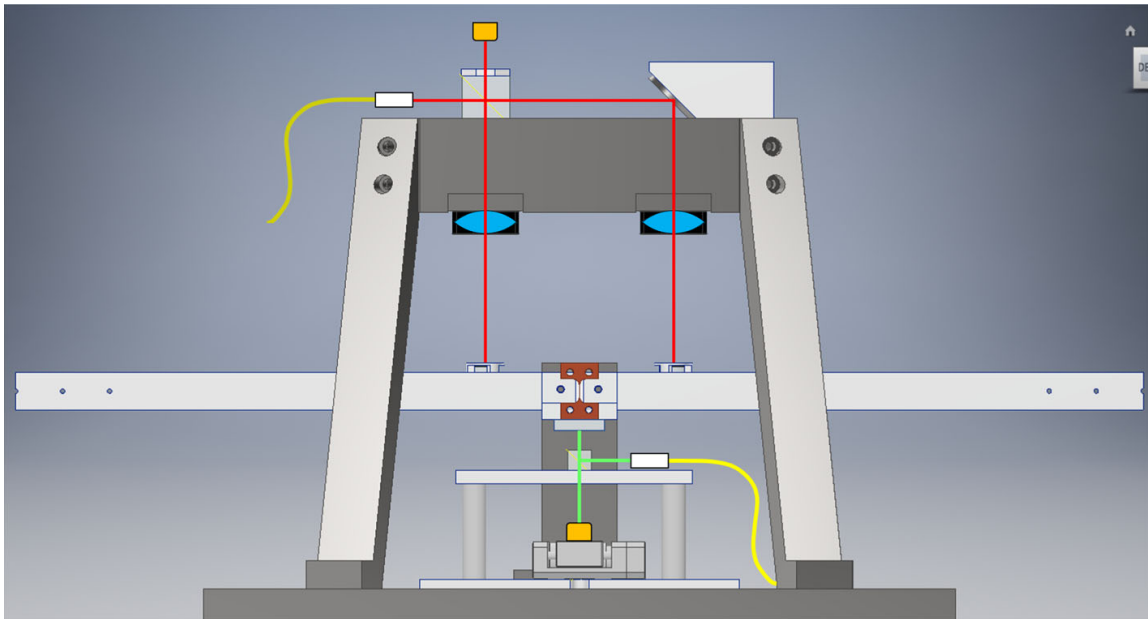


Fig. 1 Scheme of the balance prototype including the optical readout. Notice the two lenses (in light blue), with focal length equal to their distance from the arm. The displacement and relative tilts of the two beams recombining at the beam splitter are of the second order with respect to the arm tilt

by using thin suspensions with a $0.5 \text{ mm} \times 0.1 \text{ mm}$ section. This force, together with the distance between the arm center of mass and its center of rotation, determines the resonance frequency of the balance. The center of mass of the prototype has been tuned to be within $10 \mu\text{m}$ from the center of rotation, giving a resonance frequency of 25 mHz.

2.1 Optical readout: interferometer and optical lever

The balance angular motion can be monitored by two different optical readouts: a Michelson interferometer, with higher sensitivity, and an auxiliary optical lever, with wider dynamic range. Both the optical systems are physically bolted to the ground; hence, the arm angular motion is measured with respect to it. The interferometer has been designed with the following requirements: (1) minimize coupling with undesired degrees of freedom; (2) maintain good contrast even for relatively high tilts; and (3) allow realignment by moving optical elements not lying on the reference nor on the measurement arm.

The first condition has been obtained with the beams impinging on the mirrors perpendicularly. To keep a simple optical scheme, a Michelson interferometer with unequal arm lengths has been chosen, for a path length difference of 10 cm. In the present version of the prototype, the length difference is not compensated and the laser frequency is not yet stabilized. However, the frequency noise is not a limiting source in the present condition. Optical path compensation and laser frequency stabilization are planned for the next improvement of the balance.

The second condition has been fulfilled by designing the interferometer in such a way that the angular and translation separations of the two interfering beams are of the second order with respect to the arm tilts. This has been obtained by adding in both the beam paths a lens with focal length L_f equal to the distance between the lens itself and the mirror, so that the beam is focused on the arm mirror (see Fig. 1). This scheme allows also the fulfillment of the third specification. Indeed, if the arm tilt α is higher than a few mrad, the interferometer can be realigned by translating the input beam vertically by the quantity $\delta y = L_f \alpha$. In this

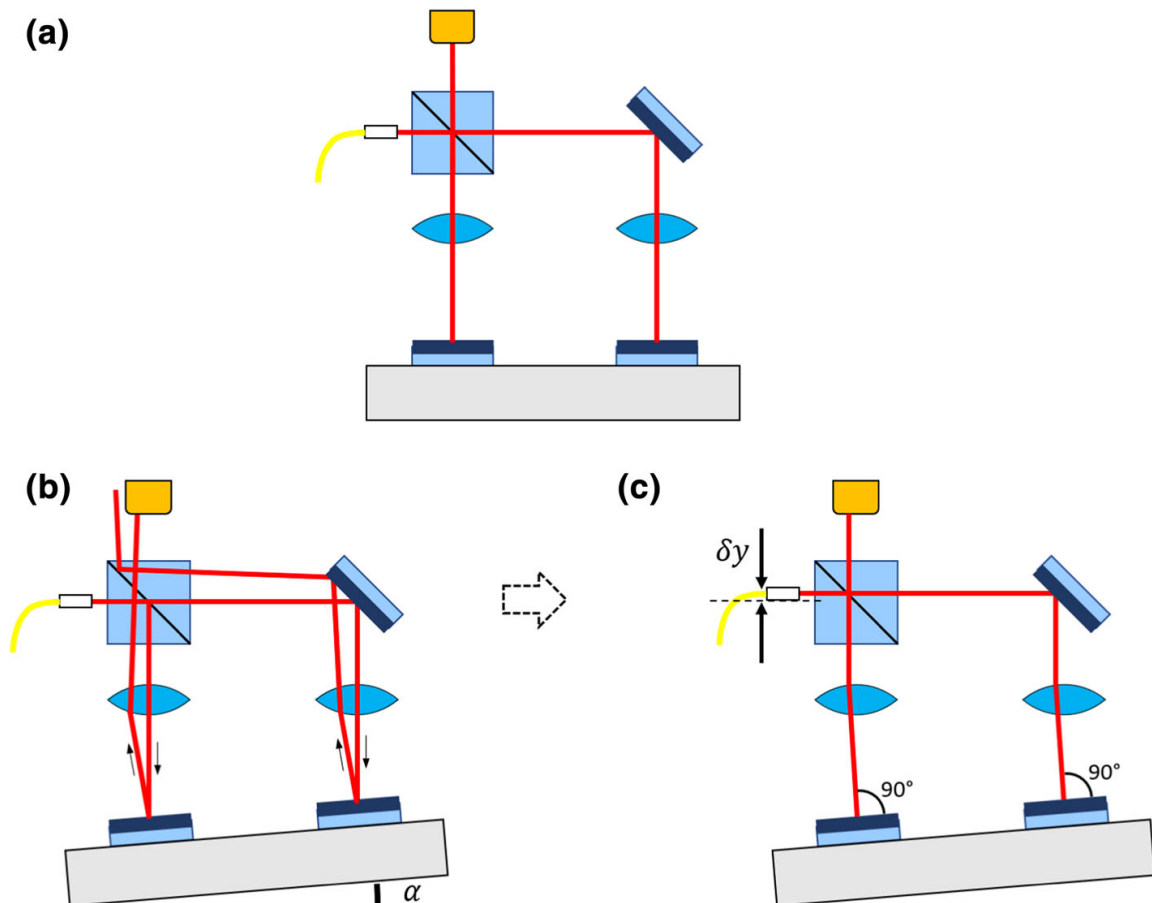


Fig. 2 Optical scheme of the interferometric readout. In figure (a), the interferometer is aligned, while the balance arm is horizontal. An arm tilt α would misalign the interferometer (b), but the presence of lenses in both arms permits the realignment by moving vertically the input laser beam by an amount δy (c)

condition, the beams impinge again orthogonally on the arm mirrors; then, they are reflected on the incoming path and recombine correctly at the beam splitter, as sketched in Fig. 2.

As mentioned above, the readout is completed by an auxiliary optical lever, powered by a superluminescent diode (SLED) and read by a quadrant photodiode. The lever is designed to have the beam impinging perpendicularly on a mirror placed on the lower face of the balance arm, and it is used as an initial reference position for the arm tilt.

2.2 Center of mass positioning

Beam balances and tiltmeter signals should not be induced by translation ground motion, but only by weight variations or ground rotations, respectively. It is known [19,20] that, if the tiltmeter center of mass does not lie on its rotation axis, a ground acceleration along the arm direction \ddot{z} generates a torque on the arm $\tau = m\delta\ddot{z}$, where m is the arm mass and δ is the distance from the center of mass to the rotation axis. This means that, in order to minimize the coupling between \ddot{z} and the arm tilt, the distance δ needs to be tuned as close as possible to zero.

Several tests have been performed to ascertain the difficulties in setting this distance within the limits of about $10\mu\text{m}$, as required by the Archimedes experiment [17]. The tuning of the center of mass position is done by regulating a set of screws placed on the arm. With the finest screw rotation, the center of mass can be moved by about $1\mu\text{m}$. Tuning operations are performed in air, and tiny mechanical displacements can occur while going into vacuum.

This implies that the tuning accuracy in vacuum is at best around $10\mu\text{m}$, which is still compliant with the requirements. However, in the design of the final balance, the center of mass positioning will be performed by acting remotely on the screws while the system is already in vacuum.

During operation at the Virgo site, the decoupling from translation ground noise has been tested with two methods. The first coarse one was to compare the balance signal with those of nearby seismometers during a far earthquake. In this case, the arrival times of various seismic waves are well separated: The first to occur are the primary waves (P-waves), which are essentially translation pressure waves, hence the secondary waves (S-waves), which are shear waves that can have tilt components depending on their polarization, and finally the surface waves, which have tilt components. While seismometers sense the ground motion, an ideal tiltmeter is expected to be sensitive to surface waves but not to P-waves. The behavior of our tiltmeter during a far earthquake is shown in Fig. 3. As expected, P-waves did not produce a signal above the noise level, while the effect of surface waves has been clearly observed.

A second, more refined method to test the decoupling from \ddot{z} was based on the comparison between tiltmeter and seismometer signals at a frequency where there is mainly translation seismic noise, that is, 0.4 Hz, around the microseismic peak frequency. At this frequency, a seismometer, which is more sensitive to translations than to tilts, would give a signal in which the component due to the ground tilt is negligible, unlike a tiltmeter, which is more sensitive to tilts than to translations. It follows that at 0.4 Hz the coherence between two such signals would be much less than 1, and this is what has been actually observed in our case, where $Coh \approx 0.25$, as shown in Fig. 4. The residual coherence is the consequence of a non-null distance δ . Indeed, if the tiltmeter center of mass does not lie on its rotation axis ($\delta \neq 0$), ground translations give rise to a signal, which is read as a tilt. The *shift-to-tilt* coupling allows an estimate of δ . The coupling, measured as:

$$C = \sqrt{Coh} \frac{\theta}{\ddot{z}/g}$$

results $C \approx 1.2 \times 10^{-3}$, where θ is the balance signal at 0.4 Hz and g is the gravitational acceleration. At first order, the coupling is given by

$$C = \frac{mg \cdot \delta}{I\omega^2}$$

where I and m are the momentum of inertia and the mass of the arm, respectively, and $f = \omega/2\pi$ is the measurement frequency [19]. In the hypothesis that a microseism does not produce ground tilts, the value of the coupling $C = 1.2 \times 10^{-3}$ corresponds to the upper limit $\delta = 15 \times 10^{-6}$ m, consistent with expectations.

2.3 Actuators and control loop

The beam balance is kept at the desired working point through a feedback control system. The loop is closed with electrostatic actuators, as typically used for the control of torsion pendulums [9, 10]. In our case, they are four metallic plates placed along the two sides of the balance arm. This latter is grounded, while the actuators are powered by a DC voltage supplier that can reach the maximum voltage of 2000 V. The actuator torque $\tau = \beta \cdot V^2$ is quadratic in the applied voltage V , with $\beta = 2.5 \times 10^{-11}$ Nm/V². The maximum torque is $\tau_{\max} = 10^{-4}$ Nm. The control signal is linearized by performing the square root of the correction signal before sending it to the actuators. The error signal is provided by the optical

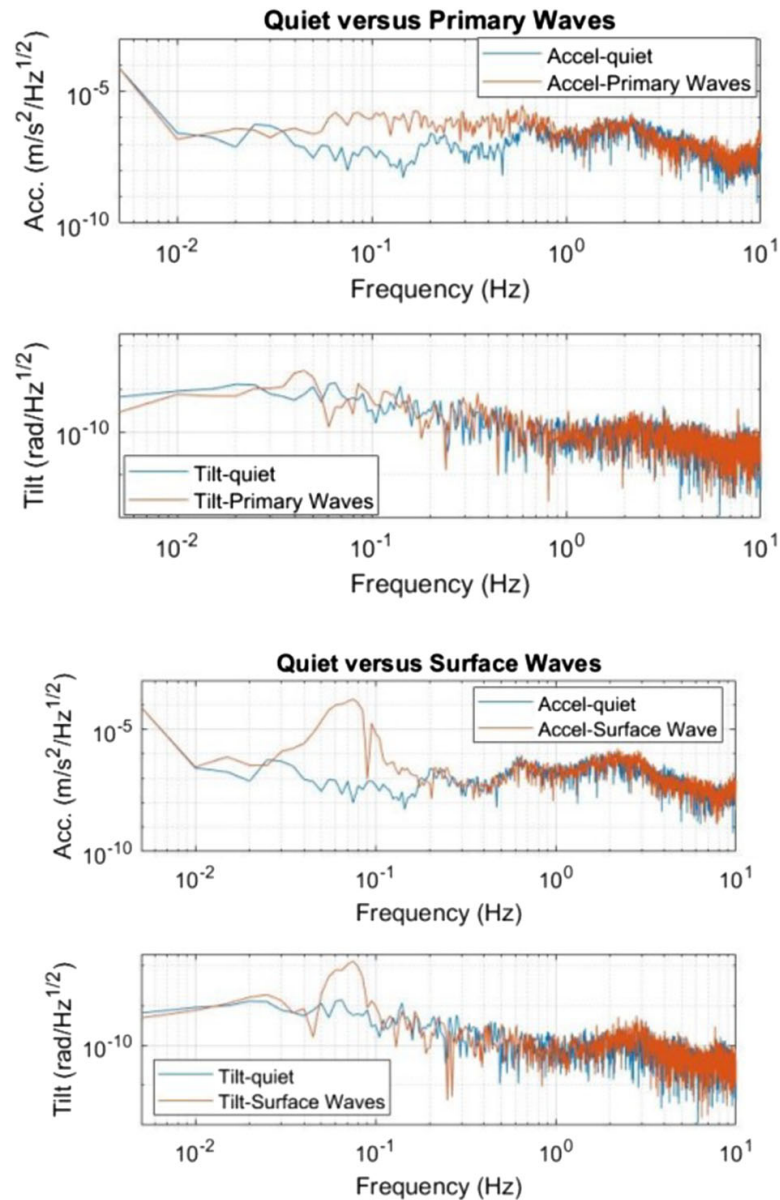


Fig. 3 Earthquake as read by a seismometer and by the tiltmeter. Top figure, upper plots: seismometer signal before (blue) and during (red) the P-waves; Top figure, lower plots: balance signal during the same period. It can be noticed that, during the earthquake, the seismometer senses the higher ground motion while the balance does not, as expected. Bottom figure: the same signals as in Top figure but referring to quiet period (blue) and surface waves. It can be noticed that, as expected, both the seismometer and the tiltmeter sense the higher ground motion

readout, as described in Sect. 2.1. After obtaining a coarse positioning with the optical lever signal, the error signal is switched to the interferometric signal, which provides a finer reference. During the operations at the Virgo site, the error and control signals are acquired and computed by the Virgo processing system [3]. The control loop has unity gain at 0.2 Hz.

3 Results at low frequencies

In the region of tens of mHz, the torque sensitivity reaches the value $\tilde{\tau} \simeq 8 \times 10^{-12} \text{Nm}/\sqrt{\text{Hz}}$. To our knowledge, this result is comparable with or even better than the currently best torque

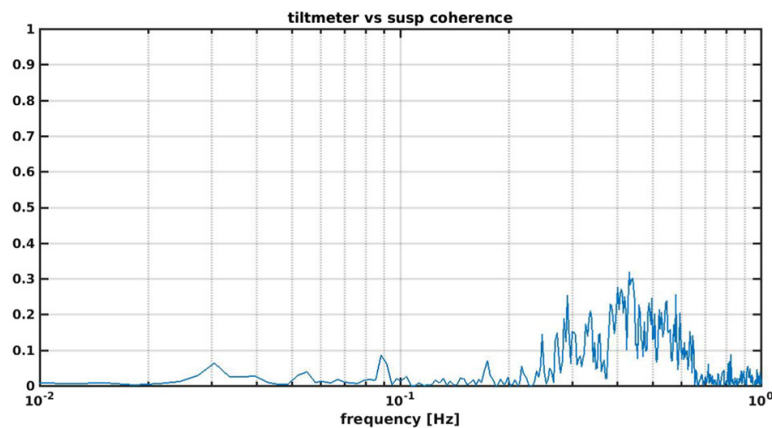


Fig. 4 Coherence of the tilmeter with a combination of accelerometers at the upper stage of the Virgo superattenuator

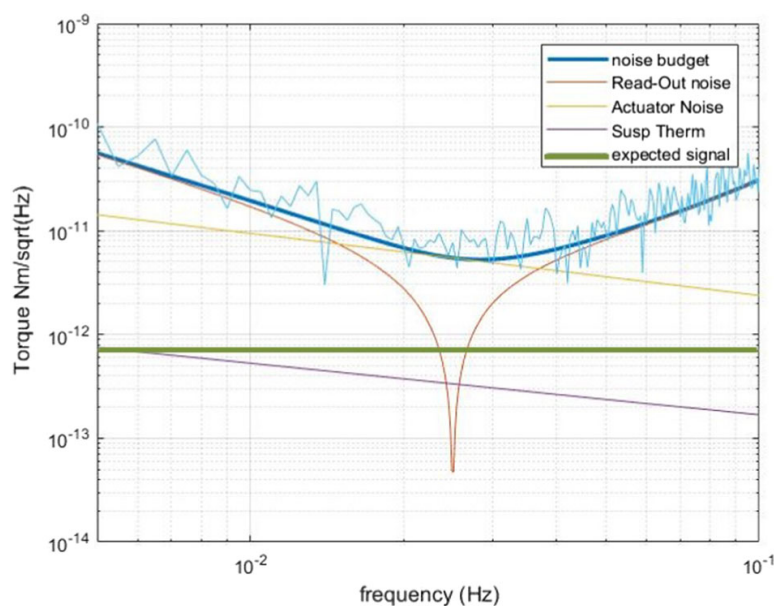


Fig. 5 Sensitivity and noise budget of the balance prototype compared with the expected signal (green line)

sensitivities in the world for balance systems [11]. Actuation and sensing noise are the main limiting noise sources, as reported in Fig. 5. At frequencies below 10 mHz and above 100 mHz, the interferometer signal is indeed coherent with the laser power fluctuations read at the input of the interferometer by an auxiliary photodiode.

In the intermediate region, the major contribution is given by the actuator noise. This can be evaluated considering that presently the actuation is obtained by applying a DC voltage control signal (i.e., not modulated). This implies that the actuation noise \tilde{A}_n , at first order, is proportional to V_{RMS} , the RMS of the control signal: $\tilde{A}_n = \beta \cdot V_{RMS} \tilde{V}_n$, where \tilde{V}_n is the voltage output noise of the amplifier. In the best condition, the balance was operated with tens of volts of static correction, corresponding to the noise reported in Fig. 5.

4 Sensitivity to tilts at high frequencies

Beam balances can be used as rotational sensors. In our case, in the low-frequency region, the sensitivity is not yet sufficiently good to use the balance as tilmeter to control the Virgo

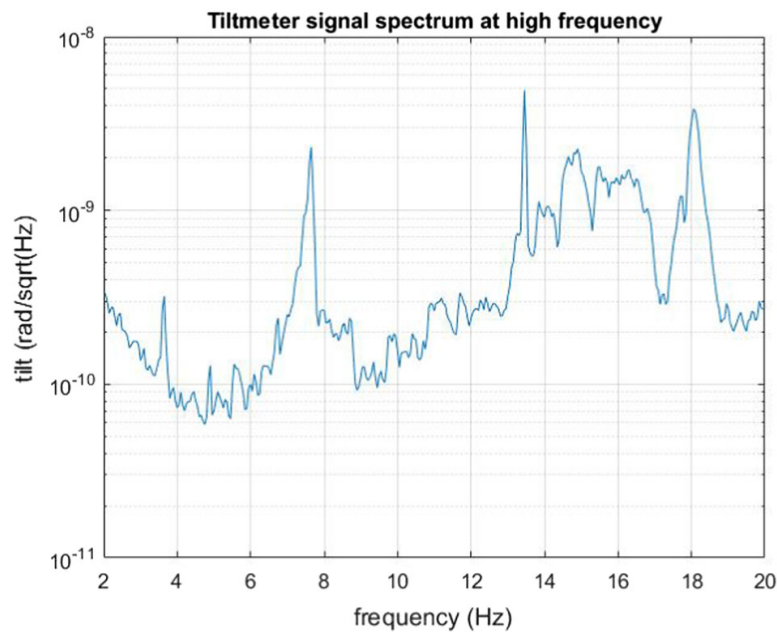


Fig. 6 Spectral density of the tilt amplitude in a quiet night at the Virgo site

interferometer. This is due to the choice of a very light arm, which helps in reaching a very good sensitivity in torque, but makes more difficult its use as a tilt reference. On the contrary, at higher frequencies, far above the resonance frequency, a light arm is not a limitation. Above a few Hz, rotation sensors are expected to be used in future detectors as ground tilt sensors for Newtonian noise subtraction.

The balance has been positioned at the North-end building, on the same floor where other auxiliary systems, like seismometers and other sensors, are located. The balance has been installed just before the start of the Virgo observation run O3 and remained on site for several months. The data taking allowed us to measure the ground tilts and test the coherence with seismometers and with the Virgo interferometer signal.

The results of the tilt measurement are shown in Fig. 6 for the frequency region from 2 to 20 Hz. This interval is particularly interesting for both Virgo and the future Einstein Telescope, whose observation band will extend down to 2 Hz. At a few Hz, the measured tilt reaches $\tilde{\theta} \approx 8 \times 10^{-11} \text{ rad}/\sqrt{\text{Hz}}$. Above 10 Hz, it shows a plateau of a few times $10^{-10} \text{ rad}/\sqrt{\text{Hz}}$ and a series of resonances larger than $10^{-9} \text{ rad}/\sqrt{\text{Hz}}$. The tilt measurement at lower frequencies, around a few Hz, highlights the property of the Virgo site to be quiet in this range.

In the 10–20 Hz interval, the measured tilt is similar to that at the LIGO site [13]. In particular, in the outer ranges (10–13 Hz and 18–20 Hz) the plateau is comparable, whereas in the middle range (between 13 and 18 Hz) the noise is higher. This result is still under investigation. Several resonances are coherent with seismometer signals, corroborating the hypothesis that they are structural resonances of the building. Figure 7 shows the correlation between the tiltmeter and the Virgo interferometer (i.e., gravitational wave) signals. At several frequencies, the tiltmeter is partially coherent with the Virgo interferometer and with seismometers placed in the building. On the other hand, at some frequencies, like 18.65 Hz, the balance signal is coherent with the Virgo interferometer, but not with the seismometers. However, in both cases, estimates of the Newtonian noise coupling is not compatible with a direct Newtonian coupling of ground motion with tilt masses, but rather with, for instance, a coupling mechanism through diffused light.

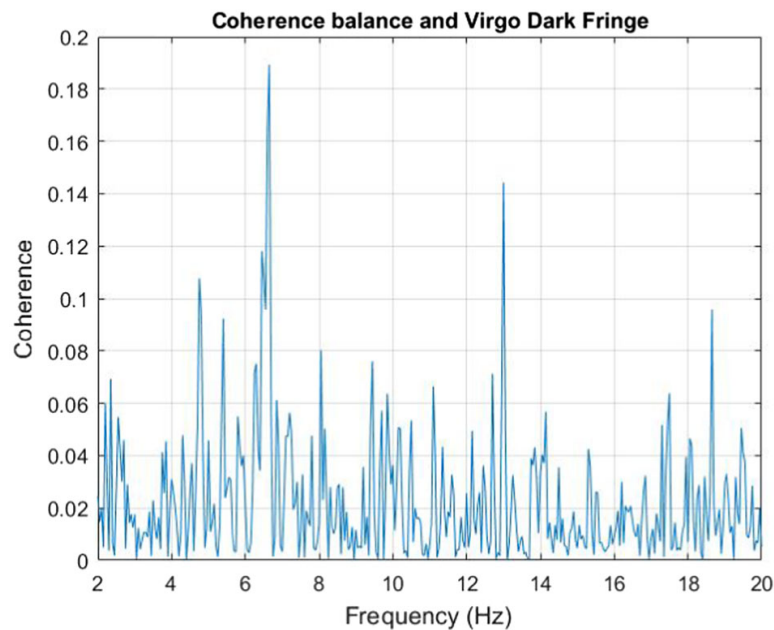


Fig. 7 Coherence of the balance signal with the Virgo interferometer signal

5 Conclusions and next steps

The measurement campaign with the beam balance performed at the Virgo site provided very encouraging results toward the definitive measurement of the weight of electromagnetic vacuum. Indeed, the torque sensitivity at low frequencies reaches the value $8 \times 10^{-12} \text{ Nm}/\sqrt{\text{Hz}}$, which is only a factor ≈ 10 higher than the torque expected in the measurement of vacuum weight.

At present, the sensitivity is limited by the laser amplitude and actuators noises. These can be reduced by stabilizing the laser and using voltage amplifiers with a lower noise. The latter improvement will be possible once the balance will be moved to a more quiet site, such as the SAR-GRAV laboratory, in Sardinia. In these seismic conditions, the force needed to maintain the interferometer locked is expected to be at least an order of magnitude lower; therefore, we could use amplifiers with a lower voltage and hence with a lower noise.

At high frequencies, the balance has shown a very good sensitivity to tilts, allowing us to measure the ground tilt at the Virgo site and to show that at some frequencies the Virgo dark-fringe signal is correlated with the tiltmeter signal. Moving the balance to the SAR-GRAV laboratory will permit a better study of the sensitivity to lower tilts, which will allow a new version of the balance to be used to measure ground tilts in the next Virgo run.

Acknowledgements This work has been partially funded by the PRIN 2017SYRTCN (Progetto di Ricerca Interesse Nazionale—Ministry of University and Research, Italy).

Funding Open access funding provided by Università degli Studi di Napoli Federico II within the CRUI-CARE Agreement.

Data Availability Statement This manuscript has associated data in a data repository. [Authors' comment: This manuscript has associated data in the Virgo Gravitational-Wave detector Data Repository. All data included in this manuscript are available upon request by contacting with the corresponding author.]

Open Access This article is licensed under a Creative Commons Attribution 4.0 International License, which permits use, sharing, adaptation, distribution and reproduction in any medium or format, as long as you give appropriate credit to the original author(s) and the source, provide a link to the Creative Commons licence,

and indicate if changes were made. The images or other third party material in this article are included in the article's Creative Commons licence, unless indicated otherwise in a credit line to the material. If material is not included in the article's Creative Commons licence and your intended use is not permitted by statutory regulation or exceeds the permitted use, you will need to obtain permission directly from the copyright holder. To view a copy of this licence, visit <http://creativecommons.org/licenses/by/4.0/>.

Appendix: The Archimedes and Virgo Collaboration

F. Acernese^{1,2,§}, M. Agathos^{3,§}, L. Aiello^{4,5,§}, A. Ain^{6,7,§}, A. Allocca^{2,8,†,§}, A. Amato^{9,§}, S. Ansoldi^{10,11,§}, S. Antier^{12,§}, M. Arène^{12,§}, N. Arnaud^{13,14,§}, P. Astone^{15,§}, F. Aubin^{16,§}, S. Avino^{2,96,†}, S. Babak^{12,§}, F. Badaracco^{4,5,§}, M. K. M. Bader^{17,§}, S. Bagnasco^{18,§}, J. Baird^{12,§}, G. Ballardin^{14,§}, G. Baltus^{19,§}, C. Barbieri^{20,21,22,§}, P. Barneo^{23,§}, F. Barone^{2,24,§}, M. Barsuglia^{12,§}, D. Barta^{25,§}, A. Basti^{6,7,§}, M. Bawaj^{26,27,§}, M. Bazzan^{28,29,§}, M. Bejger^{30,§}, I. Belahcene^{13,§}, V. Benedetto^{31,§}, S. Bernuzzi^{3,§}, D. Bersanetti^{32,§}, A. Bertolini^{17,§}, M. Bischi^{33,34,§}, M. Bitossi^{6,14,§}, M.-A. Bizouard^{35,§}, F. Bobba^{36,37,§}, M. Boer^{35,§}, G. Bogaert^{35,§}, M. Boldrini^{15,38,§}, F. Bondu^{39,§}, R. Bonnand^{16,§}, B. A. Boom^{17,§}, V. Boschi^{6,§}, V. Boudart^{19,§}, Y. Bouffanais^{28,29,§}, A. Bozzi^{14,§}, C. Bradaschia^{6,§}, M. Branchesi^{4,5,§}, M. Breschi^{3,§}, T. Briant^{40,§}, A. Brillet^{35,§}, J. Brooks^{14,§}, G. Bruno^{41,§}, T. Bulik^{42,§}, H. J. Bulten^{17,43,§}, D. Buskulic^{16,§}, G. Cagnoli^{9,§}, E. Calloni^{2,8,†,§}, M. Canepa^{32,44,§}, M. Cannavacciuolo^{36,§}, S. Caprara^{15,38,§}, G. Carapella^{36,37,§}, F. Carbognani^{14,§}, M. Carpinelli^{45,46,†,§}, G. Carullo^{6,7,§}, J. Casanueva Diaz^{14,§}, C. Casentini^{47,48,§}, S. Caudill^{17,49,§}, F. Cavalier^{13,§}, R. Cavalieri^{14,§}, G. Cella^{6,§}, P. Cerdá-Durán^{50,§}, E. Cesarini^{48,§}, W. Chaibi^{35,§}, P. Chanial^{14,§}, E. Chassande-Mottin^{12,§}, F. Chiadini^{37,51,§}, R. Chierici^{52,§}, A. Chincarini^{32,§}, M. L. Chiofalo^{6,7,§}, A. Chiummo^{14,§}, N. Christensen^{35,§}, S. Chua^{40,§}, G. Ciani^{28,29,§}, M. Cieřlar^{30,§}, P. Ciecielag^{30,§}, M. Cifaldi^{47,48,§}, R. Ciolfi^{29,53,§}, F. Cipriano^{35,§}, A. Cirone^{32,44,§}, S. Clesse^{54,§}, F. Cleva^{35,§}, E. Coccia^{4,5,§}, P.-F. Cohadon^{40,§}, D. E. Cohen^{13,§}, M. Colpi^{20,21,§}, L. Conti^{29,§}, I. Cordero-Carrion^{55,§}, S. Corezzi^{26,27,§}, D. Corre^{13,§}, S. Cortese^{14,§}, J.-P. Coulon^{35,§}, M. Croquette^{40,§}, J. R. Cudell^{19,§}, E. Cuoco^{6,14,56,§}, M. Curyło^{42,§}, T. Dal Canton^{13,§}, B. D'Angelo^{32,44,§}, S. D'Antonio^{48,§}, V. Dattilo^{14,§}, M. Davier^{13,§}, M. De Laurentis^{2,8,†,§}, F. De Lillo^{41,§}, F. De Matteis^{47,48,§}, R. De Pietri^{57,58,§}, R. De Rosa^{2,8,§}, C. De Rossi^{14,§}, R. De Simone^{51,§}, J. Degallaix^{59,§}, S. Deléglise^{40,§}, W. Del Pozzo^{6,7,§}, A. Depasse^{41,§}, L. Di Fiore^{2,§}, C. Di Giorgio^{36,37,§}, F. Di Giovanni^{50,§}, T. Di Girolamo^{2,8,§}, A. Di Lieto^{6,7,§}, S. Di Pace^{15,38,§}, I. Di Palma^{15,38,§}, F. Di Renzo^{6,7,§}, T. Dietrich^{17,§}, L. D'Onofrio^{2,8,§}, M. Drago^{4,5,§}, J.-G. Ducoin^{13,§}, O. Durante^{36,37,§}, D. D'Urso^{45,46,†,§}, P.-A. Duverne^{13,§}, M. Eisenmann^{16,§}, L. Errico^{2,8,†,§}, D. Estevez^{60,§}, V. Fafone^{4,47,48,§}, S. Farinon^{32,§}, M. Fays^{19,§}, F. Feng^{12,§}, E. Fenyvesi^{25,61,§}, I. Ferrante^{6,7,§}, F. Fiducaro^{6,7,§}, P. Figura^{42,§}, I. Fiori^{14,§}, R. Fittipaldi^{37,62,§}, V. Fiumara^{37,63,§}, R. Flaminio^{16,64,§}, J. A. Font^{50,65,§}, S. Frasca^{15,38,§}, F. Frasconi^{6,§}, G. G. Fronzè^{18,§}, G. Gagliardi^{2,96,†}, R. Gamba^{3,§}, B. Garaventa^{32,44,§}, F. Garufi^{2,8,§}, G. Gemme^{32,§}, A. Gennai^{6,§}, Archisman Ghosh^{66,§}, B. Giacomazzo^{20,21,22,§}, L. Giacoppo^{15,38,§}, P. Giri^{6,7,§}, F. Gissi^{31,§}, M. Gosselin^{14,§}, R. Gouaty^{16,§}, A. Grado^{2,67,§}, M. Granata^{59,§}, V. Granata^{36,§}, G. Greco^{26,§}, G. Grignani^{26,27,§}, M. Grilli^{15,38,†}, A. Grimaldi^{68,69,§}, S. J. Grimm^{4,5,§}, P. Gruning^{13,§}, G. M. Guidi^{33,34,§}, G. Guixé^{23,§}, Y. Guo^{17,§}, P. Gupta^{17,49,§}, L. Haegel^{12,§}, O. Halim^{11,70,§}, O. Hannuksela^{17,49,§}, T. Harder^{35,§}, K. Haris^{17,49,§}, J. Harms^{4,5,§}, B. Haskell^{30,§}, A. Heidmann^{40,§}, H. Heitmann^{35,§}, P. Hello^{13,§}, G. Hemming^{14,§}, E. Hennes^{17,§}, S. Hild^{17,71,§}, D. Hofman^{59,§}, V. Hui^{16,§}, B. Idzkowski^{42,§}, A. Iess^{47,48,§}, G. Intini^{15,38,§}, T. Jacqmin^{40,§}, K. Janssens^{72,§}, P. Jaranowski^{73,§}, R. J. G. Jonker^{17,§}, F. Kéfélian^{35,§}, C. Karathanasis^{74,§}, S. Katsanevas^{14,§},

I. Khan^{4,48,§}, N. Khetan^{4,5,§}, G. Koekoek^{17,71,§}, S. Koley^{17,§}, M. Kolstein^{74,§}, A. Królak^{75,76,§}, I. La Rosa^{16,§}, D. Laghi^{6,7,§}, A. Lamberts^{35,77,§}, A. Lartaux-Vollard^{13,§}, C. Lazzaro^{28,29,§}, P. Leaci^{15,38,§}, A. Lemaître^{78,§}, N. Leroy^{13,§}, N. Letendre^{16,§}, F. Linde^{17,79,§}, M. Llorens-Monteagudo^{50,§}, A. Longo^{80,81,§}, M. Lorenzini^{47,48,§}, V. Lorette^{82,§}, G. Losurdo^{6,§}, D. Lumaca^{47,48,§}, A. Macquet^{35,§}, C. Magazzù^{6,§}, E. Majorana^{15,38,§}, I. Maksimovic^{82,§}, N. Man^{35,§}, V. Mangano^{15,38,†,§}, M. Mantovani^{14,§}, M. Mapelli^{28,29,§}, F. Marchesoni^{26,83,§}, F. Marion^{16,§}, A. Marquina^{55,§}, S. Marsat^{12,§}, M.A. Marsella^{15,38,†}, F. Martelli^{33,34,§}, M. Martinez^{74,§}, V. Martinez^{9,§}, A. Masserot^{16,§}, S. Mastrogiovanni^{12,§}, A. Menendez-Vazquez^{74,§}, L. Mereni^{59,§}, M. Merzougui^{35,§}, A. Miani^{68,69,§}, C. Michel^{59,§}, L. Milano^{8,§}, A. Miller^{41,§}, E. Milotti^{11,70,§}, O. Minazzoli^{35,84,§}, Y. Minenkov^{48,§}, Ll. M. Mir^{74,§}, M. Montani^{33,34,§}, F. Morawski^{30,§}, B. Mours^{60,§}, F. Muciaccia^{15,38,§}, R. Musenich^{32,44,§}, A. Nagar^{18,85,§}, I. Nardecchia^{47,48,§}, L. Naticchioni^{15,§}, J. Neilson^{31,37,§}, G. Nelemans^{86,§}, C. Nguyen^{12,§}, S. Nissanke^{17,87,§}, F. Nocera^{14,§}, G. Oganessian^{4,5,§}, C. Olivetto^{14,§}, C. Périgois^{16,§}, G. Pagano^{7,6,§}, G. Pagliaroli^{4,5,§}, C. Palomba^{15,§}, P. T. H. Pang^{17,49,§}, F. Pannarale^{15,38,§}, F. Paoletti^{6,§}, A. Paoli^{14,§}, A. Paolone^{15,88,§}, D. Pascucci^{17,§}, A. Pasqualetti^{14,§}, R. Passaquieti^{6,7,§}, D. Passuello^{6,§}, B. Patricelli^{6,14,§}, M. Pegoraro^{29,§}, G.P. Pepe^{2,8,†}, M. Perciballi^{15,†,§}, A. Perego^{68,69,§}, A. Pereira^{9,§}, A. Perreca^{68,69,§}, S. Perriès^{52,§}, K. S. Phukon^{17,79,§}, O. J. Piccinni^{15,§}, M. Pichot^{35,§}, M. Piendibene^{6,7,§}, F. Piergiovanni^{33,34,§}, L. Pierini^{15,38,§}, V. Pierro^{31,37,§}, G. Pillant^{14,§}, F. Pilo^{6,§}, L. Pinard^{59,§}, I. M. Pinto^{31,37,89,§}, K. Piotrkowski^{41,§}, E. Placidi^{15,38,§}, W. Plastino^{80,81,§}, R. Poggiani^{7,6,§}, E. Polini^{16,§}, P. Popolizio^{14,§}, E. K. Porter^{12,§}, M. Pracchia^{16,§}, T. Pradier^{60,§}, M. Principe^{31,37,89,§}, G. A. Prodi^{69,90,§}, P. Prospero^{47,48,§}, A. Puecher^{17,49,§}, M. Punturo^{26,§}, F. Puosi^{6,7,§}, P. Puppo^{15,†,§}, G. Raaijmakers^{17,87,§}, N. Radulesco^{35,§}, P. Rapagnani^{15,38,†,§}, M. Razzano^{6,7,§}, T. Regimbau^{16,§}, L. Rei^{32,§}, P. Rettegno^{18,91,§}, F. Ricci^{15,38,†,§}, G. Riemschneider^{18,91,§}, F. Robinet^{13,§}, A. Rocchi^{48,§}, L. Rolland^{16,§}, M. Romanelli^{39,§}, R. Romano^{1,2,§}, A. Romero^{74,§}, L. Rosa^{2,8,†,§}, D. Rosińska^{42,§}, C. Rovelli^{97,98,99,†}, D. Rozza^{45,46,†,§}, P. Ruggi^{14,†,§}, N.L. Saini^{15,38,†}, O. S. Salafia^{20,21,22,§}, L. Salconi^{14,§}, F. Salemi^{68,69,§}, A. Samajdar^{17,49,§}, N. Sanchis-Gual^{92,§}, A. Sanuy^{23,§}, B. Sassolas^{59,§}, O. Sauter^{16,§}, S. Sayah^{59,§}, M. Seglar-Arroyo^{16,§}, D. Sentenac^{14,§}, V. Sequino^{2,8,§}, A. Sharma^{4,5,§}, N. S. Shcheglov^{78,§}, M. Sieniawska^{42,§}, N. Singh^{42,§}, A. Singha^{17,71,§}, V. Sipala^{45,46,†,§}, V. Sordini^{52,§}, F. Sorrentino^{32,§}, N. Sorrentino^{7,6,§}, R. Soulard^{35,§}, V. Spagnuolo^{17,71,§}, M. Spera^{28,29,§}, C. Stachie^{35,§}, D. A. Steer^{12,§}, J. Steinlechner^{17,71,§}, S. Steinlechner^{17,71,§}, D. Stornaiuolo^{2,8,†}, G. Stratta^{93,34,§}, A. Sur^{30,§}, B. L. Swinkels^{17,§}, P. Szewczyk^{42,§}, M. Tacca^{17,§}, F. Tafuri^{2,8,†}, A. Tagliacozzo^{2,8,§}, A. J. Tanasijczuk^{41,§}, E. N. Tapia San Martin^{17,§}, M. Tonelli^{6,7,§}, A. Torres-Forné^{50,§}, I. Tosta e Melo^{45,46,†,§}, A. Trapananti^{26,83,§}, F. Travasso^{26,83,§}, M. C. Tringali^{14,§}, L. Troiano^{37,94,§}, A. Trovato^{12,§}, K. W. Tsang^{17,49,95,§}, M. Turconi^{35,§}, A. Utina^{17,71,§}, M. Valentini^{68,69,§}, N. van Bakel^{17,§}, M. van Beuzekom^{17,§}, J. F. J. van den Brand^{17,43,71,§}, C. Van Den Broeck^{17,49,§}, L. van der Schaaf^{17,§}, J. V. van Heijningen^{41,§}, M. Vardaro^{17,79,§}, M. Vasúth^{25,§}, G. Vedovato^{29,§}, D. Verkindt^{16,§}, F. Vetrano^{33,§}, A. Viceré^{33,34,§}, J.-Y. Vinet^{35,§}, H. Vocca^{26,27,§}, R. C. Walet^{17,§}, M. Was^{16,§}, A. Zadrożny^{76,§}, T. Zelenova^{14,§}, J.-P. Zendri²⁹.

¹Dipartimento di Farmacia, Università di Salerno, I-84084 Fisciano, Salerno, Italy ²INFN, Sezione di Napoli, Complesso Universitario di Monte S. Angelo, I-80126 Napoli, Italy

³Theoretisch-Physikalisches Institut, Friedrich-Schiller-Universität Jena, D-07743 Jena, Germany ⁴Gran Sasso Science Institute (GSSI), I-67100 L'Aquila, Italy ⁵INFN, Laboratori Nazionali del Gran Sasso, I-67100 Assergi, Italy ⁶INFN, Sezione di Pisa, I-56127 Pisa, Italy ⁷Università di Pisa, I-56127 Pisa, Italy ⁸Università di Napoli "Federico II," Complesso Universitario di Monte S. Angelo, I-80126 Napoli, Italy ⁹Université de Lyon, Université

Claude Bernard Lyon 1, CNRS, Institut Lumière Matière, F-69622 Villeurbanne, France
¹⁰Dipartimento di Matematica e Informatica, Università di Udine, I-33100 Udine, Italy
¹¹INFN, Sezione di Trieste, I-34127 Trieste, Italy ¹²Université de Paris, CNRS, Astroparticule et Cosmologie, F-75006 Paris, France ¹³Université Paris-Saclay, CNRS/IN2P3, IJCLab, 91405 Orsay, France ¹⁴European Gravitational Observatory (EGO), I-56021 Cascina, Pisa, Italy ¹⁵INFN, Sezione di Roma, I-00185 Roma, Italy ¹⁶Laboratoire d'Annecy de Physique des Particules (LAPP), Univ. Grenoble Alpes, Université Savoie Mont Blanc, CNRS/IN2P3, F-74941 Annecy, France ¹⁷Nikhef, Science Park 105, 1098 XG Amsterdam, the Netherlands
¹⁸INFN Sezione di Torino, I-10125 Torino, Italy ¹⁹Université de Liège, B-4000 Liège, Belgium ²⁰Università degli Studi di Milano-Bicocca, I-20126 Milano, Italy ²¹INFN, Sezione di Milano-Bicocca, I-20126 Milano, Italy ²²INAF, Osservatorio Astronomico di Brera sede di Merate, I-23807 Merate, Lecco, Italy ²³Institut de Ciències del Cosmos, Universitat de Barcelona, C/ Martí i Franquès 1, Barcelona, 08028, Spain ²⁴Dipartimento di Medicina, "Chirurgia e Odontoiatria Scuola Medica Salernitana," Università di Salerno, I-84081 Baronissi, Salerno, Italy ²⁵Wigner RCP, RMKI, H-1121 Budapest, Konkoly Thege Miklós út 29-33, Hungary ²⁶INFN, Sezione di Perugia, I-06123 Perugia, Italy ²⁷Università di Perugia, I-06123 Perugia, Italy ²⁸Università di Padova, Dipartimento di Fisica e Astronomia, I-35131 Padova, Italy ²⁹INFN, Sezione di Padova, I-35131 Padova, Italy ³⁰Nicolaus Copernicus Astronomical Center, Polish Academy of Sciences, 00-716, Warsaw, Poland ³¹Dipartimento di Ingegneria, Università del Sannio, I-82100 Benevento, Italy ³²INFN, Sezione di Genova, I-16146 Genova, Italy ³³Università degli Studi di Urbino "Carlo Bo," I-61029 Urbino, Italy ³⁴INFN, Sezione di Firenze, I-50019 Sesto Fiorentino, Firenze, Italy ³⁵Artemis, Université Côte d'Azur, Observatoire Côte d'Azur, CNRS, F-06304 Nice, France ³⁶Dipartimento di Fisica "E.R. Caianiello," Università di Salerno, I-84084 Fisciano, Salerno, Italy ³⁷INFN, Sezione di Napoli, Gruppo Collegato di Salerno, Complesso Universitario di Monte S. Angelo, I-80126 Napoli, Italy ³⁸Università di Roma "La Sapienza," I-00185 Roma, Italy ³⁹Univ Rennes, CNRS, Institut FOTON - UMR6082, F-3500 Rennes, France ⁴⁰Laboratoire Kastler Brossel, Sorbonne Université, CNRS, ENS-Université PSL, Collège de France, F-75005 Paris, France ⁴¹Université catholique de Louvain, B-1348 Louvain-la-Neuve, Belgium ⁴²Astronomical Observatory Warsaw University, 00-478 Warsaw, Poland ⁴³VU University Amsterdam, 1081 HV Amsterdam, the Netherlands ⁴⁴Dipartimento di Fisica, Università degli Studi di Genova, I-16146 Genova, Italy ⁴⁵Università degli Studi di Sassari, I-07100 Sassari, Italy ⁴⁶INFN, Laboratori Nazionali del Sud, I-95125 Catania, Italy ⁴⁷Università di Roma Tor Vergata, I-00133 Roma, Italy ⁴⁸INFN, Sezione di Roma Tor Vergata, I-00133 Roma, Italy ⁴⁹Institute for Gravitational and Subatomic Physics (GRASP), Utrecht University, Princetonplein 1, 3584 CC Utrecht, the Netherlands ⁵⁰Departamento de Astronomía y Astrofísica, Universitat de València, E-46100 Burjassot, València, Spain ⁵¹Dipartimento di Ingegneria Industriale (DIIN), Università di Salerno, I-84084 Fisciano, Salerno, Italy ⁵²Institut de Physique des 2 Infinis de Lyon (IP2I), CNRS/IN2P3, Université de Lyon, Université Claude Bernard Lyon 1, F-69622 Villeurbanne, France ⁵³INAF, Osservatorio Astronomico di Padova, I-35122 Padova, Italy ⁵⁴Université libre de Bruxelles, Avenue Franklin Roosevelt 50 - 1050 Bruxelles, Belgium ⁵⁵Departamento de Matemáticas, Universitat de València, E-46100 Burjassot, València, Spain ⁵⁶Scuola Normale Superiore, Piazza dei Cavalieri, 7 - 56126 Pisa, Italy ⁵⁷Dipartimento di Scienze Matematiche, Fisiche e Informatiche, Università di Parma, I-43124 Parma, Italy ⁵⁸INFN, Sezione di Milano Bicocca, Gruppo Collegato di Parma, I-43124 Parma, Italy ⁵⁹Laboratoire des Matériaux Avancés (LMA), Institut de Physique des 2 Infinis (IP2I) de Lyon, CNRS/IN2P3, Université de Lyon, Université Claude Bernard Lyon 1, F-69622 Villeurbanne, France ⁶⁰Université de Strasbourg, CNRS, IPHC UMR 7178, F-67000 Strasbourg, France ⁶¹Institute for Nuclear Research,

Hungarian Academy of Sciences, Bem t'er 18/c, H-4026 Debrecen, Hungary ⁶²CNR-SPIN, c/o Università di Salerno, I-84084 Fisciano, Salerno, Italy ⁶³Scuola di Ingegneria, Università della Basilicata, I-85100 Potenza, Italy ⁶⁴gravitational wave Science Project, National Astronomical Observatory of Japan (NAOJ), Mitaka City, Tokyo 181-8588, Japan ⁶⁵Observatori Astronòmic, Universitat de València, E-46980 Paterna, València, Spain ⁶⁶Universiteit Gent, B-9000 Gent, Belgium ⁶⁷INAF, Osservatorio Astronomico di Capodimonte, I-80131 Napoli, Italy ⁶⁸Università di Trento, Dipartimento di Fisica, I-38123 Povo, Trento, Italy ⁶⁹INFN, Trento Institute for Fundamental Physics and Applications, I-38123 Povo, Trento, Italy ⁷⁰Dipartimento di Fisica, Università di Trieste, I-34127 Trieste, Italy ⁷¹Maastricht University, P.O. Box 616, 6200 MD Maastricht, the Netherlands ⁷²Universiteit Antwerpen, Prinsstraat 13, 2000 Antwerpen, Belgium ⁷³University of Białystok, 15-424 Białystok, Poland ⁷⁴Institut de Física d'Altes Energies (IFAE), Barcelona Institute of Science and Technology, and ICREA, E-08193 Barcelona, Spain ⁷⁵Institute of Mathematics, Polish Academy of Sciences, 00656 Warsaw, Poland ⁷⁶National Center for Nuclear Research, 05-400 Świerk-Otwock, Poland ⁷⁷Laboratoire Lagrange, Université Côte d'Azur, Observatoire Côte d'Azur, CNRS, F-06304 Nice, France ⁷⁸NAVIER, École des Ponts, Univ Gustave Eiffel, CNRS, Marne-la-Vallée, France ⁷⁹Institute for High-Energy Physics, University of Amsterdam, Science Park 904, 1098 XH Amsterdam, the Netherlands ⁸⁰Dipartimento di Matematica e Fisica, Università degli Studi Roma Tre, I-00146 Roma, Italy ⁸¹INFN, Sezione di Roma Tre, I-00146 Roma, Italy ⁸²ESPCI, CNRS, F-75005 Paris, France ⁸³Università di Camerino, Dipartimento di Fisica, I-62032 Camerino, Italy ⁸⁴Centre Scientifique de Monaco, 8 quai Antoine Ier, MC-98000, Monaco ⁸⁵Institut des Hautes Etudes Scientifiques, F-91440 Bures-sur-Yvette, France ⁸⁶Department of Astrophysics/IMAPP, Radboud University Nijmegen, P.O. Box 9010, 6500 GL Nijmegen, the Netherlands ⁸⁷GRAPPA, Anton Pannekoek Institute for Astronomy and Institute for High-Energy Physics, University of Amsterdam, Science Park 904, 1098 XH Amsterdam, the Netherlands ⁸⁸Consiglio Nazionale delle Ricerche - Istituto dei Sistemi Complessi, Piazzale Aldo Moro 5, I-00185 Roma, Italy ⁸⁹Museo Storico della Fisica e Centro Studi e Ricerche "Enrico Fermi," I-00184 Roma, Italy ⁹⁰Università di Trento, Dipartimento di Matematica, I-38123 Povo, Trento, Italy ⁹¹Dipartimento di Fisica, Università degli Studi di Torino, I-10125 Torino, Italy ⁹²Centro de Astrofísica e Gravitação (CENTRA), Departamento de Física, Instituto Superior Técnico, Universidade de Lisboa, 1049-001 Lisboa, Portugal ⁹³INAF, Osservatorio di Astrofisica e Scienza dello Spazio, I-40129 Bologna, Italy ⁹⁴Dipartimento di Scienze Aziendali - Management and Innovation Systems (DISA-MIS), Università di Salerno, I-84084 Fisciano, Salerno, Italy ⁹⁵Van Swinderen Institute for Particle Physics and Gravity, University of Groningen, Nijenborgh 4, 9747 AG Groningen, the Netherlands ⁹⁶Consiglio Nazionale delle Ricerche, Istituto Nazionale di Ottica (INO), via Campi Flegrei 34-Comprensorio A. Olivetti, 80078 Pozzuoli (Na), Italy ⁹⁷Centre de Physique Théorique Campus of Luminy, Case 907, F-13288 Marseille, France ⁹⁸Aix-Marseille Université Site du Pharo - 58 bd Charles Livon - F-13284 Marseille, France ⁹⁹Université de Toulon, Campus de La Garde - La Valette Avenue de l'Université F-83130 LA GARDE Toulon, France.

References

129

1. B.P. Abbott et al., LIGO-Virgo collaboration: "Observation of gravitational waves from a Binary Black Hole Merger". *Phys. Rev. Lett.* **116**(6), 061102 (2016)

2. B.P. Abbott et al., LIGO-Virgo collaboration: “GWTC-1: a gravitational-wave transient catalog of compact binary mergers observed by LIGO and Virgo during the first and second observing runs”. *Phys. Rev. X* **9**(3), 031040 (2019)
3. F. Acernese et al., Virgo Coll: “Advanced Virgo: a second-generation interferometric gravitational wave detector”. *Class. Quantum Gravit.* **32**(2), 024001 (2015)
4. J. Aasi et al., LIGO Scientific Collaboration: “Advanced LIGO”. *Class. Quantum Gravit.* **32**, 074001 (2015)
5. T. Akutsu, KAGRA collaboration: “KAGRA: 2.5 Generation Interferometric gravitational wave Detector”. *Nat. Astron.* **3**(1), 35–40 (2019)
6. K.L. Dooley, J.R. Leong et al., GEO 600 and the GEO-HF upgrade program: successes and challenges. *Class. Quantum Gravit.* **33**, 075009 (2016)
7. N. Bartolo, C. Caprini et al., Science with the space-based interferometer LISA. IV: Probing inflation with gravitational waves. *JCAP* **12**, 026 (2016)
8. L. Zhu, Q. Liu et al., Test of the equivalence principle with chiral masses using a rotating torsion pendulum. *Phys. Rev. Lett.* **121**(26), 261101 (2018)
9. G. Russano, A. Cavalleri et al., Measuring fN force variations in the presence of constant nN forces: a torsion pendulum ground test of the LISA Pathfinder free-fall mode. *Class. Quantum Gravit.* **35**(3), 035017 (2018)
10. M. Bassan, M. De Laurentis et al., Improving sensitivity and duty-cycle of a double torsion pendulum. *Class. Quantum Gravit.* **36**(12), 125004 (2019)
11. K. Venkateswara, C.A. Hagedorn et al., A high-precision mechanical absolute-rotation sensor. *Rev. Sci. Instrum.* **85**, 015005 (2014)
12. P. Ross, K. Venkateswara et al., Towards windproofing LIGO: Reducing the effect of wind-driven floor tilt by using rotation sensors inactive seismic isolation” e-Print: 2003.06447
13. M. Coughlin, J. Harms et al., Implications of dedicated seismometer measurements on Newtonian-noise cancellation for Advanced LIGO. *Phys. Rev. Lett.* **121**(22), 221104 (2018)
14. F. Badaracco, J. Harms, Optimization of seismometer arrays for the cancellation of Newtonian noise from seismic body waves. *Class. Quantum Gravit.* **36**(14), 145006 (2019)
15. J. Harms, K. Venkateswara, Newtonian-noise cancellation in large-scale interferometric GW detectors using seismic tiltmeters. *Class. Quantum Gravit.* **33**(23), 234001 (2016)
16. G. Bimonte, E. Calloni, G. Esposito, L. Rosa, Energy-momentum tensor for a Casimir apparatus in a weak gravitational field. *Phys. Rev. D* **74**, 085011 (2006)
17. E. Calloni, M. De Laurentis, R. De Rosa, L. Di Fiore, G. Esposito, F. Garufi, L. Rosa, C. Rovelli, P. Ruggi, F. Tafuri et al., Towards weighing the condensation energy to ascertain the Archimedes force of vacuum. *Phys. Rev. D* **90**, 022002 (2014)
18. S. Avino, E. Calloni et al., Progress in a vacuum weight search experiment. *MDPI Phys.* **2**(1), 1–13 (2020)
19. C.C. Speake, D.B. Newell, The design and application of a novel high frequency tiltmeter. *Rev. Sci. Instrum.* **61**, 1500 (1990)
20. F. Matichard, M. Evans, Review: tilt-free low-noise seismometry. *Bull. Seismol. Soc. Am.* **105**(2A), 497–510 (2015)

Appendix C

Picoradiant tiltmeter and direct ground tilt measurements at the Sos Enattos site



Picoradiant tiltmeter and direct ground tilt measurements at the Sos Enattos site

Annalisa Allocca^{1,2}, Saverio Avino^{2,3}, Enrico Calloni^{1,2}, Sergio Caprara^{4,5}, Massimo Carpinelli^{6,7}, Domenico D'Urso^{6,7}, Martina De Laurentis^{1,2}, Rosario De Rosa^{1,2}, L. Errico^{1,2,a} , G. Gagliardi^{2,3}, Marco Grilli^{4,5}, Valentina Mangano^{4,5}, Maria Marsella^{4,5}, Luca Naticchioni⁵, Antonio Pasqualetti⁸, Gianpiero Pepe^{1,2}, Maurizio Perciballi⁵, Luca Pesenti^{9,10}, Paola Puppo⁵, Piero Rapagnani^{4,5}, Fulvio Ricci^{4,5}, Luigi Rosa^{1,2}, Carlo Rovelli^{11,12,13}, Davide Rozza^{6,7}, P. Ruggi⁸, Naurang L. Saini^{4,5}, Valeria Sequino^{1,2}, Valeria Sipala^{6,7}, Daniela Stornaiuolo^{1,2}, Francesco Tafuri^{1,2}

¹ Università di Napoli Federico II - Via Cinthia, I-80126 Naples, Italy

² INFN - sez. Napoli - Via Cinthia, I-80126 Naples, Italy

³ Centro Nazionale Ricerche - Istituto Nazionale di Ottica (CNR-INO), Firenze, Italy

⁴ Università di Roma La Sapienza, I-00185 Roma, Italy

⁵ INFN - sezione di Roma 1, I-00185 Roma, Italy

⁶ Università degli Studi di Sassari, I-07100 Sassari, Italy

⁷ INFN - Laboratori Nazionali del Sud, I-95125 Catania, Italy

⁸ European Gravitational Observatory (EGO), Via E Amaldi, 56021 Cascina, PI, Italy

⁹ Università degli Studi di Milano Bicocca, I- 20126 Milano, Italy

¹⁰ INFN - sezione di Milano-Bicocca, I - 20126 Milano, Italy

¹¹ Centre de Physique Theorique Campus of Luminy - Case 907, F-13288 Marseille, France

¹² Aix-Marseille Université Site du Pharo, 58 bd Charles Livon, F-13284 Marseille, France

¹³ Université de Toulon - Campus de La Garde - La Valette Avenue de l'Université, La Garde, F-83130 Toulon, France

Received: 21 July 2021 / Accepted: 24 September 2021

© The Author(s) 2021

Abstract We report the tilt sensitivity reached by the ARCHIMEDES tiltmeter in the 2–20 Hz frequency region, where seismic noise is expected to give an important limitation to the sensitivity in the next future Gravitational Waves detection, particularly through Newtonian noise. The tilt noise level $\tilde{\theta}(f)$ is about $10^{-12} \text{ rad}/\sqrt{\text{Hz}}$ in most of the band, reaching the minimum of $\tilde{\theta} = 7 \cdot 10^{-13} \text{ rad}/\sqrt{\text{Hz}}$ around 9 Hz. The tiltmeter is a beam balance with a 0.5 m suspended arm and interferometric optical readout, working in closed loop. The results have been obtained by a direct measurement of the ground tilt at the Sos Enattos site (Sardinia, Italy). This sensitivity is a requirement to use the tiltmeter as part of an effective Newtonian noise reduction system for present Gravitational Waves detectors, and also confirms that Sos Enattos is among the quietest sites in the world, suitable to host the third-generation Gravitational Waves detector Einstein Telescope.

^a e-mail: lerrico@na.infn.it (corresponding author)

1 Introduction

Since the first discovery of Gravitational Waves (GW) announced in 2016 [1], the Advanced LIGO and Advanced Virgo experiments have detected gravitational radiation emitted by Binary Black Holes and Binary Neutron Star mergers [2,3]. These detections represented a breakthrough in astrophysics, as they widely improve the knowledge on Black Holes and Binary Neutron Stars population, on gravity in the strong field regime, and opened the way to the multi-messenger astronomy [4,5].

At present, existing GW detectors have been upgraded and are now under commissioning until the beginning of the Observing Run 4 (O4), which is planned to start in middle 2022. Meanwhile, the scientific GW community is proposing the realization of third-generation ground-based detectors, namely Einstein Telescope (ET) [6] and Cosmic Explorer (CE) [7]. In their design, a strong effort is devoted to improve the sensitivity and to extend the observation band toward lower frequencies. This will allow for the search of intermediate mass black holes and low-frequency spinning neutron stars, as well as a better estimation of coalescing binary parameters thanks to a longer lifetime in the detection window.

The low-frequency limit, which is around 10 Hz in the present detectors, will be extended to even lower frequencies in the next generation. In particular, the Einstein Telescope is designed to reach about 2 Hz [6,8]. Seism is the dominant noise in the 2–20 Hz frequency band. It can affect the sensitivity either through its direct transmission to the Test Masses (TM) or through the so-called Newtonian noise (NN), the coupling due to gravitational field variation produced on the TM by the displacements of surrounding masses [9–11]. Historically, the isolation of test masses from direct seismic shaking has been accomplished with complex isolation systems capable of reducing the coupling up to ten orders of magnitude [12,13]. Further improvements will require either an even better seismic isolation or the installation of the new detectors in suitable quieter sites, such as Sos Enattos, which is indeed a candidate site to host the ET underground detector [14,15].

While direct shaking can be reduced with suitable passive isolators, gravitational coupling must be subtracted by measuring the seismic field, inferring the gravitational field variation and finally by subtracting this effect from the detector signal.

NN has until now not limited the detectors' sensitivity, but it is expected that it will be the dominant noise if no reduction will be implemented. This procedure requires the measurement of the seismic field, with a signal-to-noise ratio (SNR) of about 100 in case of Virgo and LIGO detectors [16].

One of the possible strategies that could simplify the reconstruction of the gravity field is the measurement of the seismic field with a tiltmeter [17].

A tiltmeter consists of an absolute rotational sensor, capable of measuring the inclination of the ground surface with respect to a suspended reference arm. Such a device is specifically designed to minimize the coupling with ground translations, so to be mainly sensitive to ground tilts [18,19]. In recent scientific runs, both in Advanced LIGO and Advanced Virgo, preliminary tests with tiltmeters have been conducted [20,21]. The measured tilt was of the order of 10^{-10} rad/ $\sqrt{\text{Hz}}$ (or slightly higher, depending on frequency). In the next runs, the sensitivity of the GW detectors might be limited by the NN and tiltmeters with sufficient SNR would help measuring this motion. In this paper, we show the results of an upgraded version of our tiltmeter, tested at the quiet site of Sos Enattos (Sardinia, Italy), whose sensitivity verifies the required characteristics. The paper is organized as follows: A first section is devoted to describe the experimental setup, and a second section will present and discuss the sensitivity and the noise budget. Implications for NN reduction and future developments will be discussed in the last, conclusive, section.

2 Experimental setup

Within the Archimedes experiment, devoted to measure the interaction of vacuum fluctuations and gravity [22–24], an high sensitivity prototype balance has been developed [21]. If no samples are suspended at the end of the arm, it can be used as a tiltmeter. It consists of a 0.5 m long arm, whose mechanical design is similar to LIGO tiltmeters [19]. The arm is suspended by its center through two thin wire-like suspensions (Cu-Be, $100\mu\text{m} \times 500\mu\text{m}$), as shown in Fig. 1.

The tiltmeter center of mass is positioned within $10\mu\text{m}$ of the bending point, which allows for a reduction of the translation-to-tilt coupling. Depending on the center of mass positioning, its resonance frequency is around 20–30 mHz. The free oscillations of the suspended arm are read with a Michelson interferometer, whose optical design is an improved version of the one described in [21]. In the old version, the interferometer had unequal optical paths and it was more affected by common noise coupling, such as laser frequency and amplitude noise.

In the present improved version, these two noise sources have been reduced by using an optical delay line to equalize the optical paths, and normalizing the output signal to the input laser power. The delay line is located after the beam splitter reflection and is made of 4 right-angle prisms, exploiting total internal reflection, as shown, in blue, in Fig. 1. In this way, the length difference between the optical paths has been reduced from 100 mm to 2 mm at worst, yielding to a frequency noise reduction by a factor 50.

The tiltmeter working point (interferometer output on half-fringe) is kept by controlling the arm position through electrostatic actuators. They consist of 4 metallic $2\text{ cm} \times 10\text{ cm}$ plates located along the arm ends, as shown in Fig. 2. The control signal is given by a digital filter fed with the interferometer output. This control suppresses tiltmeter motion at low frequency (the unity gain frequency is 0.3 Hz), while leaving the arm free to oscillate at higher frequencies. In this way, the control loop has no effect in the NN frequency region and, together with the low resonance frequency, makes the tiltmeter arm an inertial reference for ground tilts in the frequency band of interest for Gravitational Wave detectors, particularly in

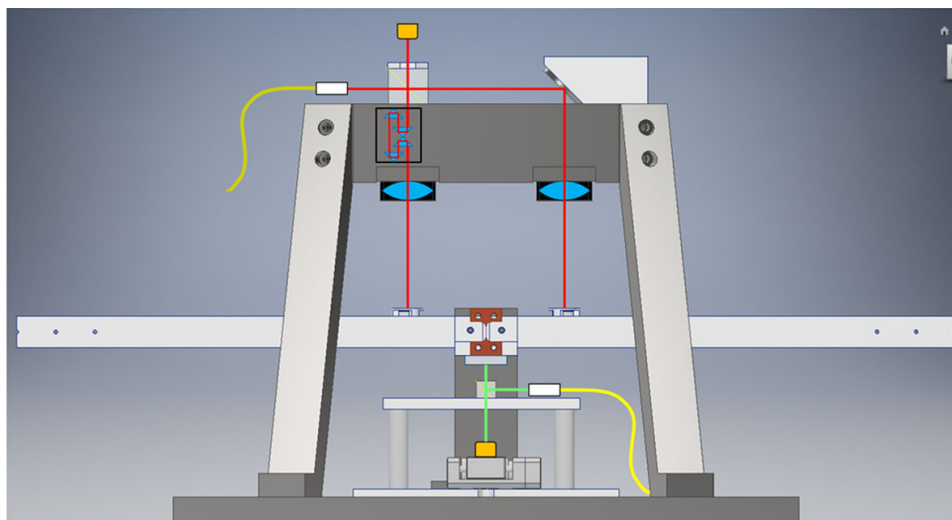


Fig. 1 Tiltmeter scheme. The red line identifies the path of the laser light in the interferometer. The light is injected with the fiber (in yellow at the top left) and split by the beam splitter. In the shorter interferometer arm, there is a delay line, consisting of prisms, which equalizes the pathlength. The two lenses, shown in blue, have focal lengths equal to their distance from the balance arm, so that the interferometer contrast is sensitive only to the second order to the tilts of the arm itself. Below the arm is the optical lever, which serves as an initial alignment reference

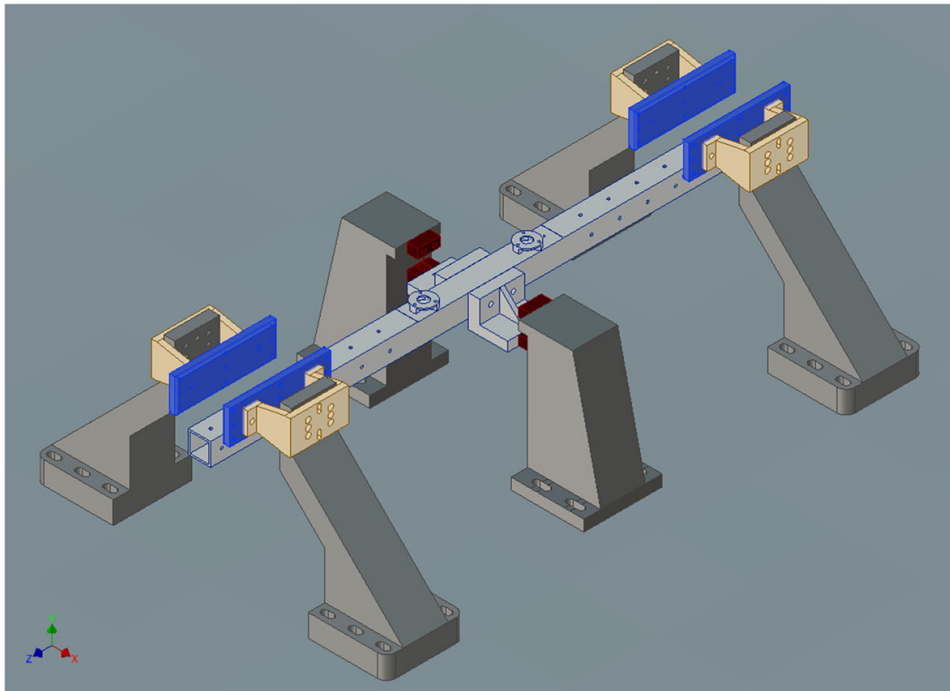


Fig. 2 Scheme of the electrostatic actuators, reported in blue in the picture

the band 2–20 Hz. Notice that the upper bound of the tiltmeter sensitivity is presently above 20 Hz, extending up to about 100 Hz where a low-pass filter is used as anti-aliasing.

3 Sensitivity and noise budget

The results obtained from these measurements are shown in Fig. 3. The figure shows the previous ground tilt measurement, performed at the Virgo site, and the current one, on the Sos Enattos site. The ground tilt measured at Sos Enattos remains around picoradians/ $\sqrt{\text{Hz}}$ in most of the frequency band, reaching the minimum value of $7 \cdot 10^{-13} \text{ rad}/\sqrt{\text{Hz}}$ in the region of a few Hz and the maximum value of $6 \cdot 10^{-11} \text{ rad}/\sqrt{\text{Hz}}$, at a resonance peak of the infrastructure, at 17.5 Hz. We also notice a peak at 7.5 Hz, with a tilt value of $10^{-11} \text{ rad}/\sqrt{\text{Hz}}$, due to a resonance of the vacuum chamber, and a resonance at 4 Hz, still to be investigated. As can be seen from the figure, if we exclude the infrastructural resonance peaks, the value of the ground tilt measured at Sos Enattos is at least two orders of magnitude lower than at the Virgo site. It reaches almost three orders of magnitude in the region just above 10 Hz, where Virgo has a number of infrastructure resonances. If the value measured at Sos Enattos is taken conservatively as the sensitivity, we deduce that the tiltmeter is capable of measuring the Virgo site tilt with an SNR greater than 100, which is more than sufficient to be used for NN reduction. The sensitivity of the tiltmeter was also analyzed by evaluating the main fundamental noises. These included shot noise, laser radiation pressure noise, thermal noise and acquisition noise.

Main noise sources contributing:

- **Shot noise**

135

The shot noise contribution to the tilt is evaluated as [25]:

$$\theta_{SN} = \frac{1}{2} \frac{\lambda}{\pi L} \sqrt{\left(\frac{h\nu}{\eta P}\right) \frac{1}{C}}; \quad (1)$$

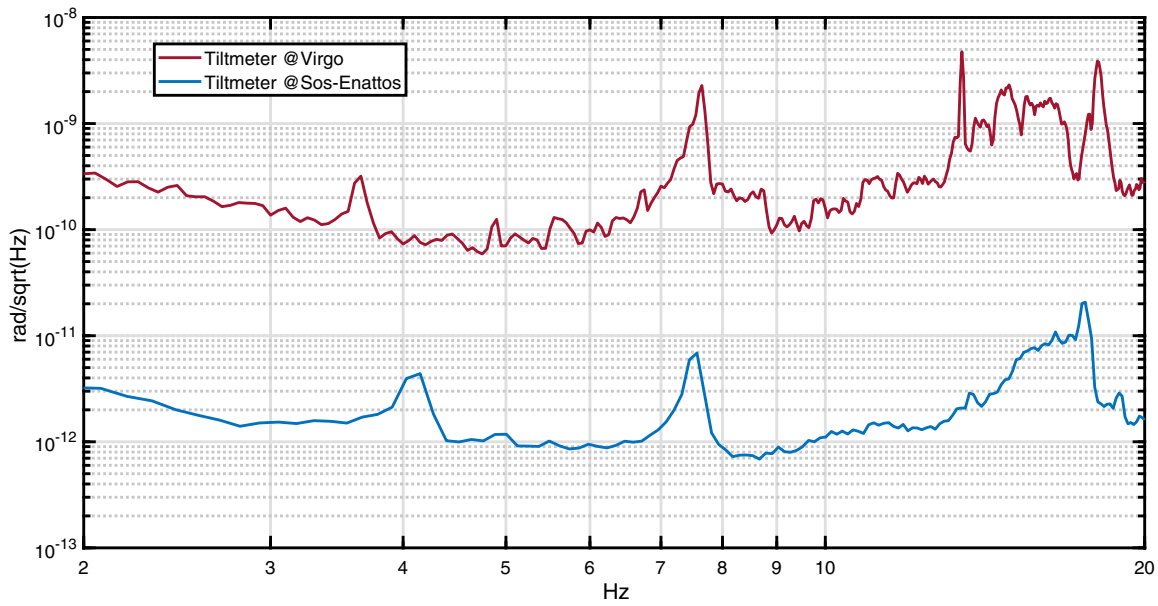


Fig. 3 Ground tilt in Virgo and Sos Enattos sites

where we have taken into account that the working point of the interferometer is the half fringe. In the above equation, h is the Planck constant, $\lambda = 532\text{nm}$ is the laser wavelength, $L=0.1\text{ m}$ is the interferometer arm length, $\nu = c/\lambda$, $\eta = 0.9$ is the photodiode quantum efficiency, $P = 3\text{ mW}$ is the input power, and $C = \frac{(V_{\max}-V_{\min})}{(V_{\max}+V_{\min})} \simeq 0.5$ is the contrast, computed by measuring the voltage at bright (V_{\max}) and dark (V_{\min}) fringe. The shot noise is independent of the frequency, and its level is $1.9 \times 10^{-14}\text{rad}/\sqrt{\text{Hz}}$.

– **Radiation pressure noise**

Given the tiltmeter arm momentum of inertia as $I = 1.3 \times 10^{-2}\text{kg} \cdot \text{m}^2$, the radiation pressure noise can be written as:

$$\theta_{RP} = \frac{1}{2} \frac{L}{I\omega^2} \sqrt{\frac{Ph\nu}{c^2}} \tag{2}$$

where $\omega = 2\pi f$. The radiation pressure noise contribution is absolutely negligible, as it corresponds to $10^{-22}\text{rad}/\sqrt{\text{Hz}}$ at 10Hz.

– **Suspension thermal noise**

To compute the suspension thermal noise contribution, we must define the *loss angle* as the inverse of the Q of the arm resonance: $\phi_{loss} = 1/Q = 0.01$. Given the resonance frequency $f_0 = 0.025\text{ Hz}$, suspension thermal noise can be written as [26]:

$$\theta_{SThN} = \sqrt{\frac{1}{2} \frac{4k_B T (I\omega_0^2) \phi_{loss}}{\omega((I\omega_0^2 - I\omega^2)^2 + (I\omega_0^2)^2 \phi_{loss}^2)}} \tag{3}$$

where k_B is the Boltzmann constant and $T = 300\text{ K}$ is the temperature. The contribution remains well below $10^{-13}\text{rad}/\sqrt{\text{Hz}}$ over the entire frequency band.

– **Internal thermal noise**

For this contribution, the resonance frequency of the arm has been considered as equal to $f_{0_i} = 950\text{ Hz}$, and the internal $Q_i = 1000$. The noise results to be [26]:

$$\theta_{I_{ThN}} = \sqrt{\frac{4k_B T (I\omega_{0_i}^2) \cdot \phi_{loss_i}}{\omega((I\omega_{0_i}^2 - I\omega^2)^2 + (I\omega_{0_i}^2)^2 \phi_{loss_i}^2)}} \tag{4}$$

The contribution is almost flat and is about 10^{-15} rad/ $\sqrt{\text{Hz}}$ at 10 Hz.

– **ADC noise**

The ADC noise has been measured by using a 50 Ω BNC termination at the ADC input. The noise level results to be 2.2×10^{-13} , almost flat over the 2–20 Hz frequency band. The value and the verified dependence from the square root of the sampling rate are consistent with the theoretical expectations. It is the main instrumental contribution to the noise budget.

The noise level shown in the figure is typically reached during the night or during the weekend. On working days, due to activities related to mine maintenance, the noise is significantly higher. From the noise budget and the above considerations, we can interpret the curve of Fig. 3 as an upper limit of the site seismic noise when not disturbed by anthropogenic noise. Further commissioning activities are planned to ensure that there are no other noises that are limiting the sensitivity. These include, in particular, laser frequency noise due to the residual asymmetry of the arms or scattered light.

4 Discussion and future developments

The tiltmeter has reached the required sensitivity to be used in Newtonian noise reduction in the next scientific runs of the Virgo gravitational wave detectors. In this case, in fact, to obtain an effective Newtonian noise reduction it is necessary that the ground tilt is measured with a good SNR. The ground tilt $\tilde{\theta}$ at the Virgo site (similarly at the LIGO site [17]) is of the order of $\tilde{\theta} \approx 10^{-10}$ rad/ $\sqrt{\text{Hz}}$; the sensitivity achieved ensures an SNR of around 100, which is more than sufficient to meet the specifications. For future-generation detectors, in particular the Einstein Telescope, the study of Newtonian noise subtraction is still at a preliminary stage and moreover the detectors' sites have not yet been chosen. At this preliminary stage, it is particularly important to measure the characteristics of the candidate sites in order to make an appropriate choice, keeping in mind that the band of interest of future detectors will extend down to frequencies of around 2 Hz. The sensitivity achieved, which to our knowledge is, in this region of frequencies, at the best in the world for ground tilt measuring devices [17, 27, 28], makes it available for the characterization of the various candidate sites for third-generation gravitational wave observatories. For Sos Enattos, the measurements show that at low frequency, the site is about 100 times quieter than the sites where Virgo and LIGO are installed. This result is expected, because it is compatible with similar results obtained with seismometers [14, 29] and confirms that Sos Enattos is one of the quietest sites in the world where to install the future ET observatory.

Funding Open access funding provided by Università degli Studi di Napoli Federico II within the CRUI-CARE Agreement.

Data Availability Statement This manuscript has associated data in a data repository. [Authors' comment: The data are stored in the Archimedes' repository and are available upon request. Please contact the corresponding author.]

Open Access This article is licensed under a Creative Commons Attribution 4.0 International License, which permits use, sharing, adaptation, distribution and reproduction in any medium or format, as long as you give appropriate credit to the original author(s) and the source, provide a link to the Creative Commons licence, and indicate if changes were made. The images or other third party material in this article are included in the article's Creative Commons licence, unless indicated otherwise in a credit line to the material. If material is not included in the article's Creative Commons licence and your intended use is not permitted by statutory

regulation or exceeds the permitted use, you will need to obtain permission directly from the copyright holder. To view a copy of this licence, visit <http://creativecommons.org/licenses/by/4.0/>.

References

1. B.P. Abbot et al., Observation of gravitational waves from a binary black hole merger. *Phys. Rev. Lett.* **116**, 061102 (2016)
2. B.P. Abbot et al., GW170817: observation of gravitational waves from a binary neutron star inspiral. *Phys. Rev. Lett.* **119**, 161101 (2017)
3. B.P. Abbot et al., GWTC-1: a gravitational-wave transient catalog of compact binary mergers observed by LIGO and virgo during the first and second observing runs. *Phys. Rev. X* **9**, 031040 (2019)
4. B.P. Abbot et al., Binary black hole population properties inferred from the first and second observing runs of advanced LIGO and advanced virgo. *Astrophys. J. Lett.* **882**, 2, L24 (2019)
5. B.P. Abbot et al., Low-latency gravitational-wave alerts for multimessenger astronomy during the second advanced LIGO and virgo observing run. *Astrophys. J.* **875**, 2161 (2019)
6. M. Punturo et al., The einstein telescope: a third-generation gravitational wave observatory. *Class. Quantum Grav.* **27**, 194002 (2010)
7. D. Reitze et al., Cosmic explorer: the U.S. CoNTRibution to gravitational-wave astronomy beyond LIGO. *Bull. Am. Astron. Soc.* **51**, 51 (2019)
8. B. Sathyaprakash et al., Scientific objectives of Einstein telescope, *Class.Quant.Grav.* 29 (2012) 124013, *Class.Quant.Grav.* 30, (2013) 079501 (erratum)
9. P.R. Saulson, Terrestrial gravitational noise on a gravitational wave antenna. *Phys. Rev. D* **30**, 732–736 (1984)
10. M.G. Beker et al., Improving the sensitivity of future GW observatories in the 1-Hz to 10-Hz band: Newtonian and seismic noise. *Gen. Rel. Grav.* **43**, 623–656 (2011)
11. J.C. Driggers et al., Subtraction of newtonian noise using optimized sensor arrays. *Phys. Rev. D* **86**, 102001 (2012)
12. F. Acernese et al., Measurements of Superattenuator seismic isolation by Virgo interferometer. *Astropart. Phys.* **33**(3), 182–189 (2010)
13. F. Matichard et al., Seismic isolation of advanced LIGO: review of strategy, instrumentation and performance. *Class. Quant. Grav.* **32**, 185003 (2015)
14. M. Di Giovanni et al., A seismological study of the Sos Enattos area, the Sardinia candidate site for the Einstein telescope. *Seismol. Res. Lett.* **92**, 352–364 (2021)
15. F. Amann et al., Site-selection criteria for the Einstein telescope. *Rev. Sci. Instrum.* **91**, 9 (2020)
16. F. Badaracco, J. Harms, Optimization of seismometer arrays for the cancellation of Newtonian noise from seismic bodywaves *Class. Quant. Grav.* **36**, 145006 (2019)
17. J. Harms, K. Venkateswara, Newtonian-noise cancellation in large-scale interferometric GW detectors using seismic tiltmeters. *Class. Quant. Grav.* **33**, 234001 (2016)
18. C.C. Speake, D.B. Newell, The design and application of a novel highfrequency tiltmeter. *Rev. Scient. Instr.* **61**, 1500 (1990)
19. K. Venkateswara, C.A. Hagedorn, M.D. Turner, T. Arp, J.H. Gundlach, A high-precision mechanical absolute-rotation sensor. *Rev. Sci. Instrum.* **85**, 015005 (2014)
20. M.W. Coughlin et al., Implications of dedicated seismometer measurements on Newtonian-noise cancellation for Advanced LIGO. *Phys. Rev. Lett.* **121**, 22 (2018)
21. E. Calloni et al., High-bandwidth beam balance for vacuum-weight experiment and Newtonian noise subtraction. *Eur. Phys. J. Plus* **136**, 335 (2021)
22. G. Bimonte, E. Calloni, G. Esposito, L. Rosa, Energy-momentum tensor for a Casimir apparatus in a weak gravitational field. *Phys. Rev. D* **74**, 085011 (2006)
23. E. Calloni, M. De Laurentis, R. De Rosa, L. Di Fiore, G. Esposito, F. Garufi, L. Rosa, C. Rovelli, P. Ruggi, F. Tafuri et al., Towards weighing the condensation energy to ascertain the Archimedes force of vacuum. *Phys. Rev. D* **90**, 022002 (2014)
24. S. Avino, E. Calloni et al., Progress in a vacuum weight search experiment. *MDPI Phys.* **2**, 1–13 (2020)
25. D.V. Martynov et al., The sensitivity of the advanced LIGO detectors at the beginning of gravitational wave astronomy. *Phys. Rev. D* **93**, 112004 (2016)
26. P.R. Saulson, Thermal noise in mechanical experiments. *Phys. Rev. D* **42**, 2437–2445 (1990)
27. F. Matichard, M. Evans, Bulletin of the seismological society of america, review: tilt-free low-noise seismometry 105 No. 2A, pp. 497-510

28. N. Azaryan, J. Budagov et al., The seismic angular noise of an industrial origin measured by the precision laser inclinometer in the LHC location area. *Phys. Particles Nuclei Lett.* **16**, 343–353 (2019)
29. L. Naticchioni et al., Microseismic studies of an underground site for a new interferometric gravitational wave detector. *Class. Quantum Grav.* **31**, 105016 (2014)

Appendix D

Progress in a Vacuum Weight Search Experiment

Article

Progress in a Vacuum Weight Search Experiment

Saverio Avino ^{1,2}, Enrico Calloni ^{2,3,*} , Sergio Caprara ^{4,5} , Martina De Laurentis ^{2,3},
Rosario De Rosa ^{2,3}, Tristano Di Girolamo ^{2,3}, Luciano Errico ^{2,3}, Gianluca Gagliardi ^{1,2} ,
Marco Grilli ^{4,5} , Valentina Mangano ^{4,5}, Maria Antonietta Marsella ^{4,5} , Luca Naticchioni ^{4,5},
Giovanni Piero Pepe ^{2,3}, Maurizio Perciballi ⁵, Gabriel Pillant ⁶, Paola Puppo ⁵, Piero Rapagnani ^{4,5},
Fulvio Ricci ^{4,5}, Luigi Rosa ^{2,3}, Carlo Rovelli ^{7,8,9}, Paolo Ruggi ⁶, Naurang L. Saini ^{4,5}, Daniela
Stornaiuolo ^{2,3}, Francesco Tafuri ^{2,3} and Arturo Tagliacozzo ^{2,3}

¹ National Institute of Optics (CNR-INO), Sezione di Napoli, Via Campi Flegrei 34—Comprensorio “A. Olivetti”, I-80078 Pozzuoli (NA), Italy; saverio.avino@ino.cnr.it (S.A.); gianluca.gagliardi@ino.cnr.it (G.G.)

² Istituto Nazionale Fisica Nucleare (INFN), Sezione di Napoli, Complesso Universitario Monte S. Angelo, Edificio 6, Via Cinthia, I-80126 Naples, Italy; martina.delaurentis@na.infn.it (M.D.L.); rosario.derosa@na.infn.it (R.D.R.); tristano.digirolamo@na.infn.it (T.D.G.); luciano.errico@na.infn.it (L.E.); gpepe@na.infn.it (G.P.P.); luigi.rosa@na.infn.it (L.R.); daniela.stornaiuolo@unina.it (D.S.); Francesco.Tafuri@na.infn.it (F.T.); arturo@na.infn.it (A.T.)

³ Università Federico II Napoli, Dipartimento di Fisica “Ettore Pancini”, Complesso Universitario Monte S. Angelo, Edificio 6, Via Cinthia, I-80126 Naples, Italy

⁴ Università di Roma La Sapienza, Dipartimento di Fisica, Piazzale Aldo Moro, I-00185 Roma, Italy; sergio.caprara@roma1.infn.it (S.C.); marco.grilli@roma1.infn.it (M.G.); valentina.mangano@roma1.infn.it (V.M.); maria.marsella@uniroma1.it (M.A.M.); luca.naticchioni@roma1.infn.it (L.N.); piero.rapagnani@roma1.infn.it (P.R.); fulvio.ricci@roma1.infn.it (F.R.); naurang.saini@roma1.infn.it (N.L.S.)

⁵ Istituto Nazionale Fisica Nucleare (INFN), Sezione di Roma, Piazzale Aldo Moro, I-00185 Roma, Italy; maurizio.perciballi@roma1.infn.it (M.P.); paola.puppo@roma1.infn.it (P.P.)

⁶ European Gravitational Observatory EGO, via E. Amaldi, Santo Stefano a Macerata, I-56021 Cascina (Pisa), Italy; gabriel.pillant@ego-gw.it (G.P.); paolo.ruggi@ego-gw.it (P.R.)

⁷ Centre de Physique Théorique Campus of Luminy, Case 907, F-13288 Marseille, France; rovell@cpt.univ-mrs.fr

⁸ Aix-Marseille Université, Site du Pharo, 58 bd Charles Livon, F-13284 Marseille, France

⁹ Université de Toulon, Campus de La Garde, La Valette Avenue de l'Université, F-83130 Toulon, France

* Correspondence: enrico.calloni@na.infn.it

Received: 31 October 2019; Accepted: 13 December 2019; Published: 25 December 2019



Abstract: We present the status of the art of the Archimedes experiment, devoted to measuring the debated interaction of quantum vacuum fluctuations and gravity. The method is essentially the weighing of the transition energy of a layered superconductor where the contribution of vacuum energy to the transition energy is expected to be relevant. The transition is obtained by modulating the temperature of the superconducting sample at a frequency of about 10 mHz and the expected change of weight is measured with a suitably designed high sensitivity cryogenic beam balance. In this paper, we present an overview of the experiment, discussing the expected signal to be measured, and presenting in particular the result of a prototype balance operated in our present laboratory. In the frequency range of the measurement, the sensitivity is affected mainly by seismic, thermal, sensor, and control noise. We discuss these points showing in particular the design of the cryogenic apparatus, the final balance, and the quiet seismic site that will host the final measurement.

Keywords: quantum fluctuations; gravity; vacuum energy; Casimir energy

1. Introduction

In current physics, the contribution of vacuum energy to the stress–energy tensor in the Einstein equations [1] is still an open question. Despite long and deep investigations, there is not yet a convincing explanation of the fact that the enormous amount of energy attributed by quantum mechanics to mechanics does not significantly determine the geometry of our universe [2–8] and, moreover, it is still questioned how and whether the vacuum fluctuations do interact with gravity [9–13]. Theoretical results can be controversial even in the usual approach of quantum field theory in weak gravitational field [14] so that, even if the general expectation is that vacuum energy does gravitate, a deeper understanding is generally required and experiments are considered [15].

From an experimental point of view, it is important to note that in the recent past the scientific community focused on the possibility of verifying or discarding the various hypotheses by measuring the effects of the gravitational field on a Casimir cavity [16–21], in particular by performing a weighing measurement on a rigid Casimir cavity [22–24].

The expected force that on Earth the gravitational field can exert on a suitable realized Casimir cavity is in any case very small but it could be detectable if a suitable modulation of the force and an extremely sensitive apparatus were used. In principle, energy modulation in a Casimir cavity could be obtained by radiating semi-conductive plates with light to move electrons from the valence to conductive band, resulting in a modulation of plates reflectivity and thus of the vacuum energy. Such kind of modulations has been proved to be efficient when measuring a change of the Casimir force among moving plates [25–27], but unfortunately it would be useless for the weight measurement in a rigid cavity because the change of the Casimir energy would be several orders of magnitude lower than the electromagnetic energy deposited through the light. A possible way to change the plates reflectivity using an amount of energy comparable with Casimir variation is by using a superconductive transition. In particular, type I superconductors can be used to test the modulation of the Casimir energy in a suitable cavity formed by superconductive plates separated by a dielectric [28–31]. Unfortunately, in this case, even if the behavior of the superconductor were very well known, the absolute value of the energy variation would be too small to be weighed. On the contrary, if type II layered superconductors were considered, the absolute energy variation could be compatible with a weigh measurement. Type II layered superconductors, such as the Yttrium Barium Copper Oxide (YBCO) or the Bismuth Strontium Calcium Copper Oxide (BiSCCO), are formed by planes that undergo a superconductive transition separated by nanometric layers that remain dielectric. As first noticed by Kempf, they are naturally rigid Casimir cavities, so that in these samples not only the absolute energy variation could be compatible with a weight measurement, but also the relative contribution of Casimir energy is expected to be high [32–34]. On this basis, we recently started an experiment, called Archimedes, to measure the weight variation of a type II superconductive sample undergoing a superconductive transition in order to evaluate the force exerted by the gravitational field on a Casimir cavity.

The measurement must be performed with an extremely sensitive balance working at cryogenic temperature, modulating the superconductive transition at very low frequencies, about tens of mHz, and operating in a seismically quiet site, in order not to be limited by seismic noise. In the following, we describe the main issues of the experiment, recalling the magnitude of the expected signal, explaining in particular the main choices and studies of the experimental apparatus and the first results on a prototype of beam balance. Details on the mechanical, optical, and control loop are presented to show the most interesting results. The other cornerstone of the experiment, the cryogenic system, is also presented: the final design is shown, discussing the main items. Considering that the measurement greatly benefits from being performed in quiet seismic environments, we briefly describe the site chosen for the measurement: the underground laboratory named Sardinia Gravitation Laboratory (SAR-GRAV),

presently under construction in Lula (Sardinia, Italy). Finally, the path toward the final measurement is presented.

Interestingly, such an apparatus turns out to be of interest also for low mass dark matter search [35]. More generally, extremely sensitive beam balances can be used as absolute rotation sensors, which are becoming now relevant instruments for Newtonian Noise subtraction in gravitational wave detectors [36,37]. The balance prototype that is discussed is in fact presently acquiring seismic data at the Virgo site during its scientific Run O3.

2. General Scheme of the Experiment

In various papers [23,24], the force exerted by the gravitational field on a rigid Casimir cavity at rest on Earth has been calculated: it is directed upward and it is equal to:

$$\vec{F} = \frac{E_c}{c^2} \vec{g} \quad (1)$$

where E_c is the (negative) Casimir energy, c is the speed of light, and \vec{g} is the Earth gravitational acceleration. The theoretical calculation of this force assumes that the pressure of the vacuum fluctuation also follows the equivalence principle, thus the Archimedes measurement is actually a zero measurement of the red-shifting of vacuum pressure in gravitational field [16,23]. The force is extremely tiny and thus the measurement must be performed by modulating the effect.

The method proposed to modulate the Casimir energy in a rigid cavity is by modulating the plates reflectivity with a superconducting transition: when the plates are superconducting they are more reflective and the vacuum is better expelled from the cavity, resulting in a lowering of the energy and, if it gravitates, of the weight [23,31]. If the Casimir cavity is composed of type I superconductors plates, for temperatures lower but not far from the transition temperature, the contribution of the vacuum energy variation to the total condensation energy is comparable with the contribution of the variation of the chemical binding energy [28–31]. Under these conditions, once the weight measurement is performed, it would be not an issue to recover the contribution of the vacuum energy to the weight.

Unfortunately, as already stated, the absolute value of energy variation is too small to be weighed. The superconductors, instead, will be of a layered type II, such as YBCO or BiSCCO: layered superconductors are a natural stack of partially-reflecting, coupled Casimir cavities, whose condensation energy is much higher with respect to type one superconductors, and is expected to be directly influenced by vacuum fluctuations, as firstly noticed by Kempf [32]. The percentage of condensation energy that is due to the Casimir energy is still under evaluation. In the most optimistic case, it is almost the totality [32]; further theoretical and experimental studies are not in disagreement with Kempf's order of magnitude estimation of the effect [33,34]. It is important to note that all calculations to estimate the vacuum fluctuations contribution to the superconductor condensation energy have been performed until now within a macroscopic approximation. Although the results obtained with this approach are not in contradiction with experimental tests, they cannot be considered yet completely satisfactory. A microscopic scattering approach which includes virtual scattering of photons within the layers with Cooper pair breaking and recombination can account for the change of the electromagnetic spectrum, according to the Anderson–Higgs mechanism [38] and the change of Casimir energy with respect to the normal metal phase, and it is presently under development in our group.

The actual weight measurement will have an accuracy of a few percent, thus it will be possible to ascertain the interaction of gravitational field with vacuum fluctuations even if the contribution were proven to be of this order of magnitude.

The proposed scheme of the measurement is given in Figure 1: two discs of layered superconductor are suspended to the arm of the balance. The two discs are made of the same material but with different

doping and oxygen content. The arm is in aluminum to maintain low weight and momentum of inertia. The length of the arm is 1.4 m and it is suspended on low dissipative joints. The temperature modulation is the same in the two discs but only one undergoes the superconductive transition, thanks to the different oxygen content [39,40]: in this way, the phonon energy variation, which is equal on both samples, is cancelled out (does not give a signal on the balance).

The superconductive samples are 3 mm thick and have a radius of 0.15 m. Therefore, the expected amplitude of the force modulation is $f_a = 5 \times 10^{-16}$ N [23]. The expected integration time is $T = 4 \times 10^6$ s (about two months). To compare the signal with noises, usually expressed in terms of amplitude spectral density, and taking into account the two months of integration time, the equivalent amplitude spectral density of the torque signal is $\tilde{\tau} = 7 \times 10^{-13}$ N/ $\sqrt{\text{Hz}}$.

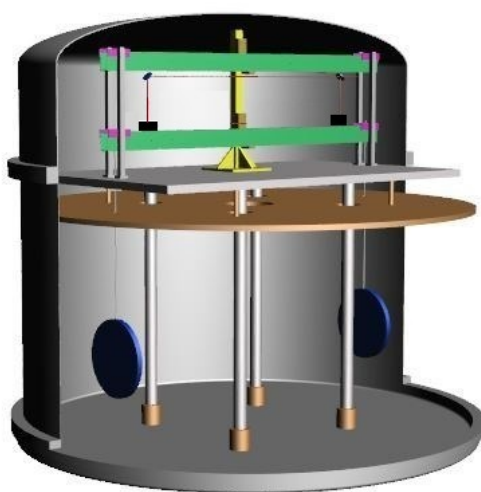


Figure 1. Sketch of the final balance experiment. Each disc is suspended on one end-arm and surrounded by a metallic enclosure for thermal actuation (not shown). The optical read-out is a Michelson interferometer and the signal is taken with respect to a reference arm.

3. The Cryogenic System

The Archimedes experiment is designed to work at a temperature of about 90 K. To reach this goal, a particular cryostat, working with liquid nitrogen, has been designed and its construction is expected to be finished in 2020. The cryostat is given in Figure 2.

The chamber where the experiment is housed can be completely covered with liquid nitrogen. However, even when the nitrogen level falls below the upper chamber flange, an aluminum screen attached to the steel chamber ensures a good thermal uniformity. The volume of liquid nitrogen in the tank is about 4000 L. Considering a typical thermal input of about 2 W/m^2 , the evaporation time of nitrogen will be about five months. The cryostat is equipped with a level probe for liquid nitrogen, a series of thermometers, and a heater of several kW located at the bottom of the experimental chamber and soaked in cryogenic liquid. In this way, it is possible to force the evaporation of the liquid nitrogen and reduce the time needed to access the experiment when necessary, as could be required in the first period of commissioning. The cryostat is designed in such a way that the experimental chamber can also be used as a simple vacuum chamber to operate the experiment at room temperature, as requested in the first period. For this purpose, all flanges have the possibility of being closed with Viton or indium gaskets. The upper socket, from which all the electrical and optical connections will enter the inner experimental zone, is

designed in such a way that can be used both at cryogenic temperature and at room temperature, when, in the first period, only the inner part of the cryostat will be mounted.

The idea behind the design of the cryostat and therefore the experimental chamber is to provide a rigid platform, the lower flange of the chamber, over which to build the experiment. Once the inner part of the experiment is assembled and pre-commissioned, the cylinder of the cryostat will be positioned. Finally, the upper flange will be installed. In this way, the cryostat will only minimally perturb the rest of the experimental apparatus during its assembly. This setup will allow the needed tests and commissioning at room temperature. When the cooling down will be necessary, the two external cylinders will be installed and the upper socket connected to the outermost chamber.

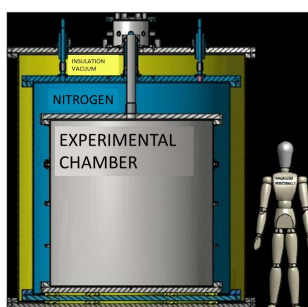


Figure 2. Cryostat. It is formed by three chambers: the experimental chamber, the liquid nitrogen chamber and the insulation chamber. The total height is 3.15 m, the diameter of the inner chamber is 1.8 m, and the diameter of the most external chamber is 2.4 m. The basement is formed by three flanges, the most external has diameter of 2.6 m.

Temperature Actuators

Temperature modulation is needed to force the superconductor to enter and exit the superconducting state, in order to obtain the desired modulation of the Casimir energy. The temperature must be modulated around the sample transition temperature with amplitude of a few K. Thermal exchange must happen without direct mechanical contact with the sample, since this would imply uncontrolled forces on the sample and destroy the force measurement. The only allowed solution is to have the sample in thermal equilibrium with the radiation bath. The temperature is regulated by the surrounding screen, heated from outside. The modulation frequency depends on the thermal properties of the sample and of the surrounding screen. Accurate simulation and geometry definition is necessary to obtain an efficient modulation. In this way, the cavity (the multi-cavity formed by the multi-layer superconductor) exchanges energy only with the radiation and the vacuum, and the radiation is used to confine and expel the vacuum from the cavity. The only variation of the sample is its transition from normal to superconductor state, and vice versa. The weight variation is the condensation energy weight, which in turn is the weight of the vacuum energy confined/expelled from the cavity. Several simulations have been carried out with the help of finite elements analysis, with transition temperatures in the range 90–130 K. The sample is suspended on the arm balance with a low conductivity thin wire and it is completely surrounded by the thermal screen. The temperature of the screen, made of copper, is modulated by a laser. The laser solution is preferred since it is simple and safer compared with other solutions, such as heating with electrical currents, which could interact with the sample. The screen is attached to the cryostat. A typical sample temperature modulation curve is given in Figure 3. It is evident that an amplitude of a few degrees is obtained at the frequency of 5 mHz, compatible with the requirements.

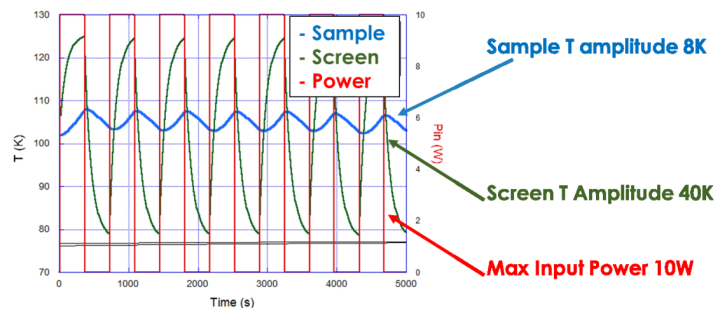


Figure 3. Simulation of the temperature modulation.

4. The Balance Prototype

To test the most critical points in the realization of this extremely sensitive device, a balance prototype, working at room temperature, was realized and tested. The balance prototype shares with the final one several mechanical parts and the sensing scheme. The arm length prototype is 0.5 m long, with respect to 1.4 m of that in the final balance. In the prototype, the reference arm is not suspended. The optical read-out of the balance prototype is very similar to the final one, being composed by an optical lever and a Michelson interferometer. As shown in Figure 4, the arms of the Michelson interferometer have different length. Other optical configurations, such as a Mach–Zehnder, would warrant an easy design with equal arm-lengths, but the Michelson interferometer was chosen since its optics on the measurement arm are simple mirrors impinged at 90 degrees. This configuration minimizes spurious couplings with other degrees of freedom of the balance arm. It is presently under study an equalization of the two arm-lengths with optics added on the balance reference arm. The optical lever is a high range sensor used in feedback mode to bring the interferometer in the linear regime. In the configuration with the loop closed on the optical lever, the balance can work even in the presence of high seismic noise, recover from earthquakes, and operate for quite long time, of the order of weeks, without need of external actions. The apparatus has been used in this configuration since the seismic noise in the laboratory is quite high. The balance prototype scheme is given in Figure 4. The light path in the Michelson interferometer is shown in green. The light path of the optical lever is shown in red: the light is first reflected on the back of the arm, and then transmitted by the beam splitter to a quadrant photodiode. In this configuration, the majority of the light is not used, being both partially transmitted when impinges the first time on the beam splitter and partially back-reflected when impinges on the beam splitter for the second time. This is not a problem since we are not limited by shot noise and, moreover, in the future, the light transmitted at the first impingement can be used for noise subtraction, if necessary.

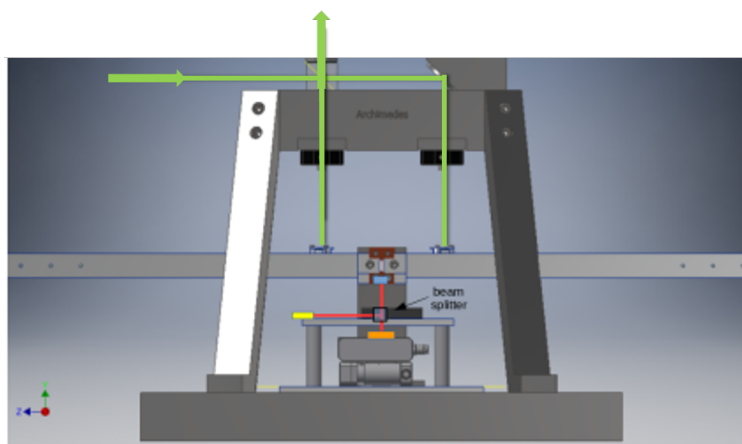


Figure 4. Sketch of the prototype balance and of the read-out system.

In the mechanics, particularly important is the design of the joints from which the balance arm is suspended: they contribute to the restoring torque and directly affect the sensitivity. They must be sufficiently soft to obtain readable signals and keeping the resonance frequency in the tens of mHz frequency region. The design implemented is inspired by the joints used in the rotational sensor of Venkateswara et al. [41]. In that case, the stiffness was lowered thanks to a very thin thickness, as small as 0.02 mm. In our case, we designed a bundle with a thickness of 0.1 mm, height of 6 mm, and width of 0.5 mm. Our design made easier the joint machining, and hence is cheaper. The joints design is given in Figure 5.

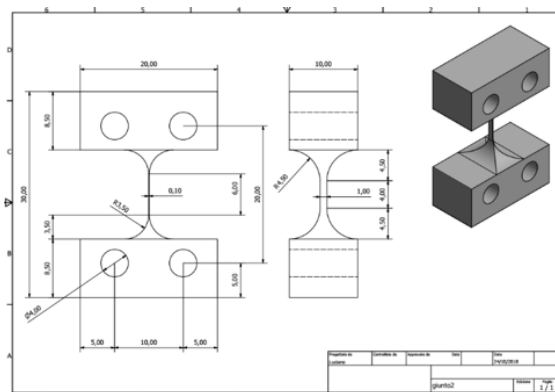


Figure 5. Technical sketch of the joints.

The first test of the balance was performed in our laboratory in Naples. Unfortunately, in the laboratory, the seismic noise is very high even at high frequencies, above 10 Hz, so that the interferometer signal is extremely noisy even at high frequencies. The best way to run the apparatus in these conditions is to close the feedback loop on the optical lever, without closing the control loop with the interferometer, and to recover the interferometer sensitivity by subtracting the optical lever noise with an off-line analysis. The actuation system is composed of electrostatic actuators as typically used in the control of torsion pendulums [42,43]. In our case, the actuators are four metallic plates located at the sides of the balance beam. The balance beam is grounded while the actuators are driven by a DC voltage supplier, which can reach the maximum voltage of 2000 V. The actuator torque is quadratic in the applied voltage with coupling factor $\beta = 2.5 \cdot 10^{-11} \text{ Nm/V}^2$. The maximum torque is $t_{max} = 10^{-4} \text{ Nm}$. The control signal is

linearized by operating the square root of the error signal before sending it to the actuators. Such a kind of control is extremely useful to test the validity of control loops, to test the long term behavior of the balance, and to define a noise budget for future commissioning when the balance will be operated in a quiet site. The control scheme is given in Figure 6.

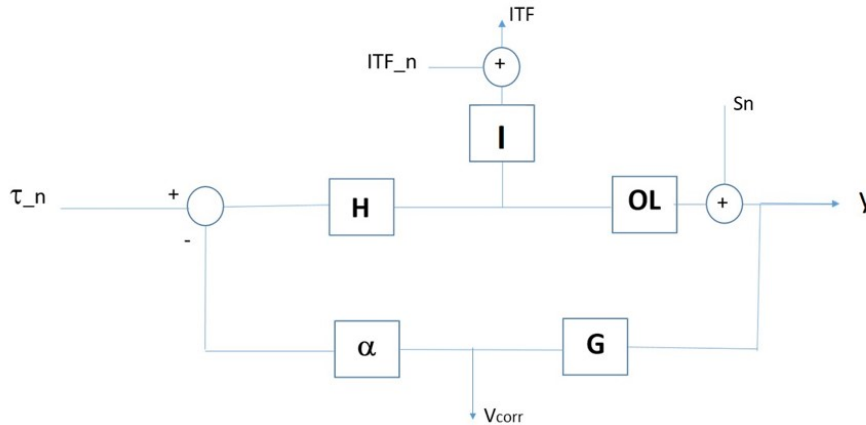


Figure 6. Block diagram of the balance control loop. See text for the meaning of each block and signal names.

The optical lever has a relatively modest sensitivity since its role is to lead the system to working point and then leave the loop closed on the error signal of the interferometer. However, as mentioned above, the high frequency seismic noise prevents closing the loop on the interferometric signal. Without complicating the system and in view of using the instrument in the much better conditions of the Sos-Enattos site, a check of the balance performance can be done anyway. The starting point is the consideration that at very low frequencies, below 100 mHz, the sensitivity of the interferometer is better than the optical lever even under these conditions. Therefore, even if the signal is not compatible with the closing of the loop, it can be used off-line as a noise subtraction. To explain the subtraction procedure, it is useful to illustrate the loop diagram (Figure 6). The signal read by the optical lever is y , the one read from the interferometer is ITF , and the correction voltage sent to the amplifiers is V_{corr} . The H function is the plant (measured in rad/Nm), I is the sensitivity of the interferometer (measured in V/rad), OL is the sensitivity of the optical lever (measured in V/rad), G is the control filter (dimensionless), and α is the function (which is a constant in this case) describing the amplifiers and actuators (Nm/V). τ_n indicates the equivalent external torque noise and ITF_n and S_n indicate the read-out noises of the interferometer and of the optical lever, respectively. Since the system is linear, for sake of simplicity, the outputs y , ITF , and V_{corr} can be written separately as linear functions of the input signals S_n and τ_n . In particular, for S_n , we obtain:

$$y = \frac{S_n}{1+\alpha GH}, ITF = -\frac{\alpha GH}{1+\alpha GH} S_n, V_{corr} = -\frac{G}{1+\alpha GH} S_n, \text{ and, as a function of } \tau_n:$$

$$y = \frac{H}{1+\alpha GH} \tau_n, ITF = \frac{\alpha H}{1+\alpha GH} \tau_n, V_{corr} = -\frac{GH}{1+\alpha GH} \tau_n$$

The signal of interest is called *Out* and it is defined as: $Out = ITF - \alpha HV_{corr}$. It cancels the noise from the optical lever using the interferometer signal. This effect is evident by writing it explicitly:

$$Out = ITF - \alpha HV_{corr} = \left[-\frac{\alpha GH}{1 + \alpha GH} + \frac{\alpha GH}{1 + \alpha GH} \right] S_n + H \left[\frac{1}{1 + \alpha GH} + \frac{\alpha GH}{1 + \alpha GH} \right] \tau_n + ITF_n \quad (2)$$

Notice that the read-out noise of the interferometer is added as a last term since it does not enter the loop. In the out signal, the contribution of the sensing noise of the optical lever is cancelled and the signal is a measure of the torque acting on the balance and the measurement noise is determined by the interferometer sensitivity:

$$Out = H \left[\frac{1}{1 + \alpha GH} + \frac{\alpha GH}{1 + \alpha GH} \right] \tau_n + ITF_n = H\tau_n + ITF_n \quad (3)$$

This signal can be better understood if we consider the high gain regime, typical of the low frequency region, where the weight measurement will be performed. If the signal of the optical lever is dominated by the external torque, ITF signal is suppressed, the whole signal is found in V_{corr} , and from their difference $H\tau_n$ is recovered, being dominated by V_{corr} . Conversely, if the signal of the optical lever is dominated by the lever noise, the arm is tilted by the control loop to cancel the optical lever error signal, and ITF reads exactly the movement generated by V_{corr} . In this case, the subtraction of these signals cancels the lever noise. As stated above, this subtraction is useful only in conditions of high seismic noise. In the quiet conditions at Sos-Enattos, the optical lever will be used only to bring the interferometer to the working point, and then the loop error signal will become the interferometer signal.

Preliminary results are given in Figures 7 and 8. Figure 7 shows the tilt signals. It can be noticed how the interferometer signal and the correction $V_{corr} \cdot H$ are similar at low frequencies. In this condition, the interferometer is actually reading the tilt of the arm forced by the loop to cancel the error signal of the optical lever, dominated by the optical lever read-out noise, and the combination of the signals as previously described is expected to be effective. Figure 8 shows the result of the subtraction. The low-frequency signal is efficiently subtracted, being in the high gain regime. In the high-frequency region, where the gain of the loop is lower than unity, as expected, no gain is observed in the combined signal. The main outcome of these results is the demonstration of the effectiveness of the mechanical, sensing, and actuating systems, of the robustness of the control loop and of the effectiveness of the noise subtraction techniques thanks to a very good knowledge of the system. All these features are very promising in view of the installation of the balance in the seismically quiet Sos-Enattos site. However, the resulting sensitivity is also quite interesting, since in the frequency region lower than 100 mHz, down a few mHz, the torque sensitivity is comparable with the best in the world [41], reaching a few times 10^{-11} Nm/ $\sqrt{\text{Hz}}$.

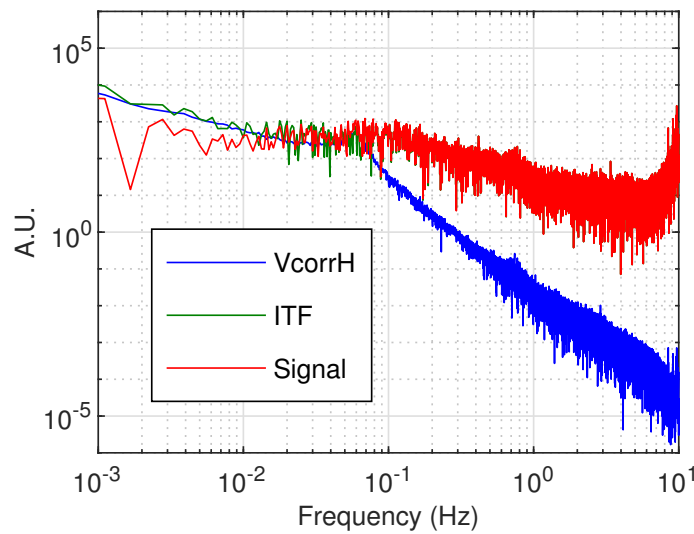


Figure 7. Interferometric signal (green), the signal $\alpha H \cdot V_{corr}$ (blue), and the subtracted signal named *Out* (red), see text for the definitions of the variables.

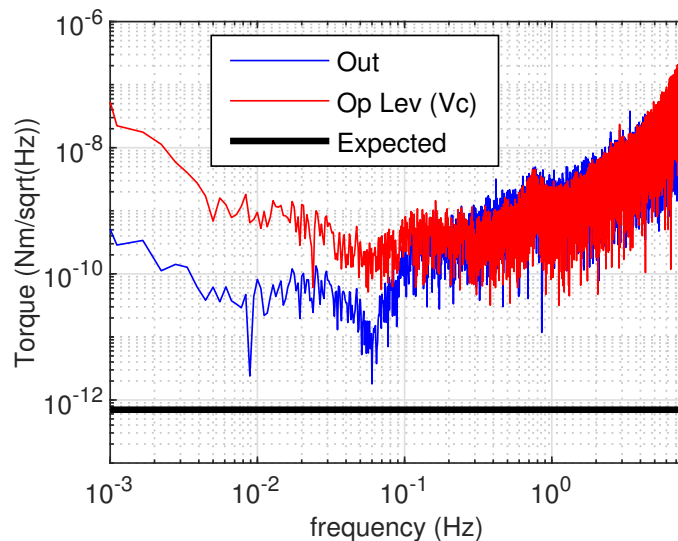


Figure 8. Balance sensitivity to torque before (blue) and after (red) subtraction. The final expected signal is shown in black.

5. Discussion

Working in a high seismic noise environment is problematic for the balance. High seismicity prevents easily closing the loop on the interferometer error signal, forcing to maintain the error signal on the more noisy optical lever. Our results demonstrate that the balance can indeed be controlled with good efficiency and good sensitivity, therefore they are very promising. Nonetheless, the optimal configuration for the balance is to work in a quiet seismic environment.

In Italy, after long investigations, an extremely quiet site has been individuated: the Sos-Enattos mine, on Sardinia Island. In this region, the seismic noise, also at frequencies lower than 0.1 Hz, lies very near

the New Low Noise Model (NLNM) from Peterson [44]. This site is so quiet that it has been proposed as a strong candidate to host the European underground third generation gravitational wave detector, named Einstein Telescope (ET) [45,46]. The mine is preserved by the I.G.E.A. s.p.a. company and is located near the village of Lula in Sardinia. It is a former mine of schist rocks composed by sphalerite ([Zn,Fe]S) and galena (PbS). While waiting for the final choice of the site for the ET, several Italian institutions decided to build an underground laboratory SAR-GRAV, devoted to hosting experiments on gravitation or seismology that need particularly quiet seismic conditions. At the surface, a laboratory for medium size experiments (e.g., Archimedes) is already available. The underground laboratory is presently under construction, the designed cavern being about 200 m² area with a 10 m height.

Archimedes installation on site will start on February 2020 and the first period of commissioning and testing of the apparatus will be performed at the surface and at room temperature. The sensitivity of the balance, already promising, is expected to greatly benefit from working in such good seismic conditions (especially if compared with the really noisy conditions of our laboratory in Naples), and, indeed, it is expected to gain, during two years of commissioning, the two orders of magnitude which separate the present sensitivity from the final one.

Author Contributions: Conceptualization, E.C., L.E., F.R., P.R. (Paolo Ruggi), P.R. (Piero Rapagnani), L.R., C.R., P.P. and A.T.; and Investigation, S.A., E.C., S.C., M.D.L., R.D.R., L.E., T.D.G., G.G., M.G., V.M., M.A.M., L.N., N.L.S., M.P., G.P.P., G.P., P.P., P.R. (Paolo Ruggi), D.S. and F.T. All authors have read and agreed to the published version of the manuscript.

Funding: This research was funded by INFN.

Conflicts of Interest: The authors declare no conflict of interest.

References

- Weinberg, S. The Cosmological Constant Problem. *Rev. Mod. Phys.* **1989**, *61*, 1–23. [[CrossRef](#)]
- Bianchi, E.; Rovelli, C. Why all these prejudices against a constant? *arXiv preprint* **2010**, arXiv:1002.3966.
- Padmanabhan, T.; Padmanabhan, H. Cosmological Constant from the Emergent Gravity Perspective. *Int. J. Mod. Phys. D* **2014**, *23*, 1430011. [[CrossRef](#)]
- Padmanabhan, T. The Atoms Of Space, Gravity and the Cosmological Constant. *Int. J. Mod. Phys. D* **2016**, *25*, 1630020. [[CrossRef](#)]
- Sola, J. Cosmological constant and vacuum energy: Old and new ideas. *J. Phys. Conf. Ser.* **2013**, *453*, 012015. [[CrossRef](#)]
- Cree, S.S.; Davis, T.M.; Ralph, T.C.; Wang, Q.; Zhu, Z.; Unruh, W.G. Can the fluctuations of the quantum vacuum solve the cosmological constant problem? *Phys. Rev. D* **2018**, *98*, 063506. [[CrossRef](#)]
- Lombrise, L. On the cosmological constant problem. *Phys. Lett. B* **2019**, *797*, 134804. [[CrossRef](#)]
- Kohri, K.; Matsui, H. Cosmological Constant Problem and Renormalized Vacuum Energy Density in Curved Background. *JCAP* **2017**, *1706*, 006. [[CrossRef](#)]
- Wang, Q.; Zhu, Z.; Unruh, W.G. How the huge energy of quantum vacuum gravitates to drive the slow accelerating expansion of the Universe. *Phys. Rev. D* **2017**, *95*, 103504. [[CrossRef](#)]
- Mazzitelli, F.D.; Trombetta, L.G. Comment on “How the huge energy of quantum vacuum gravitates to drive the slow accelerating expansion of the Universe”. *Phys. Rev. D* **2018**, *97*, 068301. [[CrossRef](#)]
- Wang, Q.; Unruh, W.G. Reply to “Comment on ‘How the huge energy of quantum vacuum gravitates to drive the slow accelerating expansion of the Universe’”. *Phys. Rev. D* **2018**, *97*, 068302. [[CrossRef](#)]
- Bengochea, G.R.; Okon, E.; Sudarsky, D. Can the quantum vacuum fluctuations really solve the cosmological constant problem? *arXiv* **2019**, arXiv:1906.05406.
- Mostepanenko, V.M.; Klimchitskaya, G.L. Whether an Enormously Large Energy Density of the Quantum Vacuum Is Catastrophic. *Symmetry* **2019**, *11*, 314. [[CrossRef](#)]

14. Lima, A.P.C.M.; Alencar, G.; Muniz, C.R.; Landim, R.R. Null second order corrections to Casimir energy in weak gravitational field. *JCAP* **2019**, *1907*, 011. [[CrossRef](#)]
15. Sorge, F. Casimir effect in a weak gravitational field: Schwinger's approach. *Class. Quantum Grav.* **2019**, *36*, 235006. [[CrossRef](#)]
16. Bimonte, G.; Calloni, E.; Esposito, G.; Rosa, L. Energy-momentum tensor for a Casimir apparatus in a weak gravitational field. *Phys. Rev. D* **2006**, *74*, 085011. [[CrossRef](#)]
17. Milton, K.A.; Shajesh, K.V.; Fulling, S.A.; Parashar, P. How does Casimir energy fall? IV. Gravitational interaction of regularized quantum vacuum energy. *Phys. Rev. D* **2014**, *89*, 064027. [[CrossRef](#)]
18. Blasone, M.; Lambiase, G.; Petruzzello, L.; Stabile, A. Casimir effect in Post-Newtonian Gravity with Lorentz-violation. *Eur. Phys. J. C* **2018**, *78*, 976. [[CrossRef](#)]
19. Lambiase, G.; Stabile, A. Casimir effect in Extended Theories of Gravity. *Phys. Rev. D* **2017**, *95*, 084019. [[CrossRef](#)]
20. Buoninfante, L.; Lambiase, G.; Petruzzello, L.; Stabile, A. Casimir effect in quadratic theories of gravity. *Eur. Phys. J. C* **2019**, *79*, 41. [[CrossRef](#)]
21. Burdyuzha, V. The Dark Components of the Universe Are Slowly Clarified. *J. Exp. Theor. Phys.* **2017**, *124*, 358–368. [[CrossRef](#)]
22. Chen, X. Vacuum fluctuation force on a rigid Casimir cavity in de Sitter and Schwarzschild-de Sitter spacetime. *Int. J. Mod. Phys. A* **2012**, *27*, 1250166. [[CrossRef](#)]
23. Calloni, E.; De Laurentis, M.; De Rosa, R.; Di Fiore, L.; Esposito, G.; Garufi, F.; Rosa, L.; Rovelli, C.; Ruggi, P.; Tafuri, F.; et al. Towards weighing the condensation energy to ascertain the Archimedes force of vacuum. *Phys. Rev. D* **2014**, *90*, 022002. [[CrossRef](#)]
24. Shevchenko, V.; Shevrin, E. Archimedes Force on Casimir Apparatus. *Mod. Phys. Lett. A* **2016**, *31*, 1650166. [[CrossRef](#)]
25. Chen, F.; Klimchitskaya, G.L.; Mostepanenko, V.M.; Mohideen, U. Control of the Casimir force by the modification of dielectric properties with light. *Phys. Rev. B* **2007**, *76*, 035338. [[CrossRef](#)]
26. Banishev, A.A.; Chang, C.C.; Castillo-Garza, R.; Klimchitskaya, G.L.; Mostepanenko, V.M.; Mohideen, U. Modifying the Casimir force between indium tin oxide film and Au sphere. *Phys. Rev. B* **2012**, *85*, 045436. [[CrossRef](#)]
27. Decca, R.S. Differential Casimir measurements on an engineered sample: Some experimental details. *Int. J. Mod. Phys. A* **2016**, *31*, 1641024. [[CrossRef](#)]
28. Bimonte, G.; Calloni, E.; Esposito, G.; Milano, L.; Rosa, L. Towards measuring variations of Casimir energy by a superconducting cavity. *Phys. Rev. Lett.* **2005**, *94*, 180402. [[CrossRef](#)]
29. Bimonte, G.; Calloni, E.; Esposito, G.; Rosa, L. Variations of Casimir energy from a superconducting transition. *Nucl. Phys. B* **2005**, *726*, 441. [[CrossRef](#)]
30. Bimonte, G.; Born, D.; Calloni, E.; Esposito, G.; Huebner, U.; Il'ichev, E.; Rosa, L.; Tafuri, F.; Vaglio, R. Low noise cryogenic system for the measurement of the Casimir energy in rigid cavities. *J. Phys. A* **2008**, *41*, 164023. [[CrossRef](#)]
31. Allocca, A.; Bimonte, G.; Born, D.; Calloni, E.; Esposito, G.; Huebner, U.; Il'ichev, E.; Rosa, L.; Tafuri, F. Results of measuring the influence of Casimir energy on superconducting phase transitions. *J. Supercond. Novel Magn.* **2012**, *25*, 2557. [[CrossRef](#)]
32. Kempf, A. On the Casimir effect in the high- T_c cuprates. *J. Phys. A Math. Theor.* **2008**, *41*, 164038. [[CrossRef](#)]
33. Orlando, M.T.D.; Rouver, A.N.; Rocha, J.R.; Cavichini, A.S. Correlation among the effective mass (m^*), λ_{ab} and T_c of superconducting cuprates in a Casimir energy scenario. *Phys. Lett. A* **2018**, *382*, 1486–1491. [[CrossRef](#)]
34. Rosa, L.; Avino, S.; Calloni, E.; Caprara, S.; De Laurentis, M.; De Rosa, R.; Esposito, G.; Grilli, M.; Majorana, E.; Pepe, G.P.; et al. Casimir energy for two and three superconducting coupled cavities: Numerical calculations. *Eur. Phys. J. Plus* **2017**, *132*, 478. [[CrossRef](#)]
35. Nozzoli, F. A balance for Dark Matter bound states. *Astropart. Phys.* **2017**, *91*, 22–33. [[CrossRef](#)]
36. Harms, J.; Venkateswara, K. Newtonian-noise cancellation in large-scale interferometric GW detectors using seismic tiltmeters. *Class. Quant. Grav.* **2016**, *33*, 234001. [[CrossRef](#)]

37. Coughlin, M.W.; Harms, J.; Driggers, J.; McManus, D.J.; Mukund, N.; Ross, M.P.; Slagmolen, B.J.J.; Venkateswara, K. Implications of dedicated seismometer measurements on Newtonian-noise cancellation for Advanced LIGO. *Phys. Rev. Lett.* **2018**, *121*, 221104. [[CrossRef](#)]
38. Negele, J.W.; Orland, H. *Quantum Many-Particle Systems*; Frontiers in Physics; Addison Wesley Publishing Company: Boston, MA, USA, 1987.
39. Rodriguez, J.E.; Lopez, J. Thermoelectric figure of merit of oxygen-deficient YBCO perovskites. *Phys. B* **2007**, *387*, 143–146. [[CrossRef](#)]
40. Peng, Y.Y.; Dellea, G.; Minola, M.; Conni, M.; Amorese, A.; Di Castro, D.; De Luca, G.M.; Kummer, K.; Salluzzo, M.; Sun, X.; et al. Influence of apical oxygen on the extent of in-plane exchange interaction in cuprate superconductors. *Nat. Phys.* **2017**, *13*, 1201–1206. [[CrossRef](#)]
41. Venkateswara, K.; Hagedorn, C.A.; Turner, M.D.; Arp, T.; Gundlach, J.H. A high-precision mechanical absolute-rotation sensor. *Rev. Sci. Instrum.* **2014**, *85*, 015005. [[CrossRef](#)]
42. Ciani, G.; Chilton, A.; Apple, S.; Olatunde, T.; Aitken, M.; Mueller, G.; Conklin, J.W. A New Torsion Pendulum for Gravitational Reference Sensor Technology Development. *Rev. Sci. Instrum.* **2017**, *88*, 064502. [[CrossRef](#)] [[PubMed](#)]
43. Bassan, M.; Cavalleri, A.; De Laurentis, M.; De Marchi, F.; De Rosa, R.; Di Fiore, L.; Dolesi, R.; Finetti, N.; Garufi, F.; Grado, A.; et al. Actuation crosstalk in free-falling systems: Torsion pendulum results for the engineering model of the LISA path finder gravitational reference sensor. *Astropart. Phys.* **2018**, *97*, 19–26. [[CrossRef](#)]
44. Naticchioni, L.; Perciballi, M.; Ricci, F.; Coccia, E.; Malvezzi, V.; Acernese, F.; Barone, F.; Giordano, G.; Romano, R.; Punturo, M.; et al. Microseismic studies of an underground site for a new interferometric gravitational wave detector. *Class. Quant. Grav.* **2014**, *31*, 105016. [[CrossRef](#)]
45. Punturo, M.; Somira, K. Underground gravitational wave observatories: KAGRA and ET. *Int. J. Mod. Phys.* **2013**, *D22*, 1330010. [[CrossRef](#)]
46. Schiavinato, L.; Mazzalai, P.; Gemme, G.; Losurdo, G.; Punturo, M.; Paoli, A.; Ricci, F.; Calloni, E.; Oggiano, G.; Carpinelli, M. A new underground laboratory for exploring the universe: The design of a third generation gravitational wave observatory. In *Tunnels and Underground Cities: Engineering and Innovation Meet Archaeology, Architecture and Art. Proceedings of the WTC2019 ITA-AITES World Tunnel Congress, Naples, Italy, 3–9 May 2019*; Peila, D., Viggiani, G., Celestino, T., Eds.; CRC Press/Balkema: Leiden, The Netherlands, 2019; pp. 4225–4234.



© 2019 by the authors. Licensee MDPI, Basel, Switzerland. This article is an open access article distributed under the terms and conditions of the Creative Commons Attribution (CC BY) license (<http://creativecommons.org/licenses/by/4.0/>).

Bibliography

- Abbott, B. P. et al. (2016a). GW151226: Observation of Gravitational Waves from a 22-Solar-Mass Binary Black Hole Coalescence. *Phys. Rev. Lett.*, 116(24):241103.
- Abbott, B. P. et al. (2016b). Observation of Gravitational Waves from a Binary Black Hole Merger. *Phys. Rev. Lett.*, 116(6):061102.
- Abbott, B. P. et al. (2017a). GW170814: A Three-Detector Observation of Gravitational Waves from a Binary Black Hole Coalescence. *Phys. Rev. Lett.*, 119(14):141101.
- Abbott, B. P. et al. (2017b). GW170817: Observation of Gravitational Waves from a Binary Neutron Star Inspiral. *Phys. Rev. Lett.*, 119(16):161101.
- Abbott, R. et al. (2002). Seismic isolation for Advanced LIGO. *Class. Quant. Grav.*, 19:1591–1597.
- Abbott, R. et al. (2021). Observation of Gravitational Waves from Two Neutron Star–Black Hole Coalescences. *Astrophys. J. Lett.*, 915(1):L5.
- Acernese, F. et al. (2010). Measurements of Superattenuator seismic isolation by Virgo interferometer. *Astropart. Phys.*, 33(3):182–189.
- Acernese, F. et al. (2015). Advanced Virgo: a second-generation interferometric gravitational wave detector. *Class. Quant. Grav.*, 32(2):024001.
- Allocca, A., Bimonte, G., Born, D., Calloni, E., Esposito, G., Huebner, U., Il'ichev, E., Rosa, L., and Tafuri, F. (2012). Results of measuring the influence of Casimir energy on superconducting phase transitions. *Jour. Super. and Novel Mag.*, 25:2557.
- Badaracco, F. and Harms, J. (2019). Optimization of seismometer arrays for the cancellation of newtonian noise from seismic body waves. *Classical and Quantum Gravity*, 36(14):145006.

- Bardeen, J. M., Carter, B., and Hawking, S. W. (1973). The Four laws of black hole mechanics. *Commun. Math. Phys.*, 31:161–170.
- Bassan, M., De Laurentis, M., De Rosa, R., Di Fiore, L., Errico, L., Garufi, F., Grado, A., Minenkov, Y., Pucacco, G., and Visco, M. (2019a). Liquid actuated gravity experiments. *Int. J. Mod. Phys. D*, 28(09):1950115.
- Bassan, M. et al. (2016). Approaching Free Fall on Two Degrees of Freedom: Simultaneous Measurement of Residual Force and Torque on a Double Torsion Pendulum. *Phys. Rev. Lett.*, 116(5):051104.
- Bassan, M., Laurentis, M. D., Rosa, R. D., Fiore, L. D., Errico, L., Garufi, F., Grado, A., Minenkov, Y., Pucacco, G., Spagnuolo, V., Stanga, R., and Visco, M. (2019b). Improving sensitivity and duty-cycle of a double torsion pendulum. *Classical and Quantum Gravity*, 36(12):125004.
- Bekenstein, J. D. (1972). Black holes and the second law. *Lett. Nuovo Cim.*, 4:737–740.
- Bekenstein, J. D. (1973). Black holes and entropy. *Phys. Rev. D*, 7:2333–2346.
- Beker, M., Cella, G., and et al. (2011). Improving the sensitivity of future gw observatories in the 1-hz to 10-hz band: Newtonian and seismic noise. *General Relativity and Gravitation*, 43.
- Bimonte, G., Born, D., Calloni, E., Esposito, G., Huebner, U., Il'ichev, E., Rosa, L., Tafuri, F., and Vaglio, R. (2008a). Low noise cryogenic system for the measurement of the Casimir energy in rigid cavities. *Journal of Physics A: Mathematical and Theoretical*, 41(16):164023.
- Bimonte, G., Calloni, E., Esposito, G., Milano, L., and Rosa, L. (2005a). Towards measuring variations of Casimir energy by a superconducting cavity. *Physical Review Letters*, 94:180402.
- Bimonte, G., Calloni, E., Esposito, G., and Rosa, L. (2005b). Variations of Casimir energy from a superconducting transition. *Nuclear Physics B*, 726:441–463.
- Bimonte, G., Calloni, E., Esposito, G., and Rosa, L. (2006). Energy-momentum tensor for a Casimir apparatus in a weak gravitational field. *Physical Review D*, 74(8).
- Bimonte, G., Calloni, E., Esposito, G., and Rosa, L. (2007). Relativistic mechanics of Casimir apparatuses in a weak gravitational field. *Physical Review D*, 76:025008.

- Bimonte, G., Calloni, E., and Rosa, L. (2008b). Gravity of magnetic stresses and energy. *Physical Review D*, 77:044026.
- Bordag, M. (2006). The casimir effect for thin plasma sheets and the role of the surface plasmons. *Journal of Physics A: Mathematical and General*, 39(21):6173.
- Bordag, M., Klimchitskaya, G., Mohideen, U., and Mostepanenko, V. (2009). *Advances in the Casimir Effect*. International Series of Monographs on Physics. Oxford University Press.
- Bressi, G., Carugno, G., Onofrio, R., and Ruoso, G. (2002). Measurement of the Casimir force between parallel metallic surfaces. *Physical Review Letters*, 88(4).
- Brown, L. and Maclay, G. (1969). Vacuum Stress between Conducting Plates: An Image Solution. *Physical Review - PHYS REV X*, 184:1272–1279.
- Calloni, E., De Laurentis, M., De Rosa, R., Di Fiore, L., Esposito, G., Garufi, F., Rosa, L., Rovelli, C., Ruggi, P., and Tafuri, F. (2014). Towards weighing the condensation energy to ascertain the Archimedes force of vacuum. *Physical Review D*, 90:022002.
- Calloni, E., Di Fiore, L., Esposito, G., Milano, L., and Rosa, L. (2002). Vacuum fluctuation force on a rigid Casimir cavity in a gravitational field. *Physics Letters A*, 297.
- Carroll, S. M. and Remmen, G. N. (2016). What is the entropy in entropic gravity? *Phys. Rev. D*, 93:124052.
- Cree, S., Davis, T., Ralph, T., Wang, Q., Zhu, Z., and Unruh, W. (2018). Can the fluctuations of the quantum vacuum solve the cosmological constant problem? *Physical Review D*, 98.
- Einstein, A. (1907). On the Relativity Principle and the conclusions drawn from it. *Jahrbuch der Radioaktivitat und Elektronik*, 4.
- Einstein, A. (1915). The Field Equations of Gravitation. *Sitzungsber. Preuss. Akad. Wiss. Berlin (Math. Phys.)*, 1915:844–847.
- Fulling, S. A., Milton, K. A., Parashar, P., Romeo, A., Shajesh, K. V., and Wagner, J. (2007). How does Casimir energy fall? *Physical Review D*, 76:025004.
- Harms, J. (2019). Terrestrial gravity fluctuations. *Living Reviews in Relativity*, 22(6).

- Harms, J. and Venkateswara, K. (2016). Newtonian-noise cancellation in large-scale interferometric GW detectors using seismic tiltmeters. *Classical and Quantum Gravity*, 33(23):234001.
- Harry, G. M. (2010). Advanced LIGO: The next generation of gravitational wave detectors. *Class. Quant. Grav.*, 27:084006.
- Hua, W. et al. (2004). Low-frequency active vibration isolation for advanced LIGO. *Proc. SPIE Int. Soc. Opt. Eng.*, 5500:194–205.
- Hubble, E. (1929). A relation between distance and radial velocity among extra-galactic nebulae. *Proceedings of the National Academy of Sciences*, 15(3):168–173.
- Itzykson, C. and Zuber, J. B. (1980). *Quantum Field Theory*. McGraw-Hill International Book Company.
- Kerr, R. P. (1963). Gravitational field of a spinning mass as an example of algebraically special metrics. *Phys. Rev. Lett.*, 11:237–238.
- Klimchitskaya, G., Mohideen, U., and Mostepanenko, V. (2009). The Casimir force between real materials: Experiment and theory. *Reviews of Modern Physics*, 81(4).
- Kohri, K. and Matsui, H. (2017). Cosmological constant problem and renormalized vacuum energy density in curved background. *Journal of Cosmology and Astroparticle Physics*, 2017(06):006–006.
- Kolekar, S. and Padmanabhan, T. (2010). Ideal gas in a strong gravitational field: Area dependence of entropy. *Physical Review D*, 83.
- Kragh, H. S. and Overduin, J. M. (2014). *The Weight of the Vacuum: A Scientific History of Dark Energy*. SpringerBriefs in Physics. Springer.
- Lombriser, L. (2019). On the cosmological constant problem. *Physics Letters B*, 797:134804.
- Losurdo, G. (2002). The inertial damping of the VIRGO superattenuator and the residual motion of the mirror. *Class. Quant. Grav.*, 19:1631–1637.
- Misner, C. W., Thorne, K. S., and Wheeler, J. A. (1973). *Gravitation*. W. H. Freeman, San Francisco.

- Naticchioni, L., Perciballi, M., Ricci, F., Coccia, E., Malvezzi, V., Acernese, F., Barone, F., Giordano, G., Romano, R., Punturo, M., De Rosa, R., Calia, P., and Loddo, G. (2014). Microseismic studies of an underground site for a new interferometric gravitational wave detector. *Classical and Quantum Gravity*, 31:105016.
- Padmanabhan, T. (2002a). Gravity from spacetime thermodynamics. *Astrophysics and Space Science*, 285.
- Padmanabhan, T. (2002b). The Holography of gravity encoded in a relation between entropy, horizon area and action for gravity. *Gen. Rel. Grav.*, 34:2029–2035.
- Padmanabhan, T. (2015). Gravity and its thermodynamics. *Current Science*, 109:2236.
- Padmanabhan, T. (2016). The atoms of space, gravity and the cosmological constant. *International Journal of Modern Physics D*, 25(07):1630020.
- Padmanabhan, T. and Padmanabhan, H. (2014). Cosmological constant from the emergent gravity perspective. *International Journal of Modern Physics D*, 23(06):1430011.
- Peskin, M. E. and Schroeder, D. V. (1995). *An introduction to quantum field theory*. Westview Press.
- Peterson, J. (1993). Observations and modeling of seismic background noise. *Open-file Report*.
- Riess, A. G., Filippenko, A. V., Challis, P., Clocchiatti, A., Diercks, A., Garnavich, P. M., Gilliland, R. L., Hogan, C. J., Jha, S., Kirshner, R. P., Leibundgut, B., Phillips, M. M., Reiss, D., Schmidt, B. P., Schommer, R. A., Smith, R. C., Spyromilio, J., Stubbs, C., Suntzeff, N. B., and Tonry, J. (1998). Observational evidence from supernovae for an accelerating universe and a cosmological constant. *The Astronomical Journal*, 116(3):1009–1038.
- Rosa, L., Avino, S., Calloni, E., Caprara, S., De Laurentis, M., De Rosa, R., Esposito, G., Grilli, M., Majorana, E., P. Pepe, G., Petrarca, S., Puppo, P., Rapagani, P., Ricci, F., Rovelli, C., Ruggi, P., Saini, N., Stornaiolo, C., and Tafuri, F. (2017). Casimir energy for two and three superconducting coupled cavities: Numerical calculations. *The European Physical Journal Plus*, 132.
- Ross, M. P., Venkateswara, K., Mow-Lowry, C. M., Cooper, S., Warner, J., Lantz, B., Kissel, J., Radkins, H., Shaffer, T., Mittleman, R. K., Pele, A., and Gundlach, J. H.

- (2020). Towards windproofing ligo: reducing the effect of wind-driven floor tilt by using rotation sensors in active seismic isolation. *arXiv: Instrumentation and Detectors*.
- Singha, A. et al. (2021). Characterization of the seismic field at Virgo and improved estimates of Newtonian-noise suppression by recesses. *Class. Quant. Grav.*, 38(24):245007.
- Solà Peracaula, J. (2013). Cosmological constant and vacuum energy: Old and new ideas. *Journal of Physics Conference Series*, 453.
- Tinkham, M. (1975). *Introduction to superconductivity*. International series in pure and applied physics. McGraw-Hill International Book Company.
- Tolman, R. C. (1930). On the weight of heat and thermal equilibrium in general relativity. *Phys. Rev.*, 35:904–924.
- Tolman, R. C. and Ehrenfest, P. (1930). Temperature equilibrium in a static gravitational field. *Phys. Rev.*, 36:1791–1798.
- Venkateswara, K., Hagedorn, C. A., Turner, M. D., Arp, T., and Gundlach, J. H. (2014). A high-precision mechanical absolute-rotation sensor. *Review of Scientific Instruments*, 85(1):015005.
- Wald, R. M. (1984). *General Relativity*. The University of Chicago Press.
- Weinberg, S. (1989). The cosmological constant problem. *Reviews of Modern Physics*, 61(1).